DGK Ausschuss Geodäsie (DGK)
der Bayerischen Akademie der Wissenschaften

Reihe C | Dissertationen | Heft Nr. 974

Igor Koch

Spectral and Spatial Investigation of Ocean Tide Signatures in GRACE(-FO) Post-Fit Residuals

München 2026

Verlag der Bayerischen Akademie der Wissenschaften, München

ISSN 0065-5325 ISBN 978 3 7696 5386 1

DGK Ausschuss Geodäsie (DGK)
der Bayerischen Akademie der Wissenschaften

Reihe C Dissertationen Heft Nr. 974

Spectral and Spatial Investigation of Ocean Tide Signatures in GRACE(-FO) Post-Fit Residual

Von der Fakultät für Bauingenieurwesen und Geodäsie
der Gottfried Wilhelm Leibniz Universität Hannover
zur Erlangung des akademischen Grades
Doktor-Ingenieurin (Dr.-Ing.)
genehmigte Dissertation

von

Igor Koch, M. Sc.

München 2026

Verlag der Bayerischen Akademie der Wissenschaften, München

ISSN 0065-5325 ISBN 978 3 7696 5386 1

Adresse des Ausschusses Geodäsie (DGK)
der Bayerischen Akademie der Wissenschaften:

Ausschuss Geodäsie (DGK) der Bayerischen Akademie der Wissenschaften
Alfons-Goppel-Straße 11 ● D – 80 539 München
Telefon +49 – 89 – 23 031 1113 ● Telefax +49 – 89 – 23 031 - 1283 / - 1100
e-mail post@dgk.badw.de ● http://www.dgk.badw.de

Prüfungskommission:
Vorsitzender: Prof. Dr.-Ing. habil. Monika Sester
Referent: Prof. Dr.-Ing. Jakob Flury
Korreferenten: Prof. Dr.-Ing. habil. Florian Seitz
PD Dr.-Ing. Hamza Alkhatib

Tag der mündlichen Prüfung: 30.07.2025

:

Diese Dissertation ist auf dem Server des Ausschusses Geodäsie (DGK)
der Bayerischen Akademie der Wissenschaften, München unter <http://dgk.badw.de/>
sowie unter Wissenschaftliche Arbeiten der Fachrichtung Geodäsie und Geoinformatik
der Leibniz Universität Hannover (ISSN 0174-1454), Nr. 419,
<https://doi.org/10.15488/20291>, Hannover 2026, elektronisch publiziert

ISSN 0065-5325 ISBN 978 3 7696 5386 1

Abstract

The Gravity Recovery and Climate Experiment (GRACE, 2002–2017) was the first satellite mission to utilize low-low Satellite-to-Satellite Tracking (ll-SST), and the first mission able to monitor mass variations on Earth. Since 2018, the successor mission GRACE Follow-On (GRACE-FO) has been in orbit. The ll-SST concept involves two identical co-orbiting satellites separated by a distance of approximately 220 km. The distance between the satellites is precisely tracked by a K/Ka-band ranging system and serves as the main observable for the derivation of monthly gravity field solutions. These gravity field products are of major importance for studying mass variations within the Earth's system. The process of computing the monthly gravity field solutions involves satellite orbit modeling and parameter estimation as central components. Since the precise distance measurements provided by the K/Ka-band ranging system contain information on all influences affecting satellite dynamics, various background models are employed during satellite orbit modeling. These models are used to separate the signals that should conventionally be part of the gravity field solutions from disturbances related, for example, to tides, gravitational attraction from celestial bodies, and rapid mass variations in the atmosphere and oceans. Imperfections of ocean tide models are considered among the primary factors limiting the quality of GRACE and GRACE-FO gravity field products. Ocean tide models are known to exhibit significant inaccuracies, especially in polar regions where precise satellite altimetry observations are lacking, and in shallow water regions where ocean tide dynamics are more complex than those in open ocean areas.

As part of this work, a spectral analysis was conducted for the first time to examine ocean tide signatures in the ll-SST post-fit residuals. Monthly gravity field solutions and the corresponding range-rate post-fit residuals for the period from April 2002 to September 2023 were computed. The obtained range-rate post-fit residuals were low-pass filtered, numerically differentiated, and assigned to a global $5^\circ \times 5^\circ$ grid. Lomb–Scargle periodograms were computed for the time series in each grid, and then analyzed for frequencies with significant amplitudes occurring on a global scale. In total, over 30 prominent tidal frequencies were identified, which correspond not only to the major gravitationally excited tidal constituents but also to minor degree-2 tides, degree-3 tides, non-linear tides, and radiational tides. With the exception of a few tidal constituents, the corresponding amplitude maps almost exclusively show increased amplitudes in polar regions, along coastlines and confined to some regions of the open ocean. The most complex region where a large number of tidal frequencies show increased amplitudes is the Weddell Sea. Although most of the identified tidal frequencies were considered during orbit modeling, meaning that the amplitudes in the periodograms represent residual signal relative to the ocean tide model used, several unmodeled frequencies were identified. These include degree-3 tides $^3M_1$, $^3L_2$, $^3N_2$, $^3M_3$, the compound tides $2SM_2$ and $2MK_3/MO_3$, and the radiational triple S_3, T_3, R_3, with the latter two sharing their frequencies with the compound tides SP_3 and SK_3, respectively. All of these unmodeled tides have been scarcely studied or not studied at all thus far. A global altimetry-constrained ocean tide model for $^3M_3$ was just recently published. At the moment, for $^3M_1$, $^3L_2$, $^3N_2$ altimetry-based solutions are only available for the latitudes from -66° to $+66^\circ$, but not for the polar regions, where according to the performed spectral analysis large tidal variations exist. Data-constrained ocean tide solutions do not exist for the other frequencies. It was shown that purely hydrodynamic solutions can explain a large part of the degree-3 and radiational signal in the post-fit residuals. For the identified compound tides at the moment not even hydrodynamic models have been published yet. An analysis of altimetry data reveals a qualitative agreement with the $2SM_2$ and $2MK_3/MO_3$ patterns observed in the post-fit residuals. The findings presented suggest that the analysis of ll-SST post-fit residuals offers significant potential for validating ocean tide models. Future research should also explore the potential for assimilating ll-SST measurements into hydrodynamic models.

Keywords: Gravity field recovery, K-band post-fit residuals, Ocean tides

Kurzfassung

Das Gravity Recovery And Climate Experiment (GRACE, 2002–2017) war die erste Satellitenmission, die das Low-Low-Satellite-To-Satellite-Tracking (LL-SST) einsetzte, und die erste Mission, die in der Lage war, Massenvariationen auf der Erde zu verfolgen. Seit 2018 befindet sich die Nachfolgemission GRACE Follow-On (GRACE-FO) im Orbit. Das LL-SST-Konzept besteht aus zwei identischen Satelliten, die die Erde in einem gemeinsamen Orbit hintereinander umkreisen und durch einen Abstand von etwa 220 km getrennt sind. Dabei wird der Abstand zwischen den Satelliten präzise von einem K/Ka-Band-Ranging-System erfasst und dient als Hauptbeobachtung für die Berechnug monatlicher Schwerefeldlösungen. Diese Schwerefeldprodukte sind von zentraler Bedeutung für die Untersuchung von Massenvariationen im Erdsystem. Der Prozess der Berechnung monatlicher Schwerefeldlösungen umfasst die Satellitenorbitmodellierung und die Parameterschätzung als zentrale Komponenten. Da die präzisen Distanzmessungen des K/Ka-Band-Ranging-Systems Informationen über alle auf die Satellitendynamik wirkenden Einflüsse enthalten, werden während der Satellitenorbitmodellierung verschiedene Hintergrundmodelle eingesetzt, um die Signale, die konventionell Teil der Schwerefeldlösungen sein sollten, von Störbeiträgen zu trennen, die beispielsweise mit Gezeiten, gravitativer Anziehung durch Himmelskörper und schnellen Massenvariationen in der Atmosphäre und den Ozeanen zusammenhängen. Ungenauigkeiten der Ozeangezeitenmodelle gelten als wesentliche Faktoren, welche die Qualität der GRACE- und GRACE-FO-Schwerefeldprodukte beeinträchtigen. Ozeangezeitenmodelle weisen insbesondere in Polargebieten erhebliche Ungenauigkeiten auf, da dort präzise Satellitenaltimetrie-Beobachtungen fehlen, sowie in Flachwasserbereichen, wo die Dynamik der Ozeangezeiten komplexer ist als in offenen Ozeangebieten.

Im Rahmen dieser Arbeit wurde erstmals eine Spektralanalyse durchgeführt, um Ozeangezeiten-Signaturen in den LL-SST-Post-Fit-Residuen zu untersuchen. Monatliche Schwerefeldlösungen und die dazugehörigen K-Band-Range-Rate-Post-Fit-Residuen für den Zeitraum von April 2002 bis September 2023 wurden berechnet. Die erhaltenen Range-Rate-Post-Fit-Residuen wurden einer Tiefpassfilterung unterzogen, numerisch differenziert und einem globalen $5°\times5°$-Gitter zugewiesen. Lomb–Scargle-Periodogramme wurden für die Zeitreihen in jedem Raster berechnet und anschließend auf Frequenzen mit signifikanten Amplituden auf globaler Ebene analysiert. Insgesamt wurden über 30 auffällige Gezeitenfrequenzen identifiziert, die nicht nur den wichtigsten gravitationsbedingt angeregten Gezeitenkonstituenten entsprechen, sondern auch kleineren Grad-2-Gezeiten, Grad-3-Gezeiten, nichtlinearen Gezeiten und Strahlungsgezeiten. Mit Ausnahme einiger weniger Gezeitenkomponenten zeigen die entsprechenden Amplitudenkarten fast ausschließlich erhöhte Amplituden in Polarregionen, entlang von Küstenlinien und in einigen begrenzten Regionen des offenen Ozeans. Die komplexeste Region, in der eine große Anzahl von Gezeitenfrequenzen erhöhte Amplituden aufweist, ist das Weddellmeer. Obwohl die meisten der identifizierten Gezeitenfrequenzen während der Orbitmodellierung berücksichtigt wurden, was bedeutet, dass die Amplituden in den Periodogrammen ein Residualsignal gegenüber dem verwendeten Ozeangezeitenmodell darstellen, wurden mehrere unmodellierte Frequenzen identifiziert. Dazu gehören die Grad-3-Gezeiten $^3M_1$, $^3L_2$, $^3N_2$, $^3M_3$, die zusammengesetzten Gezeiten $2SM_2$ und $2MK_3/MO_3$, sowie die Strahlungsgezeiten S_3, T_3, R_3, wobei die beiden letzteren ihre Frequenzen jeweils mit den zusammengesetzten Gezeiten SP_3 und SK_3 teilen. Alle diese unmodellierten Gezeiten sind bisher kaum oder gar nicht untersucht worden. Ein globales Ozeangezeitenmodell für $^3M_3$, das Altimetriedaten verwendet, wurde erst kürzlich veröffentlicht. Zurzeit sind für $^3M_1$, $^3L_2$, $^3N_2$ altimetriebasierte Lösungen nur für die Breitengrade von $-66°$ bis $+66°$ verfügbar, nicht jedoch für die Polarregionen, wo gemäß der durchgeführten Spektralanalyse große Gezeitenvariationen existieren. Messdatenbasierte Ozeangezeitenlösungen sind für die anderen Frequenzen nicht vorhanden. Es wurde gezeigt, dass rein hydrodynamische Lösungen einen großen Teil des Grad-3- und des Strahlungssignals in den Post-Fit-Residuen erklären können. Für die identifizierten zusammengesetzten Gezeiten gibt es derzeit noch keine veröffentlichten hydrodynamischen Modelle. Eine Analyse von Altimetriedaten zeigt eine qualitative Übereinstimmung mit den $2SM_2$- und $2MK_3/MO_3$-Mustern in den Post-Fit-Residuen.

Die vorgestellten Ergebnisse deuten darauf hin, dass die Analyse von LL-SST-Post-Fit-Residuen, ein erhebliches Potenzial zur Validierung von Ozeangezeitenmodellen bietet. Zukünftige Untersuchungen sollten auch das Potenzial der Assimilation von LL-SST-Messungen in hydrodynamische Modelle untersuchen.

Schlagwörter: Schwerefeldbestimmung, K-Band-Post-Fit-Residuen, Ozeangezeiten

Acronyms

AIUB Astronomical Institute of the University of Bern

AOD Atmosphere and Ocean De-Aliasing

ASC Advanced Stellar Compass

ASD Amplitude Spectral Density

CCD Charge-Coupled Device

CHAMP Challenging Minisatellite Payload

CIO Celestial Intermediate Origin

CIP Celestial Intermediate Pole

CNES Centre National d'Études Spatiales (French National Space Agency)

CSR Center for Space Research

DE Development Ephemeris

DFT Discrete Fourier Transform

DGFI Deutsches Geodätisches Forschungsinstitut (German Geodetic Research Institute)

DLR Deutsches Zentrum für Luft- und Raumfahrt (German Aerospace Center)

DOWR Dual One-Way Ranging

DTU Technical University of Denmark

ECMWF European Centre for Medium-Range Weather Forecasts

Envisat Environmental Satellite

EOP Earth Orientation Parameter

EOT Empirical Ocean Tide

ERA Earth Rotation Angle

ERS European Remote Sensing satellite

EWH Equivalent Water Height

FES Finite Element Solution

FFT Fast Fourier Transform

GCRS Geocentric Celestial Reference System

GFZ Deutsches GeoForschungsZentrum (German Research Centre for Geosciences)

GIA Glacial Isostatic Adjustment

GNSS Global Navigation Satellite Systems

GOT Goddard Ocean Tide

GPS Global Positioning System

GRACE Gravity Recovery and Climate Experiment

GRACE(-FO) GRACE and GRACE Follow-On

GRACE-FO GRACE Follow-On

GRACE-SIGMA GRACE-Satellite Orbit Integration and Gravity Field Analysis in Matlab

GRGS Groupe de Recherche de Géodésie Spatiale (Spatial Geodesy Research Group)

IAU International Astronomical Union

ICGEM International Centre for Global Earth Models

IERS International Earth Rotation and Reference Systems Service

IfE Institut für Erdmessung (Institute of Geodesy, Leibniz University Hannover)

IHO International Hydrographic Organization

ITRS International Terrestrial Reference System

Jason Joint Altimetry Satellite Oceanography Network

JPL Jet Propulsion Laboratory

KBR K/Ka-Band Ranging

L1B Level-1B

ll-SST low-low Satellite-to-Satellite Tracking

LRI Laser Ranging Interferometer

LUH Leibniz University Hannover

MSSH Mean Sea Surface Height

NASA National Aeronautics and Space Administration

ODE Ordinary Differential Equation

OpenADB Open Altimeter Database

POD Precise Orbit Determination

PS Power Spectrum

PSD Power Spectral Density

RK Runge–Kutta

RL Release

RMS Root Mean Square

SDS Science Data System

SLA Sea Level Anomaly

SRF Science Reference Frame

SSH Sea Surface Height

STAR Space Three-Axis Accelerometer for Research

TAI International Atomic Time

TGP Tide-Generating Potential

TiME Tidal Model Forced by Ephemerides

TIO Terrestrial Intermediate Origin

TOPEX/Poseidon Topography Experiment/Poseidon

TPXO Oregon State University TOPEX/Poseidon Global Inverse Solution

TT Terrestrial Time

TUG Graz University of Technology

UT1 Universal Time 1

UTC Coordinated Universal Time

VCE Variance Component Estimation

VLBI Very Long Baseline Interferometry

Contents

Chapter 1

Introduction

1.1 GRACE(-FO) and ll-SST

The motion of artificial satellites is primarily affected by the gravitation of the Earth. When the orbit of a satellite—for example, represented as a set of positions and the corresponding time—is known, parameters describing the gravitation of the Earth, e.g., in terms of a potential field, can be inferred by linking the observed orbit to the theory of satellite dynamics through a functional model (e.g., Seeber, 2003). The specific parameters that can be inferred largely depend on general orbit characteristics, such as altitude and inclination, as well as the methods employed to observe the orbits (e.g., Nerem et al., 1995). The concept of studying Earth's gravitational potential and its variations by observing the relative positional changes of two identical satellites in the same orbit caused by gravitational and non-gravitational forces—also known as *low-low Satellite-to-Satellite Tracking* (ll-SST)—was proposed in the late 1960s (Wolff, 1969). Despite being included in various satellite gravimetry mission proposals over the next three decades, it was not until 1997 that the *Gravity Recovery And Climate Experiment* (GRACE) was proposed by the Center for Space Research (CSR, Austin), the German Research Center for Geosciences (GFZ, Deutsches GeoForschungsZentrum Potsdam) and the Jet Propulsion Laboratory (JPL, Pasadena), and then approved as part of the Earth System Science Pathfinder program of the National Aeronautics and Space Administration (NASA) as a joint mission with the German Aerospace Center (DLR, Deutsches Zentrum für Luft- und Raumfahrt) (Flechtner et al., 2021). The GRACE mission (Tapley et al., 2004), with a nominal lifetime of five years, remained operational for over 15 years following its launch in March 2002. In January 2018, after a brief gap of about one year, GRACE Follow-On (GRACE-FO) successfully continued the GRACE time series of Earth's gravitational potential measurements (Landerer et al., 2020). During the period from December 2011 to December 2012, ll-SST was employed in the NASA/JPL-operated Gravity Recovery and Interior Laboratory (GRAIL) mission to study the Moon's gravitational field (Zuber et al., 2013).

The ll-SST principle as implemented by GRACE and GRACE-FO, hereafter abbreviated as GRACE(-FO), involves the two identical co-orbiting satellites in an almost polar orbit separated by a distance of approximately 220 km at an initial low altitude of about 500 km (see Figure 1.1). The orbital variations are tracked continuously by a K/Ka-Band Ranging (KBR) assembly with micrometer precision (Bertiger et al., 2002; Dunn et al., 2003). Additionally, GRACE-FO is equipped with a nanometer-precise Laser Ranging Interferometer (LRI) for the purpose of technology demonstration for next generation satellite gravimetry and space-based gravitational wave detection missions (Abich et al., 2019). With ancillary information on the absolute position of the satellites measured by the onboard Global Navigation Satellite Systems (GNSS) receivers, the orientation of the satellite platforms in space from star cameras, and non-gravitational forces acting on the satellites sensed by the electrostatic accelerometers, it is possible to infer information about Earth's gravitation. The data from the onboard instruments is used for *gravity field recovery*, i.e., the derivation of products describing Earth's gravitational potential. The most common of these products are the so-called *gravity field solutions*, which represent the potential via a set of spherical harmonic coefficients, and are produced by various GRACE(-FO) analysis centers in Europe (e.g., Dahle et al., 2019b; Kvas et al., 2019a; Lemoine and Bourgogne, 2020; Koch et al., 2021; Lasser et al., 2023), the United States (e.g., Save, 2019a; Yuan, 2019) and China (e.g., Wang et al., 2015; Chen et al., 2019; Yu et al., 2021; Su et al., 2022; Zhong et al., 2022; Zhou et al., 2024). The temporal resolution of these solutions is typically one month, since after this period the ground track coverage is generally sufficiently dense to invert a stable solution

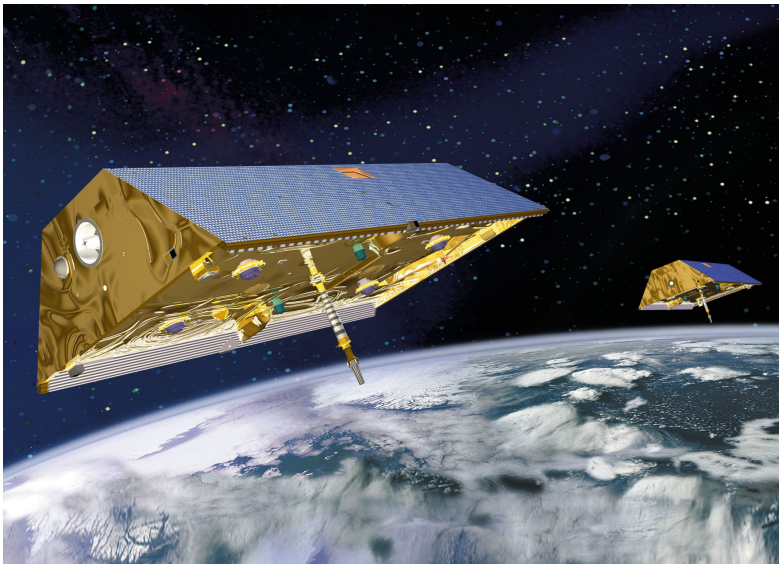

FIGURE 1.1: Artist's impression of the two satellites of the GRACE mision in orbit.[1] The GRACE(-FO) satellites were manufactured by Astrium (since 2014 part of Airbus Defense and Space) in Immenstaad am Bodensee (Germany) on behalf of JPL. The spacecraft design is based on Astrium's Flexbus platform (Zaglauer and Pitz, 2003). Dimensions of the GRACE and GRACE-FO satellites (length×height×width at bottom) are 3.1×0.7×1.9 m and 3.1×0.8×1.9 m, respectively (NASA, 2002, 2018).

without applying constraints. The monthly gravity field solutions from selected individual analysis centers are utilized by the Combination Service for Time-Variable Gravity Fields (COST-G) to produce combined solutions with improved noise characteristics (Jäggi et al., 2020; Meyer et al., 2023). The second most prevalent type of product, typically employing regularization in contrast to the commonly unconstrained spherical harmonic coefficient solutions, is known as a mass concentration (*mascon*) solution (e.g., Luthcke et al., 2013; Watkins et al., 2015; Save et al., 2016; Tregoning et al., 2022). Since GRACE(-FO) are the only satellite missions capable of tracking mass variations within the Earth's system with a relatively high spatial and temporal resolution, the gravity field products derived from their sensor data are crucial for numerous applications in Earth system sciences, as they form the data foundation, for example, for quantifying both natural variations and anthropogenic changes in terrestrial water storage, observing ice sheet melting, and evaluating the consequent impacts on sea-level rise (see, for example, the review articles by Wouters et al., 2014; Tapley et al., 2019; Chen et al., 2022; Rodell and Reager, 2023).

Insights from the analysis of the GRACE(-FO) sensor data, updated and newly developed geophysical background models, and the acquired know-how at the analysis centers over the past 20 years, have led to several reprocessing campaigns and the continuous enhancement of the monthly gravity field solutions. Currently, the quality of the derived gravity field products is largely limited by accelerometer noise, i.e., an inherent characteristic of the sensor, and by the imperfect models for ocean tides and high-frequency non-tidal mass variations in the Earth's system (e.g., Loomis et al., 2012; Flechtner et al., 2016). These models, forming part of a broader set of gravitational effects, are incorporated into the equation of motion during gravity field recovery to reduce the perturbing effects on the ll-SST measurements and to ensure that the final gravity field products primarily reflect signals related to continental hydrology, the cryosphere, and non-tidal solid Earth-related effects. Imperfections present in the models not only affect the overall orbit modeling accuracy and increase the noise level of the gravity field products but in special cases can also introduce undesirable gravity variations with periods ranging from several days to years into the gravity field solutions through the aliasing effect, i.e., the absorption of model errors by the gravity field product (e.g., Han et al., 2004; Ray and Luthcke, 2006; Seo et al., 2008; Visser et al., 2010).

[1] Image credit NASA: `https://sealevel.nasa.gov/missions/grace` (last accessed on 2025-02-28).

1.2 Ocean Tides and Ocean Tide Models

Ocean tides are periodic fluctuations of the sea level, primarily driven by the gravitational forces of the Moon and the Sun acting on the Earth (e.g., Pugh and Woodworth, 2014). The difference between the gravitational acceleration exerted by celestial bodies at a specific position and the gravitational acceleration at the Earth's center defines the theoretical tidal acceleration (e.g., Wenzel, 1997). With the ephemerides of the celestial bodies, the corresponding tidal potential can be expressed in terms of a harmonic decomposition into a set of hundreds to thousands of frequencies and amplitudes, forming the so-called *Tide-Generating Potential* (TGP) catalogues (e.g., Cartwright and Tayler, 1971; Hartmann and Wenzel, 1995). Components of this decomposition with particularly dominant amplitudes were given special alphanumeric designations, such as M_2, S_2, K_1, O_1 (see e.g., Melchior, 1966; Pugh and Woodworth, 2014), with the subscripts denoting the approximate frequency in times per day of the so-called tidal constituents. The real-world reaction to these individual components of astronomical tidal forcing creates tides in the Earth's system, including the larger part of the tidal variations in the oceans.

Ocean tide models consist of amplitudes and phases of a small set of tidal constituents, typically ranging from less than 10 to a few dozen, which aim to approximate the larger part of the tidal variation in the oceans. Ocean tide models can be classified into three categories (e.g., Stammer et al., 2014): a hydrodynamic model, a hydrodynamic model with assimilated data, and an empirical adjustment to an a priori model. A hydrodynamic model can be understood as a solution to the hydrodynamic equation (see e.g., Marchuk and Kagan, 1989; Zahel, 1997). Important variables and assumptions of a hydrodynamic model include information on the TGP, bottom friction, and bathymetry, among others. While observations from tide gauges can only contribute to an ocean tide model to a limited extent due to their uneven distribution and very localized nature, Sea Surface Height (SSH) observations from dedicated satellite radar altimetry missions play the primary role in constraining the hydrodynamic solutions by adjusting the model to assimilated real-world observations. In the empirical modeling approach, residual SSH signal derived from altimetry is used to estimate adjustments to an a priori (data-assimilated) hydrodynamic ocean tide model. TOPEX/Poseidon (1992–2006) (Fu et al., 1994) and its follow-on missions, Jason-1 (2001–2015), Jason-2 (2008–2019), and Jason-3 (since 2016), are satellite altimetry missions with sampling characteristics that are particularly well-suited for observing ocean tides. Due to the continuity of the time series, with now over 30 years of measurements, the information from these missions serves as a primary source for altimetry-based ocean tide models. However, since the primary mission objective was to study circulations in the ice-free ocean, an orbit inclination of 66° was selected. As a result, no data from these missions is available for data assimilation at latitudes beyond ±66°, consequently leading to larger ocean tide model uncertainties at higher latitudes (e.g., Stammer et al., 2014). While the higher latitudes are covered by other altimetry missions—here, ERS-1 and its successor missions, ERS-2 and Envisat, are particularly noteworthy—the seasonal and non-seasonal presence of ice in polar and near-polar regions makes the altimetry measurements only partially useful for data assimilation (e.g., Lyard et al., 2021). Furthermore, ocean tide models generally exhibit greater uncertainties near coasts and in shallow water regions. In these regions, tidal amplitudes are larger and wavelengths are shorter compared to those in the open ocean, so the effectiveness of satellite altimetry as a constraint diminishes (e.g., Ray et al., 2011; Stammer et al., 2014).

Ocean tide models that incorporate altimetry-derived SSHs are of greater importance for orbit modeling, compared to hydrodynamic models, as they provide more accurate solutions for the large amplitude tides (major tides) driven by lunisolar gravitational attraction and dominating the ocean tide spectrum. The major tides include several constituents with frequencies of approximately once and twice per day. These constituents refer to the degree 2 of the lunisolar TGP. In orbit modeling, the influence of minor gravitationally excited tides of degree 2 is typically inferred from the solutions of major constituents provided by the ocean tide model by assuming linear admittance. The concept of linear admittance relies on the assumption

that the ocean's tidal response is nearly linear with respect to the amplitude of the lunisolar forcing potential and varies smoothly with the excitation frequency (e.g., Munk and Cartwright, 1966; IERS Conventions, 2010). Consequently, the ocean's response to degree-2 tides with nearby frequencies is comparable and can be approximated to change linearly with the forcing frequency. Until recently, tides associated with the degree-3 component of the TGP played an insignificant role because of their small astronomical amplitudes and the difficulty in separating them from nearby, larger degree-2 tides. On a global scale the largest degree-3 tides were observed just a few years ago for the first time (Ray, 2020b, see also next section). In addition to these major and minor gravitationally excited tides, several other excitation mechanisms contribute to the total amplitude of the ocean tides. Non-linear effects in coastal and shallow water areas, for example, due to the friction of water with the ocean bottom topography, can generate overtides and compound tides when two or more gravitationally excited tides interact (e.g., Le Provost, 1991; Parker, 2007; Pugh and Woodworth, 2014). Periodic variations at tidal frequencies in atmospheric surface pressure caused by solar radiation lead to the formation of radiational ocean tides (e.g., Munk and Cartwright, 1966; Dobslaw and Thomas, 2005; Ray et al., 2023). The influence of solar radiation on the Earth system over seasonal timescales, for example affecting ice coverage and stratification, results in seasonal tidal modulations (e.g., Müller et al., 2014; Ray, 2022). All of these tides, which arise from more complex mechanisms rather than directly from the lunisolar gravitational forces, cannot be considered through linear admittance. The inference of minor gravitationally excited constituents can be distorted by these tides, as it is common for two or more ocean tide constituents with different origins to have the same frequency.

1.3 Research Related to ll-SST and Ocean Tides

The ability of the ll-SST technique to detect residual ocean tide signal, particularly in the polar regions where high-quality altimeter observations for ocean tide model assimilation are lacking, was recognized quite early on. One of the earliest studies related to ocean tide model errors detectable in GRACE data was carried out by Han et al. (2005c), just a few years after the start of the mission. The authors estimated 5-day gravity field models for the Antarctic region, covering the period from August 2002 to June 2004. The method used to compute the regional models is conceptually different from the processing scheme utilized for estimating monthly gravity field solutions in terms of spherical harmonic coefficients and instead relies on the estimation of along-track geopotential differences (Jekeli, 1999; Han et al., 2005b), which are then inverted to obtain the corresponding mass variations in terms of Equivalent Water Height (EWH) (Han et al., 2005a). The periodograms of the EWH time series indicated relatively large Power Spectral Density (PSD) values in the period bands 140–230 and 12–15 days, in which the GRACE aliasing periods of the constituents S_2 (≈161 days) and M_2 (≈13.6 days) are located, as had been predicted earlier, e.g., by Knudsen (2003) and Ray et al. (2003). The spatial features of sinusoidal amplitudes with periods of 161 and 13.6 days, fitted alongside a bias, linear trend, and an annual component to the 5-day EWH time series of each grid cell, revealed increased amplitudes beneath the Filchner–Ronne and Larsen Ice Shelves, suggesting residual ocean tide signal relative to the utilized CSR4.0 model (Eanes and Bettadpur, 1995, updated).

Later, the major ocean tide constituents M_2, O_1 and S_2 were directly estimated for the Antarctic region from 3 years of ll-SST observations (Han et al., 2007, 2008). The large amplitude constituent K_1 was not included due to the limited duration of the GRACE time series, while the respective aliasing period exceeds 7 years. In a manner similar to Han et al. (2005c), these estimates were parameterized as tidal sinusoids, co-estimated alongside the trend, bias, and seasonal component. A qualitative comparison with in situ measurements (King and Padman, 2005) indicated an agreement between the tidal variations observed by GRACE and the localized, sparse in situ measurements at several locations in Antarctica.

The mass anomalies from Han et al. (2007, updated) were later exploited by Egbert et al. (2009) to improve constituents M_2, S_2, O_1 of a hydrodynamic model through data assimilation. In an evaluation against independent data (tide gauges, ICESat laser altimeter crossover differences), the GRACE-constrained model

demonstrated a better performance relative to the prior ocean tide models TPXO7.1 (Egbert and Erofeeva, 2002, updated) and FES2004 (Lyard et al., 2006).

Killett et al. (2011) utilized 7 years of GRACE range-accelerations to derive ocean tide corrections expressed as point-mass mascons for the primary constituents M_2, S_2, O_1 and K_1 in the Arctic region relative to the ocean tide model FES2004, estimated simultaneously with an offset, trend, annual and semiannual variations. A similar methodology, with major modifications, was employed by Wiese et al. (2016) to estimate residual ocean tide signal in the Antarctic region from 11 years of GRACE data relative to the model GOT4.7 (Ray, 1999, updated).

Studies that extended their analysis beyond the polar regions, and particularly focused on improving gravity field recovery results, are outlined next. In the study by Bosch et al. (2009), a global assessment of residual ocean tide signal was performed by analyzing multi-mission satellite altimetry data relative to FES2004, as well as 4.5 years of monthly GRACE gravity field models (Schmidt et al., 2007) and range-rate observations (Mayer-Gürr et al., 2010). The authors found that GRACE observes tidal error signal at the S_2 and M_2 frequencies in regions similar to those identified in the residual altimetry data. While global EWH values derived from the monthly solutions were used to analyze the S_2 residual signal in GRACE data, the M_2 constituent, characterized by a submonthly aliasing period, was examined through a harmonic analysis of gridded along-track residual range-accelerations to determine the corresponding tidal amplitude and phase. Furthermore, the authors demonstrated that using the empirical ocean tide model EOT08a (Savcenko and Bosch, 2008)—which incorporates FES2004 as the a priori model along with corrections estimated from altimetry—instead of FES2004 as the background model for calculating the GRACE residual range-accelerations, led to a significant reduction of the residual ocean tide signal in the along-track data.

Building on the findings of the previous study, Mayer-Gürr et al. (2012) developed an empirical ocean tide model by combining GRACE data with EOT08a. The tidal constituents M_2, O_1, N_2 and Q_1 from GRACE were estimated together with the monthly gravity field solutions. The relative weighting of the normal matrices was determined using Variance Component Estimation (VCE) (Koch and Kusche, 2002). The evaluation of the combined model against EOT08a showed that the combined model slightly outperforms EOT08a in terms of smaller range-rate post-fit residuals and better performance across several other metrics.

Motivated by the goal of improving the quality of monthly gravity field solutions, Kvas et al. (2019a) estimated constrained tidal corrections relative to FES2014b (Lyard et al., 2021) for diurnal (O_1, P_1, S_1, K_1), semidiurnal (M_2, N_2, S_2) and long-periodic constituents (Mm, Mf, Mmtm) from 15 years of GRACE ll-SST data, together with the static gravity, constrained daily solutions, annual gravity parameters, and a trend. These corrections are used as a background model correction for their GRACE(-FO) gravity field solutions.

Several studies outlined next utilized GRACE ll-SST data primary for the validation and intercomparison of ocean tide models. In a study by Ray et al. (2009), an assessment of the four ocean tide models FES2004, TPXO7.1, and GOT00.2, GOT4.7 (both Ray, 1999, updated), was made utilizing 4 years of GRACE ll-SST data. The method employed is similar to the assessment of residual ocean tide signal in range-rate residuals as performed by Bosch et al. (2009), and involves binning the residual ll-SST data to specific grid cells, followed by a harmonic analysis at selected tidal frequencies. Ray et al. (2009) refer to this method as *qualitative* since the analyzed in-orbit residuals remain in ll-SST measurement units, and unlike in the studies discussed earlier, no estimation of tidal amplitudes and phases, spherical harmonic coefficients, or EWH is carried out (*quantitative* approach). In addition to the usual background model effects used in gravity field recovery, the authors also reduced the contribution from land hydrology (Rodell et al., 2004) and Glacial Isostatic Adjustment (GIA) (Peltier, 2004) from the range-rate measurements. Compared to the related studies discussed earlier, a greater number of tidal constituents were assessed (each of the four ocean tide models consists of 8 or more major constituents), including 16 minor tides inferred from the model

constituents using an admittance approach (Munk and Cartwright, 1966; Desai and Yuan, 2006). However, the authors explicitly only present residual tidal signal maps for a few selected constituents. Based on the regional similarities and differences among the four models highlighted by the qualitative comparison, they conclude that none of the four ocean tide models is flawless. In addition to oceanic tidal signal, the maps of selected constituents revealed indications of unmodeled atmospheric tides and/or hydrological effects (S_1, S_2, and the annual side lines of S_2). For the gravitationally excited constituent μ_2, the authors observed increased amplitudes in several shallow water regions, suggesting a possible non-linear contribution from the compound tide $2MS_2$.

Stammer et al. (2014) employed a method similar to that of Ray et al. (2009), using GRACE data from 2004 to 2010 as one of several approaches to evaluate the quality of the four major tidal constituents M_2, K_1, O_1, and S_2 across seven ocean tide models (see Stammer et al., 2014, Table 9). The authors concluded, in line with Ray et al. (2009), that no model is perfect or significantly superior in all regions of the globe. As a supplement to this work, Ray et al. (2019) presented results for FES2014, which was not included in the earlier model comparison.

The qualitative approach was used in two other studies, although not with a focus on intercomparison of ocean tide models. Line-of-sight gravity differences derived from the LRI onboard GRACE-FO were analyzed by Han et al. (2020) to examine the validity of the spherical surface and constant density assumptions, which are commonly adopted when converting gridded ocean tide model elevations into spherical harmonic coefficients for further use in orbit modeling. The authors concluded that these assumptions are responsible for a substantial part of the orbit modeling errors. The issue of the constant density assumption was already brought up by Ray et al. (2009); however, it was not as thoroughly investigated as in the work of Han et al. (2020).

In a recent seminal study by Ray (2020b), utilizing satellite altimetry data, the spatial structures of the four largest gravitationally excited tides of degree $n = 3$ (see Section 2.3.1), namely, $^3M_1$, $^3L_2$, $^3N_2$ and $^3M_3$, are—for the first time ever—mapped (almost) globally within the latitude range between $\pm 66°$. These effects are quite minute and detecting them requires the analysis of longer observation time series to overcome the low signal-to-noise ratio and, particularly for $^3M_1$, $^3L_2$, $^3N_2$, to separate them from the larger close-by tides of degree 2. By applying the qualitative approach to 7 years of GRACE ll-SST data, the study provides evidence that the GRACE ranging system is also sensitive to these small tides (see as an example the map excerpt of $^3M_3$ in Figure 2 of Ray, 2020b). Earlier, Ray et al. (2009) also examined the largest degree-3 tide $^3M_3$; however, they were unable to detect significant anomalies at this frequency within the short 4-year time series of GRACE ranging data.

1.4 Objective and Outline of the Thesis

As can be seen from the prior literature review, earlier research mainly addressed the inaccuracies of selected major ocean tide constituents. The aim of this work is to provide a more comprehensive *spectral and spatial characterization* of the most important ocean tide signatures in GRACE(-FO) K/Ka-band (hereafter simply denoted as K-band) range-rate post-fit residuals, without limiting the analysis to the usually considered tidal frequencies. To address the research objective, spectral analysis will serve as a central tool. Unlike the harmonic or tidal analysis used in the previously discussed literature, spectral analysis does not confine the investigation to a limited set of anticipated tidal frequencies. Instead, it provides a broader perspective on the most critical frequency components in the data. Since the spectrum under investigation won't be confined to tidal frequencies, this approach allows for the assessment of the significance of ocean tide signatures in relation to other unmodeled non-tidal effects. With more than two decades of data from the GRACE(-FO) missions, more conclusive results can be anticipated compared to prior related studies. The data basis for these investigations consists of 5-second K-band range rate post-fit residuals for the period from April 2002

to September 2023 (approximately 100 million epochs), obtained as part of the operational gravity field recovery at the Institute of Geodesy (IfE) of the Leibniz University Hannover (LUH).

A summary of this investigation was recently published by Koch et al. (2024b). Especially Chapter 4 follows in large part the structure of the original publication, but offers a more comprehensive description of the methodology and an extended discussion of the results.

Chapter 2 provides essential information on transformations from conventional co-rotating to inertial coordinate systems. It also gives important background on the gravitational and tide-generating potentials, ocean tides, and introduces tools for spectral analysis. Chapter 3 outlines the gravity field recovery methodology employed for the LUH series of monthly gravity field solutions from GRACE(-FO) sensor data. Chapter 4 focuses on analyzing residual and unmodeled ocean tide signal in the LUH time series of GRACE(-FO) K-band range-rate post-fit residuals. To place the obtained results within a broader context, the discussion incorporates an analysis of submonthly gravity field solutions, as well as satellite altimetry data. Chapter 5 provides the final conclusions and offers an outlook on future directions.

Chapter 2

Fundamentals

This chapter provides an overview of key concepts, tools, and algorithms essential for comprehending the material and methods in the subsequent chapters of this thesis. Section 2.1 introduces the fundamental coordinate transformation in satellite geodesy, i.e., the transformation between the body-fixed International Terrestrial Reference System (ITRS) and the inertial Geocentric Celestial Reference System (GCRS), as defined by the International Earth Rotation and Reference Systems Service (IERS) and the International Astronomical Union (IAU). As the origins of both systems are situated at the Earth's center of mass and the systems employ the same scaling, the transformation consists exclusively of a series of rotations. The time-dependent rotation angles reflect Earth's rotation, precession, nutation, and polar motion. Additional coordinate transformations are presented in the relevant sections. Section 2.2 provides an introduction to the standard representation of the Earth's gravitational potential using spherical harmonics. Furthermore, the section outlines the conversions of gravitational potential to gravitational acceleration and gravity gradient, which are particularly important for satellite orbit modeling and gravity field recovery. Additionally, the conversion to EWH, which is of importance for the geophysical interpretation of the time-variable gravity field signal, is presented. Section 2.3 addresses TGP, the driving mechanism behind tides in the Earth's system, and provides essential background information on ocean tides and ocean tide models. Finally, Section 2.4 introduces the spectral analysis tools employed in this work: the Fourier Transform and the Lomb–Scargle periodograms.

2.1 Transformations Between ITRS and GCRS

While the satellite's equation of motion is defined and generally solved in an Earth-centered inertial coordinate system, the spherical harmonic coefficients of the gravitational potential, but also of several other disturbing effects that will be discussed later in Chapter 3, are tied to an Earth-body fixed system. Therefore, the transformation of position, velocity and acceleration vectors between these two types of coordinate systems is an important aspect of orbital modeling. For this purpose, the current standard coordinate systems are the GCRS, which is an inertial system realized by a set of positions of extra-galactic radio sources obtained from Very Long Baseline Interferometry (VLBI) observations (Fey et al., 2015), and the body-fixed (i.e., co-rotating) ITRS, which is realized by positions of globally distributed stations estimated from space geodetic measurements (Altamimi et al., 2011).

The transformation of a Cartesian ITRS position vector $\mathbf{r}_e$ to its GCRS counterpart $\mathbf{r}_i$ is described by a combination of matrix multiplications (e.g., IERS Conventions, 2010):

$$\begin{aligned} \mathbf{r}_i &= (\mathbf{Q}\,\mathbf{R}\,\mathbf{W})\ \mathbf{r}_e \\ &= \mathbf{R}_e^i\,\mathbf{r}_e \end{aligned} \tag{2.1}$$

where $\mathbf{Q}$ is the combined precession-nutation matrix, $\mathbf{R}$ is the Earth's rotation matrix, and $\mathbf{W}$ is the polar motion matrix. The formation of these matrices is described in detail in Sections 2.1.2–2.1.4. Due to the mutual origin of the two systems, which is the Earth's center of mass including the oceans and atmosphere, the transformation matrix $\mathbf{R}_e^i$ is solely responsible for a position vector rotation, i.e., $\mathbf{R}_e^i$ is a rotation matrix. This rotation matrix is comprised of several individual rotations around defined angles of the Earth orientation model.

With matrix $\dot{\mathbf{R}}_e^i$ being the first time derivative of $\mathbf{R}_e^i$, e.g., obtained via numerical differentiation, the velocity vector $\dot{\mathbf{r}}_e$ can be transformed to GCRS the following way:

$$\dot{\mathbf{r}}_i = \mathbf{R}_e^i \, \dot{\mathbf{r}}_e + \dot{\mathbf{R}}_e^i \, \mathbf{r}_e \, . \tag{2.2}$$

By disregarding irrelevant smaller terms, the transformation of an acceleration vector $\ddot{\mathbf{r}}_e$ is:

$$\ddot{\mathbf{r}}_i = \mathbf{R}_e^i \, \ddot{\mathbf{r}}_e \, . \tag{2.3}$$

A second-order tensor $\mathbf{T}$, e.g., a gravity gradient or a covariance matrix, is transformed to the inertial system as follows:

$$\mathbf{T}_i = \mathbf{R}_e^i \mathbf{T}_e (\mathbf{R}_e^i)^{\mathrm{T}}. \tag{2.4}$$

The vice versa transformations from GCRS to ITRS are performed by using the transposed $\left(\mathbf{R}_e^i\right)^{\mathrm{T}}$, $\left(\dot{\mathbf{R}}_e^i\right)^{\mathrm{T}}$ or the inverted $\left(\mathbf{R}_e^i\right)^{-1}$, $\left(\dot{\mathbf{R}}_e^i\right)^{-1}$ for the rotations.

2.1.1 Rotations Around Individual Axes

The rotation of a vector in three-dimensional space about a specific axis of the coordinate system, i.e., the first (x), second (y) or third axis (z), by a general angle ϕ in anti-clockwise direction (right-hand rule) can be performed using the following rotation matrices (e.g., Seeber, 2003):

$$\mathbf{R}_1(\phi) = \begin{pmatrix} 1 & 0 & 0 \\ 0 & \cos\phi & \sin\phi \\ 0 & -\sin\phi & \cos\phi \end{pmatrix}, \quad \mathbf{R}_2(\phi) = \begin{pmatrix} \cos\phi & 0 & -\sin\phi \\ 0 & 1 & 0 \\ \sin\phi & 0 & \cos\phi \end{pmatrix}, \quad \mathbf{R}_3(\phi) = \begin{pmatrix} \cos\phi & \sin\phi & 0 \\ -\sin\phi & \cos\phi & 0 \\ 0 & 0 & 1 \end{pmatrix}. \tag{2.5}$$

2.1.2 Precession-Nutation Matrix

Precession is a periodic movement of Earth's rotational axis with respect to the inertial system with a period of approximately 26000 years, and is caused by the lunisolar and planetary gravitational pull on the Earth's equatorial bulge (e.g., Munk and MacDonald, 1975). This slow movement is superimposed with a smaller effect known as nutation, with periods ranging from a few days up to a period of 18.6 years due to the 5 degree inclination of the Moon's orbital plane with respect to the ecliptic (e.g., Torge and Müller, 2012).

The transformation matrix considering both of these effects, i.e., the precession-nutation matrix $\mathbf{Q}$, can be defined as a function of the Celestial Intermediate Pole (CIP) coordinates X and Y in GCRS, and the Celestial Intermediate Origin (CIO) locator $s(X, Y)$ in GCRS as (e.g., IERS Conventions, 2010):

$$\mathbf{Q} = \begin{pmatrix} 1 - aX^2 & -aXY & X \\ -aXY & 1 - aY^2 & Y \\ -X & -Y & 1 - a(X^2 + Y^2) \end{pmatrix} \mathbf{R}_3(s) \tag{2.6}$$

where quantity a can be approximated as:

$$a = \frac{1}{2} + \frac{1}{8}(X^2 + Y^2) \, . \tag{2.7}$$

The IAU 2006/2000A developments of the CIP coordinates X, Y with amplitudes a_c, a_s, b_c, b_s (see IERS, 2019a, Tables 5.2a,b) are defined as (Capitaine and Wallace, 2006; IERS Conventions, 2010):

$$
\begin{aligned}
X = &- 0.016617'' + 2004.191898''\, t - 0.4297829''\, t^2 \\
&- 0.19861834''\, t^3 + 0.000007578''\, t^4 + 0.0000059285''\, t^5 \\
&+ \sum_{j=0}^{4} \sum_{i=1}^{n_j} \left[(a_{s,j})_i\, t^j \sin\left(ARG_i\right) + (a_{c,j})_i\, t^j \cos\left(ARG_i\right) \right], \qquad n_j = \{1306, 253, 36, 4, 1\}
\end{aligned}
\tag{2.8}
$$

$$
\begin{aligned}
Y = &- 0.006951'' - 0.025896''\, t - 22.4072747''\, t^2 \\
&+ 0.00190059''\, t^3 + 0.001112526''\, t^4 + 0.0000001358''\, t^5 \\
&+ \sum_{j=0}^{4} \sum_{i=1}^{n_j} \left[(b_{c,j})_i\, t^j \cos\left(ARG_i\right) + (b_{s,j})_i\, t^j \sin\left(ARG_i\right) \right], \qquad n_j = \{962, 277, 30, 5, 1\}\,.
\end{aligned}
\tag{2.9}
$$

The time argument t in Equations 2.8 and 2.9 is the number of centuries of Terrestrial Time (TT) since epoch J2000.0:

$$
t = \frac{(TT - 1.\ \text{January 2000, 12:00 TT}) \quad [\text{in days}]}{36525}\,. \tag{2.10}
$$

TT can be related to the Coordinated Universal Time (UTC) via the International Atomic Time (TAI). TT is ahead of TAI by 32.184 seconds, i.e., $TT = TAI + 32.184$ s. TAI differs from UTC by a specific number of leap seconds, which are announced in the Bulletin C of the IERS and are summarized in IERS (2024, Leap_Second.dat).

In addition to the amplitudes, IERS also provides multipliers N_j for the fundamental arguments F_j of the lunisolar and planetary nutation theory, with which the quantity ARG_i can be computed as the scalar product:

$$
ARG = \sum_{j=1}^{14} N_j F_j\,. \tag{2.11}
$$

The 14 fundamental arguments F_j contain the 5 Delaunay variables (Simon et al., 1994; IERS Conventions, 2010), i.e., the Moon's longitude of the ascending node Ω, the Moon's mean anomaly l, the Sun's mean anomaly l', the difference between the mean longitude of the Moon and the Moon's longitude of the ascending node F, and the mean elongation of the Moon from the Sun D; and 9 parameters of the nutation theory consisting of the mean longitudes M of the planets (Souchay et al., 1999; IERS Conventions, 2010) and the general precession p_A (Kinoshita and Souchay, 1990; IERS Conventions, 2010). The fundamental arguments in terms of time-dependent developments are:

$$
\begin{aligned}
F_1: &\quad l &&= 134.96340251^\circ + 1717915923.2178''t + 31.8792''t^2 + 0.051635''t^3 - 0.00024470''t^4 \\
F_2: &\quad l' &&= 357.52910918^\circ + 129596581.0481''t - 0.5532''t^2 + 0.000136''t^3 - 0.00001149''t^4 \\
F_3: &\quad F &&= 93.27209062^\circ + 1739527262.8478''t - 12.7512''t^2 - 0.001037''t^3 + 0.00000417''t^4 \\
F_4: &\quad D &&= 297.85019547^\circ + 1602961601.2090''t - 6.3706''t^2 + 0.006593''t^3 - 0.00003169''t^4 \\
F_5: &\quad \Omega &&= 125.04455501^\circ - 6962890.5431''t + 7.4722''t^2 + 0.007702''t^3 - 0.00005939''t^4 \\
F_6: &\quad L_{Me} &&= 4.402608842 + 2608.7903141574\, t \\
F_7: &\quad L_{Ve} &&= 3.176146697 + 1021.3285546211\, t \\
F_8: &\quad L_E &&= 1.753470314 + 628.3075849991\, t \\
F_9: &\quad L_{Ma} &&= 6.203480913 + 334.0612426700\, t \\
F_{10}: &\quad L_J &&= 0.599546497 + 52.9690962641\, t \\
F_{11}: &\quad L_{Sa} &&= 0.874016757 + 21.3299104960\, t \\
F_{12}: &\quad L_U &&= 5.481293872 + 7.4781598567\, t \\
F_{13}: &\quad L_{Ne} &&= 5.311886287 + 3.8133035638\, t \\
F_{14}: &\quad p_A &&= 0.02438175\, t + 0.00000538691\, t^2\,.
\end{aligned}
\tag{2.12}
$$

Note that the constant terms of the Delaunay variables in Equation 2.12 are in degrees, while the coefficients are given in arcseconds ("). The fundamental arguments F_6–F_{14} are in radians. Time argument t is the number of Julian centuries of Barycentric Dynamical Time (TDB). In practice, TT (see Equation 2.10) can be used instead.

The CIP coordinates (Equations 2.8 and 2.9) deviate from VLBI-observed values, primarily since retrograde free core nutation, a diurnal quasi-periodic motion of the Earth's rotation axis (e.g., Vondrák et al., 2005), is not part of the IAU2006/2000A model. The CIP coordinates X, Y to be used in the precession-nutation matrix are obtained by correcting the model CIP coordinates using estimated time dependent celestial pole offsets ΔX, ΔY published by the IERS as part of the Earth Orientation Parameters (EOPs):

$$\begin{pmatrix} X \\ Y \end{pmatrix} = \begin{pmatrix} X \\ Y \end{pmatrix}_{IAU} + \begin{pmatrix} \Delta X \\ \Delta Y \end{pmatrix} . \tag{2.13}$$

The numerical value of the CIO locator in Equation 2.6, expressed in micro-arcseconds and compatible with the IAU2006/2000A precession-nutation, can be obtained using the development (Capitaine and Wallace, 2006; IERS Conventions, 2010):

$$\begin{aligned} s = &- \frac{XY}{2} + 94 + 3808.65\,t - 122.68\;t^2 - 72574.11\,t^3 + 27.98\,t^4 + 15.62\,t^5 \\ &+ \sum_{j=0}^{4} \sum_{i=1}^{n_j} \left[(c_{s,j})_i\, t^j \sin\left(ARG_i\right) + (c_{c,j})_i\, t^j \cos\left(ARG_i\right) \right] , \qquad n_j = \{33, 3, 25, 4, 1\} \end{aligned} \tag{2.14}$$

in which X, Y are the CIP coordinates from Equations 2.8 and 2.9 and time argument t is the number of Julian TT centuries as defined in Equation 2.10. The amplitudes c_c and c_s of the development are listed in IERS (2019a, Table 5.2d). The quantity ARG is calculated the same way as for the CIP coordinates.

2.1.3 Earth Rotation Matrix

The diurnal rotation of the Earth around its axis is considered in the matrix (IERS Conventions, 2010):

$$\mathbf{R} = \mathbf{R}_3(-ERA) \tag{2.15}$$

with the Earth Rotation Angle (ERA) in radians defined as (Capitaine et al., 2000):

$$ERA = 2\pi(0.7790572732640 + 1.00273781191135448 T_u) . \tag{2.16}$$

The time argument T_u is the number of days since epoch J2000.0 in the Universal Time 1 (UT1) system, i.e., T_u = (Julian UT1 date − 2451545.0). UT1 and UTC are related via the relationship UT1 = UTC + dUT1. The difference between these two time systems is always smaller than 0.9 seconds due to the introduction of leap seconds by the IERS, and can be calculated as follows:

$$\mathrm{dUT1} = \mathrm{dUT1}_{IERS} + \Delta\mathrm{dUT1}_{ot} + \Delta\mathrm{dUT1}_{l} . \tag{2.17}$$

The time difference $\mathrm{dUT1}_{IERS}$ is the value interpolated from the daily EOPs published by the IERS, which has to be corrected for not included ocean tide effects (Ray et al., 1994) and libration (Brzeziński and Capitaine, 2003). The ocean tide correction $\Delta\mathrm{dUT1}_{ot}$ considers the influence of 71 diurnal and semidiurnal tidal constituents. For the libration correction $\Delta\mathrm{dUT1}_{l}$, contributions at 11 semidiurnal frequencies have to be taken into account. Fortran routines for the interpolation (INTERP.F) and corrections (ORTHO_EOP.F, UTLIBR.F) are available from the IERS (2019a).

2.1.4 Polar Motion Matrix

Lunisolar and planetary gravitation and geodynamic processes are causing a complex superimposed motion of Earth's rotation axis with respect to the Earth-fixed system, consisting of secular, periodic and quasi-periodic components (e.g., Munk and MacDonald, 1975; Torge and Müller, 2012). The polar motion matrix is defined as a function of the polar motion coordinates x_p, y_p and the Terrestrial Intermediate Origin (TIO) locator s' (IERS Conventions, 2010):

$$\mathbf{W} = \mathbf{R}_3(-s')\mathbf{R}_2(x_p)\mathbf{R}_1(y_p)\,. \tag{2.18}$$

Similar to dUT1 (see Equation 2.17), it is necessary to interpolate the IERS-provided polar motion coordinates to the time of interest, and to consider the contribution of diurnal and subdiurnal ocean tides (Ray et al., 1994) and libration (Brzeziński and Capitaine, 2003) (see IERS, 2019a, ORTHO_EOP.F, PMSDNUT2.F):

$$\begin{pmatrix} x_p \\ y_p \end{pmatrix} = \begin{pmatrix} x_p \\ y_p \end{pmatrix}_{IERS} + \begin{pmatrix} \Delta x_p \\ \Delta y_p \end{pmatrix}_{ot} + \begin{pmatrix} \Delta x_p \\ \Delta y_p \end{pmatrix}_{l}\,. \tag{2.19}$$

The TIO locator s' is a function of the polar motion coordinates x_p, y_p. Due to its sensitivity to only the largest variations of the polar motion, i.e., the Chandlerian and annual wobbles, the value of the TIO locator in micro-arcseconds can be approximated as:

$$s' = -47t\,. \tag{2.20}$$

2.2 Gravitational Potential of the Earth

The gravitation of the Earth on or above its surface is usually expressed in terms of a scalar potential field using spherical harmonics. The gravitational potential V at a location in the exterior of the Earth, defined by spherical longitude λ, latitude φ, and radial distance r, can be obtained through a synthesis of different degrees n and orders m of the spherical harmonic expansion, as follows (e.g., Heiskanen and Moritz, 1967; Torge and Müller, 2012; Ilk, 2021):

$$V = \frac{GM}{r}\sum_{n=0}^{\infty}\left(\frac{R}{r}\right)^n \sum_{m=0}^{n}\left(\overline{C}_{nm}\cos m\lambda + \overline{S}_{nm}\sin m\lambda\right)\overline{P}_{nm}(\sin\varphi) \tag{2.21}$$

with GM representing the product of the gravitational constant G and the mass of the Earth M, commonly referred to as the standard gravitational parameter of the Earth or the geocentric gravitational constant; the semimajor axis of the Earth's ellipsoid R; the fully normalized spherical harmonic coefficients of the gravitational potential expansion $\overline{C}_{nm}$, $\overline{S}_{nm}$; and the fully normalized associated Legendre functions $\overline{P}_{nm}$ with argument $\sin\varphi$.

In practice, the gravitational potential can only be expanded until a finite number of degrees. Therefore, the upper limit of the first summation can be replaced with the corresponding maximum degree $n_{\max}$, representing the theoretical spatial resolution of the potential. For a maximum degree of 0, where per definition $\overline{C}_{00} = 1$ and $\overline{P}_{00} = 1$, one obtains $V = GM/r$, i.e., the gravitational potential of an Earth with a spherically symmetric mass distribution, or the mass being concentrated at a single point. With increasingly higher maximum degrees, finer spatial details of the potential can be represented. The spatial resolution corresponding to a maximum degree is given by $2\pi R/n_{\max}$. A set of spherical harmonic coefficients $\overline{C}_{nm}$, $\overline{S}_{nm}$, with the corresponding scaling constants GM, R, approximating the average gravitational potential

over a specific time period is usually referred to as a gravity field model or gravity field solution.[1] Global gravity field models typically rely on observations of satellite gravimetry missions like CHAMP (Challenging Minisatellite Payload), GRACE(-FO), GOCE (Gravity Field and Steady-State Ocean Circulation Explorer) (see e.g., Flechtner et al., 2021), as well as Satellite Laser Ranging (SLR) missions (e.g., Pearlman et al., 2019), but can also incorporate terrestrial, airborne and shipborne measurements (e.g., Zingerle et al., 2020). One can distinguish between static and temporal gravity field models. A static gravity field model assumes a time-invariant behaviour of the gravitational field, and therefore represents an average potential field over a longer period. In the case of temporal gravity field models, the average potential refers to a relatively short period, typically one month. An overview of various models from the very beginning of satellite gravimetry in the late 1960s up until now can be found on the website of the International Centre for Global Earth Models (ICGEM). The estimation of the spherical harmonic coefficients of the gravitational potential is known as *gravity field recovery*. The estimation of temporal gravity field models, so-called *monthly gravity field solutions*, from GRACE(-FO) data is a central part of this thesis, and will be outlined in Chapter 3.

Note that the gravitational potential V in Equation 2.21 is defined in a coordinate system co-rotating with the Earth. To evaluate the potential at an inertial position, a coordinate transformation to the co-rotating system is needed (see Section 2.1). The spherical coordinates $(\lambda,\, \varphi,\, r)$ and the three Cartesian components $(x,\, y,\, z)$ of a position vector in the co-rotating system are related via the following relationships:[2]

$$\lambda = \arctan\left(\frac{y}{x}\right), \qquad \varphi = \arctan\left(\frac{z}{\sqrt{x^2+y^2}}\right), \qquad r = |\mathbf{r}|\,. \tag{2.22}$$

In a coordinate system co-rotating with the Earth, the gravitational potential V and the centrifugal potential Φ form the gravity potential $W = V + \Phi$ with the non-harmonic centrifugal potential (e.g., Heiskanen and Moritz, 1967; Torge and Müller, 2012; Ilk, 2021):

$$\Phi = \frac{1}{2}\omega^2 p^2 \tag{2.23}$$

where $\omega = 7.292115 \times 10^{-5}$ rad/s is the angular velocity of Earth's rotation and $p = \sqrt{x^2+y^2}$ the distance to the rotation axis.

The following subsections address important aspects related to the gravitational potential. The derivation of the spherical harmonic representation of V starting from Newton's law of universal gravitation, categorization of spherical harmonics, and methods for spectral signal content and noise assessment are presented in Section 2.2.1. The conversions from gravitational potential to gravitational acceleration and gravity gradient, which are relevant for satellite orbit modeling and dynamic orbit determination, are described in Section 2.2.2. Recursive computation schemes for the calculating fully normalized associated Legendre functions and its derivatives, needed for evaluating the gravitational potential, acceleration and gradient, are shown in Section 2.2.3. The conversion from gravitational potential to EWH is topic of Section 2.2.4.

2.2.1 Spherical Harmonics Representation

The spherical harmonics representation of the gravitational potential of the Earth V presented earlier in Equation 2.21 can be derived from Newton's law of universal gravitation. Consider two points represented by the Cartesian position vectors $\mathbf{r} = (x,\, y,\, z)^{\mathrm{T}}$ and $\mathbf{r}' = (x',\, y',\, z')^{\mathrm{T}}$, along with their respective masses

[1] As will be described below, the terms "gravitation" and "gravity" are to be distinguished from each other, although the term "gravity field model" is used to refer to the spherical harmonic coefficients of the gravitational potential.

[2] λ to be computed with atan2.

m_1, m_2. These two point masses are separated by the distance $l = |\mathbf{l}| = |\mathbf{r} - \mathbf{r}'|$. According to Newton's law of universal gravitation, the gravitational force $\mathbf{F}$ between these two point masses, with the gravitational constant $G = 6.67428 \times 10^{-11}$ $\mathrm{m}^3/(\mathrm{kg\ s}^2)$ (Mohr et al., 2008; IERS Conventions, 2010), is given by the formula:

$$\mathbf{F} = -G\frac{m_1 m_2}{l^2}\frac{\mathbf{l}}{l}\,. \tag{2.24}$$

With the help of Newton's second law of motion, i.e., the force acting on an object is the product of its mass and acceleration; and defining m_1 as the attracted and $m_2 = m$ as the attracting point mass, the gravitational force can be expressed as the gravitational acceleration vector $\mathbf{b}$ pointing from the attracted point towards the source of gravitation:

$$\mathbf{b} = -G\frac{m}{l^2}\frac{\mathbf{l}}{l}\,. \tag{2.25}$$

Equation 2.25 can be extended to apply to a complex mass system, such as the Earth. A mass system Ω can be regarded as a composition of an infinite number of differential mass elements dm. The gravitational acceleration is then the integral over all mass elements dm:

$$\mathbf{b} = -G\int\int\int_{\Omega}\frac{\mathbf{l}}{l^3}\,dm\,. \tag{2.26}$$

The differential mass element dm can also be formulated as the product of the location-dependent density ρ and the differential volume element dv as $dm = \rho\,dv$. Since gravitational acceleration is the gradient of the gravitational potential V, i.e.:

$$\mathbf{b} = \nabla V = \left(\frac{\partial V}{\partial x}\ \frac{\partial V}{\partial y}\ \frac{\partial V}{\partial z}\right)^{\mathrm{T}}, \tag{2.27}$$

the gravitational potential of a mass system Ω is:

$$V = G\int\int\int_{\Omega}\frac{\rho}{l}\,dv\,. \tag{2.28}$$

Determining the gravitational potential using Equation 2.28 is challenging because the Earth's internal mass distribution and, consequently, its density, are not precisely known. However, it is feasible to demonstrate that modeling the gravitational potential in the exterior of the Earth is possible. Applying the Laplace operator $\Delta = \nabla \cdot \nabla$ to potential V, i.e.:

$$\Delta V = \left(\frac{\partial^2 V}{\partial x^2} + \frac{\partial^2 V}{\partial y^2} + \frac{\partial^2 V}{\partial z^2}\right) \tag{2.29}$$

gives rise to two cases:

1. If the attracted mass point is inside the Earth, i.e., $|\mathbf{r}| < |\mathbf{r}'|$, then ΔV is described by the Poisson equation: $\Delta V = -4\pi G\rho$,
2. If the attracted mass point is outside the Earth, i.e., $\rho = 0$ and $|\mathbf{r}| > |\mathbf{r}'|$, then ΔV is described by Laplace's differential equation of second order: $\Delta V = 0$.

Since the Laplace equation is valid, the gravitational potential V outside the attracting mass is *harmonic*. Spherical harmonic functions are solutions of the Laplace equation and therefore the gravitational potential in Earth's exterior can be represented as a series expansion with the help of spherical harmonics.

Using polar coordinates and applying the rule of cosines, the reciprocal distance $1/l$ between the attracted and attracting points can be formulated as:

$$\frac{1}{l} = \frac{1}{r}\left(1 + \left(\frac{r'}{r}\right)^2 - 2\frac{r'}{r}\cos\psi\right)^{-1/2} \tag{2.30}$$

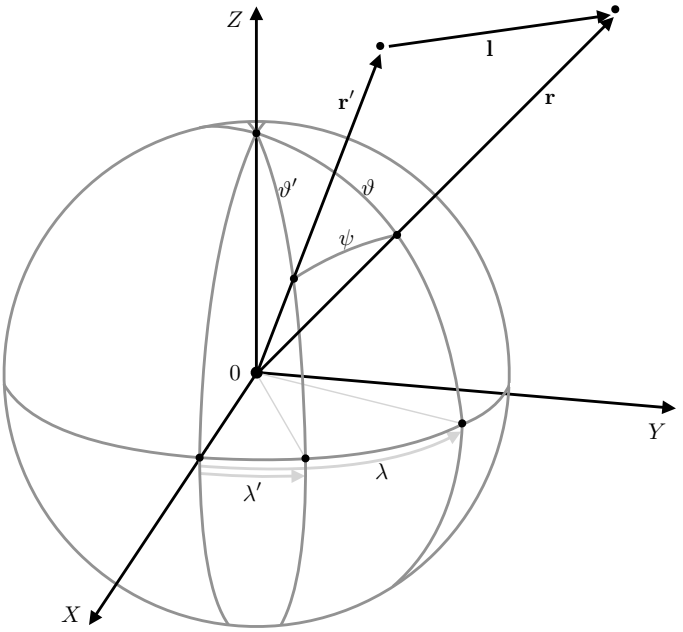

FIGURE 2.1: Relevant vectors and angles on the unit sphere for deriving the spherical harmonic coefficients representation of the gravitational potential. Vectors $\mathbf{r}'$ and $\mathbf{r}$ are the position vectors of the attracting and attracted point masses, respectively. The point masses are separated by the distance $|\mathbf{l}| = |\mathbf{r} - \mathbf{r}'|$.

where ψ is the angle between the position vectors $\mathbf{r}$ and $\mathbf{r}'$; and $r = |\mathbf{r}|$, $r' = |\mathbf{r}'|$. The reciprocal square root term in the above equation can be expressed as a series expansion with Legendre polynomials P_n (as a function of $\cos\psi$), resulting in the following expression for the reciprocal distance:

$$\frac{1}{l} = \frac{1}{r}\sum_{n=0}^{\infty}\left(\frac{r'}{r}\right)^n P_n(\cos\psi) \tag{2.31}$$

where the Legendre polynomials of degree n are defined as:

$$P_n(t) = \frac{1}{2^n n!}\frac{d^n[(t^2-1)^n]}{dt^n}\,. \tag{2.32}$$

Using the spherical law of cosines and applying the addition theorem of Legendre polynomials with the angles on the unit sphere ϑ, ϑ', λ, λ' as illustrated in Figure 2.1, P_n can be expressed as:

$$\begin{aligned} P_n(\cos\psi) = \sum_{m=0}^{n}(2-\delta_{0m})\frac{(n-m)!}{(n+m)!}(&P_{nm}(\cos\vartheta)\cos m\lambda \;\; P_{nm}(\cos\vartheta')\cos m\lambda' + \\ &P_{nm}(\cos\vartheta)\sin m\lambda \;\; P_{nm}(\cos\vartheta')\sin m\lambda') \end{aligned} \tag{2.33}$$

with associated Legendre functions P_{nm} of degree n and order m:

$$P_{nm}(t) = (1-t^2)^{m/2}\frac{d^m}{dt^m}P_n(t) \tag{2.34}$$

and the Kronecker delta:

$$\delta_{nm} = \begin{cases} 1, & n = m \\ 0, & n \neq m\,. \end{cases} \tag{2.35}$$

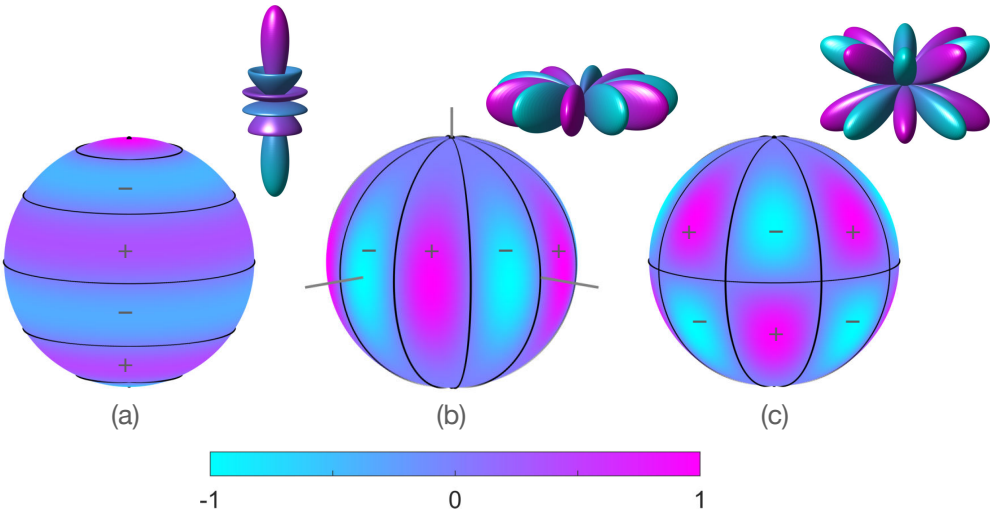

FIGURE 2.2: Spherical harmonics $P_{nm}(\cos\vartheta)\cos m\lambda$ normalized to range $[-1, 1]$ in two representations. 1: Color-coded value of the spherical harmonic on the sphere. At the solid black lines the spherical harmonic value is zero. These nodal lines divide the spherical harmonics into three categories: zonal, when $m = 0$, e.g., $P_{50}(\cos\vartheta)$ (a); sectoral, when $n = m$, e.g., $P_{55}(\cos\vartheta)\cos 5\lambda$ (b); and tesseral for $0 < m < n$, e.g., $P_{54}(\cos\vartheta)\cos 4\lambda$ (c). 2: The radial distance is distorted according to the absolute value of the spherical harmonic.

The quantities $P_{nm}(\cos\vartheta)\cos m\lambda$ and $P_{nm}(\cos\vartheta)\sin m\lambda$ in Equation 2.33 are called surface *spherical harmonics*. Based on the specific combination of degree n and order m, they can be divided into three categories:

- *Zonal* spherical harmonics when $m = 0$: Are only represented by $P_{nm}\cos m\lambda$; $P_{nm}\sin m\lambda$ is 0. The surface of the sphere is divided into $n+1$ zones, with zero lines along parallels (see Figure 2.2a for $n = 5$, $m = 0$).
- *Sectoral* spherical harmonics when $n = m$: The surface of the sphere is divided into $2m$ sectors, with zero lines along meridians (see Figure 2.2b for $n = 5$, $m = 5$).
- *Tesseral* spherical harmonics for $0 < m < n$: The surface of the sphere is divided into $2m(n - m + 1)$ cells, with zero lines along parallels and meridians (see Figure 2.2c for $n = 5$, $m = 4$).

After 1. inserting expression of the Legendre polynomials from Equation 2.33 into Equation 2.31, 2. substituting the resulting expression into Equation 2.28, 3. introducing a reference mass M (mass of the Earth) and a reference radius R (semimajor axis of the Earth ellipsoid), and 4. restructuring the resulting equation so that the distance r' appears behind the integrals, the following expression is obtained:

$$V = \frac{GM}{r}\sum_{n=0}^{\infty}\sum_{m=0}^{n}\left(\frac{R}{r}\right)^n \frac{(2-\delta_{0m})}{M}\frac{(n-m)!}{(n+m)!}\Big(P_{nm}(\cos\vartheta)\cos m\lambda \int\int\int_{\Omega}\left(\frac{r'}{R}\right)^n P_{nm}(\cos\vartheta')\cos m\lambda' dm + P_{nm}(\cos\vartheta)\sin m\lambda \int\int\int_{\Omega}\left(\frac{r'}{R}\right)^n P_{nm}(\cos\vartheta')\sin m\lambda' dm\Big)\,. \tag{2.36}$$

All quantities in Equation 2.36 related to the source of gravitation can be assigned to so-called *spherical harmonic coefficients* C_{nm} and S_{nm}:

$$\begin{pmatrix} C_{nm} \\ S_{nm} \end{pmatrix} = \frac{(2-\delta_{0m})}{M}\frac{(n-m)!}{(n+m)!}\int\int\int_{\Omega}\left(\frac{r'}{R}\right)^n P_{nm}(\cos\vartheta')\begin{cases}\cos m\lambda' dm \\ \sin m\lambda' dm\,.\end{cases} \tag{2.37}$$

The above coefficients are also called Stokes' coefficients. An alternative notation that can sometimes be found in the literature is: $J_{nm} = -C_{nm}$ and $J_n = -C_{n0}$, especially J_2 for the negative main term of the gravitational potential C_{20}.

The lower degree spherical harmonic coefficients can be interpreted physically. C_{00} is the ratio of the total mass of mass system Ω to the reference mass. Since M was introduced as reference mass, $C_{00} = 1$. Coefficients C_{10}, C_{11}, S_{11} are the coordinates of the center of mass, i.e., geocenter coordinates, with respect to the body-fixed reference system. For a coordinate system with an origin at the geocenter, these values are zero. C_{20}, C_{21}, S_{21}, C_{22}, S_{22} are related to the elements of the moment of inertia tensor (cf. e.g., Ilk, 2021, p. 114f). Coefficient C_{20}, the largest spherical harmonic coefficient after C_{00}, characterizes the polar flattening of the Earth.

In practical use, the gravitational potential is expressed by using fully normalized spherical harmonic coefficients, where the largest value equals 1:

$$\begin{pmatrix} \overline{C}_{nm} \\ \overline{S}_{nm} \end{pmatrix} = \sqrt{\frac{1}{(2-\delta_{0m})(2n+1)} \frac{(n+m)!}{(n-m)!}} \quad \begin{cases} C_{nm} \\ S_{nm} \end{cases} \tag{2.38}$$

as well as the fully normalized associated Legendre functions (see Section 2.2.3):

$$\overline{P}_{nm}(t) = \sqrt{(2-\delta_{0m})(2n+1)\frac{(n-m)!}{(n+m)!}} P_{nm}(t) \, . \tag{2.39}$$

Finally, by inserting the fully normalized spherical harmonic coefficients and associated Legendre functions into Equation 2.36, and the relations $\vartheta = \pi/2 - \varphi$, $\cos\vartheta = \sin\varphi$, one arrives at the spherical harmonics representation of the Earth's gravitational potential given in Equation 2.21.

The signal content of the coefficients of a gravity field model can be visualized by arranging the coefficients into a triangular structure with color-coded amplitudes, or by means of degree variances:

$$\sigma_n^2 = \sum_{m=0}^{n} (\overline{C}_{nm}^2 + \overline{S}_{nm}^2) \, . \tag{2.40}$$

or degree standard deviations $\sigma_n = \sqrt{\sigma_n^2}$. More common is to look at difference degree variances, i.e., utilizing spherical harmonic coefficients differences $\Delta\overline{C}_{nm}$, $\Delta\overline{S}_{nm}$ that are computed with respect to a reference model, e.g., a static gravity field model. This allows to assess time-variable signal of a temporal gravity field solution, but also the contribution of noise at different degrees/orders. An example of both representations for a monthly gravity field solution from GRACE-FO data is shown in Figure 2.3. The degree variances of a gravity field model approximately follow the shape that is described by an empirical model known as Kaula's rule of thumb: $\sigma_n^2 \approx 160 \times 10^{-12}/n^3$ (Kaula, 1966, blue line in Figure 2.3 that approximates σ_n of the monhtly gravity field solution labeled with "full"). In general, the signal content diminishes as degree n increases. For the time-variable component of a gravity field solution, i.e., a temporal gravity field model minus a reference model (in Figure 2.3a denoted as "full−static"), one can also anticipate a decrease of σ_n. Since the spherical harmonic coefficients of a GRACE(-FO) monthly gravity field solution are dominated by noise at higher degrees, the assumption of a decreasing σ_n is violated. Hence, the difference degree standard deviations can be divided into two parts: a signal dominated part for (roughly) $n \leq 40$ and a noise-dominated part for higher degrees. To obtain mass variations from the spherical harmonic coefficients of a temporal gravity field solutions, the noise contribution must be reduced, e.g., by applying filters (cf. Figure 2.3a where a Gaussian filter was applied, and the corresponding triangle plot in Figure 2.3d). The process of determining mass variations from GRACE(-FO) monthly gravity field models, including the application of filtering, is outlined in more detail in Section 2.2.4.

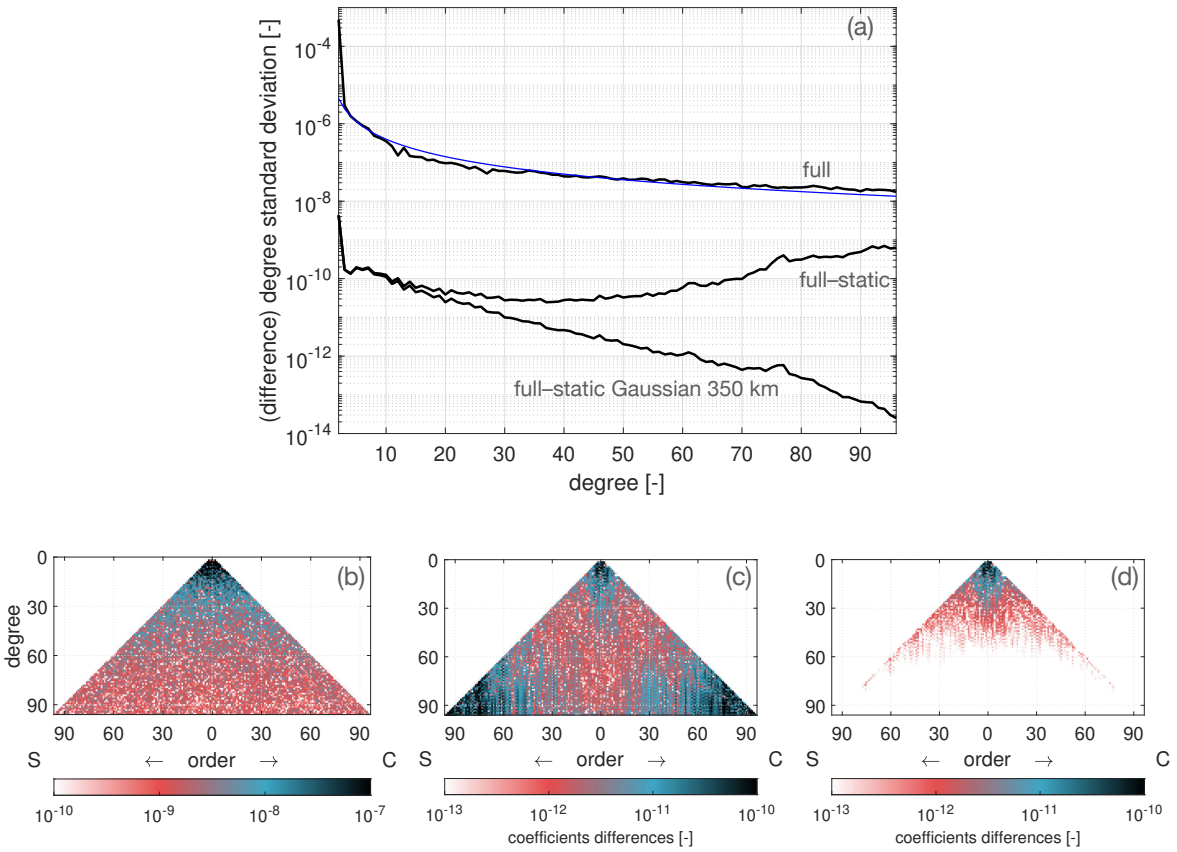

FIGURE 2.3: (a): Degree standard deviations for degrees $n = 2$ to $n = 96$ of a GRACE-FO monthly gravity field solution (January 2021); difference degree standard deviations of the monthly gravity field solution with respect to the static gravity field model GOCO06s; and difference degree standard deviations of the monthly gravity field solution with respect to GOCO06s with an additional Gaussian filtering with a 350 km half-width radius (see Section 2.2.4). The blue line represents Kaula's rule of thumb. (b)–(d): Corresponding triangle plot representation with $\overline{C}_{nm}/\Delta\overline{C}_{nm}$ on the right part of the triangle, and $\overline{S}_{nm}/\Delta\overline{S}_{nm}$ on the left.

2.2.2 From Gravitational Potential to Acceleration and Gravity Gradient

Although, as demonstrated in the previous section, gravitation can be elegantly expressed as a potential field, representing gravitation as an acceleration vector is central to many applications. In the context of this work, knowledge of the acceleration vector is necessary for the modeling of satellite dynamics, as will be shown later in Chapter 3. Furthermore, in the estimation process of the monthly gravity field solutions using dynamic orbit determination, also the so-called gravity gradient is required. The gravitational potential V and the gravitational acceleration vector $\mathbf{b}$ are related via the expression $\mathbf{b} = \nabla V$ (Equation 2.27), i.e., the acceleration is defined as the vector containing the partial derivatives of the gravitational potential with respect to the three Cartesian components x, y, z of a position vector $\mathbf{r}$ given in the co-rotating coordinate system. The gravity gradient represents the second-order partial derivatives of the gravitational potential with respect to x, y, z. The first-order and second-order partial derivatives can be obtained via a series of intermediate steps (see e.g., Tscherning, 1976; Koop, 1993; Sharifi, 2004; Wu, 2016), which will be outlined below.

The gravitational potential V presented earlier in Equation 2.21 can also be formulated as:

$$V_{i(j)} = \frac{GM}{r} \sum_{n=0}^{\infty} f \left(\frac{R}{r} \right)^n \sum_{m=0}^{n} p(\alpha \cos m\lambda + \beta \sin m\lambda) \tag{2.41}$$

Table 2.1: Expressions to be used in Equation 2.41.

Differentiation w.r.t.	f	p	α	β
–	1	$\overline{P}_{nm}(\sin\varphi)$	$\overline{C}_{nm}$	$\overline{S}_{nm}$
r	$-\frac{n+1}{r}$	$\overline{P}_{nm}(\sin\varphi)$	$\overline{C}_{nm}$	$\overline{S}_{nm}$
φ	1	$\overline{P}'_{nm}(\sin\varphi)$	$\overline{C}_{nm}$	$\overline{S}_{nm}$
λ	1	$\mathrm{m}\overline{P}_{nm}(\sin\varphi)$	$\overline{S}_{nm}$	$-\overline{C}_{nm}$
rr	$\frac{(n+1)(n+2)}{r^2}$	$\overline{P}_{nm}(\sin\varphi)$	$\overline{C}_{nm}$	$\overline{S}_{nm}$
$r\varphi$	$-\frac{(n+1)}{r}$	$\overline{P}'_{nm}(\sin\varphi)$	$\overline{C}_{nm}$	$\overline{S}_{nm}$
$r\lambda$	$-\frac{(n+1)}{r}$	$m\overline{P}_{nm}(\sin\varphi)$	$\overline{S}_{nm}$	$-\overline{C}_{nm}$
$\varphi\varphi$	1	$\overline{P}''_{nm}(\sin\varphi)$	$\overline{C}_{nm}$	$\overline{S}_{nm}$
$\varphi\lambda$	1	$m\overline{P}'_{nm}(\sin\varphi)$	$\overline{S}_{nm}$	$-\overline{C}_{nm}$
$\lambda\lambda$	-1	$m^2\overline{P}_{nm}(\sin\varphi)$	$\overline{C}_{nm}$	$\overline{S}_{nm}$

with $f = 1$, $p = \overline{P}_{nm}(\sin\varphi)$, $\alpha = \overline{C}_{nm}$, and $\beta = \overline{S}_{nm}$; where, as in Equation 2.21, (r, φ, λ) are the spherical coordinates of the evaluation point, GM is the standard gravitational parameter of the Earth, R is the semimajor axis of the Earth's ellipsoid, $\overline{C}_{nm}$ and $\overline{S}_{nm}$ are the fully normalized spherical harmonic coefficients of the gravitational potential expansion for degree n and order m; and $\overline{P}_{nm}$ are the fully normalized associated Legendre functions. The subscripts i and j refer to the first column of Table 2.1.

By replacing f, p, a and b in Equation 2.41 with the expressions provided in Table 2.1, the first-order partial derivatives $V_i = \partial V/\partial i$ and second-order partial derivatives $V_{ij} = \partial^2 V/(\partial i \partial j)$ of the gravitational potential with respect to the spherical coordinates $i, j \in \{r, \varphi, \lambda\}$ are obtained. The expressions $\overline{P}'_{nm}(\sin\varphi)$ and $\overline{P}''_{nm}(\sin\varphi)$ in Table 2.1, introduced here for the first time, represent the first-order and second-order derivatives $\overline{P}'_{nm} = \partial\overline{P}_{nm}(\sin\varphi)/\partial\varphi$ and $\overline{P}''_{nm} = \partial^2\overline{P}_{nm}(\sin\varphi)/\partial\varphi^2$, respectively. A recursive computation scheme for the fully normalized associated Legendre functions and its derivatives is given in Section 2.2.3.

With these partial derivatives with respect to the spherical coordinates, the first-order and second-order partial derivatives of the gravitational potential with respect to a local coordinate system can be formulated. With the axes defined such that x, y, and z point from the evaluation point towards the North, East, and upward directions, respectively, the partial derivatives with $i, j \in \{x, y, z\}$ are defined as:

$$
\begin{aligned}
V_x &= \frac{1}{r}V_\varphi \\
V_y &= \frac{1}{r\cos\varphi}V_\lambda \\
V_z &= V_r \\
V_{xx} &= \frac{1}{r}V_r + \frac{1}{r^2}V_{\varphi\varphi} \\
V_{xy} &= \frac{1}{r^2\cos\varphi}V_{\varphi\lambda} + \frac{\tan\varphi}{r^2\cos\varphi}V_\lambda \\
V_{xz} &= \frac{1}{r}V_{r\varphi} - \frac{1}{r^2}V_\varphi \\
V_{yy} &= \frac{1}{r}V_r - \frac{\tan\varphi}{r^2}V_\varphi + \frac{1}{r^2\cos^2\varphi}V_{\lambda\lambda} \\
V_{yz} &= \frac{1}{r\cos\varphi}V_{r\lambda} - \frac{1}{r^2\cos\varphi}V_\lambda \\
V_{zz} &= V_{rr}\,.
\end{aligned}
\tag{2.42}
$$

The gravitational acceleration vector in the co-rotating coordinate system can now be obtained as follows:

$$\frac{\partial V}{\partial \mathbf{r}} = \mathbf{R}\begin{pmatrix} V_x \\ V_y \\ V_z \end{pmatrix} \qquad \text{with} \qquad \mathbf{R} = \begin{pmatrix} -\sin\varphi\cos\lambda & -\sin\lambda & \cos\varphi\cos\lambda \\ -\sin\varphi\sin\lambda & \cos\lambda & \cos\varphi\sin\lambda \\ \cos\varphi & 0 & \sin\varphi \end{pmatrix}. \tag{2.43}$$

By taking the tensor structure into account, the symmetric gravity gradient can be transformed from the local coordinate system to the global coordinate system as follows:

$$\frac{\partial^2 V}{\partial \mathbf{r}^2} = \mathbf{R}\begin{pmatrix} V_{xx} & V_{xy} & V_{xz} \\ V_{xy} & V_{yy} & V_{yz} \\ V_{xz} & V_{yz} & V_{zz} \end{pmatrix}\mathbf{R}^{\mathrm{T}}. \tag{2.44}$$

An alternative way for obtaining the acceleration vector and gravity gradient is presented in Ilk (2021, Equations 10.4 and 10.7).

2.2.3 Fully Normalized Associated Legendre Functions

In order to evaluate the potential V, the fully normalized associated Legendre functions $\overline{P}_{nm}$ as a function of $\sin\varphi$ are needed.[3] Moreover, computing the acceleration vector and the potential tensor also requires the first-order derivatives $\overline{P}'_{nm} = \partial\overline{P}_{nm}/\partial\varphi$ and second-order derivatives $\overline{P}''_{nm} = \partial^2\overline{P}_{nm}/\partial\varphi^2$. Non-normalized and fully normalized associated Legendre functions were already defined in Equations 2.34 and 2.39. The computation of the Legendre functions using these explicit equations is time consuming. In practice, several recurrence relations can be employed to compute $\overline{P}_{nm}$ and its derivatives (see e.g., Koop, 1993; Sharifi, 2004).

To start the recursive computation as shown in Equations 2.45–2.47, the following values are used:

$$\overline{P}_{00} = 1, \quad \overline{P}'_{00} = 0, \quad \overline{P}''_{00} = 0, \quad \overline{P}_{11} = \sqrt{3}\cos\varphi, \quad \overline{P}'_{11} = -\sqrt{3}\sin\varphi, \quad \overline{P}''_{11} = -\sqrt{3}\cos\varphi\,.$$

The diagonal recursion for $n \geq 2$ reads:

$$\begin{aligned} \overline{P}_{nn} &= f_1\cos\varphi\overline{P}_{n-1,n-1} \\ \overline{P}'_{nn} &= f_1\left(\cos\varphi\overline{P}'_{n-1,n-1} - \sin\varphi\overline{P}_{n-1,n-1}\right) \\ \overline{P}''_{nn} &= f_1\left(\cos\varphi\overline{P}''_{n-1,n-1} - 2\sin\varphi\overline{P}'_{n-1,n-1} - \cos\varphi\overline{P}_{n-1,n-1}\right). \end{aligned} \tag{2.45}$$

Next recursion step for $n \geq 1$ is:

$$\begin{aligned} \overline{P}_{n,n-1} &= f_2\sin\varphi\overline{P}_{n-1,n-1} \\ \overline{P}'_{n,n-1} &= f_2\left(\cos\varphi\overline{P}_{n-1,n-1} + \sin\varphi\overline{P}'_{n-1,n-1}\right) \\ \overline{P}''_{n,n-1} &= f_2\left(\sin\varphi\overline{P}''_{n-1,n-1} + 2\cos\varphi\overline{P}'_{n-1,n-1} - \sin\varphi\overline{P}_{n-1,n-1}\right). \end{aligned} \tag{2.46}$$

Next recursion step for $n \geq m+2$ is:

$$\begin{aligned} \overline{P}_{nm} &= f_3\left(f_4\sin\varphi\overline{P}_{n-1,m} - f_5\overline{P}_{n-2,m}\right) \\ \overline{P}'_{nm} &= f_3\left(f_4\sin\varphi\overline{P}'_{n-1,m} + f_4\cos\varphi\overline{P}_{n-1,m} - f_5\overline{P}'_{n-2,m}\right) \\ \overline{P}''_{nm} &= f_3\left(f_4\sin\varphi\overline{P}''_{n-1,m} + 2f_4\cos\varphi\overline{P}'_{n-1,m} - f_4\sin\varphi\overline{P}_{n-1,m} - f_5\overline{P}''_{n-2,m}\right). \end{aligned} \tag{2.47}$$

[3] In some equations of this subsection, a comma separating n and m in $\overline{P}_{nm}$ and its derivatives is included to ensure unambiguous readability.

The quantities f_1–f_5 in Equations 2.45–2.47 are defined as:

$$f_1 = \sqrt{\frac{2n+1}{2n}}, \qquad f_2 = \sqrt{2n+1}, \qquad f_3 = \sqrt{\frac{2n+1}{(n-m)(n+m)}},$$
$$f_4 = \sqrt{2n-1}, \qquad f_5 = \sqrt{\frac{(n+m-1)(n-m-1)}{2n-3}}\,. \tag{2.48}$$

2.2.4 From Gravitational Potential to Equivalent Water Height

Equivalent Water Height (EWH) is a concept that plays a key role in interpreting the gravity field solutions from satellite gravimetry missions like GRACE(-FO). Time variability of the Earth's gravity field potential can be expressed by $\Delta\overline{C}_{nm} = \overline{C}_{nm} - \overline{C}^{\text{ref}}_{nm}$ and $\Delta\overline{S}_{nm} = \overline{S}_{nm} - \overline{S}^{\text{ref}}_{nm}$, i.e., by the change in the spherical harmonic coefficients with respect to a reference, e.g., a static gravity field model. It is assumed that $\Delta\overline{C}_{nm}$, $\Delta\overline{S}_{nm}$ represent surficial mass variations, for example, in the hydrosphere or the cryosphere. The largest mass changes happening not on the surface of the Earth are likely due to GIA and tidal effects (Chao, 2016). The contribution of tidal effects to the gravity field solutions is reduced by considering these effects as background models during gravity field recovery (see Section 3.3). EWH values can be adjusted for GIA by computing corrections from global or regional GIA models (e.g., Whitehouse et al., 2012; A et al., 2012; Peltier et al., 2018). These corrections are mainly of importance when studying gravity changes in Canada, Fennoscandia, Western Antarctica, and Greenland. The gravity field change $\Delta\overline{C}_{nm}$, $\Delta\overline{S}_{nm}$ is subsequently expressed in terms of a thin and uniform water layer on the Earth's surface. A water layer of 1 mm, i.e., $EWH = 1$ mm, on an area of 1 m^2 corresponds to a volume of 1 liter, or a mass of 1 kg, when assuming 1000 kg/m^3 as the average density of water. Time variability of the Earth's gravity field potential can be translated to EWH as follows (e.g., Wahr et al., 1998):

$$\Delta h_w = \frac{R\rho_{\text{e}}}{3\rho_{\text{w}}} \sum_{n=0}^{\infty} \sum_{m=0}^{n} \overline{P}_{nm}(\sin\varphi) \frac{2n+1}{1+k_n} W_n \left(\Delta\overline{C}_{nm}\cos m\lambda + \Delta\overline{S}_{nm}\sin m\lambda\right) \tag{2.49}$$

with the average density of the Earth $\rho_{\text{e}} = 5517$ kg/m^3 and water $\rho_{\text{w}} = 1000$ kg/m^3, the load Love numbers k_n of the solid Earth for a specific degree n (see Wahr et al., 1998, Table 1), the spherical harmonic coefficients differences $\Delta\overline{C}_{nm}$, $\Delta\overline{S}_{nm}$, the Gaussian smoothing filter coefficients W_n, and the other quantities as defined earlier (see e.g., Equation 2.21).

Not applying W_n to the coefficients differences, results in EWH values being affected by noise. An optimally chosen W_n reduces the contribution of generally noise-dominated higher degree spherical harmonic coefficients of the monthly gravity field solution (see Figure 2.3a,d and Figure 2.4). The Gaussian smoothing filter coefficients for a degree n can be computed recursively using the following relations (Jekeli, 1981; Wahr et al., 1998):

$$W_0 = \frac{1}{2\pi}, \qquad W_1 = \frac{1}{2\pi}\left(\frac{1+e^{-2b}}{1-e^{-2b}} - \frac{1}{b}\right), \qquad W_{n+1} = -\frac{2n+1}{b}W_n + W_{n-1} \tag{2.50}$$

$$\text{with} \qquad b = \frac{\ln(2)}{(1-\cos(r/R))}$$

where ln() denotes the natural logarithm, R is Earth's semimajor axis and r is the half-width radius of the filter (larger r results in greater smoothing). The choice of a suited value for r should balance noise reduction and signal preservation. Typical radii for smoothing the more recent releases of GRACE(-FO) gravity field solutions are 300 and 400 km. In addition to the widely used Gaussian filter, several other advanced filtering techniques have been developed over the years to enhance the quality of signal extraction from the gravity field solutions. These can be applied independently or in combination with the Gaussian filter, depending on the specific characteristics of the filtering approach. An overview and discussion of different filtering techniques can be found in Devaraju (2015).

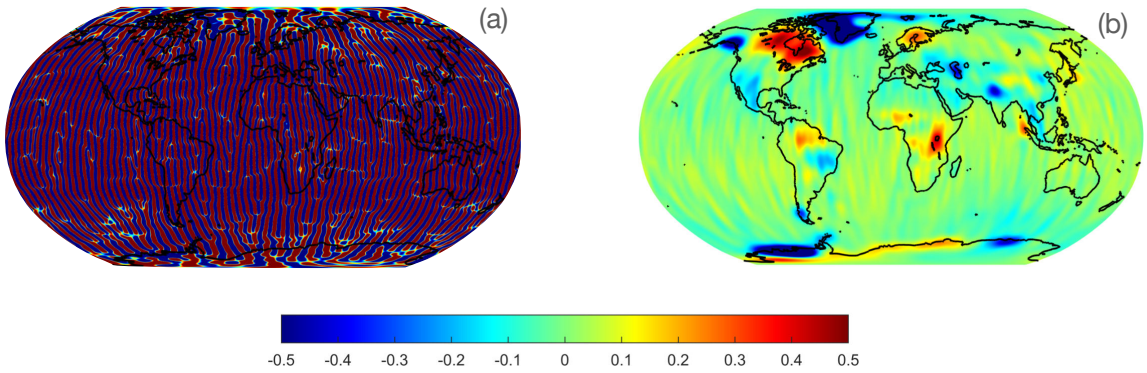

FIGURE 2.4: LUH January 2021 monthly gravity field solution in terms of EWH in meters. (a): Full signal until degree and order 96 (with C_{20} from SLR) minus static gravity field GOCO06s with reference epoch at 1 January 2010. The change in gravity is dominated by noise. (b): Gaussian filter with a half-width radius of 350 km was applied to (a).

Due to the limitations of the GRACE(-FO) satellites in observing the C_{20} coefficients—primarily because of their orbit geometry and measurement sensitivity—it is common practice to replace these coefficients in the monthly gravity field solutions with more reliable estimates derived from SLR when computing EWH and mass change (e.g., Cheng and Ries, 2017; König et al., 2019; Loomis et al., 2020).[4] The degree-1 coefficients (C_{10}, C_{11}, S_{11}) describing the geocenter motion are not included in the GRACE(-FO) monthly gravity field solutions but can be derived from the solutions and ocean bottom pressure data using the technique outlined in Swenson et al. (2008) and Sun et al. (2016).

To analyze mass changes, including long-term trends and seasonal variations, the EWH time series at a specific location of interest or at every element of a global grid, can be approximated by a suitable mathematical model, for example:

$$\Delta h_w(t) = a + bt + c\sin\left(\frac{2\pi}{p_a}t\right) + d\cos\left(\frac{2\pi}{p_a}t\right) + e\sin\left(\frac{2\pi}{p_{sa}}t\right) + f\cos\left(\frac{2\pi}{p_{sa}}t\right) \tag{2.51}$$

where $\Delta h_w(t)$ represents the value of the time series at time t, a is the bias, b the linear trend coefficient, c and d are the coefficients for the annual sine and cosine components, e and f the coefficients for the semiannual variation, and p_a and p_{sa} denote the annual and semiannual periods, respectively, given in units of t. The equation can, for example, be extended with additional periods of interest. The unknown parameters can be estimated using least squares adjustment (see Equation 3.40). The amplitudes for the annual and semiannual components are then given by $\sqrt{c^2+d^2}$ and $\sqrt{e^2+f^2}$, respectively.

2.3 Tide-Generating Potential and Ocean Tides

Ocean tides can be initially understood as the oceans' reaction to the tide-generating forces, which primarily drive the tidal oscillations in water levels and masses. Section 2.3.1 provides an introduction to the Tide-Generating Potential (TGP). The representation of the TGP using Legendre functions divides tides into different species, e.g., diurnal, semidiurnal, or long-periodic tides, and different degrees, e.g., degree-2 and degree-3 tides. Section 2.3.2 delves into the dynamics of ocean tides. Section 2.3.3 addresses the application of satellite altimetry for observing ocean tides. In Section 2.3.4, the relationship between the amplitudes and phases of the ocean tide models and the spherical harmonic coefficients representation is given. Moreover, an overview of relevant ocean tide models is provided.

[4] SLR-derived C_{20} coefficients for substitution recommended by the GRACE(-FO) Science Data System are provided in the Technical Note 14: `ftp://isdcftp.gfz-potsdam.de/grace-fo/DOCUMENTS/TECHNICAL_NOTES/TN-14_C30_C20_SLR_GSFC.txt` (last accessed on 2025-08-04).

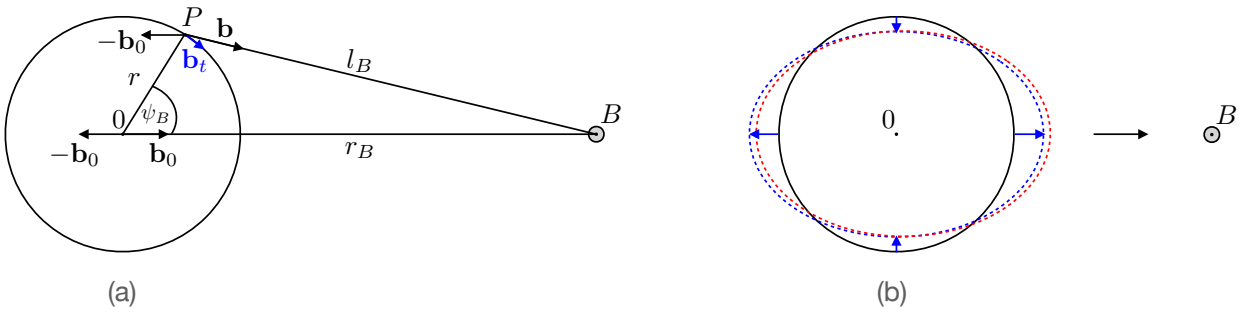

FIGURE 2.5: (a): Schematic view of the Earth–celestial body geometry for describing the tidal acceleration $\mathbf{b}_t$ in point P. 0 is the geocenter of the spherically symmetric Earth; B is the celestial body considered as a point mass. Orbital acceleration $-\mathbf{b}_0$ is constant and cancels with the gravitational acceleration $\mathbf{b}_0$ in the geocenter. (b): Symmetric tidal bulge due to degree $n = 2$ of the TGP (blue dashed ellipse) and asymmetric part due to degrees $n \geq 2$ (red), primarily $n = 3$.

2.3.1 Tide-Generating Potential

Tidal acceleration $\mathbf{b}_t = \mathbf{b} - \mathbf{b}_0$ due to a celestial body, e.g., the Moon, Sun or one of the planets, is the sum of the position-dependent gravitational acceleration $\mathbf{b}$ and the orbital acceleration $-\mathbf{b}_0$, which is the constant negative gravitational acceleration of the celestial body in the geocenter. The Moon causes by far the largest tidal acceleration at the Earth's surface, with a maximum value of approximately 1.37×10^{-6} m/s^2 (Wenzel, 1997), followed by the Sun (≈36% of Moon's acceleration), and the planets Venus (≈0.004%), Jupiter (≈0.0005%), and Mars (≈0.0001%) as the next largest contributors. Because of the much smaller contribution of the planets, it is reasonable to refer to the total tidal acceleration and the corresponding tidal (or tide-generating) potential as *lunisolar*. Nevertheless, the sensitivity of modern gravimeters also requires these planets to be considered. Newer tidal potential catalogues, which provide tabulated amplitudes for a set of waves (or frequencies) that can be used to synthesize the TGP for a specific location and time, therefore also contain terms for relevant planets (e.g., Hartmann and Wenzel, 1995; Roosbeek, 1996; Kudryavtsev, 2004).

By applying Newton's law of gravitation and using the relationship that acceleration is the gradient of the potential (see Equation 2.27), the two separate terms of the tidal acceleration and tidal potential due the gravitational pull of a celestial body can be written as (see e.g., Melchior, 1966; Wenzel, 1997; Agnew, 2009):

$$\mathbf{b} = \frac{GM_B}{l_B^2}\frac{\mathbf{l}_B}{l_B} \qquad \mathbf{b}_0 = \frac{GM_B}{r_B^2}\frac{\mathbf{r}_B}{r_B} \tag{2.52}$$

$$V = \frac{GM_B}{l_B} \qquad V_0 = \frac{GM_B}{r_B^2}\, r\cos\psi_B \tag{2.53}$$

where GM_B is the standard gravitational parameter of the celestial body, i.e., gravitational constant times the mass of the body; $\mathbf{l}_B$ is the vector pointing from the point on Earth's surface to the celestial body; $\mathbf{r}_B$ is the geocentric position vector of the body; $l_B = |\mathbf{l}_B|$, $r_B = |\mathbf{r}_B|$ are the respective distances; and r, ψ_B are the geocentric distance and zenith angle of point P, respectively. Mentioned geometric quantities and acceleration vectors are illustrated in Figure 2.5a.

With the trigonometric rule of cosines, l_B can be defined as $l_B = (r^2 + r_B^2 - 2rr_B\cos\psi_B)^{1/2}$. By reformulating the reciprocal distance $1/l_B$ in terms of a series expansion with Legendre polynomials $P_n(\cos\psi_B)$ of degree n (cf. Equations 2.30–2.32)[5], the tidal potential $V_t = V - V_0$ for a spherically symmetric Earth can

[5]Variables l, r', r, ψ in Equations 2.30–2.32 correspond to l_B, r, r_B, ψ_B in Equations 2.54 and 2.55. Also keep in mind that $P_0(\cos\psi_B) = 1$ and $P_1(\cos\psi_B) = \cos\psi_B$.

be written as:

$$V_t = GM_B \left(\frac{1}{l_B} - \frac{r \cos \psi_B}{r_B^2} - \frac{1}{r_B} \right) \tag{2.54}$$

$$= \frac{GM_B}{r_B} \sum_{n=2}^{\infty} \left(\frac{r}{r_B} \right)^n P_n(\cos \psi_B) \, . \tag{2.55}$$

Note that Equation 2.55 contains an additional term $-GM_B/r_B$ that is not part of Equations 2.53, but needs to be added so that the tidal acceleration vanishes in the geocenter, i.e., is 0 when $r = 0$ and $r_B = l_B$. The TGP is encoded in the first few degrees, with about 98% of the signal being part of the degree-2 term (Wenzel, 1997). The importance of degrees $n > 2$ as a contributor to V_t decreases fast, since r/r_B on Earth's surface is $\approx 1/60$ for the Moon and $\approx 1/23000$ for the Sun (Agnew, 2009; Hartmann and Wenzel, 1995, Table 1). State-of-the-art tidal potential catalogues (see later in this section) expand V_t until a maximum degree of 6 (Moon) and 4 (Sun), while for planets only degree 2 is considered.

Important properties of V_t become apparent when it is expressed in terms of spherical coordinates θ, λ (co-latitude and longitude of P) and Θ_B, Λ_B (co-latitude and longitude of B), instead of zenith angle ψ_B. With these geographical coordinates $\cos \psi_B$ can be formulated as: $\cos \psi_B = \cos \theta \cos \Theta_B + \sin \theta \sin \Theta_B \cos(\lambda - \Lambda_B)$, allowing to apply the addition theorem of spherical harmonics and express $P_n(\cos \psi_B)$ in Equation 2.55 in terms of normalized associated Legendre functions $\overline{P}_{nm}(\cos \theta)$ (see Section 2.2.3) dependent on degree n and order m (e.g., Wenzel, 1997):

$$P_n(\cos \psi_B) = \frac{1}{(2n+1)} \sum_{m=0}^{n} \overline{P}_{nm}(\cos \theta) \, \overline{P}_{nm}(\cos \Theta_B) \, \cos(m\lambda - m\Lambda_B) \, . \tag{2.56}$$

The two sums in Equations 2.55 and 2.56 divide the tidal potential and acceleration into terms of:

— **degree** n:

degree of a tidal wave; a tidal wave of degree n is referred to as degree-n tide, i.e.,

$n = 2$: degree-2 tide
$n = 3$: degree-3 tide
$n = 4$: degree-4 tide
...

— **order** m:

species of a tidal wave; a tidal wave of order m has a frequency of about m times per day, i.e.,

$m = 0$: long-periodic tide
$m = 1$: diurnal tide
$m = 2$: semidiurnal tide
...

While coordinates r_B, Θ_B vary only slowly in time, Λ_B is varying relatively fast due to the rotation of the Earth. With positions of the celestial bodies from ephemerides models (e.g., Bretagnon and Francou, 1988; Pitjeva, 2005; Folkner et al., 2014), V_t can be computed directly for a rigid and oceanless Earth model. However, the common method is to express the tidal potential as the sum of a set of sinusoids. By expressing the ephemerides of the Moon, Sun and planets in terms of harmonic functions of suitable astronomical quantities, a spectral decomposition of the tidal potential can be performed (e.g., Melchior, 1966; Agnew, 2009; Torge and Müller, 2012). The outcome of such a harmonic development is known as a tidal potential catalogue, which in combination with additional information, e.g., on Earths' elasticity, can be used for a more realistic modeling of Earth system's response to the tidal forcing. The first harmonic development, although limited to a very small number of main waves, was given by Ferrel in the 1870's (Doodson, 1921; Melchior, 1966). In the 1880's, Darwin published a quasi-harmonic development of the TGP, which was widely used at that time. The names he gave to the main waves (see e.g., Darwin, 1907, Table A), partly extended according to his nomenclature, are still in use and are known as *Darwin names*. Larger discrepancies between tidal observations and predictions from Darwin's development, attributed to imperfect harmonic constants and the limited amount of considered waves, led Doodson (1921) to develop a catalogue consisting of almost 400

waves utilizing a newer analytical lunar ephemerides model. The majority of recent catalogues are based on more precise numerical ephemerides, which, in contrast to analytical models, incorporate observational data. One example of such a catalogue is the HW95 model by Hartmann and Wenzel (1995), comprising 12935 waves, while the most recent, the KSM03 catalogue, includes 26753 terms (Kudryavtsev, 2004). Several other catalogues are listed in Wenzel (1997, Table 5).

The tidal potential V_t from a catalogue consisting of the waves i expanded until a maximum degree $n_{\max}$ can be represented in the HW95 format as:

$$V_t = \sum_{n=1}^{n_{\max}} \sum_{m=0}^{n} \left(\frac{r}{R}\right)^n \overline{P}_{nm}(\cos\theta) \sum_i \left[C_i^{nm}(t)\cos(\alpha_i(t)) + S_i^{nm}(t)\sin(\alpha_i(t))\right] \tag{2.57}$$

$$\text{with} \qquad \alpha_i(t) = m\lambda + \mathbf{k}_i \cdot \boldsymbol{\beta}(t)$$

where $C_i^{nm}(t)$, $S_i^{nm}(t)$ are the time-dependent spherical harmonic coefficients of the tidal potential of a wave i obtained from the spectral decomposition of the TGP computed from ephemerides[6]; R is the mean equatorial radius of the Earth; vector $\mathbf{k}_i$ contains the integer coefficients of the astronomical arguments vector $\boldsymbol{\beta}$; and the other quantities as defined in previous equations.

Note that Equation 2.57 starts at degree $n = 1$ instead of $n = 2$ as earlier defined in Equation 2.55. While Equation 2.55 is a good approximation of V_t and is valid for a spherically symmetric Earth, the newer tidal potential catalogues, e.g., by Hartmann and Wenzel (1995), Roosbeek (1996), Kudryavtsev (2004), additionally consider Earth's flattening effects, which give rise to small degree-1 terms (see e.g., Hartmann and Wenzel, 1995, Equation 1). Although these effects are relatively small compared to the lunisolar TGP, the amplitude can be comparable to that of the planets (cf. numeric values in Wenzel, 1997; Hartmann and Wenzel, 1995, Table 1).

A comparison of Equation 2.21 (gravitational potential of the Earth) with the aforementioned representation of the TGP reveals the main conceptual distinction: in contrast to the gravitational potential, the TGP is additionally separated into different frequency components i. For the case of a purely lunisolar TGP, the astronomical arguments vector contains six independent fundamental angles in the following sequence: τ (mean Lunar time), s (mean longitude of the Moon), h (mean longitude of the Sun), p (longitude of Moon's mean perigee), N' (negative longitude of Moon's mean ascending node), and p_s (longitude of Sun's mean perigee). These fundamental angles were used by Doodson (1921) for his harmonic development of the TGP; therefore also known as *Doodson arguments*. The periods of variation of the six Doodson arguments are listed in Table 2.2. Numeric values of the fundamental arguments with respect to different origin of time can be computed directly from time-dependent developments (see e.g., Doodson, 1921; Melchior, 1966). Conventional present-day developments usually refer to epoch J2000.0. The related numeric values of the six fundamental arguments can be obtained with the help of Delaunay variables F, Ω, D, l, l' (see Equation 2.12) as:

$$\boldsymbol{\beta} = \begin{pmatrix} \tau \\ s \\ h \\ p \\ N' \\ p_l = p_s \end{pmatrix} = \begin{pmatrix} GMST + \pi - s \\ F + \Omega \\ s - D \\ s - l \\ -\Omega \\ s - D - l' \end{pmatrix} \tag{2.58}$$

[6]The HW95 model and several other catalogues in the HW95 format are available as part of the Earth tide data processing software Eterna (Wenzel, 2022). KSM03 in HW95 format can be obtained here: `http://lnfm1.sai.msu.ru/neb/ksm/tgp/ksm03.dat` (last accessed on 2025-08-08).

Table 2.2: Six fundamental angles (also known as Doodson fundamental arguments), corresponding approximate periods of variation, and angular frequencies (see e.g., Melchior, 1966).

Angle	Description	Period	Frequency
τ	Mean Lunar time	24 hours 50.47 min	14.492072°/h
s	Mean longitude of the Moon	27.3216 days	0.549016°/h
h	Mean longitude of the Sun	365.2422 days	0.041068°/h
p	Longitude of Moon's mean perigee	8.847 years	0.004642°/h
N'	Negative longitude of Moon's mean ascending node	18.613 years	0.002206°/h
p_s	Longitude of Sun's mean perigee	20940 years	0.000002°/h

Table 2.3: Doodson number.

Doodson number	**135.655**	**255.555**
Darwin name	Q_1	M_2
Species	$m = 1$, i.e., diurnal tide	$m = 2$, i.e., semidiurnal tide
Group number	13	25
Constituent number	135	255
Multipliers	$\mathbf{k}_i = [1, -2, 0, 1, 0, 0]$	$\mathbf{k}_i = [2, 0, 0, 0, 0, 0]$
Argument	$\mathbf{k}_i \cdot \boldsymbol{\beta}$: $\tau - 2s + p$	$\mathbf{k}_i \cdot \boldsymbol{\beta}$: 2τ
Period	1.1195 days	0.5175 days
Frequency	13.3986°/h	28.9841°/h

with the Greenwich Mean Sidereal Time (GMST), which, according to the IAU 2000 definition (Capitaine et al., 2003), is a function of the ERA (Equation 2.16), and with time t defined in centuries since epoch J2000.0 of the TT system, can be computed the following way:

$$\begin{aligned} GMST = ERA + 0.01450'' + 4612.156534''t + 1.3915817''t^2 - 0.00000044''t^3 \\ - 0.000029956''t^4 - 0.0000000368''t^5 \,. \end{aligned} \tag{2.59}$$

Using Doodson's argument number, now also simply known as *Doodson number*, the tidal waves can be classified, and angle and frequency information can be represented in an elegant manner as exemplarily shown for two waves in Table 2.3. The Doodson number consists of six positive digits. The first three elements have a special meaning and are separated from the other three elements by a point. The first element k_1 is always equal to the order m of the TGP and therefore represents the tidal species. Tidal waves with identical first two values are part of the same tidal *group*; furthermore, they are considered to be part of the same tidal *constituent* when the first three elements are identical. In the literature, the term "constituent" is not always strictly used according to the above definition. Often distinct waves within the same constituent are also simply denoted as constituents. In some places in this thesis, Doodson's notation might also be violated. The five multipliers k_2 to k_6 are obtained by subtracting 5 from the corresponding elements of the Doodson number[7]. The scalar product of these six multipliers with the six Doodson fundamental arguments, i.e., $k_1\,\tau + k_2\,s + k_3\,h + k_4\,p + k_5\,N' + k_6\,p_s$, yields the astronomical or Doodson argument

$$\theta_i = \mathbf{k}_i \cdot \boldsymbol{\beta}(t) \tag{2.60}$$

[7]While the multiplier of τ is always positive, multipliers of the other five fundamental angles can be negative, but are only rarely outside the range of $-4...4$. Therefore, by introducing the $+5$ offset, negative values are omitted and the multipliers can be written neatly as a six digit number—at least for the most important waves. As can be seen, for example, from the group number notation in Figure 2.7, this specific notation can "run-out", e.g., after 10 or 19.

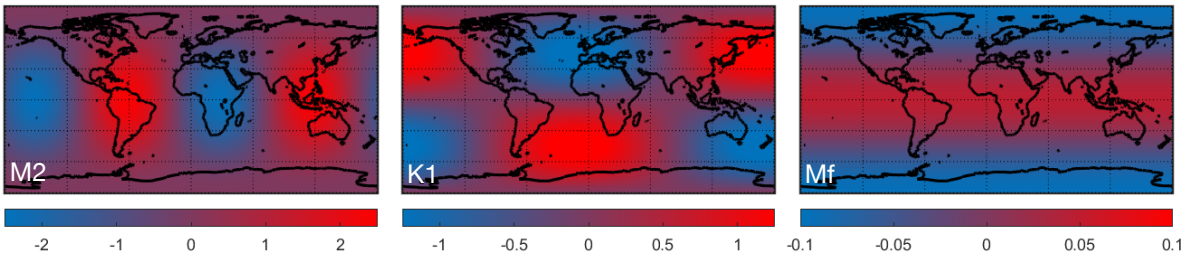

FIGURE 2.6: TGP of the largest semidiurnal, diurnal and long-periodic constituents at J2000.0 in m^2/s^2.

which has to be distinguished from the co-latitude θ in Equation 2.57. The astronomical argument can equivalently be formulated as $\theta_i = \theta_i(t_0) + \dot{\theta}_i t$, where $\theta_i(t_0)$ is the astronomical argument at an initial epoch t_0, and $\dot{\theta}_i$ is the angular velocity of the constituent i. In an analogous manner to Equation 2.60, the angular velocity is obtained as the scalar product of the multipliers $\mathbf{k}_i$ with the frequencies of the Doodson fundamental arguments expressed in appropriate units. For the corresponding frequency in degree per hours of the six Doodson fundamental arguments, see Table 2.2.

In the case of the consideration of planetary contribution to the TGP, the vector of astronomical arguments is extended by the mean longitudes of the relevant planets. Time developments for the mean longitudes of the planets are presented in Equation 2.12. For a planetary wave all multipliers are 0, except the relevant multiplier of the specific planet's mean longitude and the first element denoting the species of the wave i.

Figure 2.6 shows the TGP amplitude maps for M_2, K_1 and Mf. Here the term amplitude refers to V_t of the respective wave i at the surface of the Earth (see Equation 2.57). Ignoring the minor degree-3 tides, one can generally state that, due to the (co-)latitude dependence of the associated Legendre functions (see Figure 2.2 and the corresponding discussion), the TGP exhibits the following characteristics: the long-periodic tides divide the potential into three zones with maximum absolute values at the poles; diurnal tides are characterized by four cells with maximum values at latitudes of $\pm 45°$ and zero at the equator; and the potential of semidiurnal tides consists of four sectors with maximum values at the equator and zero at the poles. Figure 2.7 shows the diurnal and semidiurnal spectrum of the TGP amplitudes, i.e., $\sqrt{C_i^2(t_0) + S_i^2(t_0)}$ (see Equation 2.57), of the HW95 catalogue. The separation of the spectrum into individual groups is clearly recognizable. Darwin names of the main constituents are given. The Doodson numbers of these principal tides, their angular speeds, periods, relative amplitudes, and information on the origin are given in Table 2.4. The constituent with the largest amplitude is the lunar principal wave M_2 with an amplitude of approximately 1.2356 m^2/s^2. Other constituents with a relatively large TGP are K_1 (58% of the M_2 amplitude), S_2 (47%), O_1 (41%), P_1 (19%), and N_2 (19%). While most constituents in Table 2.4 are related either to the motion of the Moon or the Sun, the constituents K_1 and K_2 have both lunar and solar origins, with the lunar contribution accounting for about two-thirds of the total amplitude. Besides the celestial bodies giving rise to the individual constituents, the information on the origin in Table 2.4 also specifies the corresponding astronomical variable. Elliptical waves arise due to the ellipticity of the Moon's orbit around the Earth, and Earth's orbit around the Sun. Declinational waves are generated due to the fact that the orbital planes of the celestial bodies are inclined with respect to the equatorial plane. The variational waves arise from changes in the Sun's perturbing force on the motion of the Moon throughout a synodic month, while the evection terms are induced by the Sun's gravitational attraction altering the Moon's orbital eccentricity (e.g., Pugh and Woodworth, 2014). Note that all the principal waves listed in Table 2.4 refer to the degree-2 potential, with the exception of the terdiurnal degree-3 constituent M_3. From Equation 2.57, it is easy to see that no tides of degree $n = 2$ can exist in the terdiurnal band. Other notable degree-3 tides have amplitudes of around 0.6% of M_2 and, rather than being part of the terdiurnal species, they are found in the diurnal and semidiurnal bands, in close proximity to several larger degree-2 waves. In contrast to M_3, these waves are part of these larger constituents (in Doodson's definition of this term), and become apparent as distinct components in observational data, only when a sufficiently long time series is analyzed (e.g., Ray, 2020b).

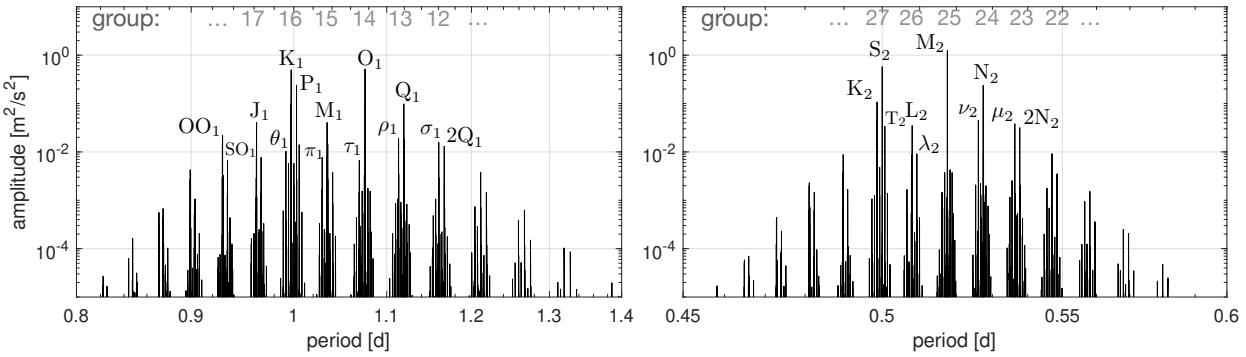

FIGURE 2.7: Amplitudes of the diurnal and semidiurnal waves of the HW95 tidal potential catalogue exceeding 10^{-5} m^2/s^2. Some of the principal waves are labeled with the respective Darwin names.

TABLE 2.4: Principal tidal waves (see e.g., Melchior, 1966; Pugh and Woodworth, 2014). The amplitudes refer to the HW95 catalogue and are expressed in percentage of the M_2 TGP (≈1.2356 m^2/s^2). Shown are constituents with amplitudes exceeding 1% of the M_2 amplitude. M: Moon, S: Sun.

Tide	Doodson number	Frequency [°/h]	Period [d]	Amplitude [% of M_2]	Origin
Long-periodic					
Sa	056.554	0.0411	365.2596	1.10	S, ellipticity
Ssa	057.555	0.0821	182.6211	6.93	S, declination
Mm	065.455	0.5444	27.5545	7.87	M, ellipticity
Mf	075.555	1.0980	13.6608	14.90	M, declination
Diurnal					
$2Q_1$	125.755	12.8543	1.1669	1.05	M, ellipticity
σ_1	127.555	12.9271	1.1604	1.27	M, variation
Q_1	135.655	13.3986	1.1195	7.94	M, ellipticity
ρ_1	137.455	13.4715	1.1135	1.51	M, evection
O_1	145.555	13.9430	1.0758	41.48	M, principal
M_1	155.655	14.4967	1.0347	3.26	M, ellipticity
π_1	162.556	14.9179	1.0055	1.13	S, ellipticity
P_1	163.555	14.9589	1.0027	19.30	S, principal
K_1	165.555	15.0411	0.9973	58.31	MS, declination
J_1	175.455	15.5854	0.9624	3.26	M, ellipticity
OO_1	185.555	16.1391	0.9294	1.78	M, declination
Semidiurnal					
$2N_2$	235.755	27.8953	0.5377	2.53	M, ellipticity
μ_2	237.555	27.9682	0.5363	3.06	M, variation
N_2	245.655	28.4397	0.5274	19.15	M, ellipticity
ν_2	247.455	28.5126	0.5261	3.64	M, evection
M_2	255.555	28.9841	0.5175	100.00	M, principal
L_2	265.455	29.5285	0.5080	2.83	M, ellipticity
T_2	272.556	29.9589	0.5007	2.72	S, ellipticity
S_2	273.555	30.0000	0.5000	46.52	S, principal
K_2	275.555	30.0821	0.4986	12.64	MS, declination
Terdiurnal					
M_3	355.555	43.4761	0.3450	1.21	M, principal

2.3.2 Ocean Tide Dynamics

The previously introduced TGP can be expressed in dimensions of elevation as a so-called *equilibrium tide* (see e.g, Marchuk and Kagan, 1989; Pugh and Woodworth, 2014). The equilibrium tide theory assumes a water-covered Earth with a depth sufficient to ensure that the ocean surface responds instantaneously to the tide-generating forces, and the ocean surface acquires the form of an equilibrium surface. The hypothetical ocean surface elevation to achieve equilibrium, i.e., the equilibrium tide $\overline{\zeta}$ of the tidal potential V_t is then $\overline{\zeta} = V_t/g$, where g is Earth's mean gravity. Using this equation, the Moon and the Sun generate a maximum equilibrium tide of approximately 0.365 m and 0.165 m, respectively. These amplitudes are rather small in comparison to the ocean tide amplitudes that can be observed in reality. The tides in the main oceans have mean amplitudes of about 0 to 0.5 m (Pugh and Woodworth, 2014). As tides originating in the open ocean move toward the continental shelves, their amplitudes increase significantly. In coastal regions meter level amplitudes are not uncommon, and can even exceed 10 m in some hypertidal coastal systems (e.g., Archer, 2013; Pugh and Woodworth, 2014). Therefore, the real response of the oceans to the TGP cannot be accurately described as an equilibrium tide.[8]

The discrepancies between elevations from the equilibrium tide theory and the observed tides can generally be attributed to the non-realistic water depth assumption. In reality, the presence of land masses makes it necessary to consider several hydrodynamic mechanisms which affect the tidal wave characteristics (e.g., Parker, 2007; Pugh and Woodworth, 2014). The consideration of hydrodynamic mechanism becomes increasingly important when the tidal waves generated in the open ocean are approaching the continental shelves and coasts. The friction between the water masses and the ocean bottom topography causes energy dissipation, reduces the amplitudes of the tidal waves, and distorts their shape as they propagate through the shallow waters. Since the continents act as barriers, tidal waves cannot propagate as long waves, are reflected in a complex way at the irregularly shaped coasts, and interact with other reflected and incoming waves (e.g., Parker, 2007; Pugh and Woodworth, 2014).

Consequently, by considering hydrodynamic principles and mechanisms governing the ocean tide dynamics, a much more realistic representation of tidal amplitudes can be achieved compared to the equilibrium theory. The local three-dimensional ocean state at time t is described by the sea surface anomaly ζ and the two-dimensional depth-averaged current velocity vector $\mathbf{v}$ with an eastward and northward component. The relationship between the ocean state, the TGP, as well as the relevant hydrodynamic mechanisms, can be formulated in the framework of the two following partial differential equations (see e.g., Marchuk and Kagan, 1989; Zahel, 1997; Weis et al., 2008; Sulzbach, 2023):

$$(\mathbf{v}\cdot\nabla)\,\mathbf{v} + \left[\, \frac{\partial \mathbf{v}}{\partial t} + \mathbf{f}\times\mathbf{v} = -g\left(\zeta - \gamma\overline{\zeta} - \zeta_{sal}\right) \right] - \frac{r}{H}|\mathbf{v}|\mathbf{v} + \mathbf{F} + \nabla V_{atm} \tag{2.61}$$

$$\nabla\cdot(\zeta\,\mathbf{v}) + \left[\, \frac{\partial \zeta}{\partial t} + \nabla\cdot(H\,\mathbf{v}) = 0 \right]. \tag{2.62}$$

The segment of the partial differential equations enclosed in the square brackets represents Laplace's hydrodynamic equations of continuity (2.62) and momentum (2.61), also known as *Laplace's tidal equations*, which here describe the dynamics of a thin fluid layer on the surface of the rotating spherical Earth (e.g., Pugh and Woodworth, 2014). The presented Laplace's tidal equations are extended by incorporating additional non-linear and radiational terms.

[8] This refers to the TGP as a whole and its broader spectrum. However, as the oscillation frequency decreases, the ocean's response to the influence of the TGP should approach a state of equilibrium (e.g., Proudman, 1960; Marchuk and Kagan, 1989). As will be discussed later in Section 2.3.4, there are individual long-periodic components of the tidal spectrum that are modeled as equilibrium tides.

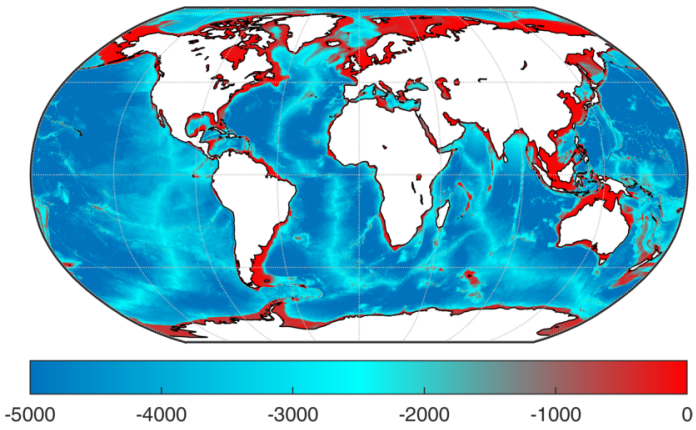

FIGURE 2.8: Bathymetry of the RTopo-2 model (Schaffer et al., 2016). Units: m. Note that the deep ocean depth can considerably exceed the lower color bar limit of −5000 m. The term "shallow water" used in this thesis refers to depths of roughly up to 1000 m (red color).

In the above system of partial differential equations, $\mathbf{f}$ represents the Coriolis acceleration vector, which is the product of the Coriolis parameter $2\Omega \sin \varphi$ and the vertically upward-oriented unit vector. The Coriolis parameter is a function of Earth's mean rotation velocity Ω, and the latitude φ. The surface gravity g of a spherical Earth multiplied with the equilibrium tide $\overline{\zeta}$ results in the TGP. The TGP is transformed into the tide-raising potential by accounting for the influence of the solid Earth's tidal deformation on the oceanic tidal potential with the scale factor $\gamma = (1 + k_n - h_n)$, which is approximately 0.69 for degree $n = 2$ and 0.80 for $n = 3$ (Wahr, 1981). Strictly, the Love numbers k_n and h_n and consequently factor γ exhibit frequency dependency, with largest deviations from the mentioned approximate values observed in the K_1 group, especially for ψ_1, due to the perturbation of the potential by the the so-called nearly diurnal free wobble resonance (e.g., Ray, 2017). The effect of self attraction and loading of the water masses is denoted as height $\overline{\zeta}_{sal}$.

The bottom friction term $r/H|\mathbf{v}|\mathbf{v}$ is parameterized as a function of the current velocity vector, the quadratic bottom friction coefficient r, and the instantaneous water depth H, which can be obtained from a bathymetric model (e.g., Weatherall et al., 2015; Schaffer et al., 2016; see also Figure 2.8). Bottom friction together with advection $(\mathbf{v} \cdot \nabla)\,\mathbf{v}$ and wave drift $-\nabla \cdot (\zeta\,\mathbf{v})$ are key variables creating *non-linear tides* (e.g., Le Provost, 1991; Parker, 2007; Pugh and Woodworth, 2014). These tides are generated in the shallow waters, and therefore are also called *shallow water tides*. As the tidal waves approach shallow waters, their originally sinusoidal shape becomes distorted and increasingly complex. This complexity implies that the waves can no longer be described solely by the original sinusoidal. Instead, energy is transferred to additional non-linear frequencies. Non-linear tides can be categorized into *overtides* and *compound tides*. Overtides have frequencies that are integer multiples of the frequency of a primary gravitationally excited constituent. For instance, M_4 is an overtide with a frequency that is twice that of the main semidiurnal tide M_2 (simplified: $M_4 = 2M_2$); and similarly: $M_6 = 3M_2$, $S_4 = 2S_2$. Compound tides represent the interaction of two or more astronomical constituents, for example, $\mathrm{Msf} = M_2 - S_2$, $2MS_2 = 2M_2 - S_2$, $MNS_2 = M_2 + N_2 - S_2$. Important non-linear tides are summarized in Pugh and Woodworth (2014, Table 4.4). More comprehensive lists of non-linear tides are available in Le Provost (1991, Table 1) and Parker (2007, Table A.1). It is important to note that compound tides of different origin can share the same frequency, e.g., MO_3 and $2MK_3$. Additionally, the frequencies of non-linear tidal constituents often coincide with those of astronomical tides, e.g., $2MS_2$ and μ_2. According to Parker (2007), a shallow water constituent is generally expected to be larger, relative to other shallow water tides, when its name is composed of fewer letters and includes letters representing some of the major astronomical constituents.

Additional frictional effects, denoted as $\mathbf{F}$ in Equation 2.61, include topographic wave drag, parameterized horizontal eddy-viscosity, and ice friction, with their equations and more details provided, for example, in Sulzbach (2023). The ice friction, a mainly seasonal variable that is of importance for the marginal seas

at high latitudes, is another mechanism causing an attenuation of tidal wave elevations and a distortion of tidal wave propagation (e.g., Zubov, 1963; St-Laurent et al., 2008). Ice friction, along with other seasonally varying factors such as ocean stratification (e.g., Kang et al., 2002; Müller et al., 2014) or meteorological surges (e.g., Huess and Andersen, 2001), can lead to *seasonal modulations* of tides. In the sea level spectrum, depending on the location, seasonal modulations of a constituent with the frequency f appear as annual ($f \pm 1$ cycle/year) and/or semiannual ($f \pm 2$ cycles/year) side lines (e.g., Ray, 2022). Especially pronounced modulations can be found for the M_2 constituent in the Arctic region (e.g., Müller et al., 2014; Kulikov et al., 2018; Bij de Vaate et al., 2021).

Periodic variations at tidal frequencies in atmospheric surface pressure caused by solar radiation lead to the formation of *radiational ocean tides* (e.g., Munk and Cartwright, 1966; Dobslaw and Thomas, 2005; Ray et al., 2023). In the hydrodynamic equations, these radiationally excited variations are forced by the acceleration term ∇V_{atm}, where the potential V_{atm} encompasses the relevant atmospheric surface pressure potential, as well as secondary potentials due to the atmospheric attraction of the water masses and atmospheric loading, but also considers wind stress (see Balidakis et al., 2022; Sulzbach, 2023). According to Balidakis et al. (2022), 16 tidal frequencies are significant for generating an ocean response that is of relevance for satellite gravimetry. The largest tidal signal in atmospheric surface pressure data can be observed for solar constituents S_1 and S_2, which correspond to frequencies of one or two cycles per solar day, and due to the seasonal modulation, also at their annual side lines P_1, K_1 and T_2, R_2, respectively.

Solving the hydrodynamic partial differential equations is a complex task. Readers seeking a deeper understanding are encouraged to consult the references provided prior to Equations 2.61 and 2.62 for further details. Depending on how the hydrodynamic equations are forced, such as with only a single partial tide or the whole potential from ephemerides (Weis et al., 2008), a harmonic analysis (see Equation 2.64) might be necessary to extract the tidal amplitudes and phases. A set of solutions of the hydrodynamic equations is referred to as a *hydrodynamic ocean tide model*.

2.3.3 Observing Ocean Dynamics with Altimetry

The fundamental operating principle of satellite altimeters involves emitting radar or lidar pulses to the ground, which are then reflected by the sea or ice surface and registered by the satellite antenna. The range R from the satellite to the ground can be calculated from the round-trip travel time Δt of the radar signal. This range is approximately $c\Delta t/2$, where c represents the speed of light. The Sea Surface Height (SSH), defined as the height of the sea surface relative to a reference ellipsoid, is a primary product of satellite altimetry for studying ocean circulation. By subtracting a model of Mean Sea Surface Heights (MSSHs) from the SSH obervations, Sea Level Anomalies (SLAs) are obtained.

The orbit height h of the altimeter satellite above an ellipsoid obtained from Precise Orbit Determination (POD), altimeter range R from the measured wave forms using retracking algorithms, and SSH are related via the following equation (e.g, Chelton et al., 2001; Seeber, 2003; Andersen and Scharroo, 2011):

$$SLA = h - R - \Delta h_R - \Delta h_{geo} - MSSH \tag{2.63}$$

where Δh_R represents range corrections that account for the modified propagation of the radar pulse through the ionosphere and troposphere, as well as the effect of the sea state on the reflected pulse (sea state bias); and corrections Δh_{geo} are applied to reduce geophysical time-variable sea-level variations from the SSH observations. The latter corrections include the influence of tidal effects, with ocean tides representing by far the largest contribution, alongside smaller effects from solid Earth tides, pole tides and loading tides; as well as the contribution from atmospheric loading (inverted barometer effect). The corrections Δh_{geo} can also include a geoid correction, which, when applied, will reference the SSH values to the geoid rather than the reference ellipsoid.

Table 2.5: Primary satellite altimetry missions used for ocean tide modeling.[1]

Mission	TOPEX/ Poseidon	Jason-1	Jason-2	Jason-3	ERS-1	ERS-2	Envisat
Agency	NASA, CNES	NASA, CNES	NASA, CNES, NOAA, EUMETSAT	NASA, CNES, NOAA, EUMETSAT	ESA	ESA	ESA
Operation time	1992-08–2006-01	2001-12–2013-07	2008-06–2019-10	2016-01–	1991-07–2000-03	1995-04–2011-07	2002-03–2012-04
Inclination [°]	66.039	66.038	66.038	66.038	98.52	98.5	98.55
Altitude [km]	1336	1336	1336	1336	782	780	800
Repeat cycle [d]	9.9156	9.9156	9.9156	9.9156	35	35	35

[1]Information from EO Portal: `https://www.eoportal.org` (last accessed on 2025-03-03). The approximate orbit parameters refer to the main mission phases. NOAA: National Oceanic and Atmospheric Administration, USA; EUMETSAT: European Organisation for the Exploitation of Meteorological Satellites. In terms of orbital parameters, the CNES/Indian Space Research Organisation mission, SARAL, can be regarded as a follow-on mission to Envisat. However, as of now, the observations from this mission are scarcely used in ocean tide modeling (see Table 2.8).

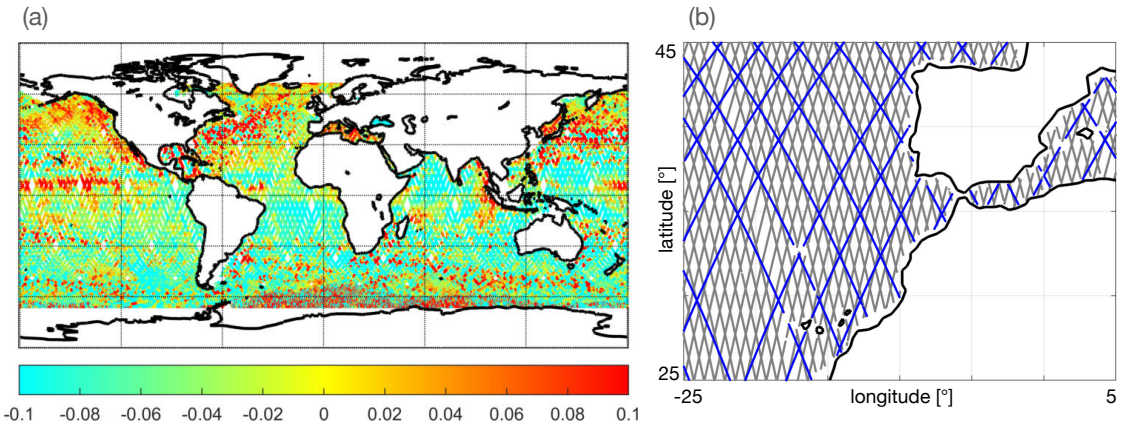

Figure 2.9: (a): TOPEX/Poseidon SLAs in meters for a cycle beginnig at 3 October 1992, 01:36 (cycle 2). SLA data obtained from OpenADB. (b): Ground tracks of TOPEX/Poseidon (blue) and ERS-1 (gray). TOPEX/Poseidon and the Jason satellites revisited the same location every 9.9156 days. In contrast, ERS-1, ERS-2, and Envisat offer better spatial coverage but have a longer repeat cycle of 35 days.

Satellite altimetry missions are designed as repeat track missions, where the satellite consistently follows a designated ground track over the Earth's surface. Throughout its cycle, the satellite collects data along this predefined path (see Figure 2.9b). After a constant period (the repeat cycle), the satellite returns to the same ground track, allowing for the collection of consistent and comparable data necessary for analyzing the state of the ocean. The repeat cycle of a satellite mission is governed by the satellite altitude and orbit inclination (e.g., Parke et al., 1987). Details of the most important satellite altimetry missions for ocean tide modeling—namely, TOPEX/Poseidon, Jason-1, Jason-2, Jason-3, ERS-1, ERS-2, and Envisat—are summarized in Table 2.5.

SSH and SLA time series from various satellite altimetry missions with a certain degree of intermission harmonization can, for example, be obtained from the *Open Altimeter Database* (OpenADB, Schwatke et al., 2024)[9] of the Deutsches Geodätisches Forschungsinsitut (DGFI) of the Technical University of Munich, and the Radar Altimeter Database System (RADS, Naeije et al., 2000)[10] of the Delft Institute for Earth-Oriented Space Research (DEOS). Figure 2.9a shows, as an example, a map of one cycle of SLAs from the

[9]`https://openadb.dgfi.tum.de` (last accessed on 2025-08-04)

[10]`http://rads.tudelft.nl/rads/rads.shtml` (last accessed on 2025-08-04)

TOPEX/Poseidon mission, with data obtained from OpenADB. The TOPEX/Poseidon satellite revisited the same location every 9.9156 days (see Table 2.5). With an orbit inclination of 66°, TOPEX/Poseidon was limited to collecting data within the latitudinal range of +66° to −66°. The SLA values are given with respect to the MSSH of the DTU15MSS model (Andersen et al., 2016), and were corrected using the EOT20 ocean tide model (Hart-Davis et al., 2021), which contains solutions of 17 constituents.

To estimate (residual) amplitudes of a set of tidal constituents and their temporal evolution at a specific location defined by longitude λ and latitude φ, a harmonic analysis of the series of SLA observations can be performed. The functional model involves an equation of the following type (e.g., Schrama and Ray, 1994; Foreman et al., 2009):

$$SLA(\varphi,\lambda,t) = c(\varphi,\lambda) + v(\varphi,\lambda,t) + \sum_{i=1}^{N} a_i(\varphi,\lambda) f_i(t) \cos(\theta_i(t) + u_i(t)) + b_i(\varphi,\lambda) f_i(t) \sin(\theta_i(t) + u_i(t)) \tag{2.64}$$

with the cosine and sine coefficients a_i and b_i of a tidal constituent i out of N frequencies to be considered, bias term c, time t relative to reference epoch t_0, the astronomical argument θ_i (see Equation 2.60), factors f_i and u_i for the amplitudes and phases of lunar constituents to account for the modulation due to the 18.6-year lunar nodal cycle, and residual signal v.

The unknowns a_i, b_i, c can be obtained by solving the over-determined system with standard least squares adjustment procedures (see Equation 3.40). The amplitudes and Greenwich phase lags of a tidal constituent i are then $\sqrt{a_i^2 + b_i^2}$ and $\arctan(b_i/a_i)$, respectively.

The specific constituents to be estimated should logically focus on those with the largest TGP, from which the spectrum of smaller gravitationally excited tides can be extended based on the linear admittance assumption (see next section), as well as on the main non-linear constituents. In general, the longer the time series, the better closely spaced constituents can be resolved. Additionally, since altimetry satellites pass over a certain location only every few days, the mission-specific signal (under)sampling causes high-frequency tidal signal to be aliased to lower frequencies, thereby affecting which tidal frequencies can be well observed and which cannot. Given the significant climate-driven seasonal fluctuations in sea level variability, it is essential for tidal analysis that the aliasing period of any specific constituent is not too close to the primary seasonal periods of one year and half a year, to avoid contamination of the tidal solution by signal of non-tidal origin. The aliasing period p_A of an ocean tide constituent with period p can be computed as (e.g., Schlax and Chelton, 1994; Chen and Lin, 2000):

$$p_A = \frac{p_S}{\left| \frac{p_S}{p} - \left[\frac{p_S}{p} + 0.5 \right] \right|} \tag{2.65}$$

where p_S is the repeat cycle of the satellite, and $[x]$ gives the greatest integer less than or equal x.

Table 2.6 presents the aliasing periods for the major constituents of the diurnal and semidiurnal bands, corresponding to the 9.9156-day repeat cycle orbits of TOPEX/Poseidon, Jason-1, -2, -3, and the 35-day repeat cycle orbits of ERS-1, -2, and Envisat. For TOPEX/Poseidon and Jason missions, K_1 can be considered as the most critical constituent due to its proximity to the semiannual period. In the case of ERS-1, -2, and Envisat, P_1 and K_1 align with the annual period, while K_2 coincides with the semiannual period, making them a target for aliased non-tidal signal. Furthermore, for S_2 and the other solar constituents S_m, e.g., S_1, S_3, the aliasing period is effectively infinite due to the Sun-synchronous orbit. These missions sample the solar tidal signal at a constant phase, making these constituents unobservable. Figure 2.10 illustrates a comparison of how a periodic dimensionless signal with an amplitude of 1 and the frequency of S_2 is sampled by TOPEX/Poseidon, Jason-1, -2, and by ERS-1, -2, and Envisat. While TOPEX/Poseidon, Jason-1, -2 sample the entire amplitude range, ERS-1, -2, and Envisat sample the signal at nearly the same phase,

TABLE 2.6: Aliasing periods (in days) of the main tidal constituents for TOPEX/Poseidon, Jason-1, -2, -3, ERS-1, -2, and Envisat. Critical aliasing periods are highlighted.

	Q_1	O_1	P_1	K_1	N_2	M_2	S_2	K_2
TOPEX/Poseidon, Jason-1, -2, -3	69	46	89	173	50	62	59	87
ERS-1, -2, Envisat	133	75	365	365	97	94	∞	183

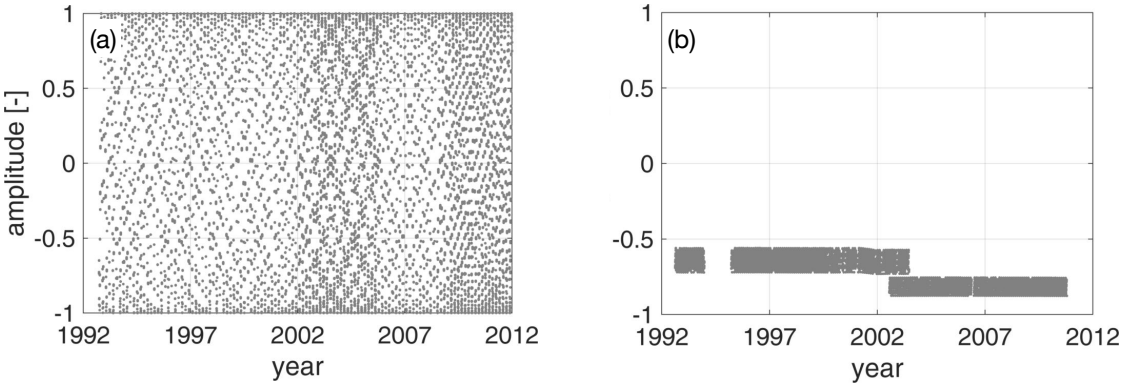

FIGURE 2.10: Sampling of S_2 signal by TOPEX/Poseidon, Jason-1, -2 (a), and by the Sun-synchronous orbits of ERS-1, -2, Envisat (b).

TABLE 2.7: Rayleigh periods p_R in days for the constituents listed in Table 2.6 (extended by Sa and Ssa). To compute p_R, aliasing periods with more decimals were utilized. ∞: period longer than 1000 years.

	O_1	P_1	K_1	N_2	M_2	S_2	K_2	Sa	Ssa	O_1	P_1	K_1	N_2	M_2	S_2	K_2	Sa	Ssa
Q_1	134	316	116	173	595	384	349	86	112	173	209	209	365	327	133	487	209	487
O_1		94	62	595	173	206	97	52	61		94	94	327	365	75	127	94	127
P_1			183	112	206	173	3341	117	173			∞	133	127	365	366	∞	365
K_1				69	97	89	173	329	3340				133	127	365	365	∞	365
N_2					244	316	116	57	68					3122	97	209	133	209
M_2						1081	220	75	94						95	196	127	196
S_2							183	70	87							183	365	183
K_2								113	165								366	∞
Sa	*TOPEX/Poseidon, Jason-1, -2, -3*								365	*ERS-1, -2, Envisat*								365

resulting in an effective tidal frequency of 0 and the observation of constant amplitudes. Due to the "frozen" character of the major solar constituent S_2, several linear and non-linear constituents cannot be separated (e.g., Andersen, 1999; Andersen et al., 2006). For example, $2SM_2$, MS_4, $2SM_6$, and Msf have the same aliasing periods as M_2; and $2MS_2$, M_4, $2MS_6$ share the same aliasing periods. For the larger linear constituents, e.g., M_2, this non-separability might not be a problem due to the large signal component; however, it makes estimating realistic amplitudes of the smaller non-linear constituents impossible.

For the major constituents in Table 2.6 that share a similar aliasing period, the question arises whether they can be sufficiently separated. To assess the separability of two constituents, the so-called *Rayleigh criterion* is often employed, according to which two tidal constituents are considered separated when they differ in phase by at least a full cycle over the length of the analyzed time series (e.g., Godin, 1972; Smith, 1999):

$$2\pi \leq p_R |f_1 - f_2| \tag{2.66}$$

where in the context of altimetry f_1 and f_2 represent the aliasing frequencies of the two constituents, and p_R is referred to as the Rayleigh period, which is the minimum time needed to distinguish between the two constituents. As a function of the corresponding aliasing periods p_1 and p_2, the Rayleigh period can also be

written as (e.g., Godin, 1972; Smith, 1999):

$$\frac{1}{p_R} = \left| \frac{1}{p_1} - \frac{1}{p_2} \right| . \tag{2.67}$$

The approximate Rayleigh periods for the main diurnal and semidiurnal constituents, as well as for the annual and semiannual variations (denoted with the respective tidal names Sa and Ssa), are listed in Table 2.7. For TOPEX/Poseidon and Jason-1, -2, and -3, around 9 years of data is required to be able to distinguish K_1 from semiannual variations. The same duration is also required to separate P_1 and K_2. To uncouple the two largest semidiurnal constituents, M_2 and S_2, 3 years of observations are needed. For separating the other listed constituents, a time series length ranging from a few months to one and a half years is sufficient. From today's perspective, with more than 30 years of observations from TOPEX/Poseidon, Jason-1, -2, and -3, all major constituents can be uncoupled. The extraction of tides from ERS-1, -2, and Envisat data is more problematic. According to the Rayleigh criterion, P_1, K_1, and Sa cannot be distinguished from each other, and the same applies for K_2 and Ssa. To separate M_2 and N_2, approximately 8.5 years of measurements are needed, whereas all other constituents can be separated within a maximum of one and a half years.

Note that the Rayleigh periods presented are only valid for a tidal analysis at a specific location. At the cost of spatial resolution, processing altimetry observations grid-wise by incorporating data from neighboring tracks, rather than point-wise, enhances the ability to resolve specific tides when there are significant phase differences between neighboring tracks (see e.g., Cartwright and Ray, 1990; Schrama and Ray, 1994; Smith et al., 2000).

2.3.4 Ocean Tide Models in Orbit Modeling

Amplitudes and Greenwich phase lags for the three constituents M_2, K_1 and Mf from the EOT20 ocean tide model are shown in Figure 2.11. Each one of these constituents is according to the TGP the largest of its respective species. Note that at several coastal locations, the amplitudes surpass the color bar's maximum value. For instance, based on the model, the amplitudes of M_2 can reach nearly 5 meters, K_1 can exceed 2.5 meters, and Mf can reach up to 0.25 meters.

Due to the significant amplitudes of the diurnal and semidiurnal constituents, it is clear that tidal elevation changes at a given location will likely exhibit either a semidiurnal or diurnal pattern, but may also reveal a more complex mixed character. The tidal type is often classified by examining the amplitude ratio $F = (K_1 + O_1)/(M_2 + S_2)$, also known as the form number, calculated from the two largest diurnal and semidiurnal constituents (Courtier, 1938). For a ratio of $F < 0.25$, the semidiurnal type with two high and two low waters per day is predominant. The heights of the high waters and low waters are approximately similar during the same day. A generally diurnal character with one high and one low water is indicated when $F > 3$. When the ratio is $0.25 < F < 3$, the character can be described as mixed. This category can be further divided into the mixed semidiurnal type ($0.25 < F < 1.5$), where usually two high and two low water occur, with inequalities of the heights of the high and low waters and the intervals between them; and the mixed diurnal type ($1.5 < F < 3$), where, over the course of a month, there can be instances with one high and one low water, as well as periods with two high and two low waters. As illustrated in Figure 2.12, the predominant tidal type in most of the oceans can be classified as either mixed semidiurnal or purely semidiurnal. The diurnal or mixed diurnal tidal forms are observed only in certain areas of the oceans, primarily in shallow water regions.

The representation of the ocean tide model in terms of amplitudes and phases is quite intuitive, although not directly applicable for use in orbit modeling and gravity field recovery. However, by expressing tidal variations as changes in the Earth's gravitational potential through spherical harmonics, the potential and acceleration due to ocean tides can be evaluated at any location in Earth's exterior. The derivation of the

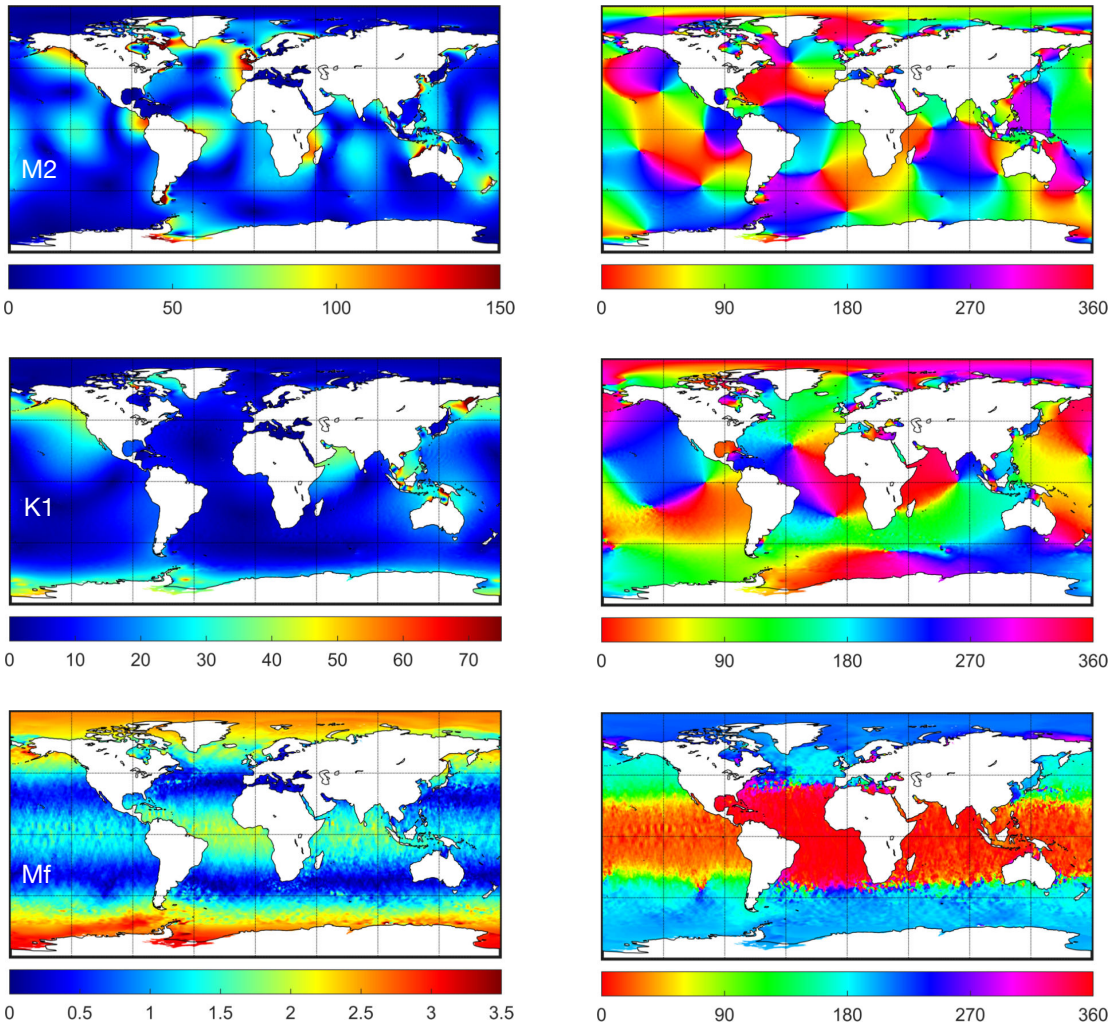

FIGURE 2.11: Amplitudes in cm (left panels) and phase lags in degrees (right panels) of the semidiurnal constituent M_2, diurnal constituent K_1 and long-periodic constituent Mf from the EOT20 ocean tide model.

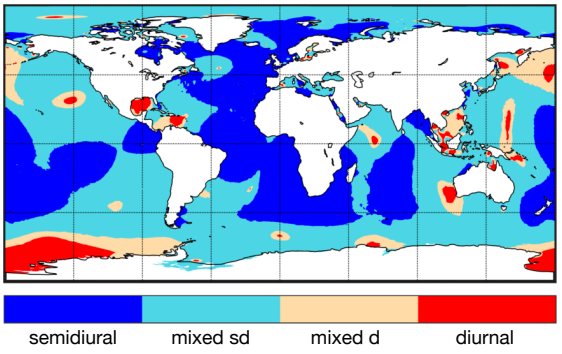

FIGURE 2.12: Four types of ocean tides according to the amplitudes ratio $F = (K_1 + O_1)/(M_2 + S_2)$. Type 1: semidiurnal ($F < 0.25$), type 2: mixed semidiurnal ($0.25 < F < 1.5$), type 3: mixed diurnal ($1.5 < F < 3$), and type 4: diurnal ($F > 3$).

representation in terms of potential can be found, for example, in Lambeck (1977) and Cazenave et al. (1977), and is outlined as next following the equations presented in Rieser et al. (2012).

The tidal height of a constituent i at a position φ, λ and time t can be defined as:

$$\zeta_i(\varphi, \lambda, t) = \xi_i(\varphi, \lambda) \cos\left[\theta_i(t) + \chi_i - \psi_i(\varphi, \lambda)\right] \tag{2.68}$$

with amplitude ξ_i, phase ψ_i, astronomical argument θ_i (see Equation 2.60), and the constituent-specific Doodson-Warburg phase bias χ_i (see IERS Conventions, 2010, Table 6.6; Sulzbach, 2023, Equation 2.7); and can also be expressed as:

$$\zeta_i = \xi_i \cos\psi_i \cos(\theta_i + \chi_i) + \xi_i \sin\psi_i \sin(\theta_i + \chi_i)\ . \tag{2.69}$$

The in-phase component $\xi_i \cos\psi_i$ and quadrature component $\xi_i \sin\psi_i$ can be expanded as:

$$\begin{aligned} \xi_i \cos\psi_i &= \sum_{n=0}^{\infty} \sum_{m=0}^{n} (a_{nm,i} \cos m\lambda + b_{nm,i} \sin m\lambda) P_{nm}(\sin\varphi) \\ \xi_i \sin\psi_i &= \sum_{n=0}^{\infty} \sum_{m=0}^{n} (c_{nm,i} \cos m\lambda + d_{nm,i} \sin m\lambda) P_{nm}(\sin\varphi) \end{aligned} \tag{2.70}$$

with spherical harmonic coefficients $a_{nm,i}$, $b_{nm,i}$, $c_{nm,i}$, $d_{nm,i}$ of degree n and order m, and the Legendre functions P_{nm} (see Equation 2.34). The tidal height of a constituent can now be synthesized using coefficients $C^{\pm}_{nm,i}$, $S^{\pm}_{nm,i}$:

$$\zeta_i = \sum_n \sum_m \sum_{+}^{-} \left[C^{\pm}_{nm,i} \cos(\theta_i + \chi_i \pm m\lambda) + S^{\pm}_{nm,i} \sin(\theta_i + \chi_i \pm m\lambda)\right] P_{nm}(\sin\varphi), \tag{2.71}$$

or amplitudes $\hat{C}^{\pm}_{nm,i}$ and phases $\epsilon^{\pm}_{nm,i}$:

$$\zeta_i = \sum_n \sum_m \sum_{+}^{-} \hat{C}^{\pm}_{nm,i} \sin\left(\theta_i + \chi_i \pm m\lambda + \epsilon^{\pm}_{nm,i}\right) P_{nm}(\sin\varphi) \tag{2.72}$$

with the relationships

$$\begin{aligned} C^{\pm}_{nm,i} &= \hat{C}^{\pm}_{nm,i} \sin\epsilon^{\pm}_{nm,i} = \frac{1}{2}\left(a_{nm,i} \mp d_{nm,i}\right) \\ S^{\pm}_{nm,i} &= \hat{C}^{\pm}_{nm,i} \cos\epsilon^{\pm}_{nm,i} = \frac{1}{2}\left(c_{nm,i} \pm b_{nm,i}\right)\ . \end{aligned} \tag{2.73}$$

Given Earth's radius R, its mass M, the density of seawater ρ_w, and degree-dependent load deformation coefficients k'_n to account for Earth's elastic deformation, one can form the dimensionless coefficients

$$\begin{aligned} \Delta C_{nm,i} &= \frac{4\pi R^2 \rho_w}{M} \left(\frac{1 + k'_n}{2n+1}\right) \left[(C^{+}_{nm,i} + C^{-}_{nm,i}) \cos(\theta_i + \chi_i) + (S^{+}_{nm,i} + S^{-}_{nm,i}) \sin(\theta_i + \chi_i)\right] \\ \Delta S_{nm,i} &= \frac{4\pi R^2 \rho_w}{M} \left(\frac{1 + k'_n}{2n+1}\right) \left[(S^{+}_{nm,i} - S^{-}_{nm,i}) \cos(\theta_i + \chi_i) - (C^{+}_{nm,i} - C^{-}_{nm,i}) \sin(\theta_i + \chi_i)\right]\ . \end{aligned} \tag{2.74}$$

Analogous to Equation 2.21, these coefficients can be utilized to assess the contribution of the tidal water layer in terms of potential at any location outside the Earth:

$$\Delta V_i = \frac{GM}{r} \sum_{n=0}^{\infty} \left(\frac{R}{r}\right)^n \sum_{m=0}^{n} \left(\Delta C_{nm,i} \cos m\lambda + \Delta S_{nm,i} \sin m\lambda\right) P_{nm}(\sin\varphi) \tag{2.75}$$

where GM is the gravitational constant of the Earth and r is the radial distance from the geocenter to the evaluation point.

The Institute of Geodesy at the Graz University of Technology (TUG) offers coefficients $C^{cos}_{nm,i}$, $C^{sin}_{nm,i}$, $S^{cos}_{nm,i}$, $S^{sin}_{nm,i}$ for various ocean tide models (Mayer-Gürr et al., 2023).[11] These coefficients can be used to calculate the normalized form of the coefficients presented in Equation 2.74 as follows:

$$\begin{aligned} \Delta\overline{C}_{nm,i} &= C^{cos}_{nm,i}\cos\theta_i + C^{sin}_{nm,i}\sin\theta_i \\ \Delta\overline{S}_{nm,i} &= S^{cos}_{f,nm}\cos\theta_i + S^{sin}_{nm,i}\sin\theta_i \,. \end{aligned} \tag{2.76}$$

An ocean tide model will only contain the amplitudes and phases for a small number of frequencies i, which are mostly gravitationally excited tides of degree 2. From these, the spectrum can be augmented with minor gravitationally excited tides of degree 2 by employing linear admittance. The concept of linear admittance assumes that the ocean's tidal response is nearly linear with respect to the lunisolar forcing amplitude and varies smoothly with the excitation frequency, allowing the response to degree-2 tides with nearby frequencies to be approximated linearly (e.g., Munk and Cartwright, 1966; IERS Conventions, 2010; Rieser et al., 2012).

To account for smaller gravitationally induced frequencies, Mayer-Gürr et al. (2023) provide linear admittance matrices, which allow the total ocean tide effect—comprising the frequencies contained in the ocean tide model and the additional inferred smaller tides—to be expressed in terms of normalized spherical harmonic coefficients, as follows:

$$\begin{pmatrix} \Delta\overline{C}_{nm} \\ \Delta\overline{S}_{nm} \end{pmatrix} = \sum_i f_i^{cos} \begin{pmatrix} C^{cos}_{nm,i} \\ S^{cos}_{nm,i} \end{pmatrix} + f_i^{sin} \begin{pmatrix} C^{sin}_{nm,i} \\ S^{sin}_{nm,i} \end{pmatrix} \tag{2.77}$$

where the factors f_i^{cos} and f_i^{sin} are defined as:

$$\begin{aligned} f_i^{cos} &= A_{i,f}\cos\theta_f \\ f_i^{sin} &= A_{i,f}\sin\theta_f \end{aligned} \qquad \text{with} \qquad \theta_f = \sum_{n=1}^{6} D_{f,n}\,\beta_n \,. \tag{2.78}$$

The elements $A_{i,f}$ are entries of the linear admittance matrix, where the row index i refers to a constituent of the ocean tide model and the column index f represents a frequency from the spectrum that includes both the ocean tide model constituents and the additional frequencies to be inferred. $D_{f,n}$ are the integer coefficients corresponding to the six astronomical arguments β_n (see Equation 2.58) for each frequency f. The entries of the linear admittance matrix are chosen in such a way that, mathematically, a linear interpolation of the waves to be inferred is performed. In the most straightforward scenario this is an interpolation between two constituents of the ocean tide model (see also IERS Conventions, 2010; Sulzbach et al., 2022):

$$\begin{aligned} C^{cos/sin}_{nm,f} &= \frac{\dot\theta_f - \dot\theta_1}{\dot\theta_2 - \dot\theta_1}\frac{\overline{A}_f}{\overline{A}_2} C^{cos/sin}_{nm,2} + \frac{\dot\theta_2 - \dot\theta_f}{\dot\theta_2 - \dot\theta_1}\frac{\overline{A}_f}{\overline{A}_1} C^{cos/sin}_{nm,1} \\ S^{cos/sin}_{nm,f} &= \frac{\dot\theta_f - \dot\theta_1}{\dot\theta_2 - \dot\theta_1}\frac{\overline{A}_f}{\overline{A}_2} S^{cos/sin}_{nm,2} + \frac{\dot\theta_2 - \dot\theta_f}{\dot\theta_2 - \dot\theta_1}\frac{\overline{A}_f}{\overline{A}_1} S^{cos/sin}_{nm,1} \end{aligned} \tag{2.79}$$

where the subscript f refers to the wave that should be inferred, subscripts 1 and 2 refer to the neighboring ocean tide model waves, where 1 has a smaller frequency than wave 2; $\dot\theta$ is the angular frequency of the corresponding wave, and $\overline{A}$ is the amplitude of the TGP. Alternatively, the tide-raising potential can be used in place of the TGP for $\overline{A}$, which additionally considers the back-action of the solid Earth tides on the oceans, and results in minor modifications to components of the admittance matrix (Sulzbach et al., 2022). A linear interpolation scheme can also be derived using more than two primary waves. Furthermore, it should be noted that the linear relationship only applies to gravitationally excited tides of the same degree

[11] `http://ftp.tugraz.at/outgoing/ITSG/oceanAndAtmosphericTides/models/` (last accessed on 2025-03-11)
`https://ifg.tugraz.at/downloads/ocean-tides` (last accessed on 2025-03-11)

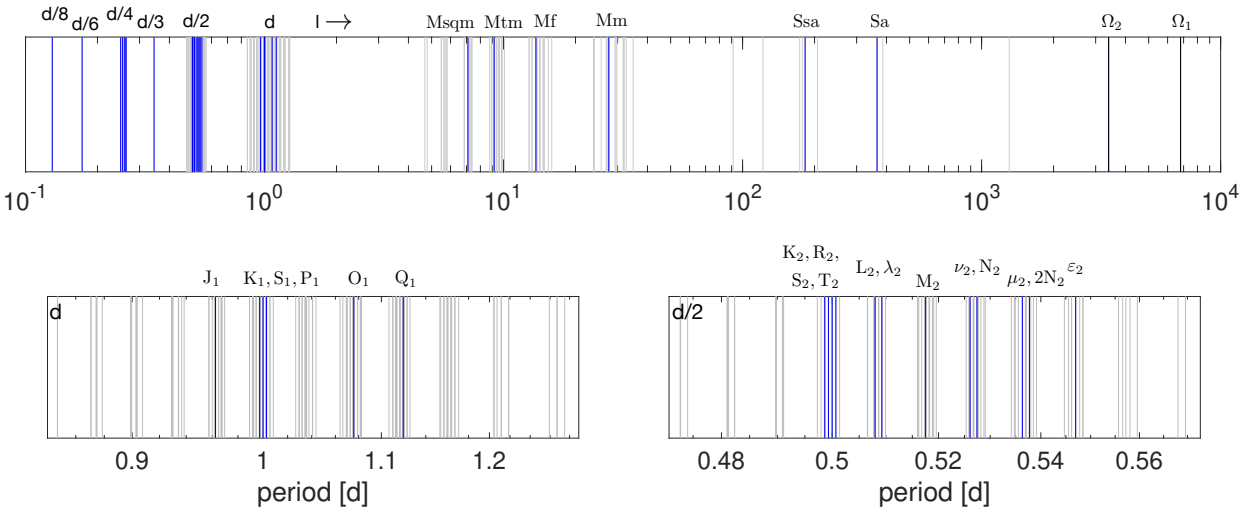

FIGURE 2.13: Considered ocean tide waves in the upper panel with zoom views on the diurnal and semidiurnal bands in the two bottom panels. Blue lines: included in the model FES2014b, gray: from linear admittance, black: equilibrium tide. d: diurnal, d/2: semidiurnal,..., d/8: 8th-diurnal, l: long-periodic.

and order. Main waves of a different type, for example, with a large radiational contribution should not be used in this process.

For the computation of gravity field results in this thesis, the FES2014b ocean tide model (Lyard et al., 2021) in the TUG spherical harmonics representation including the respective linear admittance matrix, was employed. Figure 2.13 illustrates the frequency spectrum of the ocean tide waves considered during orbit modeling. A total of 361 frequencies are accounted for, ranging from the long-periodic band to the 8th-diurnal band. Additional waves derived using admittance are included only for the long-periodic, diurnal, and semidiurnal bands. Owing to the lack of the minimum required two gravitational constituents of the same degree and order needed for an interpolation, applying linear admittance is not feasible in the other bands. In Figure 2.13, gray lines can also be recognized in the periphery of the individual bands. For these frequencies, the admittance is extrapolated rather than interpolated between two ocean tide model constituents. The two black lines at the periods corresponding to the constituents with the longest period, Ω_1 (period of 18.6 years) and Ω_2 (9.3 years), indicate that these tides were modeled using the equilibrium assumption. While in Section 2.3.2 it was discussed that the total ocean's response to the TGP does not take the form of an equilibrium tide, this is generally not the case for constituents within the long-periodic band with a period longer than that of Mm (approximately one month) (e.g., Proudman, 1960; Carton, 1983). Significant discrepancies between satellite altimetry observations and the equilibrium form are known for the fortnightly tide Mf, yet these deviations can be accurately predicted using purely hydrodynamic modeling (Egbert and Ray, 2003). Note that Mf is the largest of the long-periodic tides with maximum amplitudes of a few cm (see Figure 2.11). Due to their relatively small amplitudes and the resulting unfavorable signal-to-noise ratio, observing the other long-periodic tides with satellite altimetry is more challenging. However, some ocean tide models also include altimetry-constrained solutions for Mm and Msf tides (see later in Table 2.8). In the case of the FES2014b ocean tide model, there are 6 long-periodic purely hydrodynamic solutions available (see Figure 2.13). The solutions for Ω_1 and Ω_2 are not part of the FES2014b ocean tide model, but they are included in the spherical harmonics representation of the model from TUG. These are modeled as *self-consistent* equilibrium tides, incorporating the Earth's elastic response as well as the effect of self-attraction (see e.g. also, Agnew and Farrell, 1978; Ray and Erofeeva, 2014; Sulzbach, 2023).

An overview of various ocean tide models, specifying the assimilated data and the constituents included in each model, is provided in Table 2.8. This table features those models currently used by the GRACE(-FO) analysis centers, some of the more recent models that may be important for upcoming time series

TABLE 2.8: Ocean tide models currently used by the GRACE(-FO) analysis centers, some of the more recent models, and models that are particularly relevant to this thesis.

Model	Data and Constituents
(primarily) Data-assimilated	
FES2004 **[1]**	TOPEX/Poseidon, ERS-1, -2, tide gauges
(1/8)°	K_1, O_1, P_1, Q_1, M_2, N_2, S_2, K_2, $2N_2$
	(Mf, Mm, Msqm, Mtm, M_4) no assimilation
FES2014b **[2]**[1]	TOPEX/Poseidon, Jason-1, -2, ERS-1, -2, Envisat, tide gauges
(1/16)°	K_1, O_1, P_1, Q_1, M_2, N_2, S_2, K_2, $2N_2$, ε_2, L_2, λ_2, μ_2, ν_2, M_4
	(Msf, Mf, Mm, Msqm, Mtm, Sa, Ssa, S_1, J_1, T_2, R_2, M_3, M_6, M_8, MKS_2, MN_4,... MS_4, N_4, S_4) no assimilation
FES2022b **[3]**[1]	TOPEX/Poseidon, Jason-1, -2, -3, ERS-1, -2, Envisat, SARAL
(1/30)°	same as FES2014 but with data-constrained J_1
TPXO10 **[4]**[2]	TOPEX/Poseidon, Jason, CryoSat-2
(1/6)°	Mf, Mm, Msf, K_1, O_1, P_1, Q_1, S_1, $2Q_1$, J_1, OO_1, M_1, M_2, S_2, N_2, K_2, $2N_2$, L_2,... μ_2, ν_2, T_2, M_4, MS_4, MN_4, $^3M_3$
Empirical	
EOT11a **[5]**[3]	TOPEX/Poseidon, Jason-1, -2, ERS-2, Envisat
(1/8)°	Mf, Mm, K_1, O_1, Q_1, P_1, S_1, M_2, S_2, N_2, K_2, $2N_2$, M_4
EOT20 **[6]**[3]	TOPEX/Poseidon, Jason-1, -2, -3, ERS-1, -2, Envisat
(1/8)°	same as EOT11, additionally J_1, T_2, and Sa, Ssa containing the full signal
GOT4.8 **[7]**[4]	TOPEX/Poseidon, ERS-1, -2, Geosat Follow-On (GFO), ICESat
(1/2)°	K_1, O_1, P_1, Q_1, S_1, K_2, M_2, N_2, S_2, M_4
GOT5.6 **[8]**[4]	TOPEX/Poseidon, Jason, GFO, Envisat, SARAL, Sentinel-3A, -3B, CryoSat-2
(1/8)°	J_1, K_1, O_1, OO_1, P_1, Q_1, S_1, σ_1, $2N_2$, K_2, M_2, μ_2, N_2, S_2, M_4, MS_4 $^3M_1$, $^3L_2$, $^3N_2$, $^3M_3$ (for latitudes between ±66°)
DTU23 **[9]**	details not documented
(1/16)°	K_1, O_1, P_1, Q_1, S_1, K_2, M_2, N_2, S_2, M_4
Hydrodynamic	
TiME22 **[10]**	not data-constrained
(1/12)°	57 major and minor linear partial tides $^3M_1$, $^3L_2$, $^3N_2$, $^3M_3$ and other smaller degree-3 tides R_3, S_3, T_3 and other radiational tides

[1] Lyard et al. (2006), **[2]** Lyard et al. (2021), **[3]** Aviso+ Altimetry (2024), **[4]** Egbert and Erofeeva (2002, updated), **[5]** Savcenko and Bosch (2012), **[6]** Hart-Davis et al. (2021), **[7]** Schrama and Ray (1994, updated), Ray (1999, updated), **[8]** Ray (2025), **[9]** Andersen (2023), **[10]** Sulzbach et al. (2022)

[1] `https://www.aviso.altimetry.fr/en/data/products/auxiliary-products/global-tide-fes.html`

[2] `https://www.tpxo.net/global/tpxo10`

[3] `https://www.dgfi.tum.de/en/science-data-products/eot/`

[4] `https://earth.gsfc.nasa.gov/geo/data/ocean-tide-models`

All above links last accessed on 2025-03-03.

reprocessing, and models that are particularly relevant to this thesis. Many of these models are available in the spherical harmonic representation of TUG.[12] For a detailed description and intercomparison of ocean tide models starting from the 1980s to the more recent developments of the 2010s, refer to the publications by Andersen et al. (1995), Shum et al. (1997) and Stammer et al. (2014).

The Finite Element Solution FES2014b developed by the Laboratoire d'Etudes en Géophysique et Océanographie Spatiales (LEGOS), NOVELTIS and Collecte Localisation Satellites (CLS) is at the moment the most widely used model among the analysis centers and, for example, has been adopted by GFZ, TUG, AIUB, CNES/GRGS, ARM-SYSU, and LUH.[13] DGFI's Empirical Ocean Tide model EOT11a is, for example, utilized in the current releases of HUST, SWJTU, Tongji, WHU; and was widely used by several analysis centers for their preceding releases. CSR utilizes NASA's Goddard Ocean Tide model GOT4.8 for the diurnal and subdiurnal constituents, supplementing it with empirical estimates of the long-periodic tides Mm and Mf from TOPEX/Poseidon (Egbert and Ray, 2003) and hydrodynamic solutions of Mtm and Msm from FES2004b. In contrast, JPL employs the convolution formalism of Desai and Yuan (2006) for their ocean tide modeling, incorporating convolution weights from FES2014 and the empirical estimates of Mm and Mf from Egbert and Ray (2003).

2.4 Spectral Analysis

Spectral analysis is an integral part of time series analysis, which allows to examine—sometimes obvious, sometimes not apparent—frequency domain characteristics of a time series, by transforming the time domain signal to a spectrum of frequencies and corresponding amplitudes or related quantities such as power, density and energy. A common objective of a frequency domain characterization is the detection of relevant periodicities in the input data. Different methods exist to switch from time to frequency domain. The most well-known and widely-used method for the spectral analysis of an equally spaced time series is the Fourier transform (see Section 2.4.1). For the spectral analysis of a non-equidistant time series, least squares spectral analysis methods, e.g., the Lomb–Scargle periodogram can be used (see Section 2.4.2).

2.4.1 Fourier Transform

The complex Discrete Fourier Transform (DFT) output X_m of a complex time series x_n consisting of N equally spaced samples is defined as (e.g., Lyons, 2004; Vetterli et al., 2014):

$$X_m = \sum_{n=0}^{N-1} x_n \, e^{-\frac{i2\pi nm}{N}} \tag{2.80}$$

or equivalently with the relationship $e^{iy} = \cos y + i \sin y$ (Euler's formula):

$$X_m = \sum_{n=0}^{N-1} x_n \left[\cos\left(\frac{2\pi nm}{N}\right) - i \sin\left(\frac{2\pi nm}{N}\right)\right] \tag{2.81}$$

where $i^2 = -1$, $n = 0, 1, 2, ..., N-1$ is the index of the time series, and m is the corresponding index of the discrete Fourier transform output X_m which also goes from 0 to $N-1$.

[12] `http://ftp.tugraz.at/outgoing/ITSG/oceanAndAtmosphericTides/models/` (last accessed on 2025-03-11)

[13] Abbreviations of the analysis centers in this paragraph: GFZ: German Research Center for Geosciences; TUG: Graz University of Technology; AIUB: Astronomical Institute of the University of Bern; CNES/GRGS: Centre National d'Études Spatiales, Groupe de Recherche de Géodésie Spatiale; ARM-SYSU: Innovation Academy for Precision Measurement Science and Technology of the Chinese Academy of Science, Sun Yat-Sen University; LUH: Leibniz University Hannover; HUST: Huazhong University of Science and Technology; SWJTU: Southwest Jiaotong University; Tongji: Tongji University; WHU: Wuhan University; CSR: Center for Space Research; JPL: Jet Propulsion Laboratory.

The number of samples N and the frequency at which the original time series was sampled, i.e., the sampling frequency f_s, define the DFT analysis frequencies f_m:

$$f_m = \frac{m f_s}{N} \,. \tag{2.82}$$

The magnitude $|X_m|$ of the complex DFT output is defined with its real and imaginary parts as:

$$|X_m| = \sqrt{X_{m,real}^2 + X_{m,imag}^2} \tag{2.83}$$

and is related to the amplitude A_m of a complex input sinusoid as follows:

$$A_m = \frac{1}{N} \, |X_m| \,. \tag{2.84}$$

The classical (Schuster) periodogram, i.e., an estimate of the Power Spectrum (PS), can be computed from the DFT output as:

$$PS_m = \frac{1}{N^2} \, |X_m|^2 \,. \tag{2.85}$$

The periodogram can also be expressed in terms of Power Spectral Density (PSD) by dividing the PS with the equivalent noise bandwidth, i.e., f_s/N:

$$PSD_m = \frac{1}{f_s N} \, |X_m|^2 \tag{2.86}$$

or as Amplitude Spectral Density (ASD) by taking the square root of the PSD:

$$ASD_m = \sqrt{PSD_m} \,. \tag{2.87}$$

For the usual case of a real input time series x_n, only the information stored in the complex DFT output for $m = 0, ..., (N/2)$ is independent. Information for indices $m > (N/2)$ is redundant in the sense that the magnitudes for m and $N - m$ are the same, while their phases only differ in the sign. For a so-called single-sided spectrum the redundant second half can be disregarded. To obtain a correctly scaled amplitude, PS and PSD, Equations 2.84, 2.85 and 2.86 have to be multiplied with the factor 2. The aforementioned does not apply to $m = 0$ and $m = N/2$ (even length time series).

The time series x_n can be reconstructed from its frequency domain representation X_m using the inverse DFT:

$$x_n = \frac{1}{N} \sum_{m=0}^{N-1} X_m \, \left[\cos\left(\frac{2\pi n m}{N}\right) + i \sin\left(\frac{2\pi n m}{N}\right) \right] \,. \tag{2.88}$$

In practice, to compute a DFT sequence or its inverse efficiently, Fast Fourier Transform (FFT) algorithms are employed (e.g., Cooley and Tukey, 1965; Bluestein, 1970; Winograd, 1978). By reducing the number of necessary arithmetic operations, FFT algorithms can solve the original $\mathcal{O}(N^2)$ task in a computation time of about $\mathcal{O}(N \log N)$.

The here presented Fourier techniques are only valid for uniformly sampled time series; therefore, non-equidistant time series have to be manipulated prior to use, e.g., by applying techniques such as interpolation, downsampling, zero padding. Nevertheless, depending on the characteristics of the time series, the Fourier techniques may also be employed to non-equidistant time series, to obtain results comparable to those attained via the application of dedicated methods (see e.g., VanderPlas, 2018).

2.4.2 Lomb–Scargle Periodogram

One of the most common methods for the spectral analysis of not uniformly spaced time series is the Lomb–Scargle periodogram (Lomb, 1976; Scargle, 1982)—a technique partly based on the least squares fitting approach by Barning (1963); Vaníček (1969). The unnormalized Lomb–Scargle periodogram of an equidistant or non-equidistant time series with N mean-centered observations x_n at times t_n can be defined as:

$$P(f) = \frac{\left[\sum\limits_n x_n \cos\left(2\pi f(t_n - \tau)\right)\right]^2}{\sum\limits_n \cos^2\left(2\pi f(t_n - \tau)\right)} + \frac{\left[\sum\limits_n x_n \sin\left(2\pi f(t_n - \tau)\right)\right]^2}{\sum\limits_n \sin^2\left(2\pi f(t_n - \tau)\right)} \tag{2.89}$$

with frequency f and frequency-dependent time offset τ:

$$\tau = \frac{1}{4\pi f} \tan^{-1}\left(\frac{\sum\limits_n \sin(4\pi f t_n)}{\sum\limits_n \cos(4\pi f t_n)}\right). \tag{2.90}$$

For a so-called normalized periodogram, $P(f)$ has to be divided by two times the variance of the time series. To obtain $P(f)$, the algorithm by Press and Rybicki (1989) can be employed, which reduces the computationally intensive task from an original $\mathcal{O}(N^2)$ complexity to $\mathcal{O}(N \log N)$.

Chapter 3

Gravity Field Recovery

The orbit data of the GRACE(-FO) satellites as an approximation of their true motion in space contain information about Earth's gravitation since it exerts the main force affecting the motion of the satellites. The task of gravity field recovery is to calculate the gravitational field parameters $\overline{C}_{nm}$ and $\overline{S}_{nm}$ (see Equation 2.21). These parameters can be obtained from a method known as *dynamic orbit determination*, which utilizes orbit modeling, numerical integration, and parameter estimation to solve the satellites' equations of motion (e.g., Seeber, 2003; Montenbruck and Gill, 2005):

$$\ddot{\mathbf{r}} = -\frac{GM}{r^3}\mathbf{r} + \underbrace{\mathbf{R}_e^i \, \nabla V \; + \; \ddot{\mathbf{r}}_{ng} \; + \; \ddot{\mathbf{r}}_t \; + \; \ddot{\mathbf{r}}_{nt} \; + \; \ddot{\mathbf{r}}_{rel}}_{\ddot{\mathbf{r}}_p} \tag{3.1}$$

where $\ddot{\mathbf{r}}$ and $\mathbf{r}$ are the acceleration and position vectors of the satellite in an inertial system, $r = |\mathbf{r}|$, and GM is the standard gravitational parameter of the Earth. The first term represents the central body acceleration described by the constant $\overline{C}_{00} = 1$ coefficient of the gravitational potential V. The remaining terms of Equation 3.1, denoted as $\ddot{\mathbf{r}}_p$, form the sum of additional accelerations affecting the satellite motion. Herein, ∇V is the acceleration due to the gravitational potential of the Earth excluding $\overline{C}_{00}$ (see Section 2.2.2), which is transformed to an inertial coordinate system by applying the rotation matrix $\mathbf{R}_e^i$ (see Section 2.1). Furthermore, $\ddot{\mathbf{r}}_p$ comprises the non-gravitational acceleration $\ddot{\mathbf{r}}_{ng}$, which, in the case of GRACE(-FO), is derived from onboard accelerometers, gravitational tidal and non-tidal accelerations $\ddot{\mathbf{r}}_t$ and $\ddot{\mathbf{r}}_{nt}$, respectively, as well as a correction for general relativity $\ddot{\mathbf{r}}_{rel}$.

Equation 3.1 is a vector form of an Ordinary Differential Equation (ODE) of second order, which can be reformulated as two first order ODEs (e.g., Seeber, 2003; Montenbruck and Gill, 2005):

$$\begin{aligned} \dot{\mathbf{r}} &= \mathbf{v} \\ \dot{\mathbf{v}} &= -\frac{GM}{r^3}\mathbf{r} + \ddot{\mathbf{r}}_p \, . \end{aligned} \tag{3.2}$$

The numerical integration of these ODEs results in the satellite state vector $\mathbf{y}$ containing the position and velocity vectors. The six elements of an approximately known initial state vector $\mathbf{y}_0 = \mathbf{y}(t_0)$ at time t_0 can be introduced as integration constants. A dynamically modeled (or propagated) orbit at epochs $t_0,\ t_1,\ t_2$,... consisting of consecutive states $\mathbf{y}_0,\ \mathbf{y}(t_1),\ \mathbf{y}(t_2)$,... is obtained through the step-wise numerical integration of the two aforementioned ODEs, as shown schematically below:

$$\mathbf{y}(t) = \underbrace{\underbrace{\mathbf{y}_0 \; + \int_{t_0}^{t_1} \dot{\mathbf{y}}(t)\mathrm{d}t}_{\mathbf{y}(t_1)} \; + \int_{t_1}^{t_2} \dot{\mathbf{y}}(t)\mathrm{d}t \; + \cdots}_{\mathbf{y}(t_2)} \tag{3.3}$$

Even when the integration constants are known highly accurately, the numerically propagated orbit will diverge from a true orbit in the course of time, primarily due to the insufficiently known forces acting on the satellite, including the contribution of the time-variable part of Earth's gravitation. The concept of dynamic orbit determination involves adjusting the dynamically modeled orbit to observations. Fundamentally, in the most basic case, this involves determining optimal values for the initial state, resulting in a propagated orbit that aligns with the observations as accurately as possible, usually in terms of least squares adjustment.

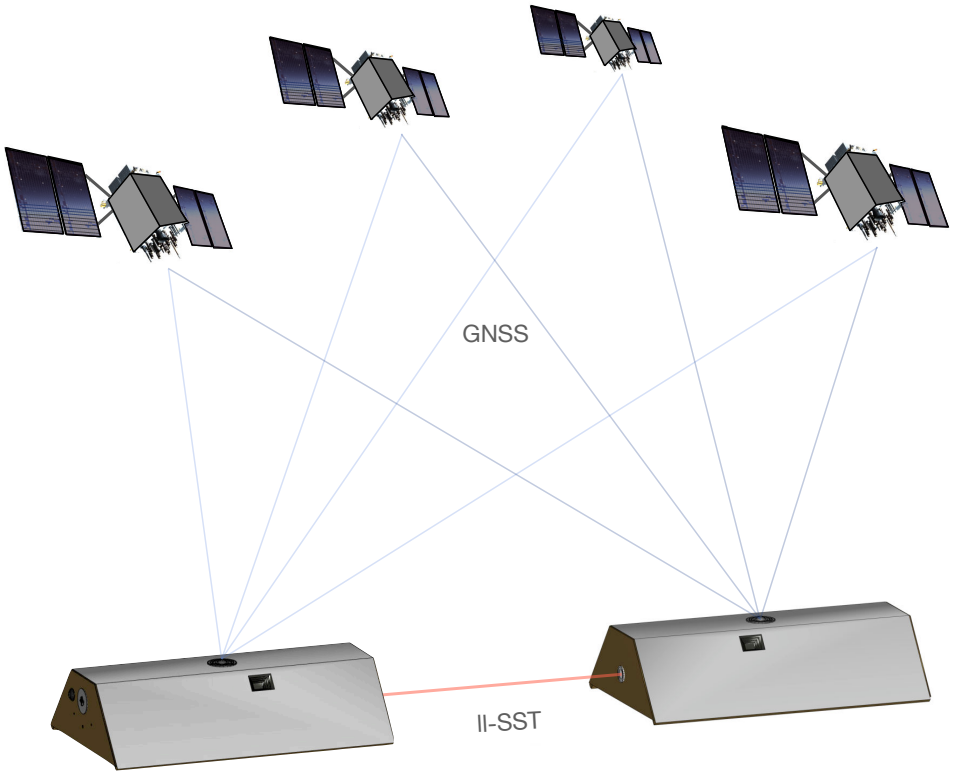

FIGURE 3.1: Tracking of the GRACE(-FO) satellites by ll-SST and GNSS. The primary observable is the distance between the two satellites from ll-SST (K-band/laser ranging). The absolute positions of the satellites (altitude of approx. 400 km) are determined from GNSS constellations (approx. 20000 km).[1]

In the case of gravity field recovery the spherical harmonic coefficients of the gravitational potential $\overline{C}_{nm}$ and $\overline{S}_{nm}$ are introduced as parameters to be estimated along with the orbit. In principle, any parameter affecting the satellite motion, or for which a viable functional relationship between orbit observations and the equation of motion can be established, can also be co-estimated. Therefore, dynamic orbit determination provides a crucial framework for various applications in satellite geodesy. Besides orbits and the gravitational potential, it enables the estimation of various variables, including, for example, Earth orientation parameters, ocean and body tide parameters, station coordinates, geocenter motion, and the geocentric gravitational constant (see e.g., Seeber, 2003; Pearlman et al., 2019). For satellites equipped with accelerometers, a co-estimation of calibration parameters is necessary, as the accelerometer measurements are not absolute. Various types of empirical parameters, which are not directly related to specific parts of the satellite's equation of motion, are often introduced as additional unknowns in the dynamic orbit determination process, which helps to compensate for model deficiencies and achieve a better fit to observational data. Examples of these additional parameters are empirical low-frequency accelerations (e.g., Colombo, 1986; Montenbruck and Gill, 2005, Equation 3.149), as well as instantaneous velocity changes (pulses), piece-wise linear and constant accelerations (e.g., Jäggi et al., 2006). Incorporating these additional parameters transitions the orbit from being purely dynamic to *reduced-dynamic*. Similarly, geometric empirical parameters can be introduced at the observation level to address modeling deficiencies (see e.g., Kim, 2000, Equation 3.16).

The GRACE(-FO) orbits are observed by two techniques, as shown in Figure 3.1. The satellites, orbiting at a low altitude of roughly 400 km and equipped with GNSS receivers, enable precise tracking of their absolute positions by the GNSS constellations (e.g., Hofmann-Wellenhof et al., 2007; Teunissen and Montenbruck, 2017). Analogous to the term "ll-SST", the tracking of the lower-altitude spacecraft by the

[1]GRACE model from: `https://nasa3d.arc.nasa.gov/detail/grace` (last accessed on 2025-04-14).

GNSS satellites can also be referred to as *high-low satellite-to-satellite tracking*. The cm-accurate positions of the satellites are determined by means of *kinematic orbit determination* using GNSS code and phase measurements (see e.g., Svehla and Rothacher, 2003; Zehentner and Mayer-Gürr, 2016; Svehla, 2017). In contrast to the (reduced-)dynamic orbits, kinematic orbits are purely geometric and are independent of the dynamics of the tracked satellites. Due to the continuous tracking, they can be obtained directly for any epoch of interest without requiring state propagation. Usually, rather than using the original GNSS observations in the gravity field recovery process, kinematic orbits are estimated before gravity field recovery, and are introduced into the estimation as pseudo-observations. Although reduced-dynamic orbits generally have superior quality compared to kinematic orbits, the dynamic information they contain makes them less suitable as pseudo-observations for gravity field recovery, due to the risk of the gravity field solution being biased towards the a priori dynamic information inherent in the pseudo-observations (e.g., Gerlach et al., 2003; Jäggi et al., 2008). Even more sensitive to orbital changes are the ll-SST measurements, making them the primary observables for gravity field determination. The biased range between the two satellites can be measured with micrometer-precision by the K-band ranging system and nanometer-precision by the LRI instrument on GRACE-FO. The determination of the monthly gravity fields by the different analysis centers almost exclusively relies on range-rates. These are obtained by numerically differentiating the biased ranges using a filter (e.g., Thomas, 1999).

The adjustment of the numerically integrated satellite orbit arc to observational data is typically accomplished using least squares adjustment. For the two types of tracking data involved, the linearized observation equations of the originally non-linear problem can be expressed in a simplified form as follows:

$$\begin{aligned} \overline{\dot{\boldsymbol{\rho}}} - \dot{\boldsymbol{\rho}} = &\quad \sum_{k=1}^{n} \frac{\partial \dot{\boldsymbol{\rho}}}{\partial \mathbf{q}_k} \Delta \mathbf{q}_k \\ \mathrm{vec}(\overline{\mathbf{r}}_A - \mathbf{r}_A) = &\quad \sum_{k=1}^{n} \frac{\partial \mathrm{vec}(\mathbf{r}_A)}{\partial \mathbf{q}_k} \Delta \mathbf{q}_k \\ \mathrm{vec}(\overline{\mathbf{r}}_B - \mathbf{r}_B) = &\quad \sum_{k=1}^{n} \frac{\partial \mathrm{vec}(\mathbf{r}_B)}{\partial \mathbf{q}_k} \Delta \mathbf{q}_k \; . \end{aligned} \tag{3.4}$$

On the left side of the equations, one can find the reduced observation vectors. These vectors, commonly known as *observed minus computed*, are formed as the differences between the kinematic (pseudo-observed) positions $\overline{\mathbf{r}}_A$, $\overline{\mathbf{r}}_B$ of the two satellites indicated by the subscripts, or the measured range-rates $\overline{\dot{\boldsymbol{\rho}}}$, and the corresponding quantities $\mathbf{r}_A$, $\mathbf{r}_B$, $\dot{\boldsymbol{\rho}}$ obtained from the numerically integrated dynamic orbits. The vectorization operator vec() converts the position matrix differences to a column vector, i.e., stacks the epoch-wise Cartesian vectors on top of each other. The right side of the equations is composed of the partial derivatives of the dynamically modeled orbits and range-rates with respect to a set of n unknown parameters $\mathbf{q}$. The partial derivatives serve as input elements for the design matrices. These are, in turn, necessary, for setting up the system of normal equations that have to be solved to obtain the parameter corrections $\Delta\mathbf{q}$. Due to the non-linear nature of dynamic orbit determination, the final parameters are derived by iteratively improving the a priori parameters.

Note that the GRACE(-FO) satellites complete one orbital revolution in approximately 94 minutes, resulting in about 15 revolutions per day (see Figure 3.2a). The nearly polar orbit of the satellites, with an inclination of 89°, combined with Earth's rotation, allows for a global ground track coverage in approximately one month (see Figure 3.2b). Therefore, the "classical" outcome of the gravity field recovery from GRACE(-FO) data is a sequence of (unconstrained) monthly gravity field solutions. With the accumulation of observations, the solution quality progressively converges towards that of the final monthly solution. This is illustrated in terms of difference degree standard deviations in Figure 3.2c,d for the accumulation of 3-hour orbital arcs of March 2006. An unconstrained solution with higher temporal resolution can only be obtained at the expense of increased noise.

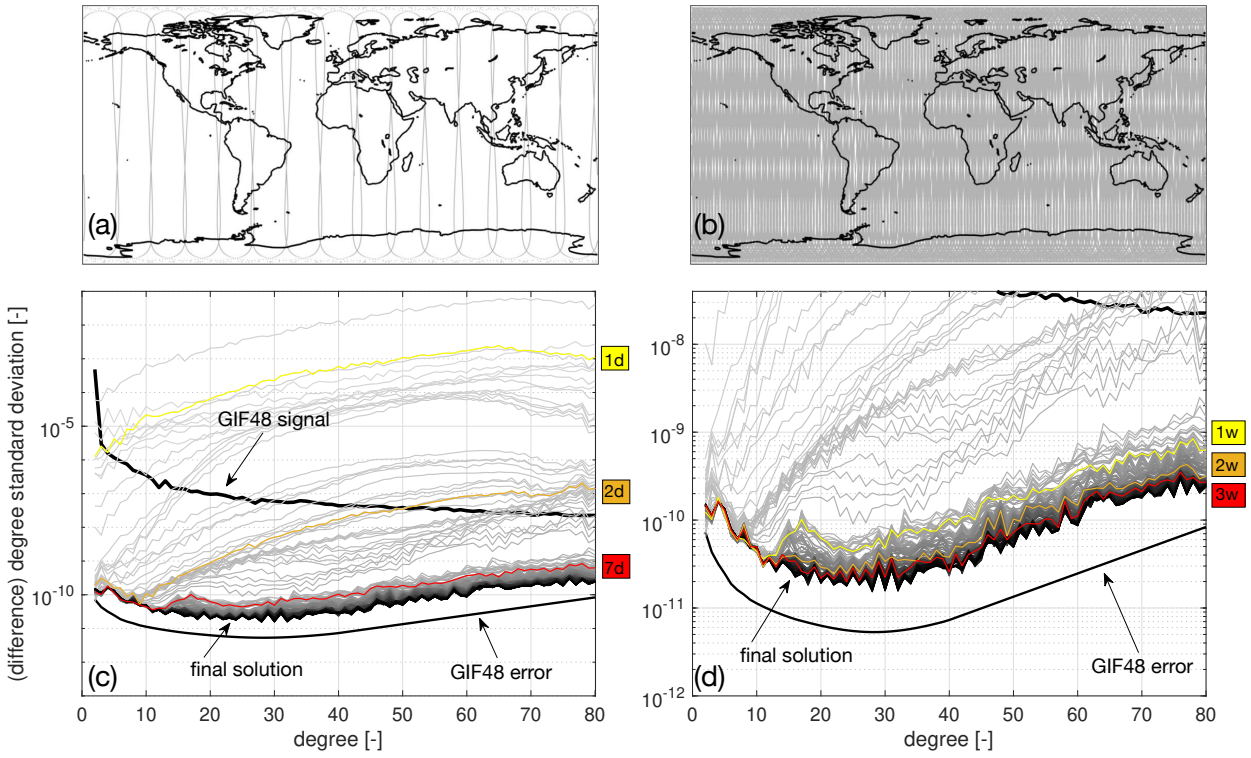

FIGURE 3.2: (a): GRACE(-FO) 1-day ground track. (b): Typical GRACE(-FO) ground track coverage after one month. (c): Successive stacking of 3-hour arcs and corresponding difference degree standard deviations with respect to static field GIF48 for March 2006. (d): Zoom view of (c). Panels (c) and (d) are taken from Koch et al. (2020, Figure 2) and were slightly modified.

While the very general idea of the gravity field recovery using dynamic orbit determination was outlined above, the aim of the following sections is to present the gravity field recovery strategy utilized for the LUH-GRACE-2020 and LUH-GRACE-FO-2020 time series of monthly gravity field solutions. First, Section 3.1 introduces the relevant GRACE(-FO) instruments, along with their corresponding data products. Section 3.2 provides an overview of the general processing details of the LUH gravity field solutions. While Earth's time-variable gravitation and the ocean tides were already introduced in the previous chapter, the computation schemes for further effects of relevance for orbit modeling are presented in Section 3.3. Numerical integration as an essential component of dynamic orbit determination is described in Section 3.4. The parameter estimation framework is topic of Section 3.5. This chapter concludes with a comparison of the obtained monthly gravity field solutions with the products of CSR, GFZ, JPL and TUG in terms of noise and signal content in Section 3.6.

3.1 Instruments and Data Products

For the purpose of precise satellite gravimetry, the satellites carry several scientific instruments: GNSS receivers for measuring the absolute position, K/Ka-band and laser ranging systems for the intersatellite link, electrostatic accelerometers for measuring the influence of non-gravitational forces, and star cameras for determining the orientation of the satellites with respect to inertial space. These gravity field recovery relevant instruments are explained in detail in the next subsections. Related products derived from the measurements of these instruments are listed in Section 3.1.2. Figure 3.3 schematically shows the spacecraft platform positions of the instruments.

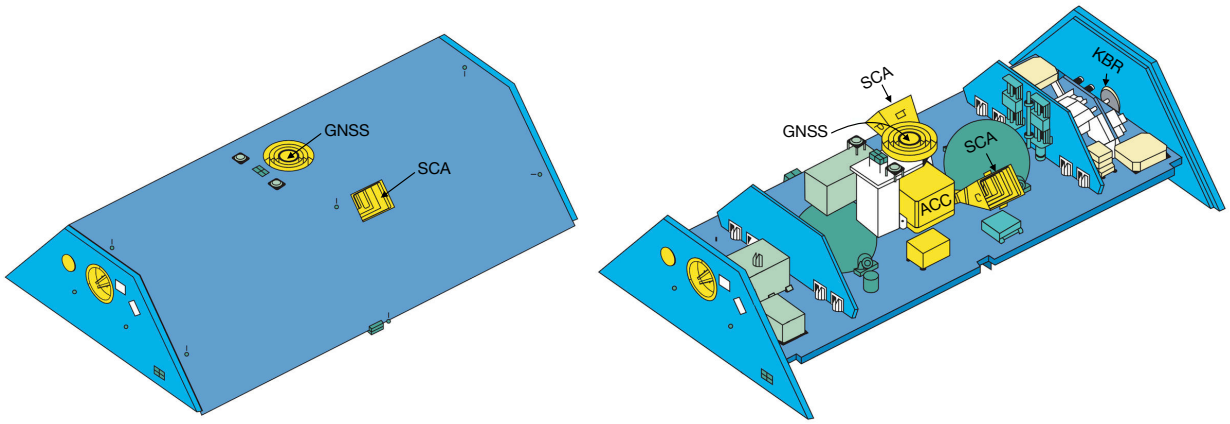

FIGURE 3.3: Placement of main instruments on the GRACE satellite. GNSS: GNSS antenna, SCA: star camera, ACC: accelerometer, KBR: K-band horn. Image credit (NASA, 2002), modified.

3.1.1 Relevant Instruments

GNSS Receiver

The GRACE(-FO) satellites were equipped with geodetic quality space GNSS receivers developed at and provided by JPL/NASA. BlackJack GPS receivers were used onboard GRACE. Since 2000 this receiver was flown on dozens of Earth observation satellites (e.g, Bertiger et al., 2000; Reichert et al., 2002; Haines et al., 2004), among them on the gravimetry mission CHAMP (Montenbruck and Kroes, 2003). The receiver onboard GRACE can track up to 14 GPS satellites (Dunn et al., 2003). In the case of GRACE-FO, the TriG GNSS receiver—an enhanced version of the BlackJack receiver design—is used, which additionally is capable of tracking the European Galileo and Russian GLONASS constellations (Tien et al., 2012). The receivers feature 3 antennas on each spacecraft: a zenith antenna on the top panel that collects positioning data for POD, a back-up positioning antenna on the aft panel, and an antenna specifically for the purpose of atmospheric radio occultation (Wickert et al., 2005, 2009) mounted on the rear panels of the satellites. In addition, the GNSS measurements provide 0.1 nanosecond-precise time tagging of the onboard measurements (Dunn et al., 2003). The bottom panels of the satellites are equipped with laser corner-cube retro-reflectors, allowing an independent quality validation of the GNSS-derived kinematic positions through the use of SLR (e.g., Combrinck, 2010). The radial accuracy of the GNSS-derived positions in terms of SLR residuals is on the level of a few centimeters (e.g, Kang et al., 2003, 2020; Jäggi et al., 2007; Arnold et al., 2019)

K/Ka-Band and Laser Ranging Systems

The ll-SST principle between the two twin satellites separated by a distance of approximately 220 km, is realized by the microwave KBR instrument supplied by JPL/NASA. The precise measuring of the inter-satellite distance is based on the Dual One-Way Ranging (DOWR, e.g., MacArthur and Posner, 1985; Thomas, 1999). The KBR horns mounted on the front panels of the spacecraft transmit and receive signals modulated on the two frequencies ≈24 GHz (K-band) and ≈32 GHz (Ka-band) (e.g, Bertiger et al., 2002). To enable an inter-satellite link, the front panel of the leading satellite is directed towards the trailing spacecraft. A phase shift measurement is obtained by combining the received signal with a reference signal utilizing a phase-locked loop algorithm. The DOWR approach allows minimizing the influence of ionosphere and oscillator frequency instability on the inter-satellite range (e.g, MacArthur and Posner, 1985; Thomas, 1999). While the medium and long period oscillator noise cancels, measurements are still affected by high-frequency noise with a period of less than 1 ms (Kim, 2000). The precision of the KBR instrument is on the micron-level

(e.g, Dunn et al., 2003; Bertiger et al., 2002). For the purpose of technology demonstration for future satellite gravimetry missions and space-based gravitational wave detection missions, in addition to the KBR instrument, a nanometer-precise LRI was placed onboard GRACE-FO (Sheard et al., 2012; Abich et al., 2019).

Electrostatic Accelerometer

To precisely measure the influence caused by non-gravitational effects such as atmospheric drag, direct and indirect solar radiation pressure, but also caused by thruster activations during manoeuvres, each GRACE(-FO) spacecraft was equipped with the Super-STAR electrostatic space accelerometer (Touboul et al., 1999, 2012) developed by Office National d'Etudes et de Recherches Aérospatiales (ONERA, French national aerospace research centre). The Super-STAR accelerometer is a further development of the Space Three-axis Accelerometer for Research (STAR) used onboard CHAMP. Accelerometers are placed in the center of mass of the satellites, therefore experiencing only non-gravitational forces. The response of the satellites to these forces in terms of (biased and not correctly scaled) linear and angular acceleration along the three axes of the satellite body-fixed frame, is derived from the measured electrostatic force that is required to maintain the instrument's proof mass motionless with respect to the sensor cage (Touboul et al., 1999). Since the space accelerometers do not provide absolute accelerations, optimal scale factors and biases are usually estimated during orbit determination and gravity field recovery. The noise level of these instruments is in the order of 10^{-10} m/s$^2/\sqrt{\text{Hz}}$ (Touboul et al., 1999; Flury et al., 2008).

In the final months of the GRACE mission, the accelerometer on GRACE-B was deactivated because of battery issues. A data processing method known as accelerometer data *transplant* was developed, which uses linear accelerations from GRACE-A to reconstruct the missing GRACE-B accelerometer data (Bandikova et al., 2019). Since 21 June 2018, the accelerometer measurements on GRACE-D have been adversely affected by bias jumps and noise that are strongly correlated across all accelerometer axes (Landerer et al., 2020). Similar to the late phase of GRACE, the accelerometer data used by the analysis centers for gravity field recovery rely on a transplantation of accelerometer measurements from GRACE-C to GRACE-D (Landerer et al., 2020; Behzadpour et al., 2021; Harvey et al., 2024).

Star Cameras

In order to relate the instrument measurements to an inertial coordinate system, but also for attitude and orbit control, the orientation of the spacecraft platforms should be known. For this purpose, each GRACE(-FO) spacecraft was equipped with Advanced Stellar Compass (ASC) star cameras (Jørgensen and Liebe, 1996; Jørgensen, 2000) developed and provided by the Technical University of Denmark (DTU). The ASC star cameras were flight-proven on dozens of missions including CHAMP and GOCE. Two star cameras with a field of view of $18° \times 16°$ were mounted on the accelerometer frame, oriented towards the port and starboard sides with a zenith direction offset of 45° (GFZ, 2024). To increase star camera data availability during Sun and Moon blinding—a lessons learned from GRACE (see e.g., Bandikova and Flury, 2014)—the GRACE-FO satellites were additionally equipped with a third star camera pointing towards the upper panel and observing the stars in zenith direction. The ASC star cameras, consisting of Charge-Coupled Device (CCD) image sensors and associated optics, are taking digital images of the stars in their field of view. The starlight reaches the CCD image sensor through the camera baffles. The orientation of a satellite in terms of quaternions is then obtained by relating the CCD coordinates of the stars to a larger catalog of known star positions via image analysis and pattern matching (see e.g., Liebe, 1993; Eisenman et al., 1997). The orientation of the satellites is measured with a precision of about 25 arcseconds (Dunn et al., 2003).

Table 3.1: Data used for gravity field recovery in this study. G: GRACE, GFO: GRACE-FO.

Product	Release		Data Description
SDS **[1]**	*G*	*GFO*	
KBR1B	RL03	RL04	5 s K-band range-rates
			5 s light-time and phase center offset corrections
GNV1B	RL02	RL04	1 s reduced-dynamic positions and velocities
SCA1B	RL03	RL04	1 s normalized quaternions
ACC1B	RL02	–	1 s linear accelerometer measurements
ACT1B[1]	–	RL04	1 s linear accelerometer (transplant) data
ACH1B[1]	–	RL04	1 s linear accelerometer transplant data
Ancillary			
AIUB kin. orbits **[2]**	RL01	RL02	10 s kinematic positions
			10 s cofactor matrices
TUG ACT[1] **[3]**			1 s linear accelerometer transplant data

[1] Case et al. (2010), Wen et al. (2019), **[2]** Arnold and Jäggi (2020b,a), **[3]** Behzadpour et al. (2021).
[1]The ACT products for GRACE-FO contain accelerometer measurements for the nominally working instrument on GRACE-C, and transplant data for GRACE-D. ACH is part of the data bundles ACX and ACX2. For GRACE-D, the following products were used: ACT for 2018-06, TUG ACT for 2018-07 to 2024-01, except for 2022-02, 2022-03, 2023-09 where ACH from ACX was utilized; and since 2024-02 ACH from ACX2.

3.1.2 Data Products

For the computation of the gravity field solutions, GRACE(-FO) Level-1B (L1B) data products are used (Case et al., 2010; Wen et al., 2019). These products are generated by the GRACE(-FO) Science Data System (SDS) and can be obtained from NASA's Physical Oceanography Distributed Active Archive Center (PO.DAAC, 2019) and from GFZ's Information System and Data Center (ISDC, 2023).

The SDS is divided into three consecutive processing levels. The satellite's downlinked telemetry data received at DLR in Neustrelitz/Germany is decommutated to Level-0 data products. These Level-0 data products form the input for the generation of so called non-destructive Level-1A data products, meaning that Level-1A data products are in general reversible to Level-0 data products. Then the Level-1A data products are used to produce L1B data products. In contrast to the previous processing step, L1B data products may not be reversed to Level-1A data products. The processing of Level-1A as well as of L1B data products is realized at JPL and is backed up at GFZ. The L1B data products contain all the necessary satellite sensor measurements and ancillary products needed to generate Level-2 products, i.e., the monthly gravity field solutions.

In addition to the SDS data products, kinematic orbits from AIUB (Arnold and Jäggi, 2020a) were utilized, along with alternative accelerometer transplant products from TUG (Behzadpour et al., 2021) for GRACE-D (July 2018 to January 2024). Table 3.1 lists the products and the specific data extracted from these products that are used for gravity field recovery in this study.

3.2 Overview of the LUH Gravity Field Recovery Approach

This section provides an overview of the gravity field recovery approach employed for the LUH-GRACE-2020 and LUH-GRACE-FO-2020 time series, using the *GRACE-SIGMA* (GRACE-Satellite orbit Integration and Gravity field analysis in MAtlab) software (Naeimi et al., 2018; Koch et al., 2020, 2021) developed at LUH's IfE. For reasons of computational efficiency, the processing is divided into two main steps. After a sensor data pre-processing, an orbit pre-adjustment is performed in which the initial states and accelerometer bias parameters are iteratively estimated without determining the gravity field parameters. The arc-wise parameters estimated from this step are used as a priori values for the local parameters in the second adjustment step. In this main adjustment, the gravity field parameters are estimated simultaneously alongside the orbit

and accelerometer parameters without additional iterations. The steps are outlined in more detail in the following subsections.

3.2.1 Pre-Processing

Daily GNV1B, SCA1B, ACC1B/ACT1B/ACH1B, KBR1B files (see Table 3.1) are imported. The epochs are synchronized to ensure that the sensor data time series begin and end at the same points in time. Apart from the KBR time series, minor gaps in the sensor data consisting of a single missing value are filled using linear interpolation. Larger gaps in the quaternion data of the SCA1B products, which are relatively smooth compared to other products, are interpolated using piece-wise cubic splines. All sensor data time series are downsampled to match the 5-second intervals of the KBR1B products. The light-time and antenna phase center offset corrections given in the KBR1B products are applied to the K-band range-rates of these products. The position and velocity vectors of the GNV1B reduced-dynamic orbits given in ITRS are transformed to GCRS. Disturbing accelerations, excluding those caused by Earth's gravitational field and due to non-gravitational effects, are evaluated along the GNV1B orbit. Later, during the orbit integration, instead of evaluating the accelerations at intermediate positions during every iteration of orbit determination, these pre-computed accelerations are employed.

3.2.2 Pre-Adjustment

The aim of this step is not to achieve the best possible orbit fit, but to estimate suitable initial values for the next phase of the gravity recovery procedure. The daily sensor data files are segmented into 6-hour intervals for GRACE and 3-hour intervals for GRACE-FO. The pre-adjustment process involves two steps, beginning with an initial coarse adjustment conducted separately for each satellite. In this step, dynamically modeled orbits are fitted to the the 5-second inertial GNV1B positions until the correction norm to the initial state's position is less than 100 meters. Here, but also in the subsequent steps, the numerical integration of the orbit, state transition, and sensitivity matrices is carried out using a modified Gauss–Jackson integration technique (Naeimi, 2018, see Section 3.4 for more details). At this stage, only the arc-wise initial states and the accelerometer bias parameters are determined. The accelerometer scale factors are kept at 1, and the off-diagonal elements are set to 0.

Once convergence is achieved, the newly determined initial states and refined accelerometer bias parameters are utilized as a priori values in the fine pre-adjustment phase, where the numerically propagated orbits of both satellites are simultaneously adjusted to fit the K-band range-rate observations and the GNSS-based kinematic positions that serve as pseudo-observations. While the range-rates are utilized at their original 5-second sampling interval, the kinematic orbits are downsampled from 10 seconds to 30 seconds. Given the typically noisy nature of kinematic orbits compared to the smoother reduced-dynamic orbits, a screening process is applied whereby epochs with position differences exceeding 8 cm relative to the reduced-dynamic GNV1B orbits are excluded from the parameter estimation process. To construct the corresponding weight matrices, an initial standard deviation of 0.2 μm/s is applied for the range rates, while a standard deviation of 0.02 m is used for the position components. The technique-specific weights are refined after each iteration of the orbit determination process using VCE (Koch and Kusche, 2002). Also in this step only the arc-wise initial states and the accelerometer bias parameters are estimated. The accelerometer scale matrix elements are not solved for, as the scale is parametrized as constant over the course of a month. The a priori values of the unknowns are iteratively adjusted using the estimated corrections until convergence is achieved, here defined as the point where the mean of the absolute range-rate reduced observation differences between two consecutive iterations is less than 0.1 μm/s.

Table 3.2: Number of estimated parameters for a 30-day month. G: GRACE, GFO: GRACE-FO.

Parameter	Number of Parameters		Number of Parameters per Month	
Local (per arc)	*G* (6 h)	*GFO* (3 h)	*G* (6 h)	*GFO* (3 h)
Initial state	6 per sat	6 per sat	1440	2880
Accelerometer bias	3 per sat	3 per sat	720	1440
Kinematic empiricals	12	6 or 8[1]	1440	1440 or 1920[1]
Global (per 30 d)				
Potential[2]	9405	9405	9405	9405
Accelerometer scale	9 per sat	9 per sat	18	18
Total			13023	15183 or 15663[1]

[1]First value: until the end of 2022, second value: starting from 2023.
[2]The gravitational potential is estimated from degree 2 until degree and order 96.

3.2.3 Main Adjustment

The arc-wise initial states and accelerometer biases derived from the pre-adjustment are employed as new a priori values for dynamic orbit modeling and the computation of the state and parameter sensitivity matrices. Here too, a standard deviation of 0.2 μm/s is used to set up the weight matrices for the K-band range-rate observations. For kinematic positions, the inertial orbit covariance information is utilized to create diagonal weight matrices. In line with the approaches used by other analysis centers (e.g., Meyer et al., 2016; Dahle et al., 2019b), a downweighting is applied to the GNSS-based positions to achieve more accurate gravity field solutions. For this purpose, the elements of the kinematic position weight matrices are divided with empirically determined factors of 500 for GRACE and 25 for GRACE-FO.

In this step, the local parameters, including the initial states and accelerometer biases, are re-estimated. Additionally, the set of local parameters is expanded to include kinematic empirical range-rate parameters (Kim, 2000), which help mitigate the effects of potential mis-modeling of disturbing forces.[2] For GRACE and GRACE-FO missions up until the end of 2022, 90-minute biases and bias-rates, along with 180-minute periodic biases and bias-rates, are co-estimated. Starting from the first 2023 solution, the length of the periodic terms has also been set to 90 minutes. A few months deviate from this parametrization of the kinematic empirical range-rate parameters. The spherical harmonic coefficients representing the monthly mean of Earth's gravitational potential are considered from degree 2 up to degree and order 96. In addition, accelerometer scale factors and rotation and shear parameters (see Klinger and Mayer-Gürr, 2016), are introduced as global unknowns. After a pre-elimination of the local parameters, the normal matrices of the global parameters from the individual arcs of the month are stacked, and the accumulated normal matrix is inverted to obtain the final global parameters. An overview of the number of parameters estimated in the main adjustment is provided in Table 3.2.

3.3 Perturbation of the Satellite Motion

The motion of a satellite around the Earth is constantly subject to so-called *perturbations* or *disturbing* effects. As a result, a satellite orbit will always deviate from a Keplerian ellipse, i.e., a perfectly elliptical orbit that would exist if the satellite's motion were influenced only by the central body term of Earth's

[2]The relation between the empirical parameters a, b,...f, the observed range-rate $\overline{\rho}$ and the computed range-rate $\dot{\rho}$ is: $\overline{\rho} - \dot{\rho} = a + bt + (e + ft)\cos u + (g + ht)\sin u$, where u is the argument of latitude of the midpoint between the two satellites (Kim, 2000, Equation 3.16). The argument of latitude is the geocentric angle measured between the ascending node of the satellite orbit and the position of the satellite (see e.g., Seeber, 2003), and is 0° or 180° at the equator, 90° at the North Pole and 270° at the South Pole.

gravitational potential. The perturbations can be divided into gravitational effects, which act on the center of mass of the satellite, and non-gravitational effects, which depend not only on the satellite's ephemerides but also on its geometry and surface properties. The gravitational disturbing effects include the influence of Earth's non-uniform and time-varying gravitational potential described by the unknown spherical harmonic coefficients to be determined during gravity field recovery, the influence of tidal effects as a reaction of the Earth system to the TGP (see Section 2.3.1), the direct attraction of the satellites by other celestial bodies (primarily the Moon and Sun), perturbations due to rapid non-tidal mass variations, as well as effects to be considered in the framework of relativity. The effects and corresponding models considered in satellite orbit modeling are also referred to as *background models*. Conventional definitions and computation schemes, which are updated every few years, exist for most of the perturbing effects, and are published by the IERS. The more recent conventional definitions are given in the IERS Conventions (2010).

While the inertial gravitational acceleration resulting from the direct attraction of celestial bodies and from relativistic effects can be obtained straightforward, most of the gravitational effects are expressed in terms of corrections $\Delta\overline{C}_{nm}$ and $\Delta\overline{S}_{nm}$ to the normalized spherical harmonic coefficients of the geopotential (Equation 2.21), consequently requiring two additional steps to determine the inertial acceleration. First, the Nabla operator has to be applied to these corrections to obtain the corresponding acceleration in the co-rotating coordinate system (see Section 2.2.2). After transforming these accelerations to the inertial coordinate system with Equation 2.3, they can be used in the equation of motion as defined in Equation 3.1. The corrections $\Delta\overline{C}_{nm}$ and $\Delta\overline{S}_{nm}$ of the individual effects can first be added up and converted to acceleration in one step; however, it is important to ensure that the corrections refer to the same (or sufficiently similar) scaling constants GM and R.

The non-gravitational perturbations acting on a satellite in a low Earth orbit, such as in the case of GRACE(-FO), include atmospheric drag, as well as direct and indirect solar radiation pressure. The direct radiation pressure is caused by photons emitted by the Sun, whereas the indirect solar radiation pressure arises from sunlight reflected by the Earth (albedo), as well as thermal radiation emitted in the infrared spectrum. The general modeling approach of these perturbation effects can, for example, be found in Seeber, 2003, Vallado, 2004, and Montenbruck and Gill, 2005. Since the non-gravitational part of the accelerations, including the contribution from thruster firings, is measured by onboard electrostatic accelerometers (see Section 3.1.1), the modeling of the individual effects is not relevant for the GRACE(-FO) orbit modeling.[3] However, the accelerometer measurements must be corrected by applying calibration parameters that are usually estimated during dynamic orbit determination and gravity field recovery.

A list of perturbing effects generally considered for GRACE(-FO) orbit modeling is given in Table 3.3. This table also contains information on the specific models used and the main model parameters. Figure 3.4 shows the corresponding magnitude of the acceleration effects for an one day orbit of GRACE-C. In general, the magnitudes of the individual effects primarily vary with the altitude of the satellites (see e.g., Seeber, 2003, Figure 3.20). The background models used by the various GRACE(-FO) analysis centers are very similar, with differences primarily concerning the choice of ocean tide and atmospheric models, as well as the gravity field model. The latter is of little significance, as the gravity model is only used as an a priori model to which the spherical harmonic coefficients corrections are determined.

The following subsections present the computation procedures for the individual effects listed in Table 3.3. The computation procedures for the acceleration due to Earth's gravitational field and ocean tides are not included below, as they have already been covered in detail in Sections 2.2 and 2.3.4.

[3] This refers to the classical gravity field recovery performed by the analysis centers utilizing L1B data products. Due to a malfunctioning of the accelerometer on GRACE-D immediately at the beginning of the science phase in June 2018, accelerometer data from the working accelerometer on GRACE-C has to be "transplanted" to GRACE-D. Depending on the method to generate these transplant products from L1A data, a modeling of the non-gravitational accelerations might be required (see e.g., Behzadpour et al., 2021; Harvey et al., 2024).

TABLE 3.3: Utilized background modeling standards. d/o: indicates the applied maximum degree/order of the spherical harmonic coefficients.

Acceleration	Model Details
Gravity field	GOCO06s (Kvas et al., 2021, 2019b) as a priori gravity field Static part (d/o: 300), time-variable part (d/o: 200)
Third-body effect	Celestial bodies: Moon, Sun, Mercury, Venus, Mars, Jupiter, Saturn Ephemerides: JPL DE430[1] (Folkner et al., 2014) J_2 effect considered for the Moon
Solid Earth tides	Moon and Sun (d/o: 4) (IERS Conventions, 2010) Nominal Love numbers: anelastic Earth model
Ocean tides	FES2014b (Lyard et al., 2021) (d/o: 180)
Relativistic effects	IERS Conventions (2010)
Solid earth pole tides	IERS Conventions (2010) Secular polar motion (IERS Conventions 2010, 01 Feb. 2018 update)
Ocean pole tides	IERS Conventions, 2010 (d/o: 180) (Desai, 2002) Secular polar motion (IERS Conventions 2010, 01 Feb. 2018 update)
Atmospheric tides	AOD1B RL06 (d/o: 180) (Dobslaw et al., 2017b)
De-aliasing	AOD1B RL06 (d/o: 180) (Dobslaw et al., 2017b)
Non-gravitational	ACC1B, ACT1B, ACH1B, TUG ACT (see Table 3.1) Full scale matrix (Klinger and Mayer-Gürr, 2016)

[1]JPL DE430 ephemerides are also used for solid Earth tides and the de-Sitter precession.

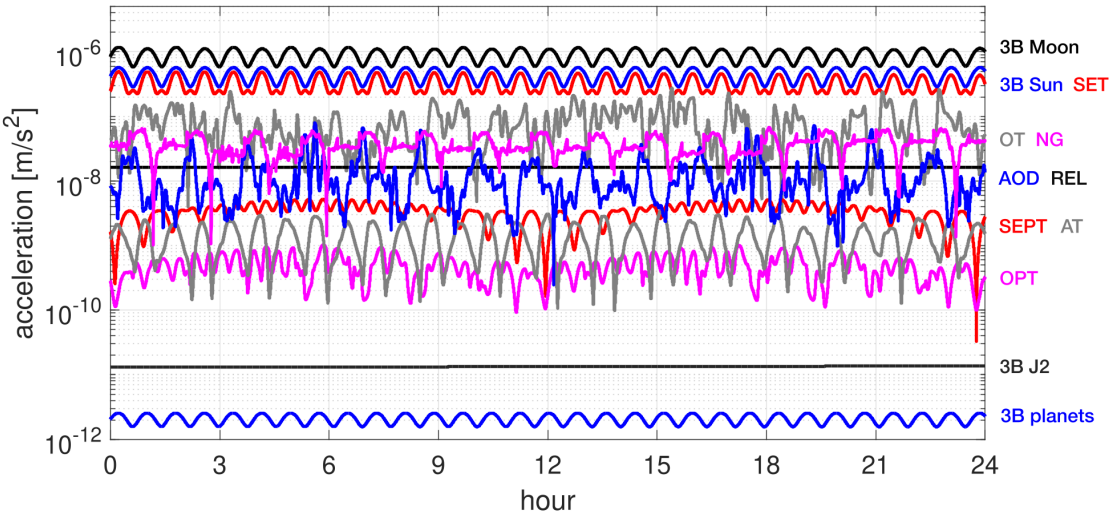

FIGURE 3.4: Magnitude of background model accelerations from Table 3.3 considered for orbit modeling. The values refer to the orbit of the GRACE-C satellite on 1 January 2021. 3B: third-body effect., SET: solid Earth tides, OT: ocean tides, NG: non-gravitational, AOD: atmosphere and ocean de-aliasing, REL: relativistic, SEPT: solid Earth pole tides, AT: atmospheric tides, OPT: ocean pole tides. Not shown is the acceleration caused by the gravitational potential with a magnitude of around 8.44±0.025 m/s^2. For benchmark data see Lasser et al. (2020).

3.3.1 Third-Body Effect

The direct influence of celestial bodies in terms of acceleration $\ddot{\mathbf{r}}_{DT}$ results from the attraction of masses. In general, the celestial bodies can be considered as point masses due to their large distances from the Earth-orbiting satellites. The total direct attraction of celestial bodies B is obtained by summing the individual acceleration contributions (e.g., Montenbruck and Gill, 2005):

$$\ddot{\mathbf{r}}_{DT} = \sum_B GM_B \left(\frac{\mathbf{r}_B - \mathbf{r}}{|\mathbf{r}_B - \mathbf{r}|^3} - \frac{\mathbf{r}_B}{|\mathbf{r}_B|^3} \right). \tag{3.5}$$

The satellite position $\mathbf{r}$, as well as the position $\mathbf{r}_B$ of the celestial body B refer to the inertial system. Positions of celestial bodies can be derived from different models. Notable examples include the Development Ephemeris (DE) from JPL (e.g., Folkner et al., 2014)[4], Ephemeris of Planets and the Moon (EPM) from the Institute of Applied Astronomy of the Russian Academy of Sciences (e.g., Pitjeva, 2005)[5], and the Intégrateur Numérique Planétaire de l'Observatoire de Paris (INPOP) from the French Institute for Celestial Mechanics and Computation of Ephemerides (e.g., Fienga et al., 2021)[6].

In this work, the positions of the Moon, Sun and planets are obtained from JPL's DE430 model (Folkner et al., 2014). The standard gravitational parameters GM_B to be used with this model are listed in the corresponding reference. The JPL ephemerides are provided in the form of piece-wise Chebyshev polynomial approximations typically valid for 32-day segments. By interpolating these segments the positions of the desired celestial bodies can be obtained.

While the direct accelerations caused by the Moon and Sun are the most significant after those caused by Earth's gravitational field, the contribution from planets is relatively small, and can generally be considered negligible (see Figure 3.4). Also the acceleration from the interaction of Earth's flattening (J_2) and the point mass Moon is several orders of magnitude smaller than the other effects, so the corresponding equation for this effect is omitted here.

3.3.2 Solid Earth Tides

The solid Earth tides are caused by the direct lunisolar attraction that is deforming the Earth's crust. Resulting variations of the geopotential are affecting the movement of satellites. The conventional computation of this effect in terms of normalized spherical harmonic coefficients $\Delta\overline{C}_{nm}$ and $\Delta\overline{S}_{nm}$ consists of two parts (IERS Conventions, 2010). In a first step, the frequency-independent components $\Delta\overline{C}^1_{nm}$ and $\Delta\overline{S}^1_{nm}$ are computed by considering the contributions of degrees 2 and 3:

$$\begin{pmatrix} \Delta\overline{C}^1_{nm} \\ \Delta\overline{S}^1_{nm} \end{pmatrix} = \begin{pmatrix} k^R_{nm}\Delta\overline{C}^*_{nm} + k^I_{nm}\Delta\overline{S}^*_{nm} \\ k^R_{nm}\Delta\overline{S}^*_{nm} - k^I_{nm}\Delta\overline{C}^*_{nm} \end{pmatrix} \tag{3.6}$$

with nominal Love numbers k^R_{nm}, k^I_{nm} for degree n and order m, and:

$$\begin{pmatrix} \Delta\overline{C}^*_{nm} \\ \Delta\overline{S}^*_{nm} \end{pmatrix} = \frac{1}{2n+1} \sum_B \frac{GM_B}{GM} \left(\frac{R}{r_B} \right)^{n+1} \overline{P}_{nm}(\sin\Phi_B) \begin{cases} \cos m\lambda_B \\ \sin m\lambda_B \end{cases} \tag{3.7}$$

where R is the Earth's equatorial radius; r_B the distance from the geocenter to the center of celestial body B; GM, GM_B are the standard gravitational parameters of the Earth or celestial body B; Φ_B, Λ_B are the

[4] `https://ssd.jpl.nasa.gov/planets/eph_export.html` (last accessed on 2025-04-25)

[5] `https://iaaras.ru/en/dept/ephemeris/epm/` (last accessed on 2025-04-25)

[6] `https://www.imcce.fr/inpop/` (last accessed on 2025-04-25)

TABLE 3.4: Nominal love numbers.

n	m	k_{nm}^R	k_{nm}^I	$k_{nm}^{(+)}$
2	0	0.30190	-0.00000	-0.00089
2	1	0.29830	-0.00144	-0.00080
2	2	0.30102	-0.00130	-0.00057
3	0	0.09300	0	–
3	1	0.09300	0	–
3	2	0.09300	0	–
3	3	0.09300	0	–

geographical latitude and longitude of the celestial body B; and $\overline{P}_{nm}$ are normalized associated Legendre polynomials (see Section 2.2.3). Note that only the Moon and Sun have to be considered here.

Additionally, the influence of degree 2 on degree 4 has to be computed as part of the first step:

$$\begin{pmatrix} \Delta\overline{C}^1_{4m} \\ \Delta\overline{S}^1_{4m} \end{pmatrix} = k_{2m}^{(+)} \begin{cases} \Delta\overline{C}^*_{2m} \\ \Delta\overline{S}^*_{2m} \end{cases} \tag{3.8}$$

The conventional nominal Love numbers k_{nm}^R, k_{nm}^I, $k_{nm}^{(+)}$ of the utilized anelastic Earth model are given in Table 3.4. The values for the elastic Earth model can be found in IERS Conventions (2010). The deviations from the nominal Love numbers have to be considered in a second step, in which frequency-dependent corrections to potential coefficients $\Delta\overline{C}^1_{20}$, $\Delta\overline{C}^1_{21}$, $\Delta\overline{S}^1_{21}$, $\Delta\overline{C}^1_{22}$, $\Delta\overline{S}^1_{22}$ are calculated. These corrections consider 21 long-periodic, 48 diurnal and 2 semidiurnal tidal frequencies f. The frequency-dependent in-phase (ip) and out-of-phase (op) amplitudes A_f^{ip}, A_f^{op} and the corresponding multipliers of the Doodson arguments are listed in IERS Conventions (2010, Tables 6.5a,b,c).

With the astronomical argument θ_f as defined earlier in Equation 2.60, the corrections can be obtained as follows:

$$\begin{aligned}
\Delta\overline{C}^2_{20} &= \sum_{f(\text{long})} \left(A_f^{ip} \cos\theta_f - A_f^{op} \sin\theta_f \right) \\
\Delta\overline{C}^2_{21} &= \sum_{f(\text{diurnal})} \left(A_f^{ip} \sin\theta_f + A_f^{op} \cos\theta_f \right) \qquad \Delta\overline{S}^2_{21} = \sum_{f(\text{diurnal})} \left(A_f^{ip} \cos\theta_f - A_f^{op} \sin\theta_f \right) \\
\Delta\overline{C}^2_{22} &= \sum_{f(\text{semidiurnal})} \left(A_f^{ip} \cos\theta_f \right) \qquad \Delta\overline{S}^2_{22} = \sum_{f(\text{semidiurnal})} \left(-A_f^{ip} \sin\theta_f \right) .
\end{aligned} \tag{3.9}$$

3.3.3 Solid Earth Pole Tides

Polar motion induces a variation in Earth's centrifugal force, which causes a re-distribution of masses in the solid Earth and consequently a deformation of the gravitational potential. The potential variation caused by the solid Earth pole tides can be described in terms of normalized spherical harmonic coefficients of degree 2 and order 1 as (IERS Conventions, 2010):

$$\begin{pmatrix} \Delta\overline{C}_{21} \\ \Delta\overline{S}_{21} \end{pmatrix} = -1.333 \times 10^{-9} \begin{cases} (m_1 + 0.0115\, m_2) \\ (m_2 - 0.0115\, m_1) \end{cases} \tag{3.10}$$

where the wobble parameters m_1 and m_2 are defined in arcseconds and can be obtained from polar motion coordinates x_p, y_p (see equation 2.19) and secular polar motion coordinates x_s, y_s:

$$\begin{aligned}
m_1 &= x_p - x_s \\
m_2 &= -(y_p - y_s) .
\end{aligned} \tag{3.11}$$

The secular pole coordiantes in milli-arcseconds obtained from a least squares fit to polar motion observations from 1900 to 2017 are defined as (IERS Conventions, 2010, 01 February 2018 update):

$$\begin{aligned} x_s &= 55.0 + 1.677\,t \\ y_s &= 320.5 + 3.460\,t\,. \end{aligned} \tag{3.12}$$

Time argument t is the number of Julian years between the current epoch and epoch J2000.0:

$$t = \frac{(TT - 1.\ \text{January 2000, 12:00 TT}) \quad [\text{in days}]}{365.25}\,. \tag{3.13}$$

3.3.4 Ocean Pole Tides

The variation of Earth's centrifugal force due to polar motion also causes a re-distribution of ocean masses, and leads to a deformation of Earth's gravitational potential. Conventionally this effect is considered with the self-consistent equilibrium model of Desai (2002) as a perturbation to the normalized spherical harmonic coefficients of the geopotential with degree n and order m as follows:

$$\begin{pmatrix} \Delta\overline{C}_{nm} \\ \Delta\overline{S}_{nm} \end{pmatrix} = R_n \left[\begin{pmatrix} \overline{A}^R_{nm} \\ \overline{B}^R_{nm} \end{pmatrix} (m_1\gamma_2^R + m_2\gamma_2^I) + \begin{pmatrix} \overline{A}^I_{nm} \\ \overline{B}^I_{nm} \end{pmatrix} (m_2\gamma_2^R + m_1\gamma_2^I) \right]. \tag{3.14}$$

In the above equation, $\overline{A}^R_{nm}$, $\overline{B}^R_{nm}$, $\overline{A}^I_{nm}$, $\overline{B}^I_{nm}$ are the coefficients of the self-consistent model until degree/order $n/m = 360$ and can be obtained from (IERS, 2019b); m_1 and m_2 are the wobble parameters (see equation 3.11); $\gamma_2^R = 0.6870$, $\gamma_2^I = 0.0036$; and the quantitiy R_n being defined as:

$$R_n = \frac{\Omega^2 a_E^4}{GM} \frac{4\pi G\rho_\omega}{g_e} \left(\frac{1 + k'_n}{2n+1} \right) \tag{3.15}$$

where GM, a_E and Ω are the standard gravitational parameter, equatorial radius and nominal mean angular velocity of the Earth, respectively; g_e is the mean equatorial gravity; G the gravitational constant; ρ_w the density of sea water; and k'_n are the degree-dependent load deformation coefficients. Numeric values of the relevant constants can be found in IERS Conventions (2010).

3.3.5 Non-Tidal Rapid Mass Variations

To consider the influence of non-tidal short-term variations in the atmosphere and oceans, Atmosphere and Ocean De-Aliasing L1B (AOD1B) RL06 (Dobslaw et al., 2017b) products provided by GFZ (ISDC, 2023) are used. The model is given in terms of normalized spherical harmonic coefficients with a temporal resolution of 3 hours. To compute the effect for a specific epoch, linear interpolation of the coefficients between two consecutive time steps, as recommended by Dobslaw et al. (2017a), is used. The atmospheric part of AOD1B RL06 is based on European Centre for Medium-Range Weather Forecasts (ECMWF) data (Dee et al., 2011), while the effect of rapid mass variations over the oceans is simulated with the Max-Planck-Institute for Meteorology Ocean Model (MPIOM) (Jungclaus et al., 2013) with ECMWF atmospheric forcing.

3.3.6 Atmospheric Tides

Atmospheric tides are periodic mass movements in the atmosphere excited gravitationally by the Moon and Sun, or thermally by the absorption of radiation (e.g., Lindzen and Chapman, 1969). As part of the computation of the time series of non-tidal rapid mass variation products (Dobslaw et al., 2017b), the atmospheric contribution at the frequencies of four main tidal constituents, i.e., the solar tides S_1, S_2, S_3 and the lunar tide M_2, is estimated from the ECMWF surface pressure data covering the period 2007–2014. For each of the four constituents, the two corresponding annual side lines are additionally estimated, to

take into account seasonal modulations. Fully normalized prograde coefficients $C^{cos}_{nm,f}$, $S^{cos}_{nm,f}$ and retrograde coefficients $C^{sin}_{nm,f}$, $S^{sin}_{nm,f}$ of the 12 constituents f until degree and order $n/m = 180$ are provided (ISDC, 2023) as a supplementary part to the AOD1B products. The effect of the atmospheric tides in terms of a correction to the normalized spherical harmonic coefficients of the geopotential can be evaluated with Equation 2.76. Note that a phase bias χ_f has to be added to the Doodson arguments to comply with the Doodson–Warburg convention (see IERS Conventions, 2010).

3.3.7 Relativistic Effects

In the framework of general relativity, the motion of satellites near the Earth is conventionally corrected by taking into account the three relativistic effects: the *Schwarzschild* term due to the spherically symmetrical part of Earth's gravitational field, *Lense–Thirring* precession (or frame dragging) caused by the rotation of the Earth, and the *de-Sitter* precession (or geodetic precession) due to the presence of the Earth as a central mass (Brumberg and Kopejkin, 1989; IERS Conventions, 2010):

$$\begin{aligned}\ddot{\mathbf{r}}_{REL} = \frac{GM}{c^2\,|\mathbf{r}|^3}\Bigg\{&\left[2(\beta+\gamma)\frac{GM}{|\mathbf{r}|} - \gamma\,\dot{\mathbf{r}}\cdot\dot{\mathbf{r}}\right]\mathbf{r} + 2(1+\gamma)(\mathbf{r}\cdot\dot{\mathbf{r}})\dot{\mathbf{r}}\Bigg\} \\ &+(1+\gamma)\,\frac{GM}{c^2\,|\mathbf{r}|^3}\left[\frac{3}{|\mathbf{r}|^2}(\mathbf{r}\times\dot{\mathbf{r}})(\mathbf{r}\cdot\mathbf{J}) + (\dot{\mathbf{r}}\times\mathbf{J})\right] \\ &+\left\{(1+2\gamma)\left[\dot{\mathbf{R}}\times\left(\frac{-GM_\odot\,\mathbf{R}}{c^2\,|\mathbf{R}|^3}\right)\right]\times\dot{\mathbf{r}}\right\}\end{aligned} \tag{3.16}$$

where GM and $GM_\odot$ are the standard gravitational parameters of the Earth and the Sun, respectively; c is the speed of light; $\mathbf{r}$ and $\dot{\mathbf{r}}$ the inertial geocentric position and velocity vectors of the satellite, respectively; $\mathbf{R}$ and $\dot{\mathbf{R}}$ are the position and velocity vectors of the Earth with respect to the Sun, respectively; $\mathbf{J}$ is the Earth's angular momentum per unit mass; and $\beta = 1$, $\gamma = 1$ the parameterized post-Newtonian parameters.

3.3.8 Non-Gravitational Acceleration

The non-gravitational components of the accelerations are measured by onboard electrostatic accelerometers (see Section 3.1.1). Positioned at the center of mass of the spacecraft, these instruments measure the total non-gravitational contribution. In addition to atmospheric drag and both direct and indirect solar radiation pressure, they also record accelerations caused by thruster firings. Calibration of the measurements is necessary to obtain accurate values for the magnitude and amplitude of the non-gravitational acceleration. The calibrated acceleration is given by:

$$\ddot{\mathbf{r}}_c = \mathbf{S}\,\ddot{\mathbf{r}}_o + \mathbf{b} \tag{3.17}$$

where $\ddot{\mathbf{r}}_o$ is the measured acceleration by the accelerometer, $\ddot{\mathbf{r}}_c$ is the calibrated acceleration vector, both given in the GRACE(-FO) Science Reference Frame (SRF); and a bias vector $\mathbf{b}$ and scale matrix $\mathbf{S}$:

$$\mathbf{b} = \begin{pmatrix} b_x \\ b_y \\ b_z \end{pmatrix} \qquad \mathbf{S} = \begin{pmatrix} s_x & \alpha+\zeta & \beta-\epsilon \\ \alpha-\zeta & s_y & \gamma+\delta \\ \beta+\epsilon & \gamma-\delta & s_z \end{pmatrix} \tag{3.18}$$

where b_x, b_y, b_z and s_x, s_y, s_z are the three components for the bias and the scaling of the three axes of the SRF, respectively; α, β, γ are symmetric shear parameters that geometrically should account for a possible cross-talk among the axes resulting from the non-orthogonality of the accelerometer axes, and ζ, ϵ, δ are skew-symmetric rotation parameters that geometrically reflect the misalignment between the SRF and the accelerometer frame (see Klinger and Mayer-Gürr, 2016). All of these bias vector and scale matrix elements are estimated during gravity field recovery (see Table 3.2).

The inertial non-gravitational acceleration vector $\ddot{\mathbf{r}}_{NG}$ can be obtained by the rotation:

$$\ddot{\mathbf{r}}_{NG} = \mathbf{R}^{\mathrm{T}}\, \ddot{\mathbf{r}}_{c} \tag{3.19}$$

with the rotation matrix formed from the quaternion elements q_0, q_1, q_2, q_3 of the SCA1B product (Wu et al., 2006):

$$\mathbf{R} = \begin{pmatrix} q_0^2 + q_1^2 - q_2^2 - q_3^2 & 2(q_1 q_2 + q_0 q_3) & 2(q_1 q_3 - q_0 q_2) \\ 2(q_1 q_2 - q_0 q_3) & q_0^2 - q_1^2 + q_2^2 - q_3^2 & 2(q_2 q_3 + q_0 q_1) \\ 2(q_1 q_3 + q_0 q_2) & 2(q_2 q_3 - q_0 q_1) & q_0^2 - q_1^2 - q_2^2 + q_3^2 \end{pmatrix}. \tag{3.20}$$

3.4 Numerical Integration

To obtain a dynamically modeled orbit, the equations of motion of the satellites in the form of the first order ODEs (Equation 3.2) must be solved. Moreover, to adjust the obtained dynamically modeled orbit to observational data, state transition matrices and sensitivity matrices are required. The complexity of the multitude of forces acting on a satellite at low altitude makes analytical integration of the ODEs infeasible, and therefore necessitates the employment of *numerical integrators*, i.e., approximative numerical integration techniques. Consequently, numerical integration is a key aspect of gravity field recovery using dynamic orbit determination. Over the past few centuries, numerous methods for the numerical integration of ODEs have been developed and refined. The most popular integrators by far used for solving the equations of motion of satellites belong to the categories of *Runge–Kutta* (RK) methods and *multi-step* methods. Due to their relevance for the generation of the gravity field recovery results, they will be briefly addressed in this section. In addition to numerical integrators from these two categories, ODEs can also be numerically solved using extrapolation, Taylor series, and collocation methods. For a comprehensive overview of different integration techniques, readers can refer to Fox (1984), Beutler (2004), Montenbruck and Gill (2005), and Hairer et al. (2008), which besides the underlying mathematical formulations also address, to a certain degree, the topics of computational efficiency and accuracy.

As will be seen later, RK methods are based on a straightforward concept, making them easy to apply to tasks in celestial mechanics as well as in various other fields. The accuracy of RK methods typically depends on their order, with higher-order integrators generally providing more accurate solutions, although this comes at the cost of computational efficiency. RK methods can also be denoted as single-step methods because they rely solely on information from the current epoch. In contrast to single-step techniques, multi-step methods utilize data from previous epochs. To be able to start a multi-step method, acceleration from prior epochs must be provided. The integration starting procedure can, for example, be initiated by a RK integrator. Due to the storing of the values from previous epochs, multi-step methods generally offer higher computational efficiency, compared to RK methods. While in RK methods, the number of function evaluations required to obtain the state for the next epoch is equal to or greater than the order of the integrator, in the case of multi-step methods generally only one or two function evaluations per epoch are required, independent of the degree of the integrator. Here, "function evaluation" refers to the computation of all disturbing accelerations (Table 3.4) for one specific epoch. The evaluation of the disturbing accelerations can be considered as the most time-consuming aspect of orbit propagation and gravity field recovery overall. In particular, the computation of the Legendre functions and their derivatives is computationally intensive. While the number of function evaluations may not pose a problem for certain applications, it is a critical factor for the numerical integration in the framework of gravity field recovery from GRACE(-FO) sensor data because the set of disturbing forces cannot be significantly simplified, and an integration with a small step size of 5 seconds is required to be able to process the KBR measurements at their original L1B sampling frequency.

The integration technique utilized in the GRACE-SIGMA software is a *Gauss–Jackson* integrator, which has been modified to enable computationally efficient numerical integration of GRACE(-FO)-like orbits, as

well as state transition and sensitivity matrices (Naeimi, 2018). To generate the starting values for this multi-step technique, the 4th-order RK integrator is employed. Both techniques are presented in the next two subsections.

3.4.1 Modified Gauss–Jackson Integrator

The classical scheme of a mth-order Gauss–Jackson integrator (see e.g., Montenbruck and Gill, 2005) to obtain the inertial position $\mathbf{r}_{i+1}$ and velocity vector $\dot{\mathbf{r}}_{i+1}$ at epoch $i+1$, i.e., $t+h$, where h is the fixed integration step size, consists of a predictor step:

$$\mathbf{r}_{i+1} = h^2 \sum_{j=0}^{m+1} \delta_j \nabla^{j-2} \ddot{\mathbf{r}}_i \tag{3.21}$$

$$\dot{\mathbf{r}}_{i+1} = h \sum_{j=0}^{m} \gamma_j \nabla^{j-1} \ddot{\mathbf{r}}_i \tag{3.22}$$

followed by a corrector step using the updated acceleration calculated with the earlier predicted state:

$$\mathbf{r}_{i+1} = h^2 \sum_{j=0}^{m+1} \delta_j^* \nabla^{j-2} \ddot{\mathbf{r}}_{i+1} \tag{3.23}$$

$$\dot{\mathbf{r}}_{i+1} = h \sum_{j=0}^{m} \gamma_j^* \nabla^{j-1} \ddot{\mathbf{r}}_{i+1} \,. \tag{3.24}$$

The quantities γ_j, γ_j^*, and (δ_j, δ_j^*) are identified as the Adams–Bashforth, Adams–Moulton, and Stoermer and Cowell coefficients, respectively. Numeric values of these coefficients until an order of $m = 8$, as well as the relations for calculating values for higher orders can be found, for example, in Montenbruck and Gill (2005). Furtheremore, $\nabla^k \ddot{\mathbf{r}}_i$ denotes kth acceleration backward differences if $k > 0$, or the first or second sums ∇^{-1} and ∇^{-2}, respectively. The backward differences are defined recursively as follows (e.g., Berry and Healy, 2004; Montenbruck and Gill, 2005):

$$\begin{aligned}
\nabla^0 \ddot{\mathbf{r}}_i &= \ddot{\mathbf{r}}_i \\
\nabla^1 \ddot{\mathbf{r}}_i &= \nabla \ddot{\mathbf{r}}_i = \ddot{\mathbf{r}}_i - \ddot{\mathbf{r}}_{i-1} \\
\nabla^2 \ddot{\mathbf{r}}_i &= \nabla \nabla \ddot{\mathbf{r}}_i = \nabla(\ddot{\mathbf{r}}_i - \ddot{\mathbf{r}}_{i-1}) = \ddot{\mathbf{r}}_i - 2\ddot{\mathbf{r}}_{i-1} + \ddot{\mathbf{r}}_{i-2} \\
&\vdots \\
\nabla^{k-1} \ddot{\mathbf{r}}_i &= \nabla^{k-2} \ddot{\mathbf{r}}_i - \nabla^{k-2} \ddot{\mathbf{r}}_{i-1} \,.
\end{aligned} \tag{3.25}$$

For the first and second sums the following relationship is valid (e.g., Berry and Healy, 2004; Montenbruck and Gill, 2005):

$$\begin{aligned}
\nabla^{-1} \ddot{\mathbf{r}}_i &= \nabla^0 \ddot{\mathbf{r}}_i + \nabla^{-1} \ddot{\mathbf{r}}_{i-1} \\
\nabla^{-2} \ddot{\mathbf{r}}_i &= \nabla^{-1} \ddot{\mathbf{r}}_i + \nabla^{-2} \ddot{\mathbf{r}}_{i-1} \,.
\end{aligned} \tag{3.26}$$

As can be recognized, the Gauss–Jackson integrator as a multi-step technique, in addition to the acceleration at epoch i, also requires the acceleration from $m-1$ previous epochs.

When the integration step size is appropriately selected and the orbit is (near-)circular, the corrector step becomes unnecessary (e.g., Fox, 1984; Berry and Healy, 2004). Naeimi (2018) quantified the position differences between the corrector and predictor steps, i.e., Equation 3.23 minus 3.21, for a GRACE-like orbit. For the standard GRACE(-FO) integration step size of 5 seconds, the corrector step can be ignored when using an integration order of 8 or higher (see Figure 3.5). However, as shown by Naeimi (2018), the corrector formulas enable a derivation of closed forms for the first and second sums. This is achieved through a series

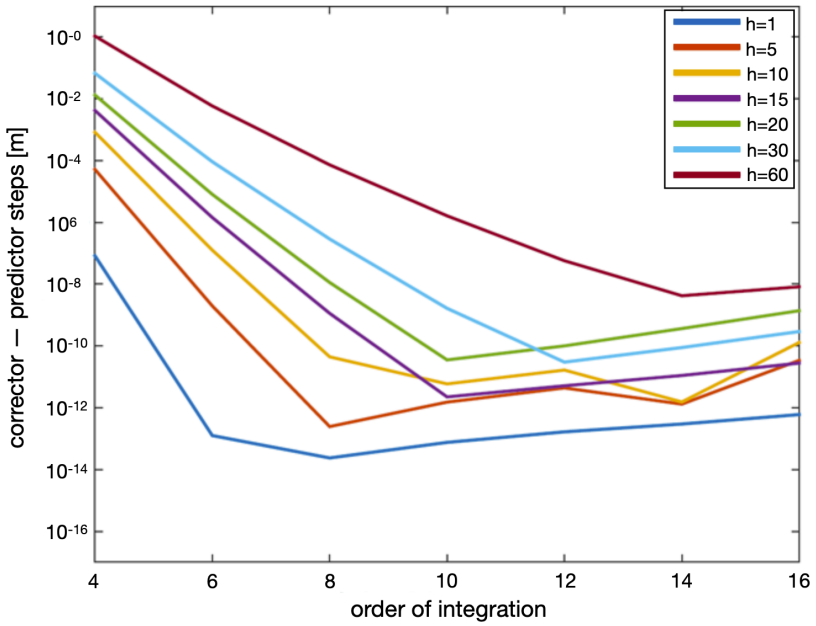

FIGURE 3.5: Difference between the corrector and predictor steps of the Gauss–Jackson integrator for different step sizes h and order of integration. Figure taken from Naeimi (2018); slightly modified.

TABLE 3.5: Parameters p_j and q_j for the numerical integration with the modified Gauss–Jackson integrator.

j	0	1	2	3	4	5	6	7	8	9	10	11
p_j	0	$\frac{1}{2}$	$\frac{1}{6}$	$\frac{1}{8}$	$\frac{19}{180}$	$\frac{3}{32}$	$\frac{863}{10080}$	$\frac{275}{3456}$	$\frac{33953}{453600}$	$\frac{8183}{115200}$	$\frac{3250433}{47900160}$	$\frac{4671}{71680}$
q_j	0	1	$\frac{1}{2}$	$\frac{5}{12}$	$\frac{3}{8}$	$\frac{251}{720}$	$\frac{665}{2016}$	$\frac{19087}{60480}$	$\frac{110397}{362880}$	$\frac{1070017}{3628800}$	$\frac{137461698}{479001600}$	$\frac{26842253}{95800320}$

TABLE 3.6: Entries of the matrix $\mathbf{B}$ for the vectorized computation of backward differences.

	$\ddot{\mathbf{r}}_i$	$\ddot{\mathbf{r}}_{i-1}$	$\ddot{\mathbf{r}}_{i-2}$	$\ddot{\mathbf{r}}_{i-3}$	$\ddot{\mathbf{r}}_{i-4}$	$\ddot{\mathbf{r}}_{i-5}$	$\ddot{\mathbf{r}}_{i-6}$	$\ddot{\mathbf{r}}_{i-7}$	$\ddot{\mathbf{r}}_{i-8}$	$\ddot{\mathbf{r}}_{i-9}$	$\ddot{\mathbf{r}}_{i-10}$
$\ddot{\mathbf{r}}_i$	1	0	0	0	0	0	0	0	0	0	0
$\nabla\ddot{\mathbf{r}}_i$	1	-1	0	0	0	0	0	0	0	0	0
$\nabla^2\ddot{\mathbf{r}}_i$	1	-2	1	0	0	0	0	0	0	0	0
$\nabla^3\ddot{\mathbf{r}}_i$	1	-3	3	-1	0	0	0	0	0	0	0
$\nabla^4\ddot{\mathbf{r}}_i$	1	-4	6	-4	1	0	0	0	0	0	0
$\nabla^5\ddot{\mathbf{r}}_i$	1	-5	10	-10	5	-1	0	0	0	0	0
$\nabla^6\ddot{\mathbf{r}}_i$	1	-6	15	-20	15	-6	1	0	0	0	0
$\nabla^7\ddot{\mathbf{r}}_i$	1	-7	21	-35	35	-21	7	-1	0	0	0
$\nabla^8\ddot{\mathbf{r}}_i$	1	-8	28	-56	70	-56	28	-8	1	0	0
$\nabla^9\ddot{\mathbf{r}}_i$	1	-9	36	-84	126	-126	84	-36	9	-1	0
$\nabla^{10}\ddot{\mathbf{r}}_i$	1	-10	45	-120	210	-252	210	-120	45	-10	1

of arithmetic calculations and substitutions—the details of which are omitted here for brevity—ultimately leading to the following expressions:

$$\begin{aligned}\nabla^{-1}\ddot{\mathbf{r}}_i &= \frac{\dot{\mathbf{r}}_i}{h} - \sum_{j=1}^{m} \gamma_j^* \nabla^{j-1}\ddot{\mathbf{r}}_i \\ \nabla^{-2}\ddot{\mathbf{r}}_i &= \frac{\mathbf{r}_i}{h^2} + \frac{\dot{\mathbf{r}}_i}{h} - \sum_{j=1}^{m} (\gamma_j^* + \delta_{j+1}^*)\nabla^{j-1}\ddot{\mathbf{r}}_i \,.\end{aligned} \tag{3.27}$$

By substituting these newly derived expressions into the predictor equations (3.21 and 3.22) and defining new coefficients

$$\begin{aligned}p_j &= \delta_{j+1} - \gamma_j^* - \delta_{j+1}^* \\ q_j &= \gamma_j - \gamma_j^* \,,\end{aligned} \tag{3.28}$$

whose numeric values are listed in Table 3.5, one arrives at the modified version of the Gauss–Jackson integrator:

$$\begin{aligned}\mathbf{r}_{i+1} &= \mathbf{r}_i + h\dot{\mathbf{r}}_i + h^2 \sum_{j=1}^{m} p_j \nabla^{j-1}\ddot{\mathbf{r}}_i \\ \dot{\mathbf{r}}_{i+1} &= \dot{\mathbf{r}}_i + h \sum_{j=1}^{m} q_j \nabla^{j-1}\ddot{\mathbf{r}}_i \,.\end{aligned} \tag{3.29}$$

The modified Gauss–Jackson integrator can be used particularly efficient in its vectorized form:

$$\begin{aligned}\mathbf{r}_{i+1} &= \mathbf{r}_i + h\dot{\mathbf{r}}_i + h^2\mathbf{pBA} \\ \dot{\mathbf{r}}_{i+1} &= \dot{\mathbf{r}}_i + h\mathbf{qBA}\end{aligned} \tag{3.30}$$

where row vectors $\mathbf{p}$ and $\mathbf{q}$ contain coefficients p_j and q_j, respectively; matrix $\mathbf{A}$ contains row-wise the acceleration vector at the current epoch i as well as the acceleration of $m-1$ prior epochs in the order of most recent (first row) to least recent; and matrix $\mathbf{B}$, which multiplied with $\mathbf{A}$ gives the backward differences, is made of elements listed in Table 3.6. The number of elements in the mentioned vectors and matrices should be adjusted to match the desired order of the integrator. For the computation of the gravity field recovery results the summation was carried out over indices $j = (1, 11)$.

3.4.2 Runge–Kutta Integrator

In order to use the modified Gauss–Jackson integrator for orbit propagation, the acceleration of prior epochs is needed. If m is the order of the multi-step integrator, then in addition to the acceleration at epoch i, the acceleration values of $m-1$ prior epochs should be known. These can, for example, be obtained with the help of a RK integrator. To compute the propagated state vector $\mathbf{y}_{i+1}$ at time $t+h$, starting from an initial state $\mathbf{y}_i$ at time t with a given integration step size h, the general RK integrator is defined as (e.g., Montenbruck and Gill, 2005):

$$\mathbf{y}_{i+1} = \mathbf{y}_i + h\mathbf{\Phi} \,. \tag{3.31}$$

Here, the classical RK integrator, i.e., the 4th-order RK integrator, is employed. The increment function for this method is:

$$\mathbf{\Phi} = \frac{1}{6}(\mathbf{k}_1 + 2\mathbf{k}_2 + 2\mathbf{k}_3 + \mathbf{k}_4) \tag{3.32}$$

with four recursively defined function evaluations:

$$\begin{aligned}\mathbf{k}_1 &= f(t_i, \mathbf{y}_i)\\ \mathbf{k}_2 &= f(t_i + h/2, \mathbf{y}_i + h\mathbf{k}_1/2)\\ \mathbf{k}_3 &= f(t_i + h/2, \mathbf{y}_i + h\mathbf{k}_2/2)\\ \mathbf{k}_4 &= f(t_i + h, \mathbf{y}_i + h\mathbf{k}_3)\,.\end{aligned} \tag{3.33}$$

3.5 Parameter Estimation

The subsequent numerical integration of the equations of motion of the satellites in terms of the ODEs, will result in a numerically propagated orbit. This orbit will deviate from an observed orbit, e.g., a kinematic orbit, in the course of time. This is not unexpected, given the discrepancy between the initially only approximately known dynamics from background models and the actual forces acting on the satellites. The objective of gravity field recovery is to estimate the mean monthly parameters of Earth's gravitational field, as well as additional parameters, by adjusting the modeled orbit to satellite observations. Therefore, the parameter estimation using least squares adjustment is an integral part of dynamic orbit determination and gravity field recovery.

The following subsections provide slightly extended versions of the equations that were previously summarized and presented in Koch et al. (2021, Appendix A). For further details on the topic of gravity field parameter estimation, readers are also encouraged to consult the lecture notes on *Global Gravity Field Modeling from Satellite-to-Satellite Tracking Data* (Naeimi and Flury, 2017). First, in Section 3.5.1, the relationship between the modeled satellite states and range-rates is shown. Section 3.5.2 outlines the least squares adjustment process, beginning with the general and well-known equations and progressing to aspects specifically relevant for gravity field recovery and this thesis, such as parameter pre-elimination, the combination of normal matrices, and the mathematical definition of range-rate post-fit residuals. The weight matrices used for kinematic positions and K-band range-rates are presented in Section 3.5.3. Section 3.5.4 focuses on the linearization of observation equations and the definition of the relevant design matrices.

3.5.1 Model for Computed Observations

The range vector pointing from one satellite to another is defined as the vector difference between the inertial position vectors:

$$\mathbf{r}_{AB} = \mathbf{r}_B - \mathbf{r}_A\,. \tag{3.34}$$

The range between these two satellites is then the Euclidean norm:

$$\rho = |\mathbf{r}_{AB}|\,. \tag{3.35}$$

By differentiating the above expression with respect to time one obtains the range-rate:

$$\dot{\rho} = \frac{\mathbf{r}_{AB} \cdot \dot{\mathbf{r}}_{AB}}{\rho}, \tag{3.36}$$

where the relative velocity vector is defined as the difference:

$$\dot{\mathbf{r}}_{AB} = \dot{\mathbf{r}}_B - \dot{\mathbf{r}}_A\,. \tag{3.37}$$

With the unit vector along the range vector, i.e., the line-of-sight vector:

$$\mathbf{e}_{AB} = \frac{\mathbf{r}_{AB}}{\rho}, \tag{3.38}$$

the range and range-rate can also be formulated as projections onto the line-of-sight vector (e.g., Rummel et al., 1978; Seeber, 2003):

$$\begin{aligned} \rho &= \mathbf{r}_{AB} \cdot \mathbf{e}_{AB} \\ \dot{\rho} &= \dot{\mathbf{r}}_{AB} \cdot \mathbf{e}_{AB} \,. \end{aligned} \tag{3.39}$$

3.5.2 Least Squares Adjustment

Least squares adjustment is an algorithm for the estimation of "optimal" values for unknown parameters from a set of observations, and is applied when the number of observations n_l exceeds the number of unknowns n_x. Although, from a mathematical point of view, all unknown parameters can be uniquely determined when $n_l = n_x$, in this case, no quality assessment can be made, and potential outliers may not be identified. The foundation for the parameter estimation is an appropriate functional model f that defines the relationship between the observations $\mathbf{l} = (l_1, \ldots, l_{n_l})^{\mathrm{T}}$ and the parameters $\mathbf{x} = (x_1, \ldots, x_{n_x})^{\mathrm{T}}$. With this functional model, the observations can be expressed as functions of the parameters, i.e., in vectorized form as $\mathbf{l} + \mathbf{v} = f(\mathbf{x})$, where vector $\mathbf{v} = (v_1, \ldots, v_{n_l})^{\mathrm{T}}$ contains errors or residuals that arise due to the stochastic nature of observations and discrepancies between the underlying model and reality. In linear form, the relationship between observations and parameters can be expressed as $\mathbf{l} + \mathbf{v} = \mathbf{A}\mathbf{x}$, where $\mathbf{A}$ is the so-called *design matrix* (Jacobian) containing the partial derivatives of the functional model with respect to the unknowns. In the method of least squares adjustment the optimal parameter estimates are found by the minimization of the residuals squares sum: $\mathbf{v}^{\mathrm{T}}\mathbf{v} \rightarrow \min$, or in the case of weighted observations, by the minimization of the weighted residuals squares sum: $\mathbf{v}^{\mathrm{T}}\mathbf{P}\mathbf{v} \rightarrow \min$, where $\mathbf{P}$ is the weight matrix containing the stochastic information of the observations.

The fundamental equation for obtaining optimal parameter estimates $\hat{\mathbf{x}}$ using weighted least squares adjustment is (e.g., Koch, 1999; Niemeier, 2008):

$$\hat{\mathbf{x}} = (\mathbf{A}^{\mathrm{T}}\mathbf{P}\mathbf{A})^{-1}\,\mathbf{A}^{\mathrm{T}}\mathbf{P}\mathbf{l}\,. \tag{3.40}$$

Equation 3.40 can be formulated more compact with the normal matrix $\mathbf{N}$ and right hand side vector $\mathbf{b}$:

$$\hat{\mathbf{x}} = \mathbf{N}^{-1}\,\mathbf{b}\,. \tag{3.41}$$

Dynamic orbit determination falls under the category of non-linear problems, requiring Equation 3.40 to be rewritten as:

$$\Delta\hat{\mathbf{x}} = (\mathbf{A}^{\mathrm{T}}\mathbf{P}\mathbf{A})^{-1}\,\mathbf{A}^{\mathrm{T}}\mathbf{P}\Delta\mathbf{l}\,. \tag{3.42}$$

For these kind of problems, the vector $\mathbf{x}_0$ containing a priori values of the unknown parameters is introduced. The functional model f can be evaluated with these a priori values, i.e., $f(\mathbf{x}_0)$, resulting in a set of computed observations. The vector $\Delta\mathbf{l}$ represents the "observed minus computed" observations, i.e., the difference between observations $\mathbf{l}$ and $f(\mathbf{x}_0)$. The vector $\Delta\hat{\mathbf{x}}$ contains corrections to the a priori parameters. With these, the parameter vector is defined as:

$$\hat{\mathbf{x}} = \mathbf{x}_0 + \Delta\hat{\mathbf{x}}\,. \tag{3.43}$$

Typically, the process of computing $\hat{\mathbf{x}}$ involves an iterative approach until convergence, where $\mathbf{x}_0$ is updated to $\hat{\mathbf{x}}$ after each iteration.

Owing to the distinction between parameters that are only valid for a specific arc (local parameters, $\sim$) and parameters that remain constant over one month (global parameters, $\oplus$), the parameter correction vector

can be divided into two parts:

$$\Delta\hat{\mathbf{x}} = (\Delta\hat{\mathbf{x}}_{\sim}^{\mathrm{T}},\ \Delta\hat{\mathbf{x}}_{\oplus}^{\mathrm{T}})^{\mathrm{T}}. \tag{3.44}$$

Taking into account the individual arcs $i = (1, 2, \ldots,\ j)$, the parameter correction vector can be further extended to:

$$\Delta\hat{\mathbf{x}} = (\Delta\hat{\mathbf{x}}_{\sim 1}^{\mathrm{T}},\ \Delta\hat{\mathbf{x}}_{\sim 2}^{\mathrm{T}}, \ldots,\ \Delta\hat{\mathbf{x}}_{\sim j}^{\mathrm{T}},\ \Delta\hat{\mathbf{x}}_{\oplus}^{\mathrm{T}})^{\mathrm{T}}. \tag{3.45}$$

Referring to Equation 3.41, with the separation of the parameter correction vector as shown above, and the assumption of j uncorrelated observation groups, the following system of normal equations is obtained:

$$\begin{pmatrix} \mathbf{N}_{\sim 1} & \mathbf{0} & \cdots & \mathbf{0} & \mathbf{N}_{\sim\oplus 1} \\ \mathbf{0} & \mathbf{N}_{\sim 2} & \cdots & \mathbf{0} & \mathbf{N}_{\sim\oplus 2} \\ \vdots & \vdots & \ddots & \vdots & \vdots \\ \mathbf{0} & \mathbf{0} & \cdots & \mathbf{N}_{\sim j} & \mathbf{N}_{\sim\oplus j} \\ \mathbf{N}_{\sim\oplus 1}^{\mathrm{T}} & \mathbf{N}_{\sim\oplus 2}^{\mathrm{T}} & \cdots & \mathbf{N}_{\sim\oplus j}^{\mathrm{T}} & \mathbf{N}_{\oplus} \end{pmatrix} \begin{pmatrix} \Delta\hat{\mathbf{x}}_{\sim 1} \\ \Delta\hat{\mathbf{x}}_{\sim 2} \\ \vdots \\ \Delta\hat{\mathbf{x}}_{\sim j} \\ \Delta\hat{\mathbf{x}}_{\oplus} \end{pmatrix} = \begin{pmatrix} \mathbf{b}_{\sim 1} \\ \mathbf{b}_{\sim 2} \\ \vdots \\ \mathbf{b}_{\sim j} \\ \mathbf{b}_{\oplus} \end{pmatrix} \tag{3.46}$$

where $\mathbf{0}$ represent zero matrices of appropriate size.

The final estimate of the global parameter corrections $\Delta\hat{\mathbf{x}}_{\oplus}$ can be obtained by an arc-wise pre-elimination of the local parameter corrections (3.48) and the stacking (3.47) of the individual arcs (e.g., Kusche and Springer, 2017):

$$\Delta\hat{\mathbf{x}}_{\oplus} = \sum_{i=1}^{j} \Delta\hat{\mathbf{x}}_{\oplus i}, \tag{3.47}$$

with

$$\Delta\hat{\mathbf{x}}_{\oplus i} = \left(\mathbf{N}_{\oplus i} - \mathbf{N}_{\sim\oplus i}{}^{\mathrm{T}}\, \mathbf{N}_{\sim i}^{-1}\, \mathbf{N}_{\sim\oplus i}\right)^{-1} \left(\mathbf{b}_{\oplus i} - \mathbf{N}_{\sim\oplus i}^{\mathrm{T}}\, \mathbf{N}_{\sim i}^{-1}\, \mathbf{b}_{\sim i}\right). \tag{3.48}$$

The normal matrices $\mathbf{N}_{\sim i}$, $\mathbf{N}_{\oplus i}$, $\mathbf{N}_{\sim\oplus i}$, and the right hand side vectors $\mathbf{b}_{\sim i}$, $\mathbf{b}_{\oplus i}$ are formulated as weighted combinations of the K-band observations (denoted by subscript K) and kinematic positions of the two satellites (subscripts A, B):

$$\begin{aligned}
\mathbf{N}_{\sim i} &= \mathbf{A}_{\sim Ai}^{\mathrm{T}}\, \mathbf{P}_{Ai}\, \mathbf{A}_{\sim Ai} + \mathbf{A}_{\sim Bi}^{\mathrm{T}}\, \mathbf{P}_{Bi}\, \mathbf{A}_{\sim Bi} + \mathbf{A}_{\sim Ki}^{\mathrm{T}}\, \mathbf{P}_{K}\, \mathbf{A}_{\sim Ki} \\
\mathbf{N}_{\sim\oplus i} &= \mathbf{A}_{\sim Ai}^{\mathrm{T}}\, \mathbf{P}_{Ai}\, \mathbf{A}_{\oplus Ai} + \mathbf{A}_{\sim Bi}^{\mathrm{T}}\, \mathbf{P}_{Bi}\, \mathbf{A}_{\oplus Bi} + \mathbf{A}_{\sim Ki}^{\mathrm{T}}\, \mathbf{P}_{K}\, \mathbf{A}_{\oplus Ki} \\
\mathbf{N}_{\oplus i} &= \mathbf{A}_{\oplus Ai}^{\mathrm{T}}\, \mathbf{P}_{Ai}\, \mathbf{A}_{\oplus Ai} + \mathbf{A}_{\oplus Bi}^{\mathrm{T}}\, \mathbf{P}_{Bi}\, \mathbf{A}_{\oplus Bi} + \mathbf{A}_{\oplus Ki}^{\mathrm{T}}\, \mathbf{P}_{K}\, \mathbf{A}_{\oplus Ki} \\
\mathbf{b}_{\sim i} &= \mathbf{A}_{\sim Ai}^{\mathrm{T}}\, \mathbf{P}_{Ai}\, \Delta\mathbf{l}_{Ai} + \mathbf{A}_{\sim Bi}^{\mathrm{T}}\, \mathbf{P}_{Bi}\, \Delta\mathbf{l}_{Bi} + \mathbf{A}_{\sim Ki}^{\mathrm{T}}\, \mathbf{P}_{K}\, \Delta\mathbf{l}_{Ki} \\
\mathbf{b}_{\oplus i} &= \mathbf{A}_{\oplus Ai}^{\mathrm{T}}\, \mathbf{P}_{Ai}\, \Delta\mathbf{l}_{Ai} + \mathbf{A}_{\oplus Bi}^{\mathrm{T}}\, \mathbf{P}_{Bi}\, \Delta\mathbf{l}_{Bi} + \mathbf{A}_{\oplus Ki}^{\mathrm{T}}\, \mathbf{P}_{K}\, \Delta\mathbf{l}_{Ki}
\end{aligned} \tag{3.49}$$

with design matrices $\mathbf{A}_{\sim Ai}$, $\mathbf{A}_{\sim Bi}$, $\mathbf{A}_{\sim Ki}$, $\mathbf{A}_{\oplus Ai}$, $\mathbf{A}_{\oplus Bi}$ and $\mathbf{A}_{\oplus Ki}$ (see Section 3.5.4); weight matrices $\mathbf{P}_{Ai}$, $\mathbf{P}_{Bi}$ and $\mathbf{P}_{K}$ representing the stochastic model of the observations (see Section 3.5.3); and reduced observation vectors $\Delta\mathbf{l}_{Ai}$, $\Delta\mathbf{l}_{Bi}$ and $\Delta\mathbf{l}_{Ki}$.

In the case of position components, the reduced observation vectors of the two satellites are:

$$\begin{aligned}
\Delta\mathbf{l}_{Ai} &= \mathrm{vec}(\bar{\mathbf{r}}_{Ai} - \mathbf{r}_{Ai}) \\
\Delta\mathbf{l}_{Bi} &= \mathrm{vec}(\bar{\mathbf{r}}_{Bi} - \mathbf{r}_{Bi})\,.
\end{aligned} \tag{3.50}$$

The matrices $\bar{\mathbf{r}}_{Ai}$, $\bar{\mathbf{r}}_{Bi}$ contain the inertial kinematic positions of an arc i, while matrices $\mathbf{r}_{Ai}$, $\mathbf{r}_{Bi}$ the corresponding dynamically modeled positions, i.e., the outcome of the numerically integrated equation of motion (see Equation 3.2).

The reduced range-rate observation vector of an arc i is accordingly defined as:

$$\Delta \mathbf{l}_{Ki} = \overline{\dot{\boldsymbol{\rho}}}_i - \dot{\boldsymbol{\rho}}_i \,. \tag{3.51}$$

The vector $\overline{\dot{\boldsymbol{\rho}}}_i$ comprises the L1B range-rate measurements, incorporating light-time and antenna phase center offset corrections. The counterpart $\dot{\boldsymbol{\rho}}_i$ is calculated from the dynamically modeled positions $\mathbf{r}_{Ai}$, $\mathbf{r}_{Bi}$ and velocities $\dot{\mathbf{r}}_{Ai}$, $\dot{\mathbf{r}}_{Bi}$, as outlined in Section 3.5.1.

Once the final global parameter corrections $\Delta\hat{\mathbf{x}}_{\oplus}$ have been estimated with Equation 3.47, the corrections to the local parameters of an arc i can be obtained (e.g., Kusche and Springer, 2017):

$$\Delta\hat{\mathbf{x}}_{\sim i} = \mathbf{N}_{\sim i}^{-1}\,\mathbf{b}_{\sim i} - \mathbf{N}_{\sim i}^{-1}\,\mathbf{N}_{\sim \oplus i}\,\Delta\hat{\mathbf{x}}_{\oplus} \,. \tag{3.52}$$

Finally, with the known local and global parameter corrections, the K-band range-rate post-fit residuals $\mathbf{v}_{Ki}$ for each of the involved arcs i can be calculated:

$$\mathbf{v}_{Ki} = \mathbf{A}_{\sim Ki}\,\Delta\hat{\mathbf{x}}_{\sim i} + \mathbf{A}_{\oplus Ki}\,\Delta\hat{\mathbf{x}}_{\oplus} - \Delta\mathbf{l}_{Ki} \,. \tag{3.53}$$

3.5.3 Weights

The accuracy information of the observations $\mathbf{l} = (l_1, \ldots, l_{n_l})^{\mathrm{T}}$ can be described by the covariance matrix (see e.g., Koch, 1999; Niemeier, 2008):

$$\boldsymbol{\Sigma}_{ll} = \begin{pmatrix} \sigma_1^2 & \sigma_{12} & \ldots & \sigma_{1n_l} \\ \sigma_{21} & \sigma_2^2 & \ldots & \sigma_{2n_l} \\ \vdots & \vdots & \ddots & \vdots \\ \sigma_{n_l1} & \sigma_{n_l2} & \ldots & \sigma_{n_l}^2 \end{pmatrix} . \tag{3.54}$$

The covariance matrix consists of variances σ_i^2 of the individual observations l_i along its diagonal, while the off-diagonal elements represent the corresponding covariances, i.e., provide information on correlations. It is often assumed that there are no correlations between individual observations. With this assumption, the covariance matrix simplifies to a diagonal matrix:

$$\boldsymbol{\Sigma}_{ll} = \mathrm{diag}(\sigma_1^2,\, \sigma_2^2, \ldots,\, \sigma_{n_l}^2) \,. \tag{3.55}$$

If one further assumes that all observations have the same accuracy, i.e., $\sigma_1^2 = \cdots = \sigma_{n_l}^2 = \sigma^2$, the covariance matrix simplifies to:

$$\boldsymbol{\Sigma}_{ll} = \sigma^2 \mathbf{I} \tag{3.56}$$

where $\mathbf{I}$ is the identity matrix. If only the accuracy relationships between the observations are known, meaning σ^2 is unknown, the covariance matrix can be expressed as follows:

$$\boldsymbol{\Sigma}_{ll} = \sigma_0^2 \mathbf{Q}_{ll} \tag{3.57}$$

where $\mathbf{Q}_{ll}$ is the cofactor matrix that describes the accuracy relations between the individual observations, and σ_0^2 is the unknown variance of the unit weight. For the estimation process, knowing σ_0^2 is not necessary, as it can be estimated during the adjustment. This parameter is often assumed to be 1.

However, for the least squares adjustment, the weight matrix $\mathbf{P}$ must be known, which is defined as the inverse of the cofactor matrix:

$$\begin{aligned}\mathbf{P} &= \mathbf{Q}_{ll}^{-1} \\ &= \left(\frac{1}{\sigma_0^2}\mathbf{\Sigma}_{ll}\right)^{-1}.\end{aligned} \tag{3.58}$$

In the case of a diagonal covariance matrix, the weight matrix is given by:

$$\mathbf{P} = \begin{pmatrix} \sigma_0^2/\sigma_1^2 & 0 & \dots & 0 \\ 0 & \sigma_0^2/\sigma_2^2 & \dots & 0 \\ \vdots & \vdots & \ddots & \vdots \\ 0 & 0 & \dots & \sigma_0^2/\sigma_{n_l}^2 \end{pmatrix}. \tag{3.59}$$

Within the scope of this thesis, for the main adjustment, a diagonal weight matrix was used for K-band range-rate observations with $\sigma_0^2 = 1$ and the constant standard deviation $\sigma = 0.2$ μm/s. For the kinematic position weight matrices, epoch-wise covariance information from the GNSS-based orbit products was used to construct diagonal weight matrices. Additionally, the relative weighting of K-band range-rates and kinematic positions was adjusted by dividing the elements of the kinematic position weight matrices by empirically derived factors of 500 for GRACE and 25 for GRACE-FO. In the pre-adjustment, a slightly different weighting procedure was applied (see Section 3.2.2).

3.5.4 Partial Derivatives

Since the functional model f for dynamic orbit determination is non-linear with respect to the unknowns, it is necessary to linearize $f(\mathbf{x})$ in order to be able to estimate parameter corrections $\Delta\hat{\mathbf{x}}$ using Equation 3.42. The linearization is performed using a first-order Taylor series expansion, which is then evaluated with the a priori values of the unknown parameters $\mathbf{x}_0$. This leads to the following relationship between the measurements $\mathbf{l} = (l_1, \dots, l_{n_l})^{\mathrm{T}}$ and unknown parameters $\mathbf{x} = (x_1, \dots, x_{n_x})^{\mathrm{T}}$ (e.g., Koch, 1999; Niemeier, 2008):

$$\mathbf{l} + \mathbf{v} = f(\mathbf{x}_0) + \left.\frac{\partial f}{\partial \mathbf{x}}\right|_{\mathbf{x}=\mathbf{x}_0} \Delta\hat{\mathbf{x}}\,. \tag{3.60}$$

The partial derivatives of the functional model with respect to the unknowns form the design matrix:

$$\mathbf{A} = \left.\frac{\partial f}{\partial \mathbf{x}}\right|_{\mathbf{x}=\mathbf{x}_0} = \begin{pmatrix} \dfrac{\partial f_1(\mathbf{x}_0)}{\partial x_1} & \dots & \dfrac{\partial f_1(\mathbf{x}_0)}{\partial x_{n_x}} \\ \vdots & \ddots & \vdots \\ \dfrac{\partial f_{n_l}(\mathbf{x}_0)}{\partial x_1} & \dots & \dfrac{\partial f_{n_l}(\mathbf{x}_0)}{\partial x_{n_x}} \end{pmatrix}. \tag{3.61}$$

Now, relating range-rate observations and kinematic positions to the unknown parameters according to the general linearization equation (3.60) in the observed minus computed form, and omitting the residuals, results in:

$$\begin{aligned} \overline{\dot{\boldsymbol{\rho}}}_i - \dot{\boldsymbol{\rho}}_i = &\sum_{k=1}^{n_\sim} \frac{\partial \dot{\boldsymbol{\rho}}_i}{\partial \mathbf{q}_{\sim ik}} \Delta\mathbf{q}_{\sim ik} + \sum_{k=1}^{n_\oplus} \frac{\partial \dot{\boldsymbol{\rho}}_i}{\partial \mathbf{q}_{\oplus ik}} \Delta\mathbf{q}_{\oplus ik} \\ \mathrm{vec}(\overline{\mathbf{r}}_{Ai} - \mathbf{r}_{Ai}) = &\sum_{k=1}^{n_\sim} \frac{\partial \mathrm{vec}(\mathbf{r}_{Ai})}{\partial \mathbf{q}_{\sim ik}} \Delta\mathbf{q}_{\sim ik} + \sum_{k=1}^{n_\oplus} \frac{\partial \mathrm{vec}(\mathbf{r}_{Ai})}{\partial \mathbf{q}_{\oplus ik}} \Delta\mathbf{q}_{\oplus ik} \\ \mathrm{vec}(\overline{\mathbf{r}}_{Bi} - \mathbf{r}_{Bi}) = &\sum_{k=1}^{n_\sim} \frac{\partial \mathrm{vec}(\mathbf{r}_{Bi})}{\partial \mathbf{q}_{\sim ik}} \Delta\mathbf{q}_{\sim ik} + \sum_{k=1}^{n_\oplus} \frac{\partial \mathrm{vec}(\mathbf{r}_{Bi})}{\partial \mathbf{q}_{\oplus ik}} \Delta\mathbf{q}_{\oplus ik} \end{aligned} \tag{3.62}$$

where vectors $\mathbf{q}_{\sim i}$ and $\mathbf{q}_{\oplus i}$ include local and global parameters, respectively; $\Delta\mathbf{q}_{\sim i}$ and $\Delta\mathbf{q}_{\oplus i}$ are the corresponding corrections to the a priori values of parameters in vectors $\mathbf{q}_{\sim i}$ and $\mathbf{q}_{\oplus i}$; and $n_\sim$ and $n_\oplus$ are the number of parameters in vectors $\mathbf{q}_{\sim i}$ and $\mathbf{q}_{\oplus i}$, respectively.

The partial derivatives in Equation 3.62, further subdivided into individual sets of local and global parameters, can now be used to set up the design matrices $\mathbf{A}_{\sim Ai}$, $\mathbf{A}_{\sim Bi}$, $\mathbf{A}_{\sim Ki}$, $\mathbf{A}_{\oplus Ai}$, $\mathbf{A}_{\oplus Bi}$ and $\mathbf{A}_{\oplus Ki}$:

$$
\begin{aligned}
\mathbf{A}_{\sim Ki} &= \begin{pmatrix} \dfrac{\partial\dot{\boldsymbol{\rho}}_i}{\partial\mathbf{y}_{0Ai}} & \dfrac{\partial\dot{\boldsymbol{\rho}}_i}{\partial\mathbf{b}_{Ai}} & \dfrac{\partial\dot{\boldsymbol{\rho}}_i}{\partial\mathbf{y}_{0Bi}} & \dfrac{\partial\dot{\boldsymbol{\rho}}_i}{\partial\mathbf{b}_{Bi}} & \dfrac{\partial\dot{\boldsymbol{\rho}}_i}{\partial\mathbf{e}_i} \end{pmatrix} \\
\mathbf{A}_{\sim Ai} &= \begin{pmatrix} \dfrac{\partial\mathrm{vec}(\mathbf{r}_{Ai})}{\partial\mathbf{y}_{0Ai}} & \dfrac{\partial\mathrm{vec}(\mathbf{r}_{Ai})}{\partial\mathbf{b}_{Ai}} & \mathbf{0} & \mathbf{0} & \mathbf{0} \end{pmatrix} \\
\mathbf{A}_{\sim Bi} &= \begin{pmatrix} \mathbf{0} & \mathbf{0} & \dfrac{\partial\mathrm{vec}(\mathbf{r}_{Bi})}{\partial\mathbf{y}_{0Bi}} & \dfrac{\partial\mathrm{vec}(\mathbf{r}_{Bi})}{\partial\mathbf{b}_{Bi}} & \mathbf{0} \end{pmatrix} \\
\mathbf{A}_{\oplus\mathrm{K}i} &= \begin{pmatrix} \dfrac{\partial\dot{\boldsymbol{\rho}}_i}{\partial\overline{\mathbf{C}}_{\mathrm{nm}i}} & \dfrac{\partial\dot{\boldsymbol{\rho}}_i}{\partial\overline{\mathbf{S}}_{\mathrm{nm}i}} & \dfrac{\partial\dot{\boldsymbol{\rho}}_i}{\partial\mathbf{s}_{Ai}} & \dfrac{\partial\dot{\boldsymbol{\rho}}_i}{\partial\mathbf{s}_{Bi}} \end{pmatrix} \\
\mathbf{A}_{\oplus Ai} &= \begin{pmatrix} \dfrac{\partial\mathrm{vec}(\mathbf{r}_{Ai})}{\partial\overline{\mathbf{C}}_{\mathrm{nm}i}} & \dfrac{\partial\mathrm{vec}(\mathbf{r}_{Ai})}{\partial\overline{\mathbf{S}}_{\mathrm{nm}i}} & \dfrac{\partial\mathrm{vec}(\mathbf{r}_{Ai})}{\partial\mathbf{s}_{Ai}} & \mathbf{0} \end{pmatrix} \\
\mathbf{A}_{\oplus Bi} &= \begin{pmatrix} \dfrac{\partial\mathrm{vec}(\mathbf{r}_{Bi})}{\partial\overline{\mathbf{C}}_{\mathrm{nm}i}} & \dfrac{\partial\mathrm{vec}(\mathbf{r}_{Bi})}{\partial\overline{\mathbf{S}}_{\mathrm{nm}i}} & \mathbf{0} & \dfrac{\partial\mathrm{vec}(\mathbf{r}_{Bi})}{\partial\mathbf{s}_{Bi}} \end{pmatrix}
\end{aligned}
\tag{3.63}
$$

where $\mathbf{y}_{0Ai}$, $\mathbf{y}_{0Bi}$ denote the initial state vectors, $\mathbf{b}_{Ai}$, $\mathbf{b}_{Bi}$ represent the accelerometer biases, $\mathbf{s}_{Ai}$, $\mathbf{s}_{Bi}$ contain the elements of the full accelerometer scale matrices, $\mathbf{e}_i$ contains the geometric empirical range-rate parameters, and the spherical harmonic coefficients of Earth's gravitational potential to be estimated form vectors $\overline{\mathbf{C}}_{\mathrm{nm}i} = (\overline{C}_{20},\, \overline{C}_{21},\, \overline{C}_{22}, \dots)$ and $\overline{\mathbf{S}}_{\mathrm{nm}i} = (\overline{S}_{21},\, \overline{S}_{22},\, \overline{S}_{31}, \dots)$.

The partial derivatives of the positions with respect to the corresponding initial states are part of the epoch-wise state transition matrices $\boldsymbol{\Phi}$, which contain the partial derivatives of a satellite state $\mathbf{y} = (\mathbf{r}^{\mathrm{T}},\, \dot{\mathbf{r}}^{\mathrm{T}})^{\mathrm{T}} = (x, y, z, vx, vy, vz)^{\mathrm{T}}$ at a specific time t with respect to the initial state $\mathbf{y}_0 = (\mathbf{r}_0^{\mathrm{T}}, \dot{\mathbf{r}}_0^{\mathrm{T}}) = (x_0, y_0, z_0, vx_0, vy_0, vz_0)^{\mathrm{T}}$ at time t_0 (e.g., Montenbruck and Gill, 2005; Vallado, 2004):

$$
\boldsymbol{\Phi}(t, t_0) = \frac{\partial\mathbf{y}}{\partial\mathbf{y}_0} = \begin{pmatrix} \dfrac{\partial x}{\partial x_0} & \cdots & \dfrac{\partial x}{\partial vz_0} \\ \vdots & \ddots & \vdots \\ \dfrac{\partial vz}{\partial x_0} & \cdots & \dfrac{\partial vz}{\partial vz_0} \end{pmatrix}. \tag{3.64}
$$

At the initial time $t = t_0$, the state transition matrix is obviously the identity matrix $\mathbf{I}$. To obtain the state transition matrices for a time t of interest, the ODE

$$
\dot{\boldsymbol{\Phi}}(t, t_0) = \begin{pmatrix} \mathbf{0}_{3\times3} & \mathbf{I}_{3\times3} \\ \dfrac{\partial\ddot{\mathbf{r}}}{\partial\mathbf{r}} & \dfrac{\partial\ddot{\mathbf{r}}}{\partial\dot{\mathbf{r}}} \end{pmatrix} \boldsymbol{\Phi}(t, t_0) \tag{3.65}
$$

has to be numerically integrated with the equations of motion of the satellites (see Section 3.4), since for precise applications, i.e., when complex accelerations $\ddot{\mathbf{r}}$ have to be considered, an analytical solution is not feasible. Besides these partial derivatives, additional partial derivatives are required for constructing the design matrices for gravity field recovery. These include the derivatives with respect to the other dynamic parameters $\mathbf{p} = (p_1, \dots, p_{n_p})^{\mathrm{T}}$ and are part of the so-called sensitivity matrices $\mathbf{S}$ (e.g., Montenbruck and

Gill, 2005; Vallado, 2004):

$$\mathbf{S}(t) = \frac{\partial \mathbf{y}}{\partial \mathbf{p}} = \begin{pmatrix} \frac{\partial x}{\partial p_1} & \cdots & \frac{\partial x}{\partial p_{n_p}} \\ \vdots & \ddots & \vdots \\ \frac{\partial vz}{\partial p_1} & \cdots & \frac{\partial vz}{\partial p_{n_p}} \end{pmatrix}. \tag{3.66}$$

Similarly, the numerical values of the sensitivity matrix at a specific time t can be obtained through numerical integration. With the integration constant $\mathbf{S}(t_0) = \mathbf{0}$, the following ODE has to be solved:

$$\dot{\mathbf{S}}(t) = \begin{pmatrix} \mathbf{0}_{3\times 3} & \mathbf{I}_{3\times 3} \\ \frac{\partial \ddot{\mathbf{r}}}{\partial \mathbf{r}} & \frac{\partial \ddot{\mathbf{r}}}{\partial \dot{\mathbf{r}}} \end{pmatrix} \mathbf{S}(t) + \begin{pmatrix} \mathbf{0}_{3\times n_p} \\ \frac{\partial \ddot{\mathbf{r}}}{\partial \mathbf{p}} \end{pmatrix}. \tag{3.67}$$

For the computation of the sensitivity matrices, the partial derivatives of the total acceleration with respect to the dynamic parameters must be available. These are obtained by differentiating the corresponding equations presented earlier in Section 2.2 (gravitational potential) and Section 3.3.8 (accelerometer calibration parameters).

Using the state transition and sensitivity matrices, the partial derivatives of a computed range-rate $\dot{\rho}$ with respect to the initial states and dynamic parameters can be formulated as:

$$\begin{aligned} \frac{\partial \dot{\rho}}{\partial \mathbf{y}_0} &= \frac{\partial \dot{\rho}}{\partial \mathbf{y}} \frac{\partial \mathbf{y}}{\partial \mathbf{y}_0} \\ \frac{\partial \dot{\rho}}{\partial \mathbf{p}} &= \frac{\partial \dot{\rho}}{\partial \mathbf{y}} \frac{\partial \mathbf{y}}{\partial \mathbf{p}} \end{aligned} \tag{3.68}$$

where, according to the geometrical relationships outlined in Section 3.5.1, the partial derivatives of the range-rate with respect to the states of satellites A and B are:

$$\frac{\partial \dot{\rho}}{\partial \mathbf{y}_A} = \left(\mathbf{e}_{AB} \frac{\dot{\rho}}{\rho} - \frac{\dot{\mathbf{r}}_{AB}}{\rho} - \mathbf{e}_{AB} \right) \qquad \text{and} \qquad \frac{\partial \dot{\rho}}{\partial \mathbf{y}_B} = -\frac{\partial \dot{\rho}}{\partial \mathbf{y}_A}. \tag{3.69}$$

The non-dynamic partial derivatives of the computed range-rates with respect to the geometric empirical range-rate parameters can be obtained straightforward from the relationship presented in Footnote [2] of Section 3.2.3.

3.6 Evaluation of the LUH Gravity Field Solutions

For the further investigations presented in Chapter 4, it is important to demonstrate that the quality of the computed monthly gravity field solutions is competitive with the state-of-the-art solutions from other analysis centers. Significant deviations in the signal content of the spherical harmonic coefficients of the obtained unconstrained gravity field solutions, or a noticeably higher noise level, could potentially undermine the quality of the post-fit residuals for the subsequent investigations. Therefore, in the concluding section of this chapter, the LUH monthly gravity field recovery results are compared with the corresponding time series from the analysis centers listed below:

- CSR: RL06 (GRACE), RL06.3 (GRACE-FO) (Bettadpur, 2019; Save, 2019a)
- GFZ: RL06 (GRACE), RL06.3 (GRACE-FO) (Dahle et al., 2019b,a)
- JPL: RL06 (GRACE), RL06.3 (GRACE-FO) (Yuan, 2018, 2019)
- TUG: ITSG-Grace2018 (GRACE), ITSG-Grace_op (GRACE-FO) (Mayer-Gürr et al., 2018; Kvas et al., 2019a).

The solutions of the reference analysis centers were downloaded from ICGEM[7]. First, the spectral noise level of the five time series in terms of difference degree standard deviations (see Equation 2.40) is compared. Since gravity field solutions might generally employ different scaling factors, all spherical harmonic coefficients are re-scaled to a common reference radius R and Earth's standard gravitational parameter GM (e.g., Meyer et al., 2019, Equation 3). A reference model, to be subtracted from the the gravity field solutions to obtain the coefficients differences $\Delta\overline{C}_{nm}$ and $\Delta\overline{S}_{nm}$, is derived by averaging in total 216×5 monthly GRACE(-FO) solutions from April 2002 to September 2023. Prior to calculating the reference model, the $\overline{C}_{20}$ coefficients in all solutions are substituted with more accurate SLR values from Technical Note 14 (Loomis et al., 2020)[8]. Note that degree-1 coefficients, which cannot be observed with GRACE(-FO), are important for deriving accurate mass changes but are not relevant for comparisons at the solution level as conducted in this section; therefore, they have not been substituted.

The spectral noise assessment in terms of mean difference degree standard deviations is shown in Figure 3.6a, separately for the GRACE and GRACE-FO period. A strong consistency is evident in the signal-dominated low-degree coefficients, which are crucial for estimating mass changes due to their significant signal content. Around degree 25, deviations between the solutions of the analysis centers become noticeable, reflecting the varying noise levels in the solutions. The spectral noise characteristics of the LUH solutions most closely resemble those of the JPL solutions. The reduced noise levels in the CSR and TUG solutions result from their distinct gravity field recovery approaches, setting them apart from the approaches of the other three analysis centers. For example, the solutions from TUG incorporate the estimation of daily gravity fields along with additional tidal corrections (Kvas et al., 2019a). The CSR processing employs a two-step approach, which may result in reduced noise levels in the higher-degree coefficients. In the two-step approach, the gravity field parameters are estimated separately from the other orbit parameters, which are determined in a prior iteration (Save, 2019a).

The noise level of the solutions in the spatial domain is usually assessed by analyzing residual mass variations in suited regions, specifically those where only relatively small mass variations are expected, for example, oceanic areas. To assess the spatial noise but also the signal content, which will be presented shortly, monthly 1°×1° EWH maps are calculated using Equation 2.49. The same reference model and corrections used for the difference degree standard deviations are also applied here. In addition, a Gaussian filter (see Equation 2.50) with a half-width radius of 400 km is applied. To the time series of each grid cell, a model consisting of a bias, linear trend, annual and semiannual variation (see Equation 2.51) is fitted to absorb the most substantial time-variability contained in the gravity field solutions. Remaining signal after the subtraction of this model from the EWH time series is shown in Figure 3.6b. While the EWH values over the continents indicate the presence of unabsorbed non-seasonal time-variable signal, residual signal over the oceans remains relatively homogeneous, although with slightly different noise levels among the analysis centers.

Figure 3.6c depicts a comparison of the monthly Root Mean Square (RMS) of the residual signal over the oceans. To avoid the influence of a possible signal leakage from the continents, and the impact of residual tidal signal, which is expected to be most pronounced in coastal and polar regions, this metric is derived from the grid cells in the boundary mask indicated in white on the LUH map in Figure 3.6b. The presented monthly RMS noise values over the ocean suggest a certain correlation with the spectral noise discussed earlier, i.e., JPL, GFZ and LUH exhibit closer values, while the CSR, and in particular, the TUG time series exhibit a considerably lower spatial noise level. A slight increase in both spatial and spectral noise levels can be observed in the GFZ time series during the GRACE-FO period.

[7] `https://icgem.gfz-potsdam.de/sl/temporal` (last accessed on 2025-08-04)

[8] `ftp://isdcftp.gfz-potsdam.de/grace-fo/DOCUMENTS/TECHNICAL_NOTES/TN-14_C30_C20_SLR_GSFC.txt` (last accessed on 2025-08-04)

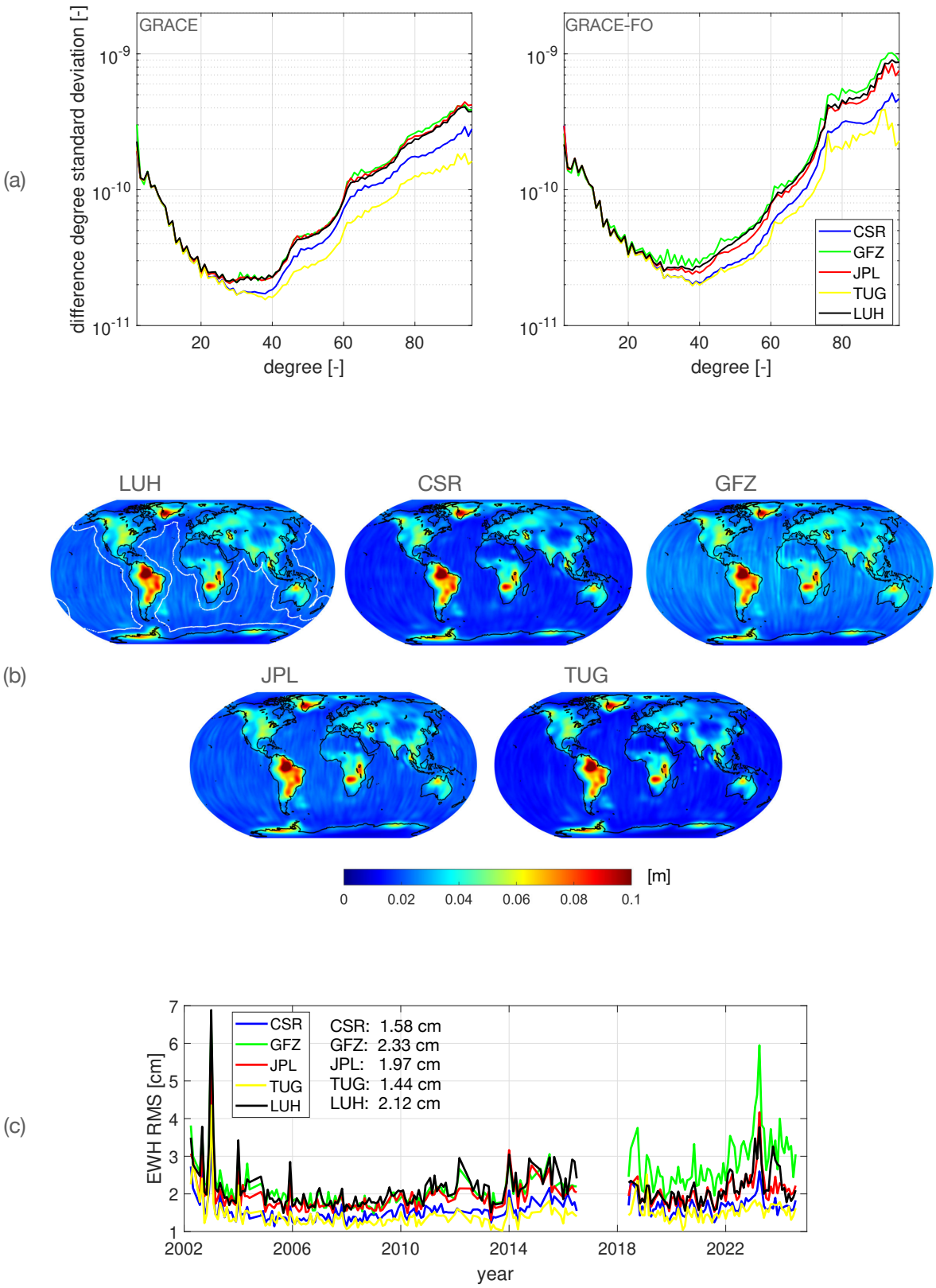

FIGURE 3.6: (a): Comparison of difference degree standard deviations (see Equation 2.40). For GRACE, 143 monthly gravity fields from April 2002 to July 2016 are considered; and 73 solutions from June 2018 to September 2023 for GRACE-FO. (b): Residual EWH signal not explained by the model in Equation 2.51. (c): RMS of the noise over the oceans computed on a $1°\times1°$ grid. The values were computed in the boundaries shown in white in the LUH map in (b). Numeric values in (c) represent the mean of the RMS time series.

Figure 3.7a shows the sum of the annual and semiannual amplitudes obtained from the fitting of the model from Equation 2.51. The regions of increased amplitudes over the continents primarily reflect seasonal hydrological variations, such as those related to surface water, snow, and soil moisture (e.g., Rodell and Reager, 2023). Seasonal variations of approximately 15 to 20 cm EWH are particularly pronounced in many tropical regions, including South America, Central Africa, India, and northern Southeast Asia. As shown in Figure 3.7b, the seasonal amplitudes derived from the time series of the five analysis centers are remarkably similar. The differences between the seasonal amplitudes from Figure 3.7a and a mean seasonal amplitude map are usually around 0.5 cm EWH, but tend to be slightly larger for the GFZ time series. Nevertheless, when computing the mean annual and semiannual amplitudes for around 180 river basins (Oki and Sud, 1998)[9], no significant systematic discrepancies between the individual analysis centers can be recognized (see Figure 3.7c).

The linear trend component obtained from the fit of the model from Equation 2.51 is illustrated in Figure 3.8a. Also the trends of the individual analysis centers generally align well, with the GFZ time series showing slightly larger deviations from the mean trend (see Figure 3.8b). A region experiencing one of the most substantial negative mass loss trends is Greenland. The corresponding mean EWH values evaluated within the boundaries of Greenland are shown in Figure 3.8c. A comparable negative trend, of around 5.1 to 5.2 cm per year, associated with ice mass loss, can be observed for the five time series. Note that when converting the yearly EWH trends presented in Figure 3.8c to mass, the obtained trends will not represent the real mass loss as presented in dedicated literature (e.g., Velicogna et al., 2020; Sasgen et al., 2020). As the purpose of this section is simply to provide a general comparison of the signal content in the time series from the individual analysis centers, no leakage correction (e.g., Baur et al., 2009; Chen et al., 2015) was applied. As a result, the presented EWH trends reflect only approximately half of the full ice mass loss signal in Greenland due to the leakage-out error.

In addition to Greenland, as shown in Figure 3.8a, pronounced negative and positive linear trends in mass changes are also observed in various other regions: in Antarctica and Alaska due to ice loss (e.g., Velicogna et al., 2020; Ciracì et al., 2020), in Antarctica's Queen Maud Land owing to steady accumulation of mass (e.g., Velicogna et al., 2020), in North America and Fennoscandia due to GIA (e.g., Riva et al., 2009; Steffen and Wu, 2011), in the Caspian Sea as a result of the imbalance between inflow from river discharge and precipitation versus evaporation (e.g., Chen et al., 2017b,a; Lahijani et al., 2023), in North India because of groundwater depletion (e.g., Rodell et al., 2009; Long et al., 2016), in West Africa driven by precipitation increase and East Africa due to water level increase of the larger lakes (e.g., Rodell et al., 2018), in the Indian Ocean near Indonesia as a result of the December 2004 Sumatra-Andaman earthquake (e.g., Han et al., 2006; Panet et al., 2007), and east of Japan due to the March 2011 Tohoku-Oki earthquake (e.g., Wang et al., 2012; Panet et al., 2018).

[9] `http://hydro.iis.u-tokyo.ac.jp/~taikan/TRIPDATA/Data/RBvect.html` (last accessed on 2025-04-23)

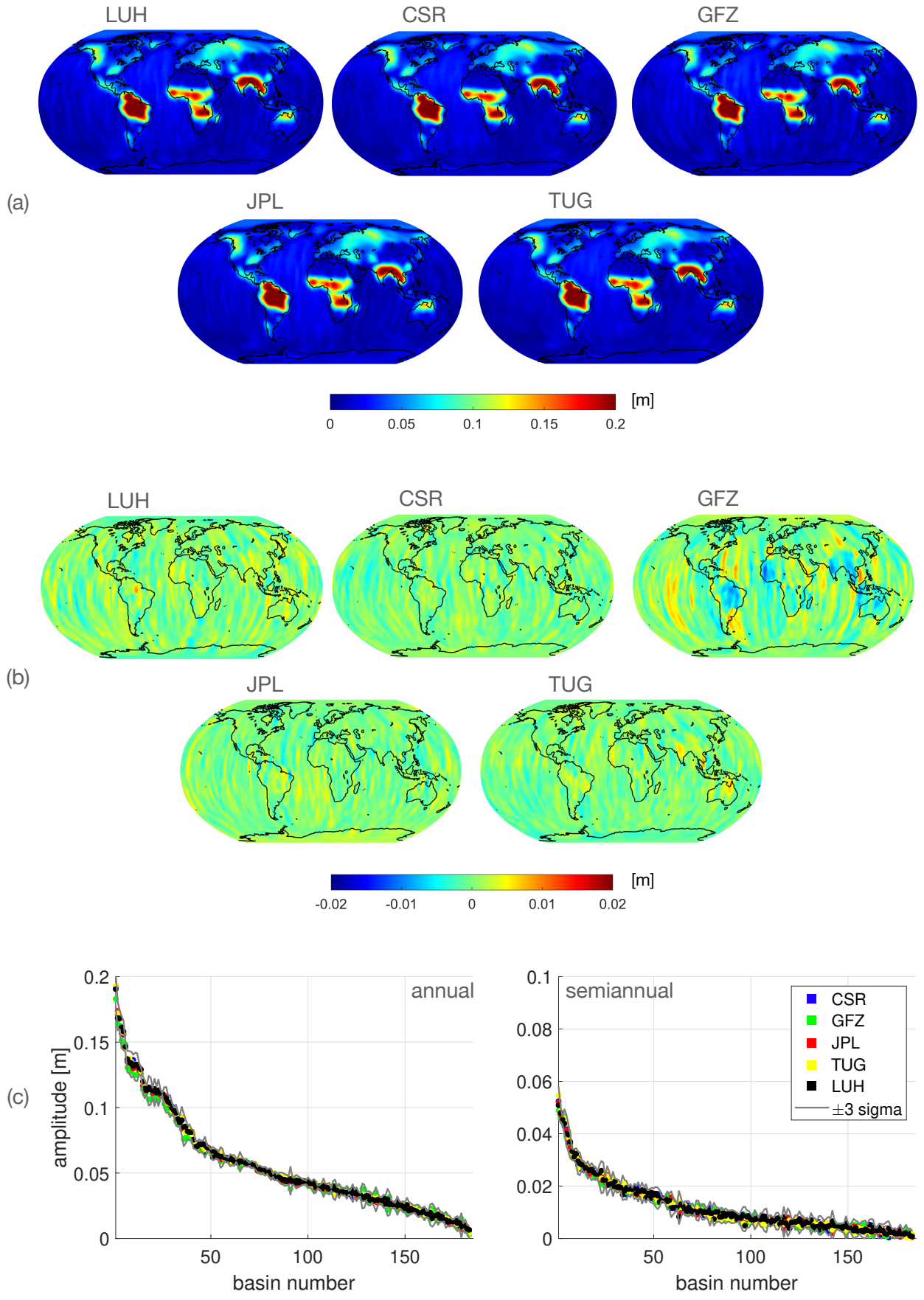

FIGURE 3.7: (a): Seasonal EWH ampitude (annual+semiannual components). In total, 216 monthly gravity fields from April 2002 to September 2023 are considered. (b): Differences relative to the mean seasonal amplitude of the five maps in (a). (c): Annual and semiannual amplitudes of around 180 river basins. Note that the river basin numbers of the annual and semiannual components do not correspond to each other.

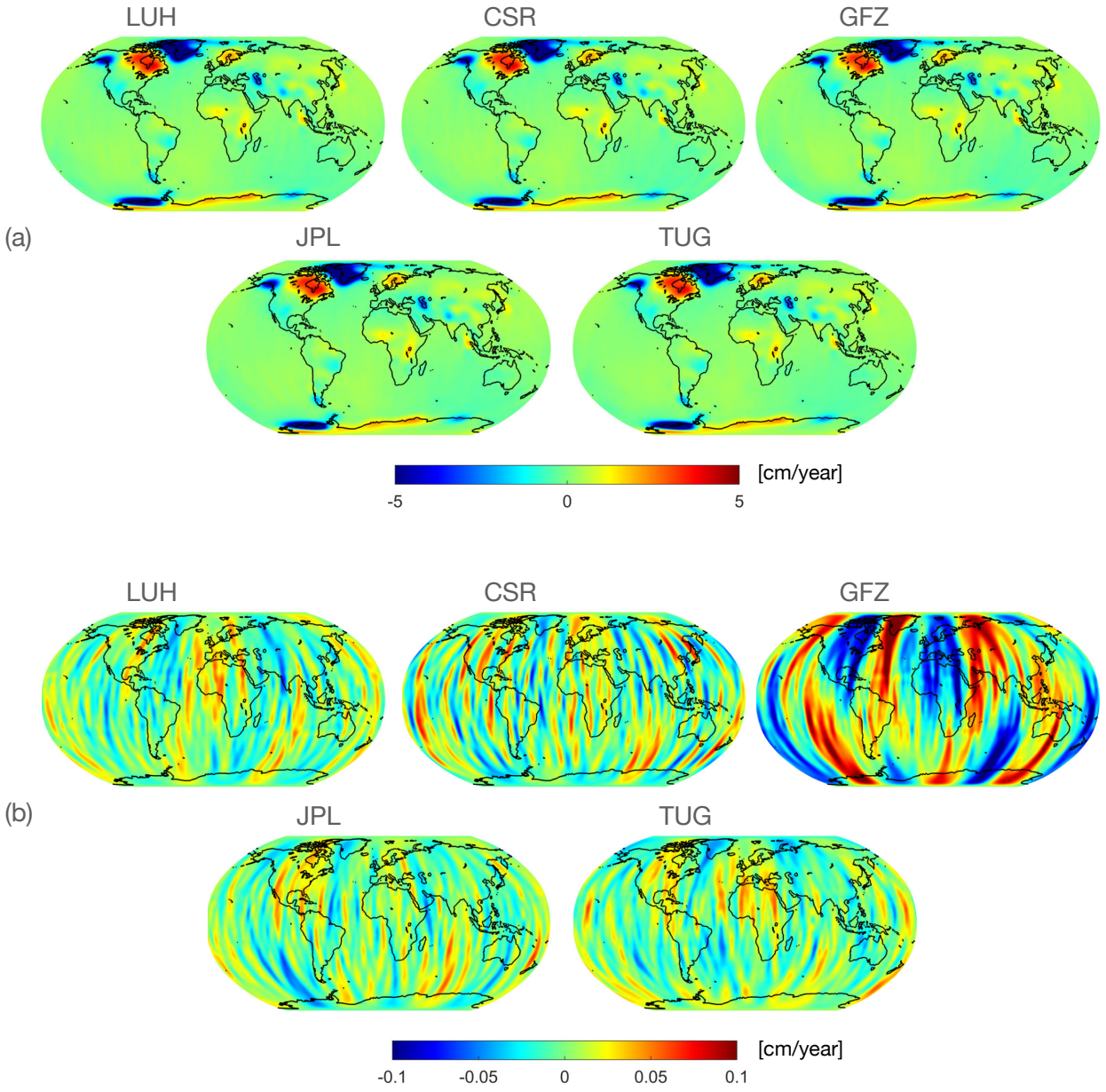

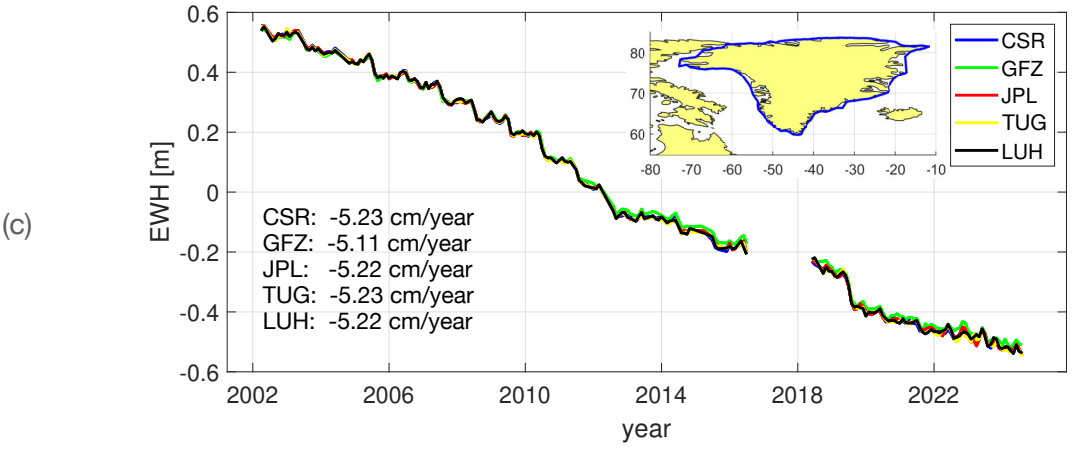

FIGURE 3.8: (a): Yearly EWH trend. In total, 216 monthly gravity fields from April 2002 to September 2023 are considered. (b): Differences relative to the mean trend of the five maps in (a). (c): Time series of EWH in Greenland. The EWH maps are Gaussian filtered with a smoothing radius of 400 km. No leakage correction applied.

Chapter 4

Ocean Tide Signatures in GRACE(-FO) K-Band Range-Rate Post-Fit Residuals

At the end of the previous chapter, the spectral and spatial noise, as well as the signal content, of the LUH monthly gravity field solutions were assessed, and compared to the corresponding gravity field recovery results of selected GRACE(-FO) analysis centers. As a byproduct of the estimation of the spherical harmonic coefficients of the gravitational potential, along with other ancillary parameters (e.g., the dynamic orbits and accelerometer calibration parameters), post-fit residuals are also obtained. The assessment of residual and unmodeled ocean tide signal in the 20+ years of GRACE(-FO) post-fit residuals data (Koch et al., 2024a) will be the subject of investigation in this chapter. By recalling Equation 3.51, which defines the reduced ll-SST observation vector as the difference between the observed and modeled range-rates, it becomes evident that the residuals must incorporate two categories of contributors:

1. *Instrumental*: effects associated with the sensor platform and its interaction with the environment, possibly also encompassing effects related to the conversion of low-level sensor data to L1B.
2. *Geophysical*: effects linked to the conversion from L1B to Level-2, including model errors of one of the effects listed in Table 3.3, or contributions from higher frequency signal not captured by the monthly spherical harmonic coefficients.

A specific effect that is part of the post-fit residuals might not always be clearly attributable to one of the two categories. The main subject of this chapter, i.e., the ocean tide signal, belongs to the second category of contributors. Taking into account the background model accelerations presented in Table 3.3 in the equations of motion of the satellites during the estimation process of the spherical harmonic coefficients of the gravitational potential, it is expected that the contribution of these specific effects would be reduced from the observations, in the case of error-free models, leading to a monthly solution containing only the conventionally defined contributions to the gravitational potential, i.e., mainly surface mass variations related to the hydrosphere and cryosphere, as well as the impact of non-tidal solid Earth mass variations. In such a case, besides sensor platform related contributions, the post-fit residuals might primarily contain the corresponding higher frequency signal components, e.g., submonthly hydrology. Yet, models inevitably include some inaccuracies due to their inherent limitations. In a rather theoretical best-case scenario, the model inaccuracies would manifest themselves solely as part of the post-fit residuals. More likely, however, is the complex case where a larger part of the inaccuracies is propagating to the post-fit residuals, and a smaller part is absorbed by specific parameters that are solved for during gravity field recovery, possibly including the spherical harmonic coefficients of the gravitational potential. The corresponding proportion between residuals and parameters will change if, for example, dedicated ocean tide parameters or empirical parameters with a high temporal resolution are co-estimated along with the gravitational potential and the secondary parameters. However, a complete absorption by the involved parameters, even when dedicated ocean tide parameters are co-estimated, appears unrealistic, simply due to the complexity of certain background model effects that need to be considered.

In terms of magnitude, ocean tides are not the most significant acceleration effects in orbit modeling, neither are they the most significant tidal effects, as can be clearly seen in Figure 3.4. The specific challenges in modeling ocean tides—particularly the rather complex dependence on various parameters in addition to the TGP, as well as the lack of globally available, accurate observations—were already discussed in Section 2.3. In comparison to the oceans, modeling the solid Earth's response to tidal forces is considerably simpler

(e.g., Agnew, 2009). While the disturbing potential due to solid Earth tides, where conventionally only degrees 2–4 need to be considered (see Section 3.3.2), has a rather global character, ocean tides have a distinctly more local spatial nature. This can also be seen very clearly in the acceleration magnitude time series presented in Figure 3.4, where the solid Earth tides have a highly periodic appearance along the orbit, with one cycle every half a revolution (≈45 min), whereas the ocean tides exhibit a much more complex pattern. Similarly complex patterns with relatively large magnitudes can only be observed in the time series of the non-gravitational acceleration, and non-tidal acceleration due to rapid mass variations in the oceans and atmosphere. Other tidal effects are one or several orders of magnitude smaller than the ocean tides. Based on this and considering that the more periodic an effect is, the more likely it is to be absorbed by the estimated dynamic or empirical parameters, one can hypothesize that ocean tides are the main contributor to the post-fit residuals at tidal frequencies.

The most significant residual signals from ocean tides are anticipated at frequencies of roughly one to two cycles per day (compare Table 2.4). These high-frequency errors are affecting the orbit modeling quality and therefore also the quality of the derived GRACE(-FO) gravity field products; however, the gravity field solutions are not suitable for detecting these kind of high-frequency errors due to the monthly sampling of the solutions. Theoretically, only a limited number of tidal constituents with known aliasing periods (see e.g., Ray and Luthcke, 2006; Seo et al., 2008)—according to the Nyquist–Shannon sampling theorem, those with periods ≥60 days—might be detectable in the monthly gravity field solutions if the tidal signal is absorbed by the spherical harmonic coefficients of the gravitational potential during gravity field recovery. An analysis of the post-fit residuals or similar quantities derived from the high-frequency ranging measurements of GRACE(-FO) is more suitable for analyzing ocean tide signal.

Section 4.1 describes the procedures used to derive the Lomb–Scargle periodograms, which will be used later to assess the residual and unmodeled ocean tide signals in the GRACE(-FO) K-band range-rate post-fit residuals. In Section 4.2, a general sampling scheme of periodic signal by the GRACE(-FO) satellites is derived, which will later be useful to interpret the obtained Lomb–Scargle periodograms. To get a more global view on the most important periods in the Lomb–Scargle periodograms of the ll-SST post-fit residuals, criteria for the extraction of "important" periods from the periodograms are introduced in Section 4.3. In Section 4.4, the spectral alignment of the extracted information from the periodograms with known ocean tide periods is assessed. Spatial characteristics of the identified tidal information are studied in Section 4.5.

4.1 Lomb–Scargle Periodograms of ll-SST Post-Fit Residuals

To derive the Lomb–Scargle periodograms, which will be used in subsequent sections as input to assess residual and unmodeled ocean tide signal in the GRACE(-FO) ll-SST data, the following steps are applied:

1. Low-pass filtering of the range-rate post-fit residuals to suppress the K-band system noise
2. Numerical differentiation of the low-pass filtered range-rate post-fit residuals to obtain residual range-acceleration, which is better suited for localizing mass variations
3. Assigning of the residual range-acceleration to a global grid based on the geographical coordinates of the satellites
4. Spectral analysis of the times series of each grid cell using Lomb–Scargle periodograms.

The following three subsections provide details on these steps and present illustrative periodograms.

4.1.1 Low-Pass Filtering Range-Rate Post-Fit Residuals

Range-rate post-fit residuals can be regarded as a complex superposition of effects reflecting the discrepancies between the measured satellite-to-satellite tracking quantities and the dynamically modeled counterparts.

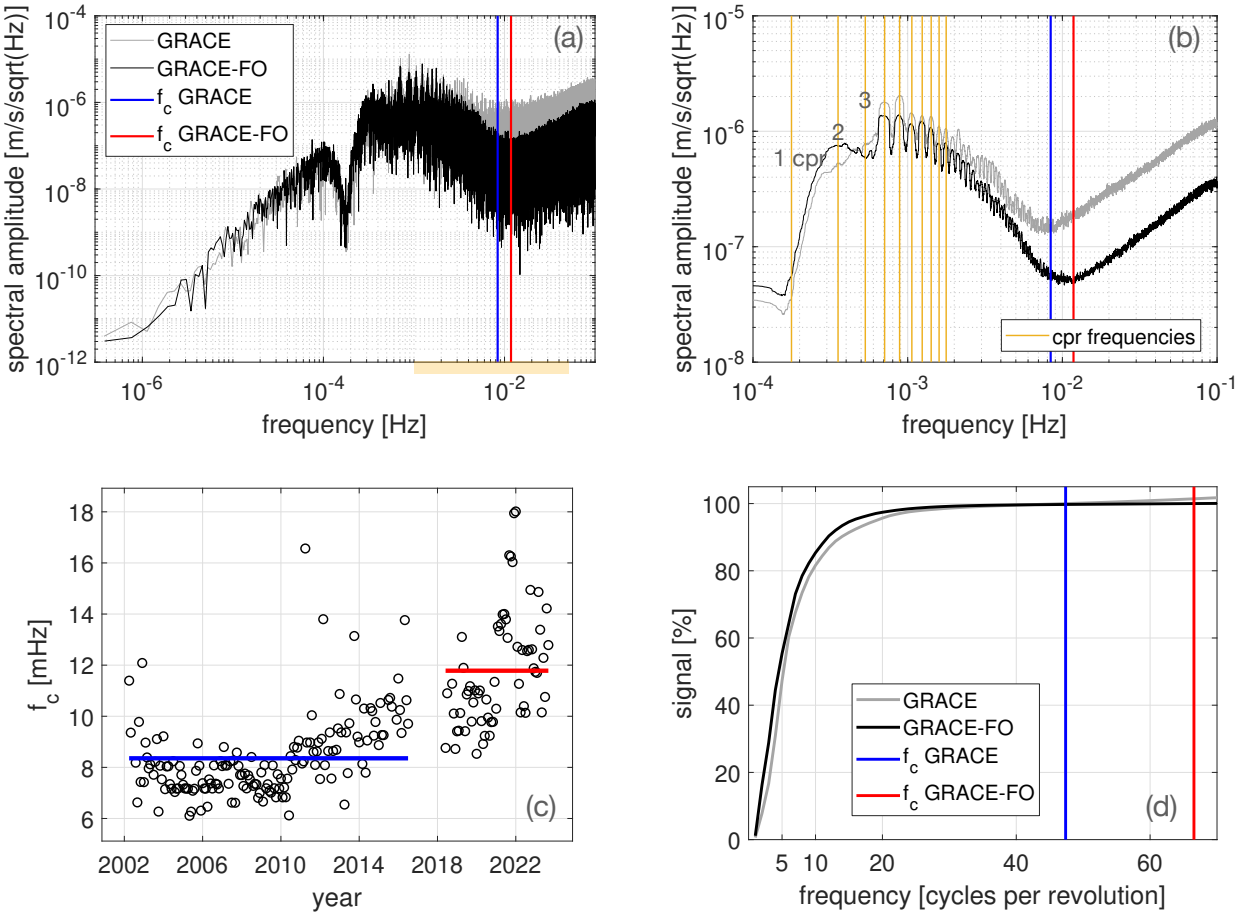

FIGURE 4.1: (a): Periodogram amplitude spectral density estimate of two monthly batches of range-rate post-fit residuals. Gray: GRACE (January 2008), black: GRACE-FO (January 2021). The frequencies from 1 to 50 mHz are highlighted in yellow. (b): Moving average filter smoothed periodogram showing the frequency range from 0.1 mHz to 0.1 Hz. Yellow lines represent the frequencies of 1 to 10 cycles per orbital revolution (cpr). (c): Monthly low-pass filter cut-off frequencies f_c. Mean f_c is 8.4 mHz (GRACE, blue) and 11.8 mHz (GRACE-FO, red). The mean f_c are also indicated in the other panels. (d): Cumulative percentage of signal as a function of cpr frequency. 100% are assumed at the respective cut-off frequencies. Panels (a) and (c) taken from Koch et al. (2024b, Figure 1).

On the one hand, there are effects of an instrumental nature, e.g., reflecting expected characteristics of the individual sensors (instrumental noise), or systematic effects related to varying orbit characteristics and the interaction of the sensor platform with the environment. As mentioned above, on the other hand, the range-rate post-fit residuals will contain contributions of geophysical nature, e.g., because the geophysical background models are not free of modeling errors, and because higher frequency gravity signal cannot be sampled by the estimated monthly gravity field solutions. In the range-rate post-fit residuals of a monthly gravity field solution, these two categories of effects are observed to dominate different frequency ranges.

Figure 4.1a depicts typical periodogram ASD estimates (see Equation 2.87) of two monthly range-rate post-fit residuals batches (GRACE: January 2008, gray; GRACE-FO: January 2021, black). A drop in power for the frequencies of approximately 0.18 mHz (one cycle per orbital revolution, 1 cpr) and smaller can be observed, which is the result of the co-estimation of empirical kinematic range-rate parameters, that absorb a large part of the orbit modeling error (including contributions from background model inaccuracies) and therefore contribute to the quality of the monthly gravity field estimates. Geophysically meaningful signal, such as residual tidal and non-tidal mass variations, is anticipated to be the dominant feature in the somewhat higher frequencies, especially around 2–8 cpr where the largest spectral amplitudes are to be found (see Figure 4.1b). However, at a frequency of approximately 10 mHz, the KBR system noise becomes

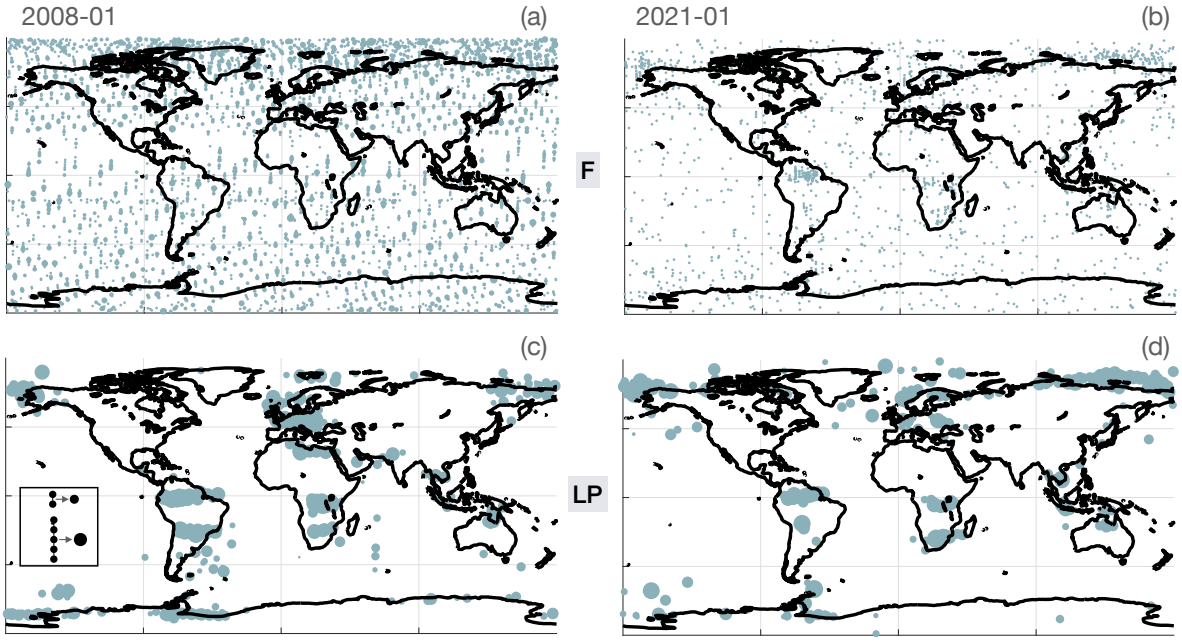

FIGURE 4.2: Location of range-rate post-fit residuals larger than three times the standard deviation with respect to the mean of full (F) and low-pass (LP) filtered signal. Left: GRACE (January 2008), right: GRACE-FO (January 2021). Continuous arcs, where the time difference between two consecutive epochs is 5 seconds, were reduced to midpoints, with the size of the midpoint set to be proportional to the arc length, as schematically shown in panel (c).

increasingly dominant. As previously mentioned, to separate geophysically meaningful signal from the KBR system noise and other known systematic effects, the range-rate post-fit residuals have to be low-pass filtered.

A suitable cut-off frequency f_c is close to 10 mHz and can be approximated as the frequency of the smallest spectral amplitude of a monthly data set of residuals in the frequency band from 1 to 50 mHz (frequency range is highlighted in yellow in Figure 4.1a). A time series of corresponding monthly cut-off frequencies, which range between 6 and 18 mHz, is shown in Figure 4.1c. Before determining the minimum amplitude frequency, the rather noisy periodogram spectral amplitudes were smoothed with a moving average filter (cf. Figures 4.1a and 4.1b) to ensure a more reliable minimum estimation. The average f_c value for the GRACE period is 8.4 mHz, while a slightly larger value of 11.8 mHz is observed for the GRACE-FO period, demonstrating a less noisy KBR system performance on the follow-on mission (e.g., Landerer et al., 2020; Koch et al., 2021). As the contribution to the total amplitude of the geophysically meaningful signal decreases with increasing frequency (see Figure 4.1d), these mission-specific cut-off frequencies are taken for the further analysis.

Figure 4.2 demonstrates the impact of low-pass filtering in extracting geophysically meaningful signal. The blue dots in the two upper maps display the locations of the epoch-wise residuals with amplitudes that exceed the mean value of the monthly time series by more than three standard deviations. Continuous arcs with a 5-second interval between consecutive epochs were reduced to their geographical midpoints, and the dot size was adjusted to be proportional to the arc's length. For residuals that solely reflect the K-band system ranging noise, one would expect to see small points relatively uniformly distributed across the globe, similar to what is depicted in Figure 4.2b. In fact, Figure 4.2b additionally reveals subtle clusters of small points, particularly over the Amazon Basin and the Arctic, suggesting that the noise of the KBR system on GRACE-FO does not entirely dominate the post-fit residuals, thereby allowing geophysical effects to become apparent. In contrast, the map of the GRACE range-rate post-fit residuals time series in Figure 4.2a displays a more homogeneous global distribution of points, suggesting that the post-fit residuals are primarily influenced by instrumental effects. However, the points are larger than those in Figure 4.2b, which indicates that the KBR system noise is not the most dominant effect in the time series. Indeed, in the examined month, the values that exceed the threshold of three sigma are related to instrument systematics

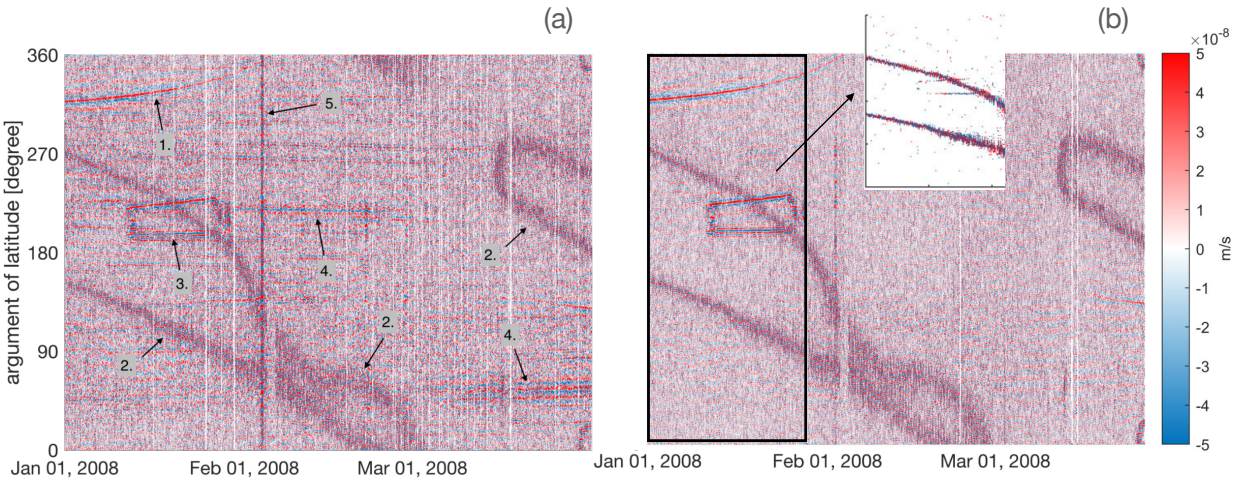

FIGURE 4.3: Time vs. argument of latitude plot of K-band range-rate post-fit residuals band-pass filtered from 5 to 20 mHz. Panel (a) is taken from (Koch et al., 2021, Figure 4) and shows post-fit residuals of an older time series of LUH solutions (Koch et al., 2020), while the post-fit residuals in (b) were computed according to the procedure described in Chapter 3. The zoom view in (b) depicts the unfiltered post-fit residuals for January 2008 exceeding three times the standard deviation.

(more context in next paragraph). The two maps in Figure 4.2c,d refer to the low-pass filtered range-rate post-fit residuals. Clusters, which are heterogeneously distributed across the globe, can be identified in regions where unmodeled geophysical effects can be expected. The larger size of the points is also evident, which aligns with expectations for unmodeled geophysical effects distorting the satellite motion significantly over several dozens of seconds. The maps in Figure 4.2 indicate that the post-fit residuals contain extractable information about geophysical effects. Depending on the highlighted region, unmodeled hydrology, ocean tide errors, or other effects might be the cause, although this cannot be readily inferred from the maps. To gain a more detailed understanding of the potential causes, it is necessary to examine longer time series using more suitable tools, as will be presented in the following sections.

Figure 4.3 depicts several effects of instrumental kind in diagrams that plot time against the argument of latitude, using data from three months of band-pass filtered (5–20 mHz) range-rate post-fit residuals. The argument of latitude is the geocentric angle measured between the ascending node of the satellite orbit and the position of the satellite (see e.g., Seeber, 2003), and is 0° or 180° at the equator, 90° at the North Pole and 270° at the South Pole. While the post-fit residuals in Figure 4.3b refer to the gravity field recovery processing scheme outlined in Chapter 3, panel (a) shows the post-fit residuals that correspond to the LUH-GRACE2018 time series, i.e., a previous release of solutions (Koch et al., 2020). The following systematic effects are highlighted with numbers in Figure 4.3a: (1) increased residuals at transitions of the satellites from light into Earth shadow and vice versa, the origin of which has not been fully clarified (see e.g., Behzadpour et al., 2019); increased residuals at frequency-related (2) and star camera baffle-related (3) signal-to-noise ratio drops of the KBR system (see Harvey et al., 2017; Goswami et al., 2018; Behzadpour et al., 2019); increased residuals (4) possibly related to the star camera assembly (Koch et al., 2021); and (5) increased residuals related to bad sensor data affecting the whole involved arc.

The time vs. argument of latitude diagram of the post-fit residuals computed with the presented updated procedure, including more recent background models, as well as KBR system and star camera data, shows overall smaller amplitudes. The earlier mentioned systematic effects remain in the post-fit residuals of the reprocessed gravity field solutions time series, with the exception of effect (4). It can be assumed that this systematic effect no longer appears due to the use of the improved sensor data (L1B RL03 instead of RL02). The RL03 sensor data products (PO.DAAC, 2018) were corrected for the stellar aberration error, and the star camera quaternion combination was revised (Bandikova and Flury, 2014). The improved star camera

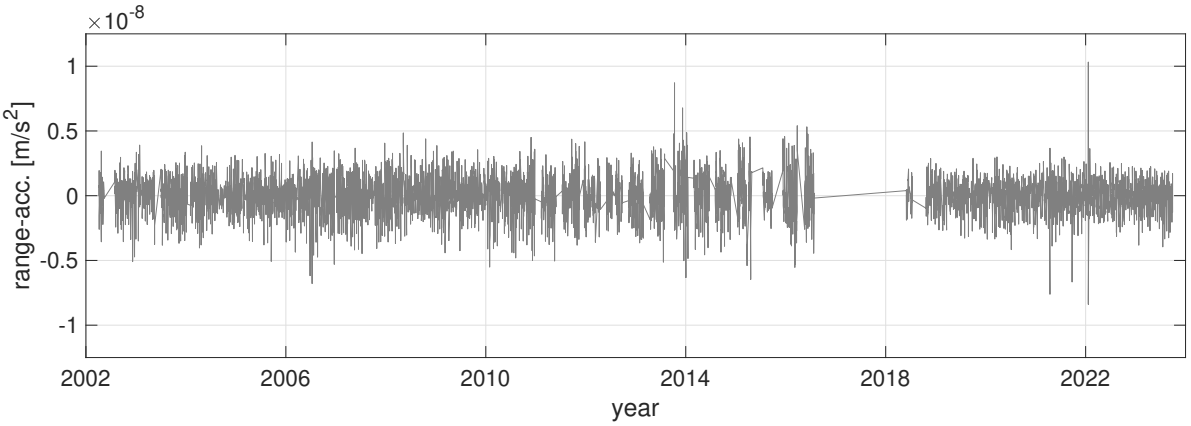

FIGURE 4.4: Exemplary time series of residual range-accelerations for a grid cell in the Weddell Sea.

products led also to a reprocessing of the KBR products. While the light-shadow transition effects are masked by the KBR system noise in the unfiltered post-fit residuals, the effects related to the signal-to-noise ratio drops of the ranging system (effects 2 and 3) are evident, displaying generally higher amplitudes than the typical noise level. This is illustrated in the zoomed view of Figure 4.3b and accounts for the previously mentioned pattern in Figure 4.2a.

Apart from the patterns related to eclipse transitions, GRACE-FO K-band range-rate post-fit residuals in the 5 to 20 mHz frequency band do not show any of the previously mentioned systematic errors (cf. Koch et al., 2021, Figure 4d). Duwe et al. (2024) studied band-pass filtered GRACE-FO LRI range-rate post-fit residuals and found the presence of the eclipse patterns also in the LRI post-fit residuals. Despite this, several other previously unknown effects were detected, which are not accessible in the K-band post-fit residuals due to the larger noise level.

4.1.2 Residual Range-Accelerations

Compared to range-rates, range-acceleration is more suitable for the further analysis of geophysical effects in the residual ll-SST data. This is because range-acceleration shows peak amplitudes directly over the causative mass anomalies, even though it may exhibit small sidelobes, as shown, for example, in Figure 1 of Ray et al. (2009). Since acceleration is the rate of change of the velocity with respect to time, residual range-acceleration can be obtained by numerically differentiating the previously filtered range-rate post-fit residuals. It is preferable to perform the low-pass filtering before numerical differentiation, since the differentiation process will amplify the high-frequency components of the input signal, i.e., will increase the high-frequency noise. An overview of various numerical differentiation techniques can, for example, be found in Hoffman (2001). The numerical derivative of a discrete time series can be obtained by approximating the data with a suitable function, followed by an analytical differentiation of that function.

A suitable approximating function is, for example, the polynomial function. In this thesis, the numerical differentiation of the residual ll-SST data is performed by fitting polynomials of degree 6 to short pieces consisting of 7 filtered range-rate post-fit residuals (evaluation point in the center ±3 epochs). Polynomial functions of even degrees 4 through 10 were evaluated, and all exhibited a similar fitting quality. The unknown polynomial coefficients describing the shape of the approximating function can be obtained using unweighted least squares adjustment (see Equation 3.40). A smoothing effect can be achieved by incorporating a few additional epochs into the estimation process. The estimated polynomial function is then differentiated with respect to time to get the residual range-acceleration of an evaluation point.

The obtained residual range-acceleration time series is then examined for large amplitude spikes, which may occur due to discontinuities in the approximated segment or poor sensor data quality. Typically, the range-acceleration values vary between $\pm 5 \times 10^{-9}$ m/s^2, as shown in Figure 4.4 for an exemplary time series. Absolute values exceeding 1.5×10^{-8} m/s^2 were excluded from the further analysis.

Grid Cell Size	Mean N	Min. p [d]
1°×1°	1542	10.78
2°×2°	6169	2.54
3°×3°	13881	1.13
4.5°×4.5°	31233	0.50
5°×5°	38559	0.41
7.5°×7.5°	86758	0.18
10°×10°	154237	0.10

TABLE 4.1: Mean N: average number of observations for approximately 21.5 years of 5-seconds sampled ll-SST data; Min. p: approximate resolvable minimum period.

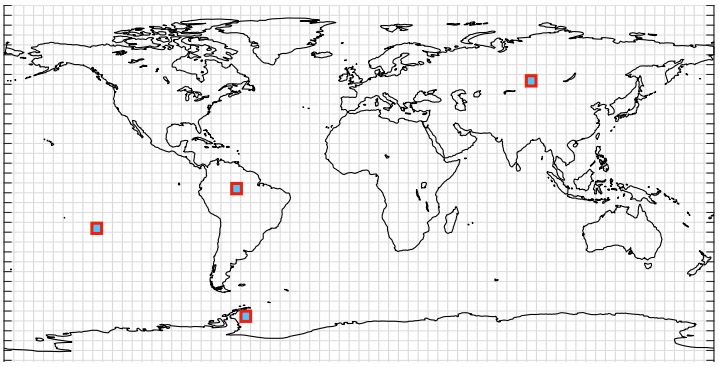

FIGURE 4.5: Global 5°×5° grid. Exemplary Lomb–Scargle periodograms of the four highlighted grid cells are shown in Figure 4.6.

4.1.3 Periodograms of Gridded Residual Range-Accelerations

In order to perform a spatio-spectral analysis, the residual range-acceleration data, which is nominally sampled every 5 seconds, can be grouped into grid cells of suitable size. The midpoint between the two satellites is considered as the location of the measurement, and the corresponding geographical longitude and latitude is used to assign the data to a specific grid cell. The number of observations within a grid cell depends on several factors, with the most significant being the chosen grid cell size (see Table 4.1). Other important factors are:

- The latitudinal location of the grid cell: The actual area covered by a cell decreases as its longitudinal distance from the equator increases. Consequently, satellites are able to gather more data over a cell located near the equator compared to one near the poles.
- The actual ground tracks, which are determined by the characteristics of the satellite orbit and satellite dynamics: The nearly polar inclination of the satellite orbits results in measurements that cover nearly all latitudes. Since the ground tracks of the GRACE(-FO) satellites converge in the polar regions, polar cells show a higher frequency of overflights; however, since the satellites pass over these cells much faster, the number of assigned measurements is lower compared to those near the equator. Furthermore, resonant orbit periods (e.g., Wagner et al., 2006; Klokočník et al., 2015) can significantly reduce the ground track coverage. This causes longitude dependent variations in observation availability.
- Sensor data availability: Although smaller gaps in the accelerometer or star camera data can be filled through interpolation, allowing for the calculation of a gravity field solution and corresponding range-rate post-fit residuals, larger gaps—sometimes lasting several days—prevent the calculation of the residuals, even when the ll-SST data remains uninterrupted. However, larger gaps in the KBR data are also not uncommon. Additionally, in order to obtain a good gravity field product, a screening process is employed during the generation of the monthly gravity field solutions to exclude poor-quality sensor data from the calculations.

Since the assumption of a uniform time sampling does not hold true for the gridded time series of residual range-accelerations, the classical FFT-based periodogram method (see Section 2.4.1) is unsuitable for a following spectral analysis without preceding data manipulations. To address the irregularly sampled time series without necessitating prior interpolation, the periodogram $P(f)$ is computed using the Lomb–Scargle method (Equation 2.89). In principle, the periodogram can be evaluated at any specified frequency f. More common is to evaluate the periodogram at frequencies $f = \overline{n}/(oNT_s)$, where $\overline{n} = \{1, ..., oN/2\}$ is the frequency number, which is dependent on the number of observations N of the time series and the oversampling factor o; and $T_s = T/(N-1)$, where T is the total time interval (approximately 21.5 years). In general,

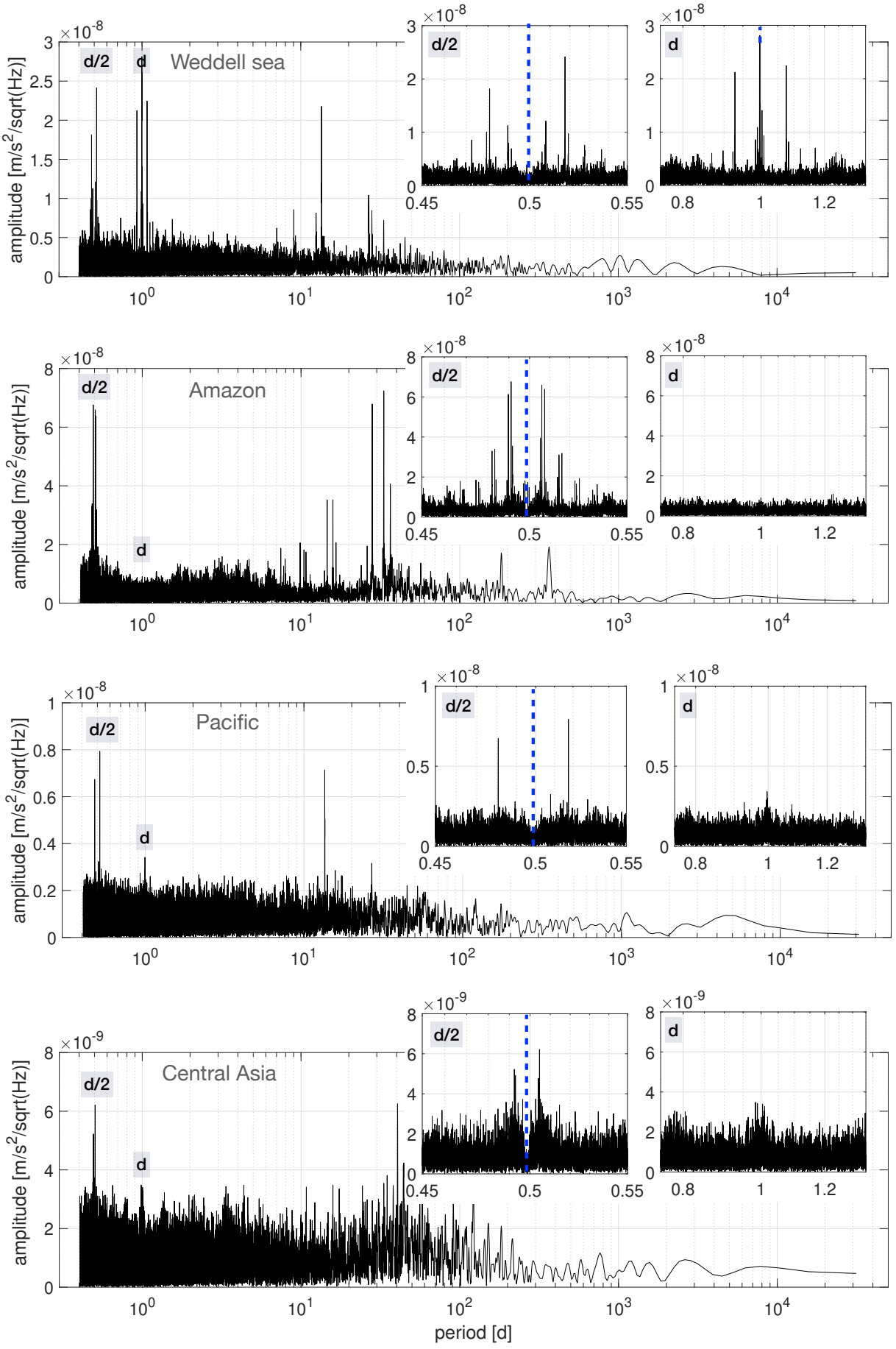

FIGURE 4.6: Exemplary Lomb–Scargle periodograms of the residual range-acceleration time series in the four grid cells highlighted in Figure 4.5. Due to the applied oversampling factor the largest periods exceed the length of the analyzed time series (21.5 years).

the periodogram at these frequencies can be computed much more efficiently than at frequencies of a self-arranged frequency array (Press and Rybicki, 1989). Using the oversampling factor enhances the frequency resolution of the periodogram, without introducing any new information into the frequency spectrum. In this study, an oversampling factor of 4 was selected.

With the chosen set of frequencies, the smallest resolvable period depends on the number of observations N within a specific grid cell and the time interval T of the corresponding time series. Table 4.1 provides an overview of the approximate minimum resolvable period for different grid cell sizes. Largest tidal contribution can be expected in the diurnal and semidiurnal bands. To resolve these important bands in the periodograms, at least a 5°×5° grid cell size is required. As will be demonstrated in the next section, despite the limit of 0.41 days, signal with a shorter period can still be assessed indirectly in the diurnal and semidiurnal bands via spectral replication.

Exemplary periodograms ($\sqrt{P_f}$, Equation 2.89) for grid cells in the Weddell Sea, the Amazon basin, the Pacific Ocean and central Asia are shown in Figure 4.6. The exact location of these grid cells is depicted in Figure 4.5. The following can be recognized in these exemplary periodograms:

- The magnitudes of the spectral amplitudes vary significantly across the exemplary regions. Please note the different upper limits of the y-axes. Largest peaks are present in the periodogram of the Amazon basin grid cell. The Amazon river basin is known for having one of the largest seasonal mass variations related to hydrology among all river basins. Relatively large are also the peaks in the periodogram of the Weddell Sea grid cell. The Weddell Sea is a challenging region for ocean tide modeling due to several factors, including scarce observations, shallow waters, complex coastlines, and the presence of ice. Smaller spectral amplitudes are observed in the other two regions, which appears to be realistic, as much weaker mass variations are expected there.

- The peaks are located in the diurnal and/or semidiurnal bands, i.e., in bands where mass variations due to tidal phenomena are expected; but also peaks at longer periods can be observed.

- A symmetric arrangement of the peaks with slightly different amplitude values can be recognized in the diurnal and semidiurnal bands. The aforementioned axial symmetry (the dashed blue lines in Figure 4.5 represent the apparent reflection axes) is caused by the presence of additional peaks, so-called spectral replicas due to the irregular signal sampling by the satellites.

4.2 Irregular Sampling of Periodic Signal by GRACE(-FO)

In the previous section, periodograms of four grid cells were presented, highlighting a symmetric arrangement of peaks in the diurnal and/or semidiurnal bands. Although tidal effects also exhibit symmetries (see the arrangement of peaks of the TGP in Figure 2.7), the observed symmetric pattern in the periodograms is related to a different effect: the presence of *spectral replicas* caused by the irregular sampling of geophysical signal by the GRACE(-FO) satellites. Figure 4.7 shows how the satellites sample simulated sinusoidal signal with periods of the K_1 (≈0.9973 d), S_2 (≈0.5000 d), R_3 (≈0.3330 d) and M_4 (≈0.2588 d) constituents at time of overflights in two 5°×5° grid cells. One grid cell is situated near the equator (upper panel), while the other near the South Pole (bottom panel). Lomb–Scargle periodograms corresponding to the individual time series illustrated in Figure 4.7 are presented in Figure 4.8. For the diurnal and semidiurnal constituents, the periodograms reveal peaks not only at the periods of the two constituents but also multiple peaks throughout the spectrum. In the periodograms of R_3 and M_4, the original periods of the constituents cannot be observed since the smallest resolvable period is around 0.41 days (see Table 4.1); nevertheless, the sampling of these higher frequency signals results in multiple peaks appearing at various periods within the periodogram.

The sampling of the sinusoidal time series by the satellites results in a frequency ambiguity. The originally unambiguously defined signal (one frequency and amplitude) can be approximated by sine waves of different—but not random—frequencies, which leads to additional peaks being visible in the periodograms.

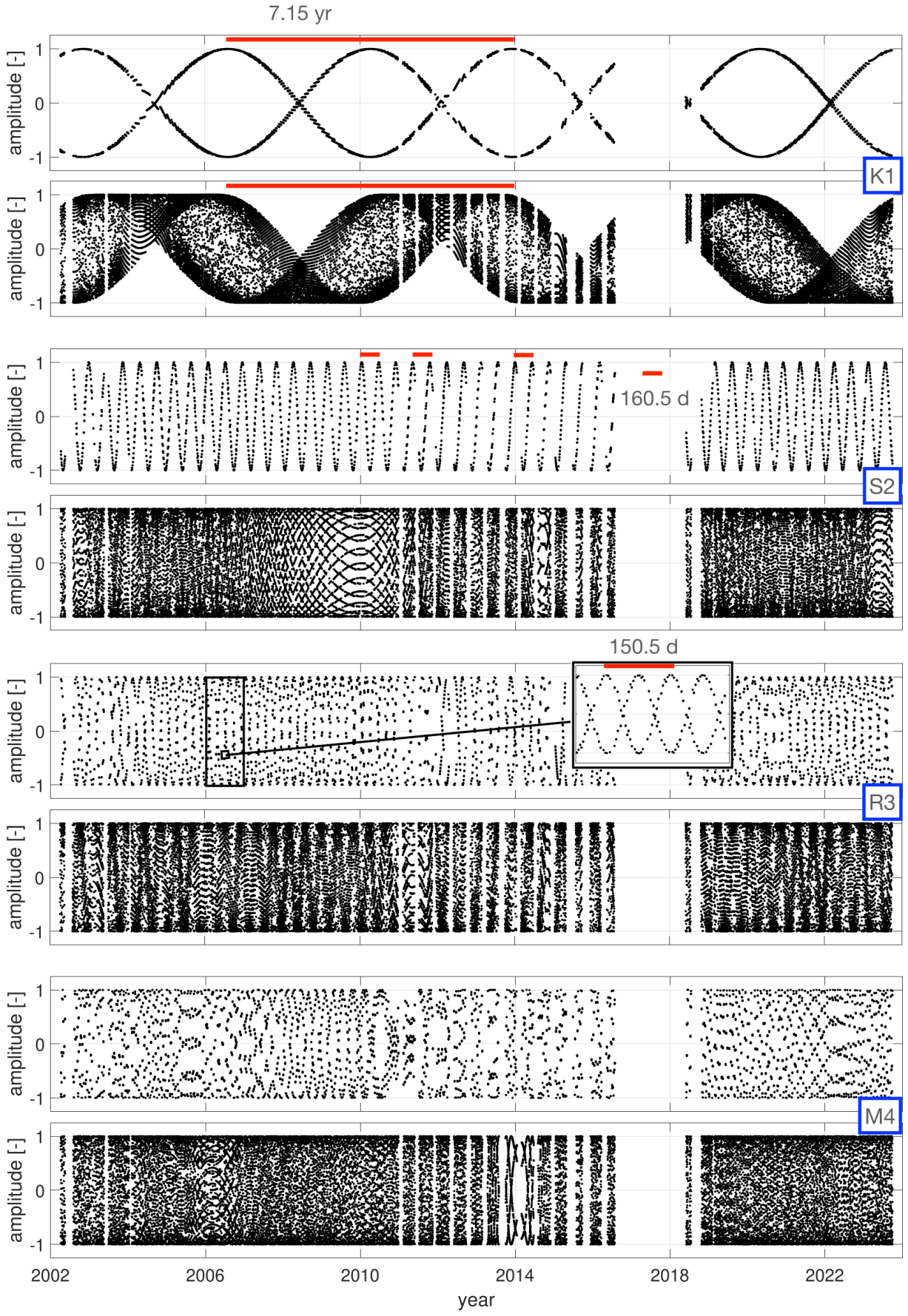

FIGURE 4.7: Continuous sinusoids with the frequencies of K_1, S_2, R_3 and M_4 waves irregularly sampled by the GRACE(-FO) satellites at a 5°×5° grid cell near the equator (upper panels) and near South Pole (bottom panels). d: days, yr: years. See, for example, also Mayer-Gürr et al. (2012, Figure 3).

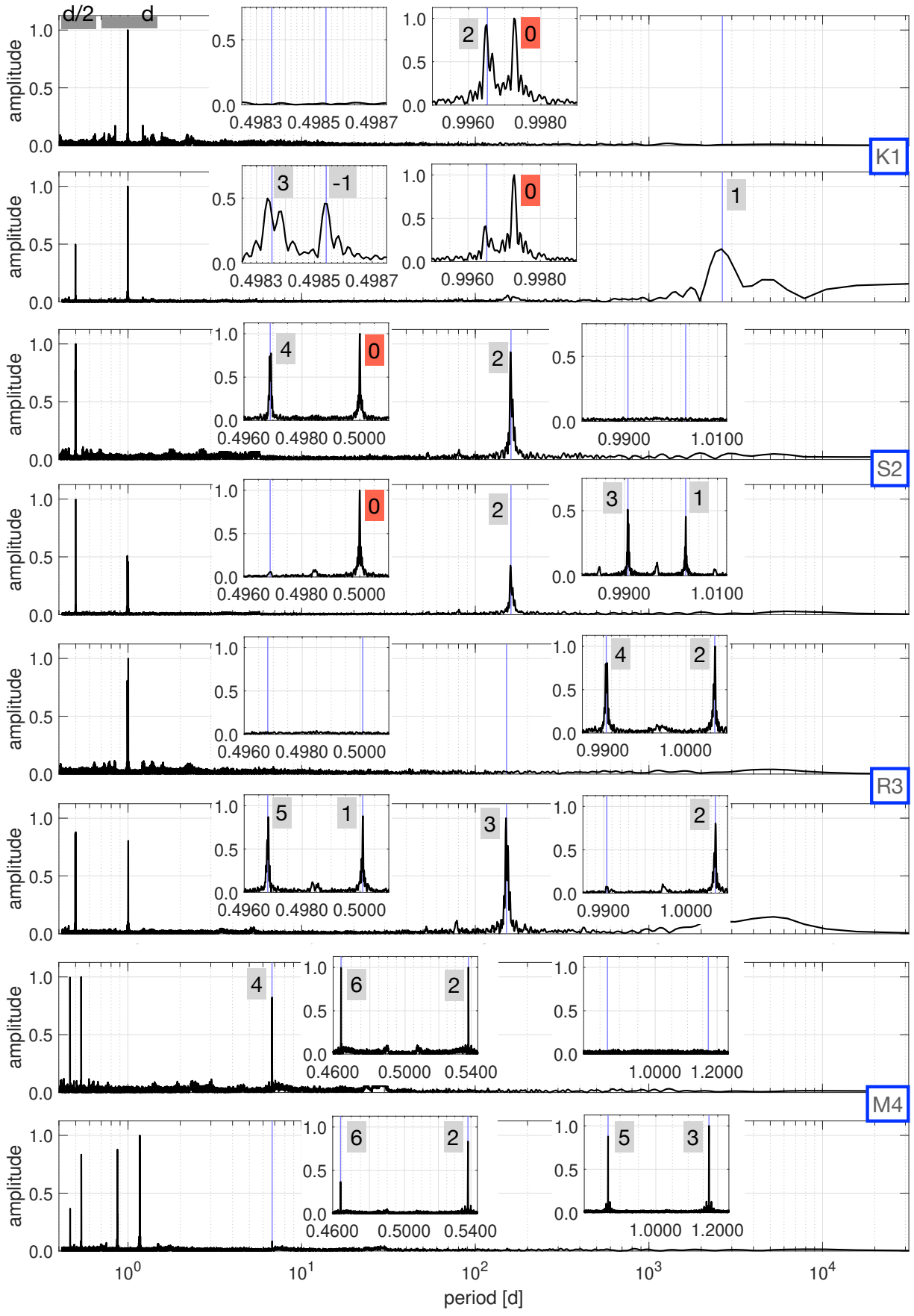

FIGURE 4.8: Lomb–Scargle periodograms of the time series from Figure 4.7. Blue vertical lines represent the spectral replica periods computed with Equation 4.1 and the sampling frequency as defined in Equation 4.2. Numbers next to the peaks depict the corresponding integer multiples n (gray box). The peak at the original period of the constituent is highlighted with a 0 (red box). d: diurnal band, d/2: semidiurnal band. Spectral amplitudes have been normalized such that the maximum value is 1.

Some of the additional longer periods can be easily identified in the equator grid cell time series without any spectral analysis, e.g., a 7.15 years (K_1), 160.5 days (S_2) and 150.5 days (R_3) period (see Figure 4.7). In general, these additional peaks of a frequency f can be expected at frequencies:

$$f_{\mathrm{A}} = |nf_s - f|\,, \quad n \in \mathbb{Z}, \quad n \neq 0 \tag{4.1}$$

where f_s is the signal sampling frequency and n an integer multiple (see e.g., Lyons, 2004; Vetterli et al., 2014; Liu, 2019).[1] For the case $n = 0$, f_A has the same value as the original frequency f.

4.2.1 Sampling Frequency

The orbital planes of the GRACE(-FO) satellites sample the surface of the Earth with a time-varying frequency (e.g., Ray and Luthcke, 2006; Liu and Sneeuw, 2021):

$$f_s = \omega - \dot{\Omega} \tag{4.2}$$

where $\omega = 360.9856\,^\circ/\mathrm{d}$ (IERS Conventions, 2010) is the sidereal rotation rate of the Earth, i.e., the angular speed at which the Earth rotates with respect to the inertial space; and $\dot{\Omega}$ denotes the eastward nodal precession rate of the orbital planes, resulting from the Earth's non-uniform mass distribution, which can be approximated by the primary gravity field term, i.e., the degree-2 zonal C_{20} coefficient. The nodal precession rate due to the flattening term is dependent on the orbit inclination i, orbit eccentricity e, orbital plane semimajor axis a, Earth's semimajor axis R, and angular velocity of satellite's motion n (e.g., Seeber, 2003):

$$\dot{\Omega} = C_{20}\frac{3}{2}\frac{nR^2}{a^2(1-e^2)^2}\cos i\,. \tag{4.3}$$

The mean nodal rate of GRACE(-FO) is illustrated in Figure 4.9. Precession occurs in the direction opposite to that of the orbital revolution. Because of the prograde orbits of the satellites, the precession of the node is westwards, i.e., $\dot{\Omega}$ is negative. The values are approx. $-0.135\,^\circ/\mathrm{d}$ at the beginning of the GRACE and GRACE-FO operation time and, due to the decreasing altitude, reach a value of $-0.145\,^\circ/\mathrm{d}$ at the end of the GRACE mission. The average nodal precession rate is approx. $-0.136\,^\circ/\mathrm{d}$ (GRACE) and $-0.135\,^\circ/\mathrm{d}$ (GRACE-FO).

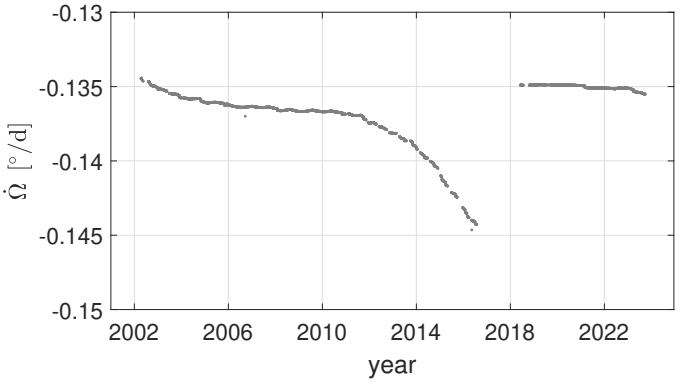

FIGURE 4.9: Nodal precession rate $\dot{\Omega}$ of GRACE(-FO).

Accordingly, the signal sampling frequency f_s is approximately $361.126\,^\circ/\mathrm{d}$, which corresponds to a period of 0.996882 days. The period of this sampling frequency, along with the period of $2f_s$, act as the reflection axes around which the peaks in the earlier shown periodograms are symmetrically arranged to the left and right (see Figure 4.8). However, this symmetry is slightly distorted by the latitudinal dependence of the GRACE(-FO) sampling characteristics (as discussed in the next section) and the phase shift between missions in the orbital plane movement. This distortion is evident in the periodograms as a double peak at

[1] With the mission-specific sampling frequencies, the altimetry aliasing periods (Equation 2.65) can also be computed with Equation 4.1 as $1/\max(f_{\mathrm{A}})$.

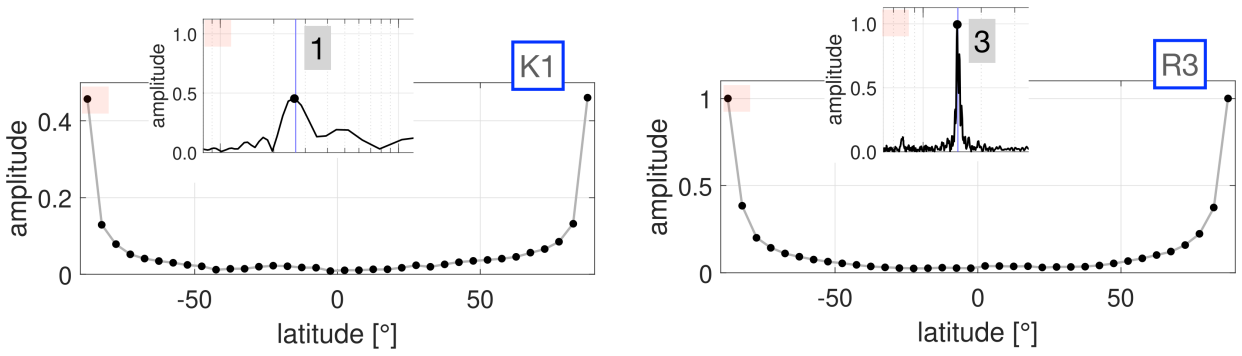

FIGURE 4.10: Spectral amplitudes at the aliasing periods of K_1 and R_3 at different latitudes. See Figure 4.8 for context.

$n \neq 0$, consisting of a primary peak and a nearby smaller peak. It can be best seen in the zoom views of K_1 in Figure 4.8, but is also present at other frequencies.

4.2.2 General Sampling Scheme

The specific integer multiples n in Equation 4.1 at which spectral replicas occur depend on the signal frequency and how it is sampled by the GRACE(-FO) satellites. In the periodograms of the sinusoidal signal in Figure 4.8, spectral replicas emerge for $n = \{-1, 1, 2, 3, 4, 5, 6\}$. A special case is when $n = m$, where m is the tidal species (see Section 2.3.1). For this case, f_A has the smallest value for any $n \in \mathbb{Z}$, and the equation represents the GRACE(-FO) aliasing periods (e.g., Ray and Luthcke, 2006; Liu and Sneeuw, 2021).

By systematically repeating the experiment shown in Figures 4.7 and 4.8 across all grid cells for any diurnal or semidiurnal constituent, it can be demonstrated that the majority of periodograms will exhibit a similar peak distribution as seen in the equator panels of Figure 4.8. The integer multiples n of the signal sampling frequency are even. Semidiurnal signal is characterized by notable peaks that occur at $n = 2$ (aliasing period) and $n = 4$. For diurnal waves, peaks typically do not appear at the aliasing periods, i.e., when $n = 1$. This is attributed to an approximately 180° phase offset in the sampling of the diurnal signal during the satellites' ascending and descending tracks; in contrast, the semidiurnal signal is sampled in phase (e.g., Ray and Luthcke, 2006). These characteristics can be recognized clearly in the equator panels of K_1 and S_2 in Figure 4.7. Owing to the near-polar orbits of the GRACE(-FO) satellites, this phase sampling rule is applicable to nearly all latitudes; however, its validity diminishes with increasing proximity to the poles (see Ray and Luthcke, 2006; Han et al., 2010, Figure 1). Figure 4.10 offers a more detailed illustration of the latitude dependence on the emergence of aliasing peaks at the poles.

To gain further insights into the spectral replication scheme in the sub-semidiurnal bands (the Lomb–Scargle periodograms in Figure 4.8 do not provide any information for periods below 0.41 days), time series of sinusoidal signals sampled at the time of GRACE(-FO) overflights over 10°×10° grids were additionally generated, and the corresponding periodograms were analyzed.

TABLE 4.2: Scheme for the sampling of a periodic signal by the GRACE(-FO) satellites. How to read (for the 2nd row as an example): sampling of a diurnal wave by the satellites will create spectral replicas in diurnal and terdiurnal bands, independent (x) of signal's latitudinal location; and in long-periodic, semidiurnal and fourth-diurnal bands if the signal is sampled at a high-latitude (o) region. Entries can be extended according to the same scheme for higher frequencies.

Waves ↓ / Replicas →	l	d	d/2	d/3	d/4	⋯
Long-periodic (l)		o	x	o	x	⋯
Diurnal (d)	o	x	o	x	o	⋯
Semidiurnal (d/2)	x	o	x	o	x	⋯
Terdiurnal (d/3)	o	x	o	x	o	⋯
4th-diurnal (d/4)	x	o	x	o	x	⋯
⋮	⋮	⋮	⋮	⋮	⋮	⋱

As a summary, Table 4.2 provides an overview over the general spectral replication scheme for different bands. In general one can say that signal from an uneven band (e.g., diurnal or terdiurnal) will create spectral replicas in its own and other uneven bands; in contrast, signal from an even band (e.g., semidiurnal or 4th-diurnal) will create spectral replicas in its own band, other even bands, and the long-periodic band. The irregular sampling of a long-periodic signal (i.e., a signal with a period outside the diurnal band) will create spectral replicas in even bands. If one disregards the higher latitudes, the following key conclusions for interpreting the Lomb–Scargle periodograms in the following sections can be made:

- Even with the frequency limitations of the periodograms, higher frequency signal can be indirectly observed in the periodograms, as long as there is no spectral overlap with a more prominent diurnal or semidiurnal constituent.
- Long-periodic signal, for example, submonthly hydrology or non-tidal mass variations in the atmosphere and oceans might superpose semidiurnal signal.

4.3 Extracting Important Periods

The spectrum of each Lomb–Scargle periodogram for the residual range-acceleration time series of a $5^\circ \times 5^\circ$ grid cell includes several thousand frequencies. The aim of the analysis in the following sections is to offer a thorough overview of the most significant tidal periods in the residual range-acceleration data on a global scale. The primary criterion for assessing the significance of a peak in the periodogram is its amplitude relative to the periodogram spectrum. Ocean tides, being global dynamic phenomena, are in general not confined to specific locations. Instead, they can achieve relatively large amplitudes in different regions, whether neighboring or distant, either simultaneously or with a time delay. This variability will be taken into account as an additional factor in identifying globally significant periods.

4.3.1 Above 3-Sigma Amplitudes

To identify the most prominent peaks, the Lomb–Scargle periodograms of each grid cell are initially reduced to a periodogram containing only peaks, i.e., local maxima. Due to the application of the oversampling factor, this is a mandatory step. The resulting periodograms are then screened for amplitudes larger than three times the standard deviation with respect to the mean amplitude of the periodogram (3-sigma, 3σ). The screening procedure is applied iteratively, since larger peaks, such as those from regionally dominant constituents, can cause the 3-sigma threshold to be set too high, potentially missing smaller but important tidal peaks. To remove nearby spectral side lines and spectral leakage of large constituents, and to a certain degree minimize redundant information in terms of spectral replicas, the following procedure is applied to the diurnal and semidiurnal bands (see also Figure 4.11):

1. The extracted amplitudes of a grid cell exceeding the 3-sigma threshold are sorted in decreasing order
2. Beginning with the period that has the highest amplitude, periodograms of sine waves sampled at GRACE(-FO) overflights are generated (compare Figure 4.8, further denoted as “simulated” periodogram)
3. The simulated periodogram is checked for peaks with amplitudes exceeding its 3-sigma threshold
4. Periods of all identified peaks in the simulated periodogram exceeding the threshold, except the largest, are eliminated from the original periodogram, and the list of sorted periods is updated
5. The procedure is subsequently carried out for the remaining periods of the sorted list.

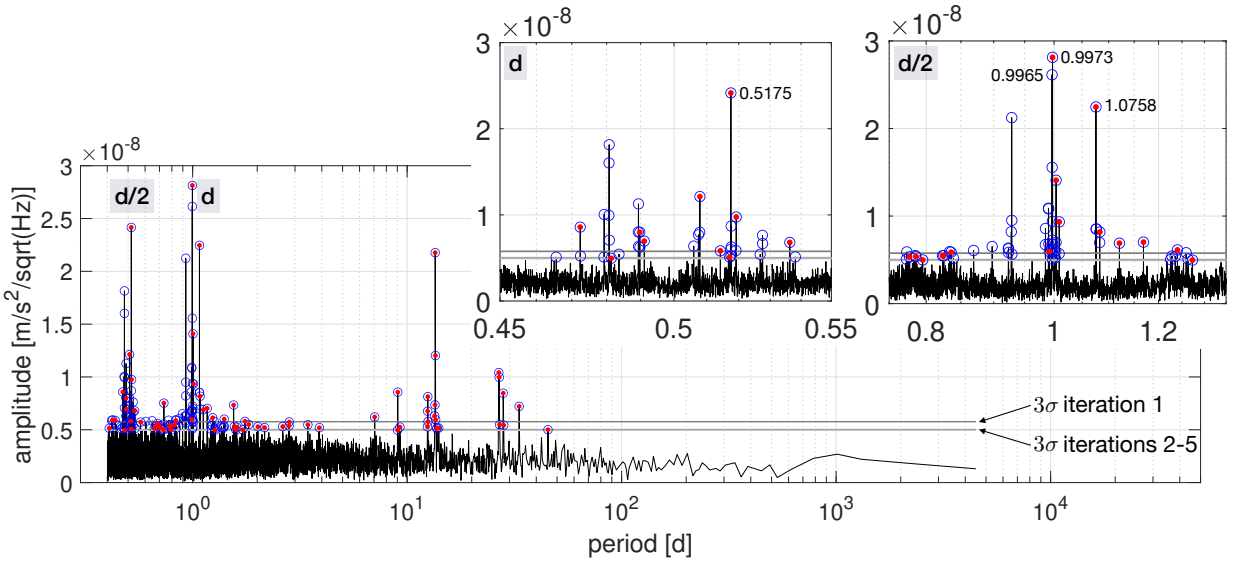

FIGURE 4.11: 3-sigma scanning and the algorithm to minimize spectral leakage and replication for one exemplary periodogram. The peaks marked with blue circles are those identified after performing the iterative 3-sigma scanning. In total, there are 116 periods within the diurnal and semidiurnal bands, which arranged in descending order based on their amplitude are: 0.9973 (K_1), 0.9965, 0.5175 (M_2), 1.0758 (O_1),... days. First, a periodogram of a sine wave with a frequency of 1/0.9973 1/d sampled at GRACE(-FO) observation time is estimated. The periodogram will resemble the one shown earlier in the K_1 panel of Figure 4.8. This periodogram is examined for periods with amplitudes surpassing its 3-sigma threshold. In this example, 16 out of the 115 periods, exceed the threshold, including the spectral replica of 0.9973 days at a period of 0.9965 days. These 16 periods are removed from the list of sorted periods resulting in the updated list: 0.5175 (M_2), 1.0758 (O_1),... days. This procedure is subsequently applied to the other listed periods, resulting at the end in a list containing 39 important periods. These are marked with red dots.

After the above procedure, the extracted periods and corresponding amplitudes of each grid cell are combined into a single plot (see Figure 4.12), providing an overview of the most significant periods in the residual range-acceleration data. From now on, this plot will be referred to as the "*above 3-sigma periodogram*".

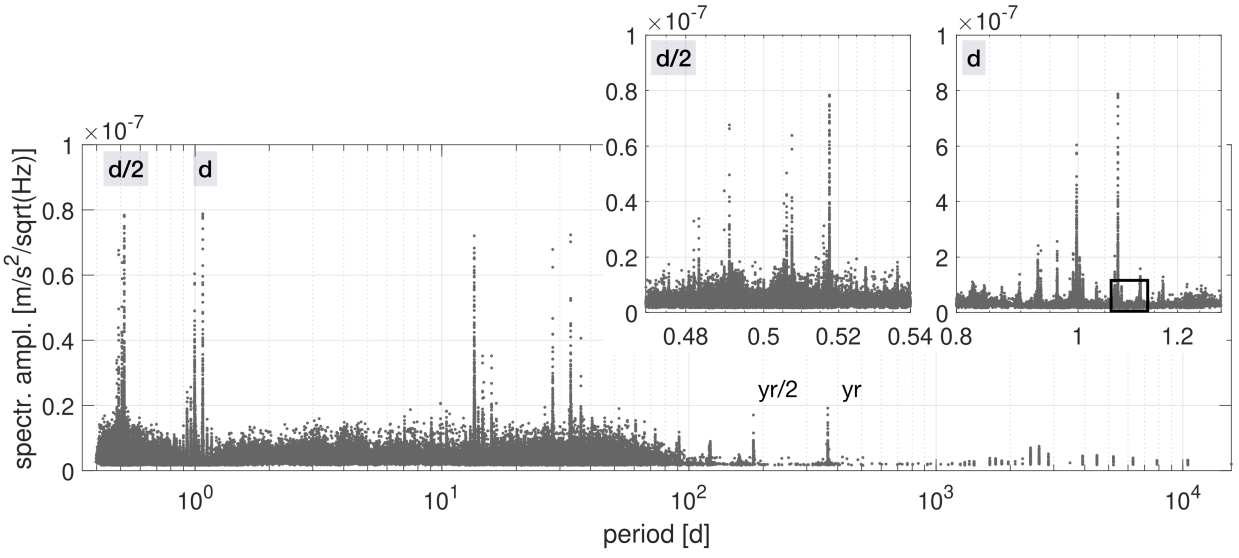

FIGURE 4.12: *Above 3-sigma periodogram*: plot containing dominant periods of the Lomb–Scargle periodograms of all grid cells (see Section 4.3.1). The black rectangle in the zoom view of the diurnal band refers to Figure 4.14.

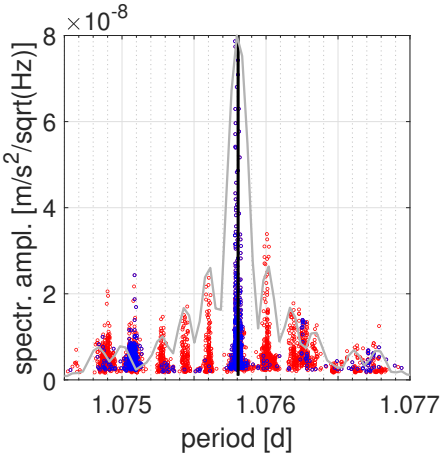

FIGURE 4.13: Zoom view of Figure 4.12 on O_1 (black line). Blue: procedure to eliminate side lines applied; red: not applied. Simulated spectral amplitudes (compare Figure 4.8) at an arbitrary grid cell scaled so that maximum value is $8{\times}10^{-8}$ m/s^2/sqrt(Hz) is shown in gray.

The effect of the procedure, particularly focusing on the side line elimination, is illustrated in Figure 4.13 for the O_1 constituent. The blue dots indicate the amplitudes of the above 3-sigma plot in Figure 4.12a at the periods around O_1, i.e., the aforementioned procedure to remove side lines has been applied. In contrast, the red dots show the amplitudes without side line elimination. Although constituents like O_1 typically have several nearby spectral lines, the lines close to O_1 in Figure 4.13 are mostly periodogram sidelobes, i.e., are representing spectral leakage from O_1 (compare in gray an excerpt from a simulated periodogram). After the side line elimination, in addition to O_1, another accumulation of points at a period of 1.0751 days is prominent. This period corresponds to the intraband replica of OO_1.

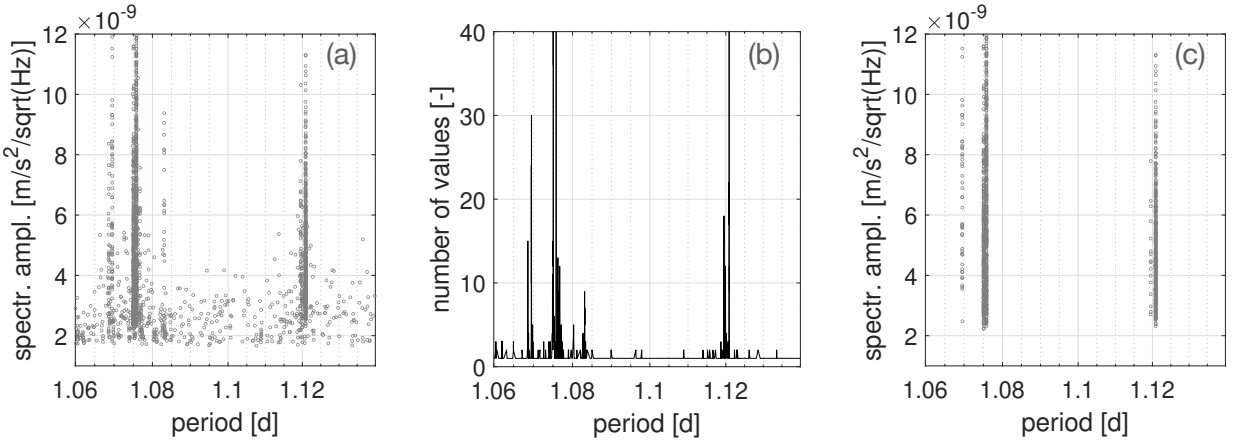

FIGURE 4.14: Extracting cluster lines from the above 3-sigma periodogram. (a): Zoom view of Figure 4.12 on 1.06 to 1.14 days. (b): Number of values (n_p) per period p in heuristic window $p \pm 0.00001$ days. (c): Extracted amplitudes where n_p >16 values. Figure is taken from Koch et al. (2024b). Data points in all three panels extend beyond the maximum value defined on the y-axis.

4.3.2 Clustering

By having a closer look on the above 3-sigma periodogram, clusters of points scattering around a central period forming distinct lines can be noticed as exemplarily shown in Figure 4.14a. This scattering of points emerges due to the individual definition of frequencies at which the Lomb–Scargle periodograms of the residual range-acceleration time series are evaluated (compare Sections 2.4.2 and 4.1.3). The evaluation frequencies depend mainly on the number of observations assigned to a grid cell. Another reason is the changing sampling frequency, which varies due to the changing precession of the orbital planes (see Section 4.2.1). It can be assumed that using predefined frequency grids, such as those containing a set of tidal frequencies, would theoretically result in the 3-sigma plot showing no scattering along the x-axis; only along the y-axis depicting different amplitudes of a specific constituent across the grid cells.

To extract relatively distinct lines from the above 3-sigma plot, for each of the periods p in Figure 4.12, the number of points n_p is calculated within a heuristically defined range $p \pm 0.00001$ days. The period range

0.00002 days approximately corresponds to the average spacing at which the periodograms are evaluated in the diurnal and semidiurnal bands. By setting an appropriate threshold for n_p, point clusters forming the characteristic lines can be identified, as illustrated in Figure 4.14. The choice of an optimal threshold value valid for larger period ranges is not trivial, and depends on the preferred level of detail and the specific period range of interest.

4.4 Assessment of the Spectral Agreement with Tidal Periods

In this section, lines are extracted from the above 3-sigma periodogram (Figure 4.12), incorporating the previously discussed point clustering (Section 4.3.2) as an additional criterion for defining the global significance of spectral components. This is followed by an assessment of whether the periods of the extracted lines align with tidal periods, using information from the standard list of tidal constituents published by the International Hydrographic Organization (IHO) Tidal Committee (IHO, 2017). Relevant to this section, the IHO list includes several hundred names of ocean tide constituents within the long-periodic to fourteenth-diurnal bands, along with the corresponding frequencies and Doodson numbers. Unlike the TGP catalogs (see Section 2.3.1), this list also includes relevant information on non-linear ocean tide components.

4.4.1 Diurnal Band

Figure 4.15 shows the spectral location assessment for the diurnal band, where a n_p threshold of 25 data points was applied to extract the most dominant spectral lines from the above 3-sigma periodogram (Figure 4.12). The empirical threshold value for the diurnal band was chosen to be slightly above the typical n_p numbers of the wider band containing the K_1, S_1 and P_1 constituents (see Figure 4.15c). The gray dots indicate the original data from Figure 4.12, whereas the data points that exceed the threshold value are highlighted in blue. Lowering the threshold value would result in a poorer line separation, especially in the immediate proximity of K_1, and would raise the likelihood of extracting irrelevant periods representing noise. As will be shown in this section, almost every extracted line can be associated with a specific ocean tide component, with few exceptions (lines without a name in Figure 4.15c) that only slightly exceed the threshold. Please note that the largest amplitudes in both the diurnal and semidiurnal bands reach up to approximately 8.0×10^{-8} $\mathrm{m/s^2/\sqrt{Hz}}$ (see Figure 4.12a). However, for the purpose of an easier visual assessment of the spectral agreement between the point clusters and the theoretical periods of the IHO list (marked by the red vertical lines), the y-axes in Figure 4.15 are restricted to 2.3×10^{-8} $\mathrm{m/s^2/\sqrt{Hz}}$. Constituents included in the FES2014b ocean tide model are indicated with downward triangles ($\triangledown$) placed above the red lines.

A significant portion of the extracted lines aligns well with the theoretical periods of the tidal constituents, with the extracted amplitudes scattering around a theoretical diurnal band period from the IHO list, which are: OO_1, SO_1, J_1/MQ_1, $K_1/SP_1/MO_1$, S_1, P_1/SK_1, τ_1/MP_1, O_1/MK_1 and $^3M_1$ (in the IHO list denoted as M_1). The solidus in the previous list separates different constituents with an identical period. Despite efforts to minimize redundancy from spectral replication (compare Section 4.3.1), the above 3-sigma periodogram still retains some information at the periods of diurnal constituent spectral replicas. Constituents identified at these frequencies are highlighted by underlined names in Figure 4.15. By recalling the algorithm described in Section 4.3.1, these redundant lines can only be explained by the fact that for some grid cells, the periodogram amplitude at the original frequency f is smaller than the amplitude at one of the corresponding frequencies f_A (see Equation 4.1). Exceptionally, in the case of Q_1, the amplitude at the spectral replica period is usually larger than at the original period, leading to an undercutting of the n_p threshold value and a missing Q_1 line at the original period (compare Figure 4.15b,f).

The spectral replicas of diurnal constituents within the diurnal band, i.e., intraband replicas, are of a redundant kind, meaning they do not provide any additional insights into residual tidal signal contained in the post-fit residuals. Despite the fact that the computed Lomb–Scargle periodograms are restricted

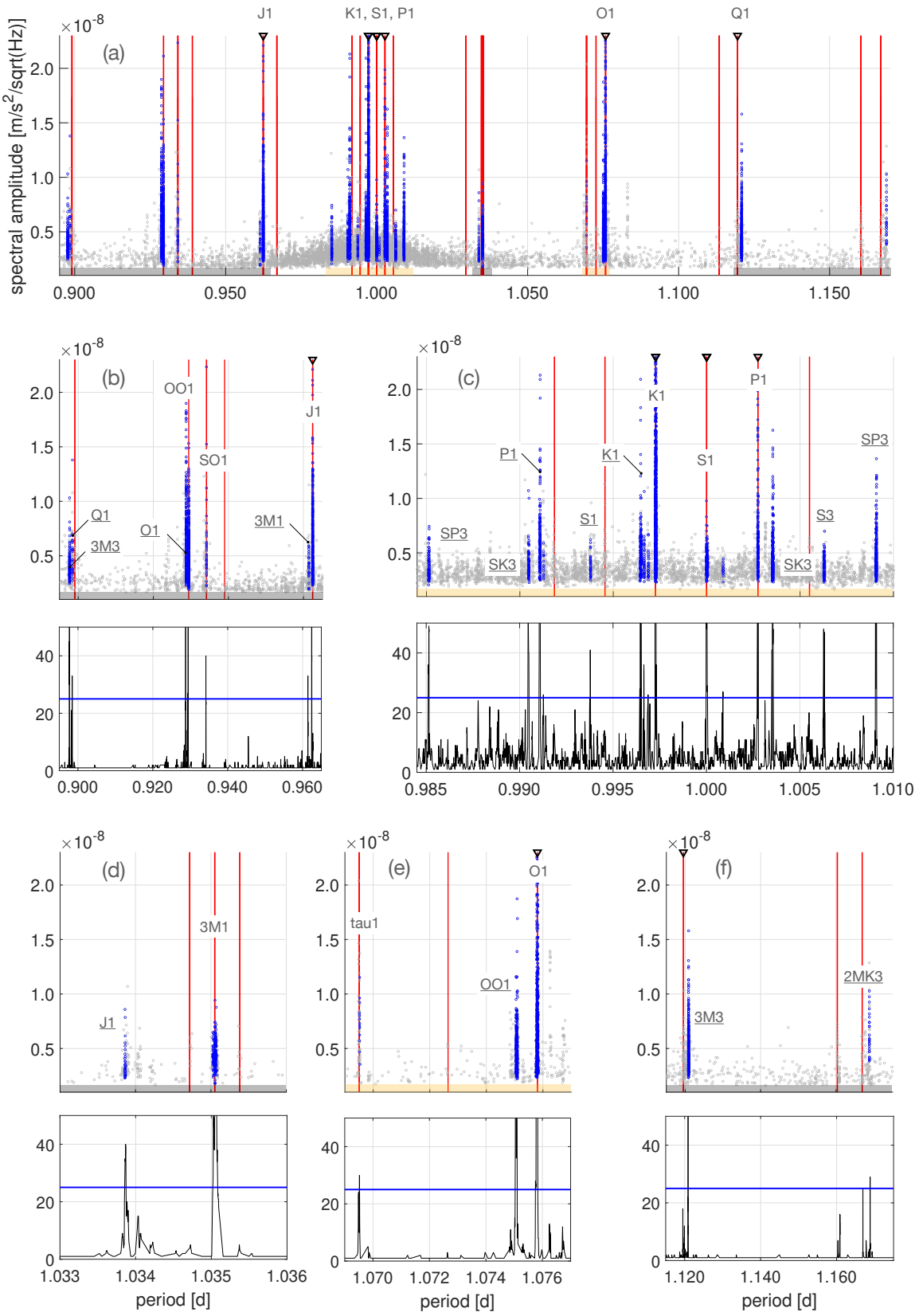

FIGURE 4.15: (a): Evaluation of spectral location alignment of extracted lines (blue) with periods from the IHO standard list of tidal constituents (red lines) in the diurnal band. (b)–(f): Zoom views of (a). ▽: FES2014b ocean tide model constituent. The lines were extracted from Figure 4.12 using a n_p threshold of 25 (see Section 4.3.2). The corresponding series of n_p is shown underneath each zoom view with the blue line representing the n_p threshold value. Underlined constituent name: spectral replicas (red lines and triangles are not included for spectral replicas). A vertical line may represent multiple constituents with the same period. For clarity, only one constituent name is displayed. Note that the values on the y-axes of all panels exceed the y-axes limits. This figure is an extended version of Koch et al. (2024b, Figure 6).

to a minimum resolvable period of around 0.41 days for a grid cell size of 5°×5° (see Table 4.2), possible interband replicas of constituents from higher species could offer additional information on unmodeled signal at higher frequencies. Generally, an imperfectly modeled and undersampled signal from uneven bands, such as the terdiurnal or fifth-diurnal, can produce replicas in the diurnal band (see Table 4.2). In the diurnal band, a scattering around the periods corresponding to spectral replicas of $^3M_3$, S_3 and the compound tides SP_3, SK_3 and $2MK_3/MO_3$ are evident. The constituent S_3 is primarily a radiational wave, with a negligible gravitational contribution (e.g., Balidakis et al., 2022; Ray et al., 2023), and two annual satellites T_3 and R_3, which share the same periods with SP_3 and SK_3, respectively (Ray et al., 2023).

Nearly all of the aforementioned astronomical constituents correspond to frequencies considered during orbit modeling; they are either directly part of FES2014b (J_1, K_1, S_1, P_1, O_1) or are interpolated from FES2014b constituents by assuming linear admittance (OO_1, SO_1, τ_1). Given that ocean tide models are expected to contain modeling errors, the appearance of these lines in Figure 4.15 is not surprising, especially since they correspond to mostly larger constituents. The only not accounted for frequency in the orbit modeling from the diurnal band is $^3M_1$ with a frequency of exactly only cycle per lunar day (Doodson number: 155.555), and therefore referring to a gravitionally excited tide of degree 3 (highlighted by the leading superscript 3), in contrast to the other here mentioned tides of degree 2. The M_1 tidal group also contains several other degree-2 tidal lines, especially the tidal line with the Doodson number 155.655, which has a larger TGP than the degree-3 component (see e.g., Cartwright and Tayler, 1971; Hartmann and Wenzel, 1995; Woodworth, 2019). Unlike $^3M_1$, increased residuals at the degree-2 M_1 lines (two red lines to the left and right of $^3M_1$ in Figure 4.15d, with the line of 155.655 to the left) are not evident. This is likely due to the their consideration via linear admittance. As the only terdiurnal constituent in the ocean tide model, FES2014b contains a data-unconstrained solution with the same frequency as the gravitationally excited degree-3 tide $^3M_3$. However, it does not take into account the corresponding astronomical forcing and only represents the non-linear contribution at this frequency, although no larger non-linear tides at the frequency of $^3M_3$ are known. The gravitational part of $^3M_3$ and the other terdiurnal tidal constituents of different and possibly mixed origin (S_3, T_3/SP_3, R_3/SK_3 and $2MK_3/MO_3$), might therefore represent the total unreduced contribution at these frequencies.

4.4.2 Semidiurnal Band

The spectral location assessment for the semidiurnal band is presented in Figure 4.16. One can notice that, in contrast to the diurnal band, the above 3-sigma periodogram in this band (gray dots) contains significantly more information. This is less related to the fact that more ocean tide constituents are present in the semidiurnal band (compare red vertical lines in Figures 4.15 and 4.16); rather, it is related to the way how GRACE(-FO) samples unmodeled long-periodic non-tidal signal, e.g., continental hydrology and non-tidal ocean mass redistribution. As outlined in Section 4.2.2, unmodeled long-periodic processes, will superpose semidiurnal signal and produce additional peaks in the periodograms. To extract significant lines from the above 3-sigma periodogram in the semidiurnal band, a larger n_p threshold of 50 values is utilized. This value was chosen to be slightly above the n_p values of the largest clusters of points in the semidiurnal band, which are found at periods of around 0.4925 and 0.505 days (see Figure 4.16c). Lines extracted applying this threshold value are highlighted in blue, indicating that a tidal constituent can be assigned, and in purple, where no agreement with a known tidal constituent can be found.

In Figure 4.16, an agreement with the following semidiurnal constituents from the IHO standard list of tidal constituents can be observed: M_2/KO_2, $\mu_2/2MS_2$, N_2/KQ_2, λ_2, $2N_2$, S_2/KP_2, $L_2/2MN_2/L_2A$, ε_2/MNS_2, $M(KS)_2$, MSP_2/MB_2, $\alpha_2/M(SK)_2$, MA_2/MPS_2, $2SM_2$, δ_2/MKS_2, η_2/KJ_2, MSN_2. The frequencies of $M(KS)_2$ (Doodson: 256.554) and MSP_2/MB_2 (256.555) are separated by only one cycle in 20940 years (longitude of Sun's perigee). Consequently, they are inseparable and represented by the same line in Figure 4.16. The same is true for $\alpha_2/M(SK)_2$ (254.556) and MA_2/MPS_2 (254.555). The frequency of the non-linear tide $M(KS)_2$ corresponds to that of the gravitational β_2 tide (not mentioned in the IHO list). In

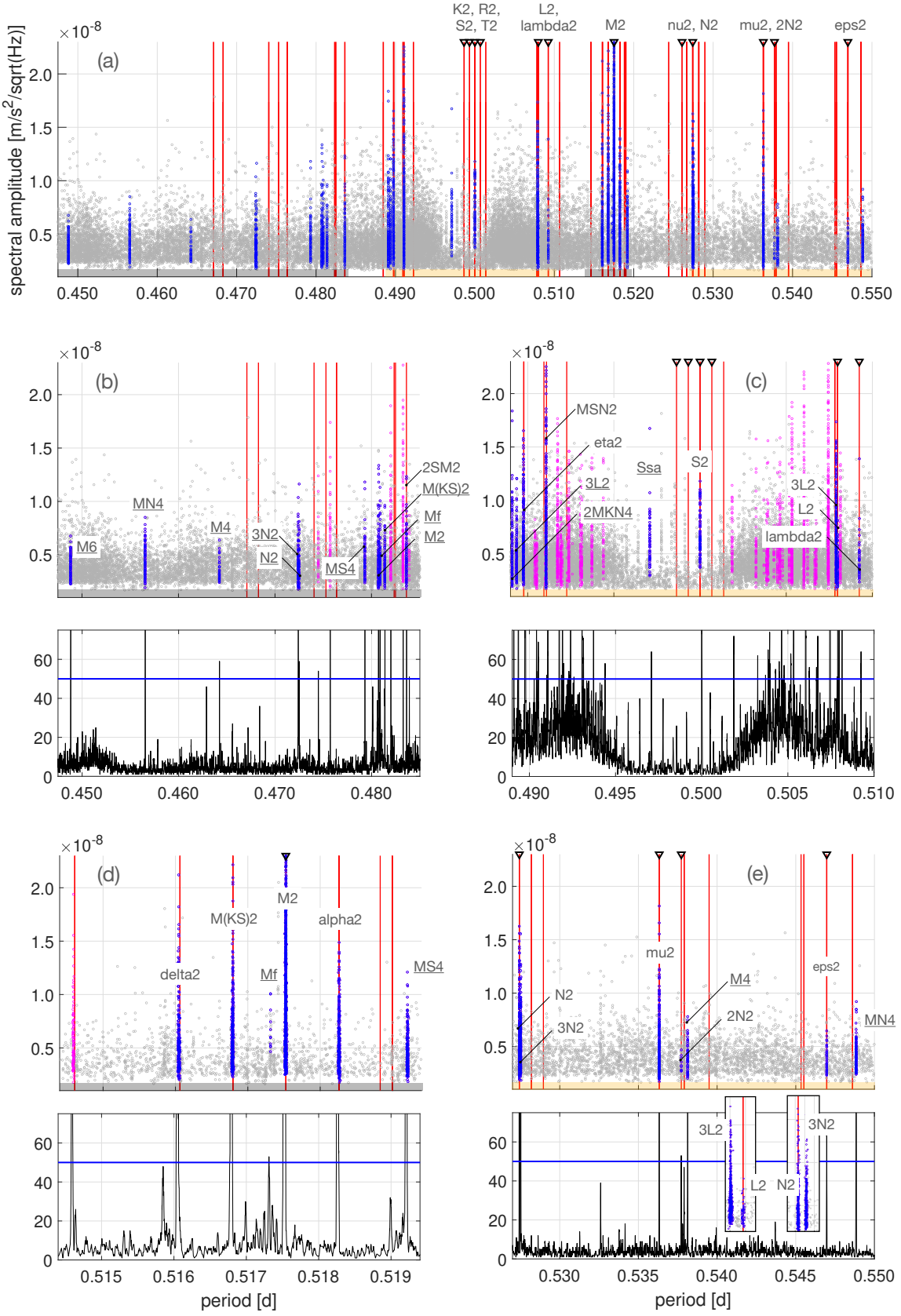

FIGURE 4.16: Similar to Figure 4.15, but here for the semidiurnal band with a n_p threshold of 50. Read text for further annotations. Highlighted in purple are lines without an agreement with a known tidal constituent. This figure is an extended version of Koch et al. (2024b, Figure 8).

the FES2014b ocean tide model, solutions for the astronomical tides M_2, μ_2, N_2, λ_2, $2N_2$, S_2, L_2 and ε_2 are available. The astronomical constituents α_2, β_2, δ_2 and η_2 are considered in the gravity field recovery processing via linear admittance. The only semidiurnal frequencies not taken into account during orbit modeling is that of the compound tide $2SM_2$, and the two largest semidiurnal degree-3 tides $^3L_2$ (Doodson: 265.555) and $^3N_2$ (245.555). The two degree-3 tides are separated by one cycle in 8.85 years from the degree-2 tides L_2 and N_2, respectively (e.g., Ray, 2020b). A closer look on these close-by located tidal lines is shown in Figure 4.16e (see also Figure 7 in Koch et al., 2024b). Note that red vertical lines are missing for these two tides since they are not included in the IHO list. Besides intraband replicas of many of the earlier mentioned constituents, in agreement with Table 4.2, also a clustering around the spectral replica periods of even band sub-semidiurnal tides M_6, M_4, MN_4, MS_4 and $2MKN_4$ can be recognized in Figure 4.16. All of them are explicitly modeled in FES2014b, except $2MKN_4$. In addition, two extracted lines are located at the spectral replica periods of Mf/KOo/MKo and the solar semiannual Ssa, with Mf as well as Ssa being included in FES2014b.

The purple lines in Figure 4.16 also exceed the introduced n_p threshold value of 50. However, these lines do not seem to correspond to any tidal frequencies and therefore likely represent non-tidal geophysical effects. The corresponding GRACE(-FO) aliasing periods of these lines cover the range from approximately 10 to 40 days. The RMS amplitude maps (with the computation method detailed in Section 4.5.1) of these lines show pronounced amplitudes over the major river basins, particularly the Amazon Basin, as well as in other regions such as the Black Sea, the Mediterranean Sea, Northern Siberia, the Gulf of Carpentaria, the Argentine Gyre, Alaska, and many more areas. While further investigations into these non-tidal frequencies could yield valuable insights, they fall beyond the scope of this thesis.

4.4.3 Long-Periodic Band

In the long-periodic band, a clustering of points around the periods of Mf/KOo/MKo, Sta, Ssa and Sa can be observed. Moreover, since the algorithm presented in Section 4.3.1 was only applied to the diurnal and semidiurnal bands, the long-periodic band additionally must also contain all of the constituents from bands such as the semidiurnal or fourth-diurnal, along with the side lines of these constituents. No significant peaks or point clusters can be found beyond the annual peak (see Figure 4.12).

4.5 Assessment of the Spatial Characteristics of the Amplitudes

4.5.1 RMS Amplitude Maps

In the previous section, it was demonstrated that many significant components of the periodograms align with tidal periods. Among these components are not only general tidal periods, which in principle may also refer to non-oceanic tidal phenomena, but also specific compound tides that are exclusively linked to ocean tides. This section will verify that the spatial patterns of the amplitudes for most of the identified tidal constituents are indeed indicative of an oceanic origin. First, Figures 4.15 and 4.16 are used to determine the spectral boundaries for each extracted line, as illustrated in Figure 4.17 for the extracted line containing the period of the O_1 constituent. The extent of a line extracted from the above 3-sigma periodogram is defined by the smallest and largest periods of the point scatter (shown by the two dashed lines in Figure 4.17a) or, equivalently, by the midpoint period (black line in Figure 4.17a) $\pm$ the half-width of the line.

To globally visualize the spatial patterns of a specific extracted line, the RMS of the amplitudes is computed from the Lomb–Scargle periodograms of each grid cell within the established boundaries (compare Figure 4.17b). Due to the limited spectral resolution of the Lomb–Scargle periodograms, it is possible that certain grid cells may lack a period within the specified boundaries to evaluate. Therefore, in instances of very narrow lines, the boundaries are slightly extended, so an (RMS) amplitude can be computed for every grid cell.

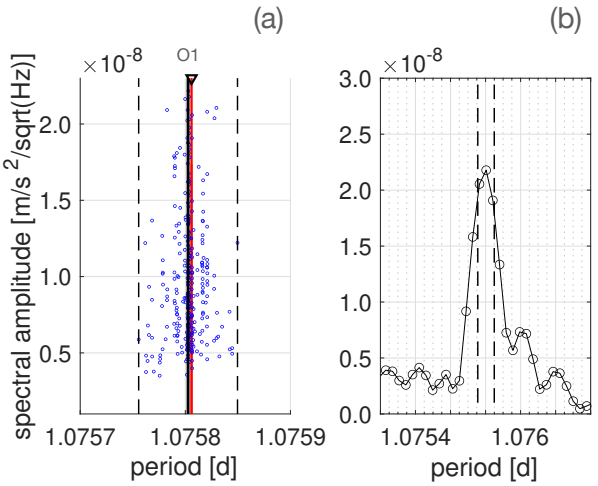

FIGURE 4.17: (a): Period limits definition of an extracted line, exemplified by O_1. (b): O_1 amplitude evaluation at one of the grid cells. Maps (Figures 4.18–4.20) show the RMS amplitudes evaluated in the defined period limits, i.e., RMS amplitudes of this grid cell will be computed from three values.

The corresponding global maps of the RMS amplitudes (hereafter referred to simply as "amplitudes") are shown in Figures 4.18–4.20. Please note the different upper limits of the color coding. Since the upper limits have been set as a compromise to ensure comparability between maps with similar amplitudes and to highlight the most critical regions of a specific constituent, the amplitudes in certain regions exceed these limits. The corresponding period boundaries used for evaluating the amplitude are given in Table 4.3. As shown, for example, in Figure 4.17a, the theoretical periods of the tidal constituents encoded by the Doodson numbers (red line), slightly deviate from the mid-periods. For each of the entries in Table 4.3, the maximum amplitude, as well as the average value of the 20 largest grid cell amplitudes (further referred to as "average maximum amplitude") are given. The entries of the table are arranged in descending order based on the latter.

Figures 4.18–4.20 show that the largest amplitudes are located over the oceans, with no significant additional widespread variations over the continental areas. Clear patterns suggestive of atmospheric tide errors (see for example the S_2 maps in Ray et al., 2009, Figure 6) cannot be recognized in the amplitude maps of the post-fit residuals. The highest amplitudes are predominantly located in shallow waters and near-coastal areas, particularly at higher latitudes, which are regions where satellite altimetry cannot serve as a constraint for the hydrodynamic solutions, suggesting ocean tides as the origin of the increased residuals. However, certain partial tides also exhibit distinct amplitude patterns over the open ocean. This mainly involves the unmodeled partial tides indicated with a "−" in the first column of Table 4.3, but also some higher frequency compound tides, like MS_4 and MN_4. Although the constituents Sa, Ssa, Sta, δ_2/MKS_2, η_2/KJ_2, MSN_2 and $2MKN_4$ are noticeable in the above 3 sigma amplitudes shown in Figure 4.16, Figures 4.18–4.20 and Table 4.3 do not include these constituents, because of their mostly non-tidal character with largest amplitudes across the continents. Due to their correspondence with the main seasonal periods, Sa, Ssa, Sta predominantly reflect long-periodic hydrological signal not captured by the monthly gravity field parameters (compare also the assessment of the signal content of the monthly gravity field solutions in Section 3.6). Constituents δ_2/MKS_2, η_2/KJ_2, MSN_2 and $2MKN_4$ have the aliasing periods of approximately 14.6, 28.1, 33.3 and 26.0 days, respectively. Most of the signal presented in these maps is likely hydrology that cannot be absorbed by the spherical harmonic coefficients of the gravitational potential due to the monthly sampling of the solutions.

TABLE 4.3: Lines in diurnal, semidiurnal and long-periodic bands (see Figures 4.15, 4.16, 4.12) that can be assigned directly or indirectly via spectral replication to an ocean tide constituent from the IHO standard list of tidal constituents.

	Name(s)	Doodson Number	Period [d]	Amplitude [nm/s^2/$\sqrt{\text{Hz}}$]	Aliasing Period [d]	TGP [% of M_2]
▽	O_1/MK_1	145.555	1.075795±4.215e-5	58.8/78.5	13.6	41.37
▽	M_2/KO_2	255.555	0.517526±1.764e-5	58.2/70.0	13.5	100.00
▽	K_1/SP_1/MO_1	165.555	0.997275±2.548e-5	42.0/59.8	2610.0	58.15
▽	P_1/SK_1	163.555	1.002751±2.320e-5	16.4/20.4	170.7	19.19
▽	J_1/MQ_1	175.455	0.962441±3.463e-5	15.5/24.7	27.9	3.25
a	β_2/M(KS)$_2$	256.554	0.516790±1.555e-5	14.3/19.7	14.0	0.30
a	OO_1	185.555	0.929429±2.831e-5	14.2/24.0	13.7	1.78
–	$^3L_2$	265.555	0.507905±1.636e-5	12.8/15.3	26.8	0.57
–	R_3/SK_3	383.555	1.003542±3.838e-5	12.4/17.0	150.5	–
▽	N_2/KQ_2	245.655	0.527432±1.551e-5	11.9/14.6	9.1	19.11
▽	μ_2/$2MS_2$	237.555	0.536322±1.300e-5	11.8/16.9	7.1	3.05
a	τ_1/MP_1	147.555	1.069520±2.027e-8	10.7/18.7	14.7	0.54
a	α_2/M(SK)$_2$	254.556	0.518262±1.708e-5	10.6/14.0	13.0	0.34
–	$^3M_3$	355.555	1.120892±3.465e-5	10.4/15.4	9.0	1.21
–	T_3/SP_3	381.555	1.009074±2.641e-5	10.2/14.5	82.6	–
a	SO_1	183.555	0.934169±2.125e-5	9.88/21.1	14.9	0.54
▽	S_2/KP_2	273.555	0.500000±7.968e-6	9.69/11.4	160.5	46.37
–	$^3N_2$	245.555	0.527515±1.631e-5	9.42/13.9	9.1	0.61
▽	M_f/KO_o/MK_o	075.555	13.660786±2.86e-3	9.02/11.0	–	14.84
▽	MS_4	473.555	0.519208±1.413e-5	8.51/11.5	12.5	0.00
–	$2MK_3$/MO_3	345.555	1.168828±2.349e-5	8.31/12.9	6.8	–
–	$2SM_2$	291.555	0.483624±1.253e-5	7.71/11.7	16.3	0.00
▽	λ_2	263.655	0.509243±5.860e-6	7.48/13.9	23.5	0.73
–	$^3M_1$	155.555	1.035051±2.809e-5	7.06/10.5	27.0	0.63
▽	$2N_2$	235.755	0.537724±5.463e-6	6.79/11.9	6.8	2.52
▽	L_2/$2MN_2$/L_2A	265.455	0.507985±9.632e-6	6.66/8.37	26.6	2.81
▽	MN_4	445.655	0.548843±1.523e-5	6.53/8.66	5.4	0.01
▽	S_1	164.556	1.000021±3.625e-8	6.21/8.87	318.8	0.45
▽	M_4	455.555	0.538130±8.882e-6	6.12/7.47	6.8	0.02
▽	ε_2/MNS_2	227.655	0.546971±5.739e-6	5.94/7.81	5.6	0.74
▽	M_6	655.555	0.448818±1.104e-5	5.54/6.66	4.5	0.00
–	S_3	382.555	1.006293±2.320e-5	5.32/6.85	106.7	0.00

Table notes: Table is identical to Koch et al. (2024b, Table 4). Constituents $^3L_2$, $^3N_2$ and S_3 are not listed in the IHO list. For M(KS)$_2$ the corresponding astronomical tide name β_2 was added. For SK_3 and SP_3 the names of radiational counterparts R_3, T_3 were included. Several constituents (separated by /) can share the same theoretical period which can be decoded from the Doodson numbers. The given period is the observed value in Figures 4.15, 4.16 and 4.12, which might differ slightly from the theoretical value (compare Figure 4.17). The listed amplitudes (separated by /) are the average of 20 largest values in a map, and the observed maximum value. The table is sorted according to the former in decreasing order. The approximate aliasing periods are computed using Equation 4.1 with $\dot{\Omega} = -0.136°$/d. The astronomical TGP is taken from the HW95 catalogue and is given in percent of the M_2 TGP (1.24×10^6 mm^2/s^2). ▽: part of FES2014b, a: modeled via linear admittance, –: unmodeled tide.

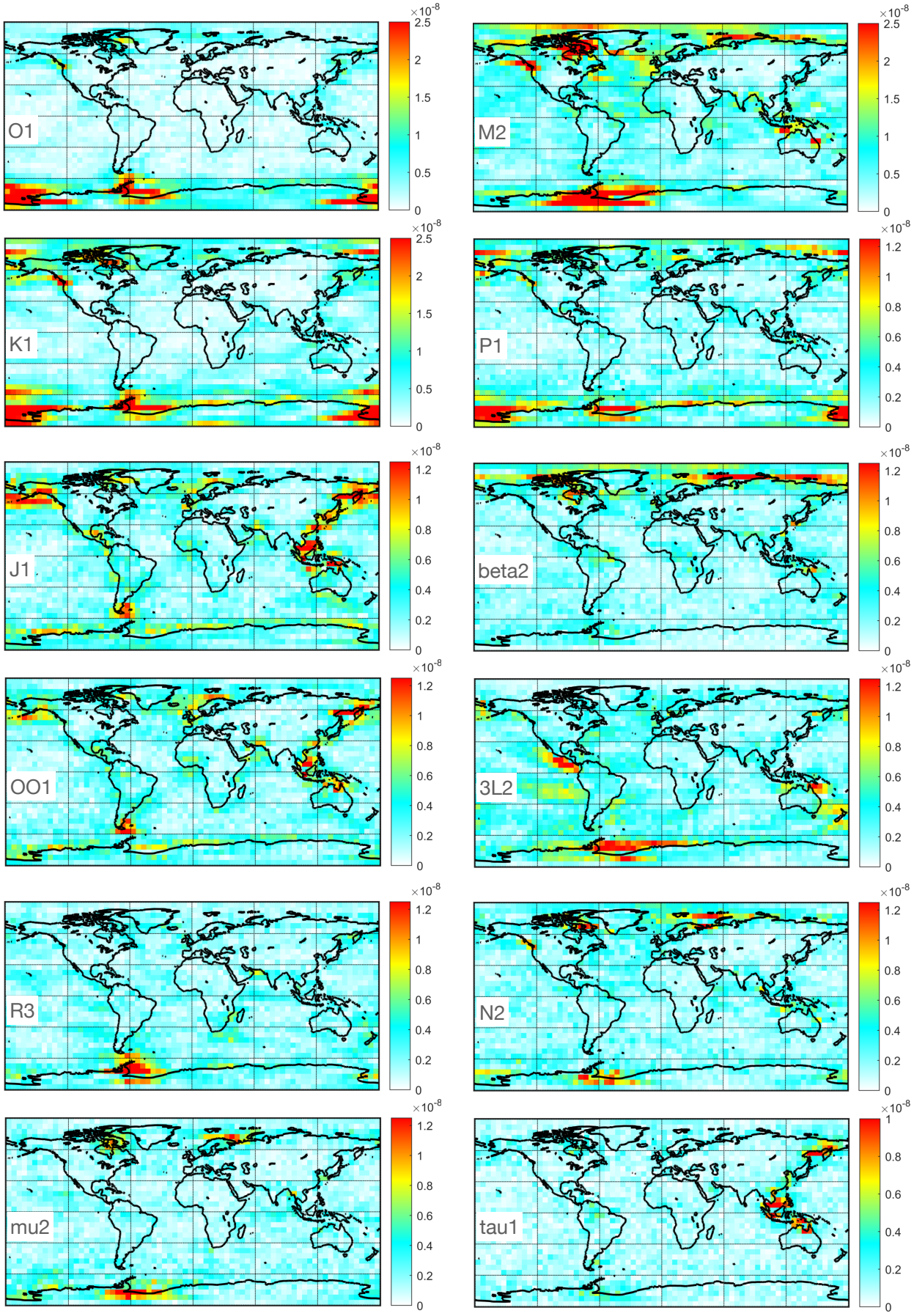

FIGURE 4.18: RMS amplitude maps of constituents listed in Table 4.3. Please note the different color bar limits. Units of the color axes are $\mathrm{m/s^2/\sqrt{Hz}}$. These maps were earlier published in Koch et al. (2024b).

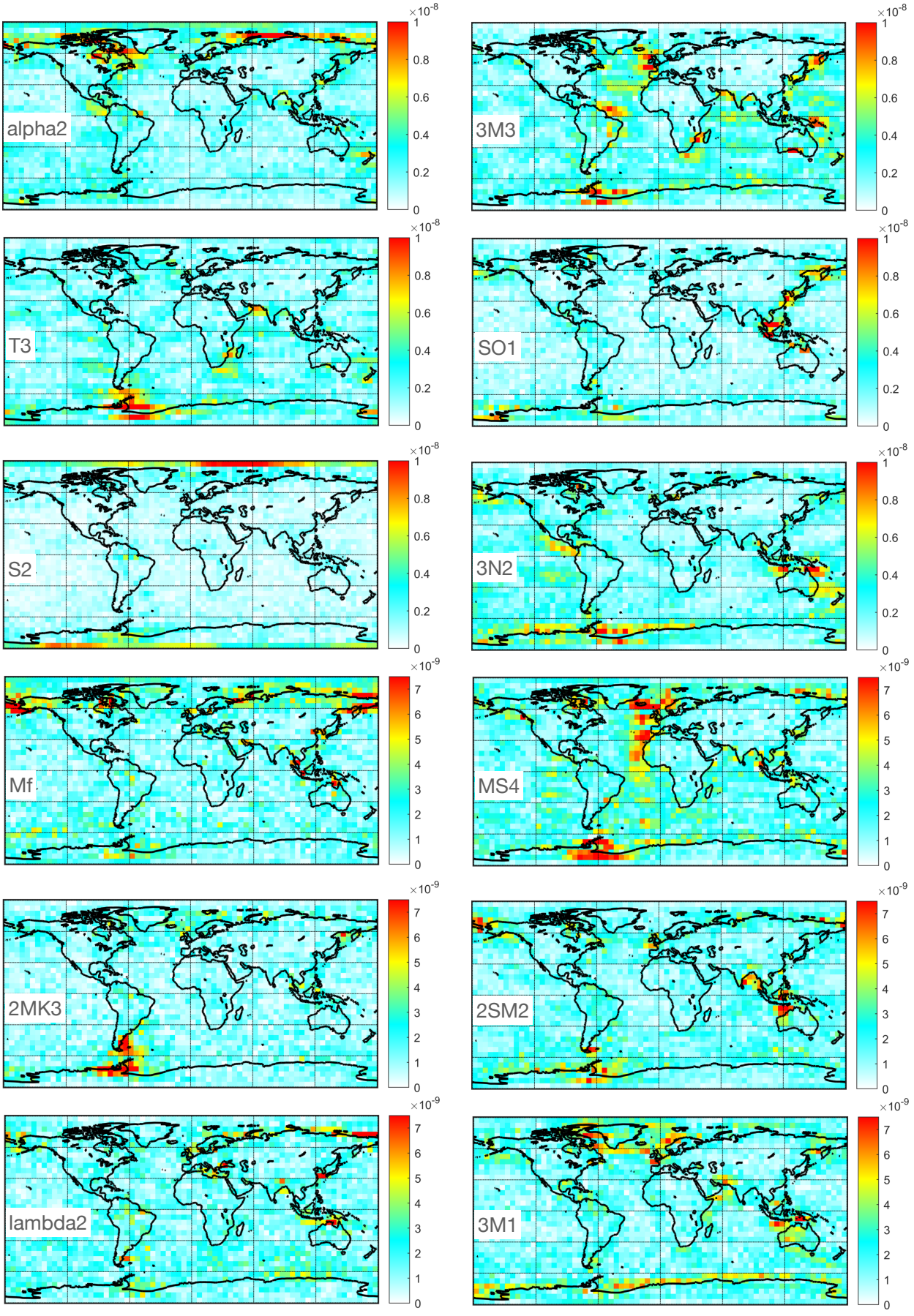

FIGURE 4.19: RMS amplitude maps of constituents listed in Table 4.3, continued. Please note the different color bar limits. Units of the color axes are $\mathrm{m/s^2/\sqrt{Hz}}$. These maps were earlier published in Koch et al. (2024b).

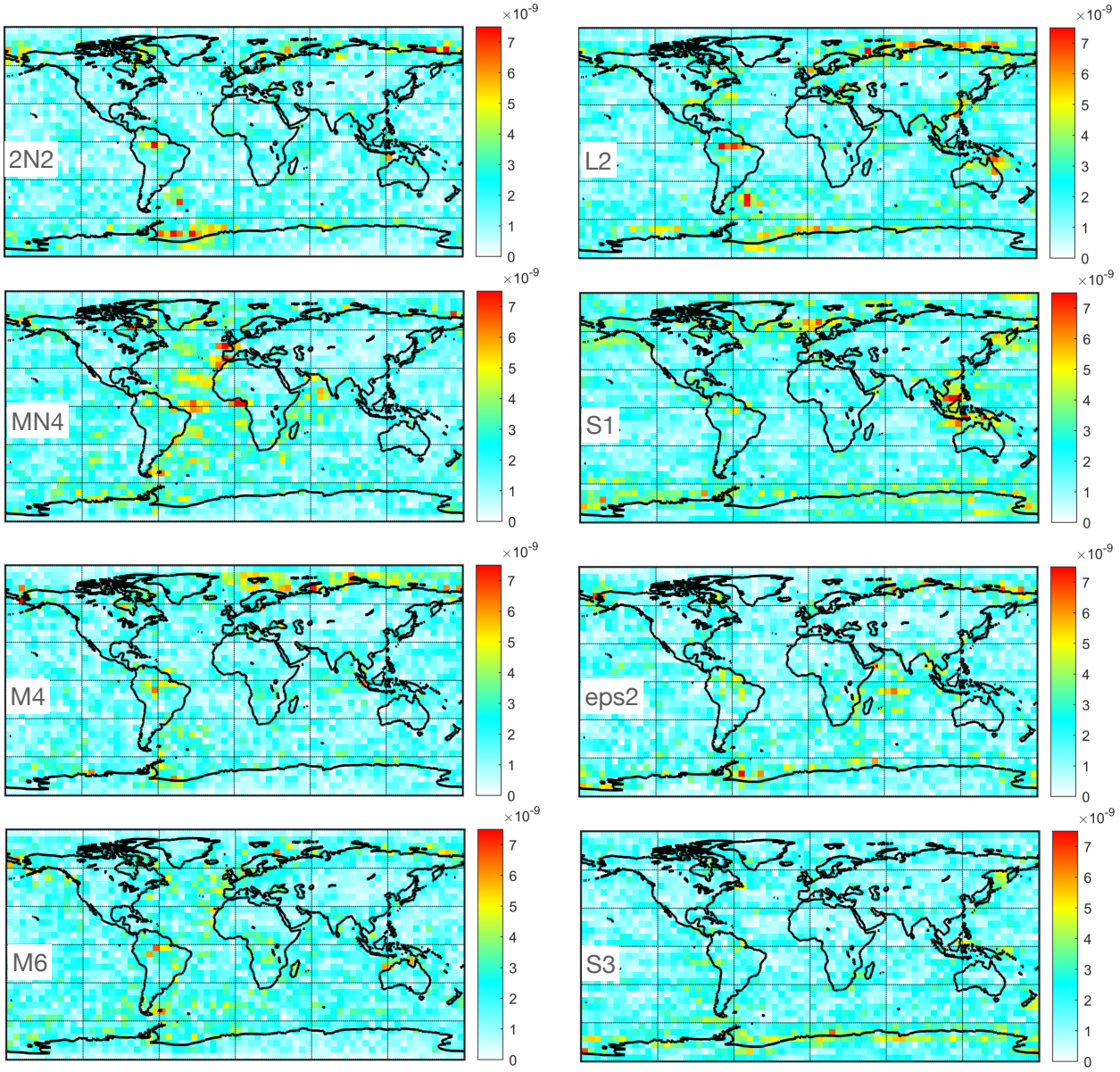

FIGURE 4.20: RMS amplitude maps of constituents listed in Table 4.3, continued. Please note the different color bar limits. Units of the color axes are $\mathrm{m/s^2/\sqrt{Hz}}$. These maps were earlier published in Koch et al. (2024b).

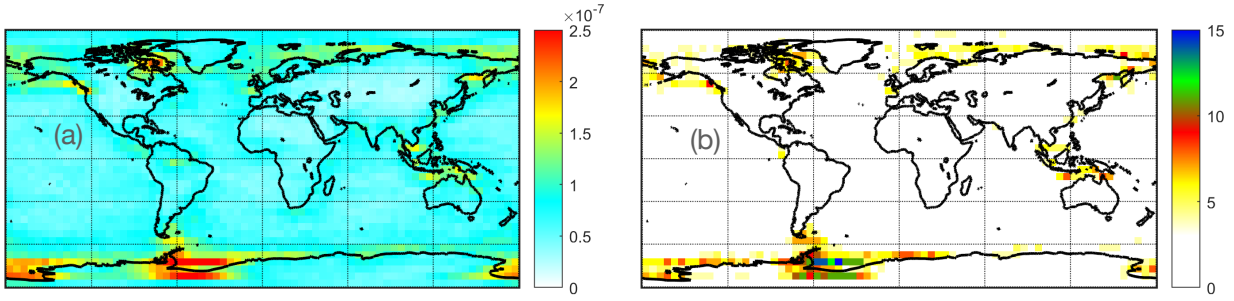

FIGURE 4.21: (a): Cumulative amplitude of the constituents in Figures 4.18–4.20. Units of the color axes are $\mathrm{m/s^2/\sqrt{Hz}}$. Largest amplitudes exceed the color bar limit and reach up to 3.65×10^{-7} $\mathrm{m/s^2/\sqrt{Hz}}$. (b): Number of waves with an amplitude larger 6.5 $\mathrm{nm/s^2/\sqrt{Hz}}$. Figure is taken from Koch et al. (2024b).

The cumulative amplitude of all constituents listed in Table 4.3, i.e., the sum of the individual maps from Figures 4.18–4.20, is presented in Figure 4.21a. The highest cumulative amplitudes are to be found at high

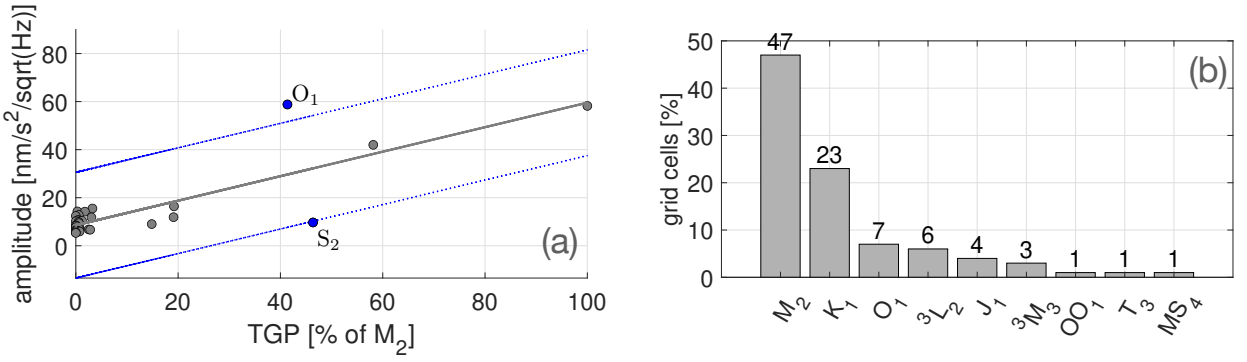

FIGURE 4.22: (a): TGP vs. amplitude for entries of Table 4.3. A line was fitted to the data (gray). Blue lines represent ±3 times the standard deviation of data minus fit. (b): Constituent has a larger amplitude in given percent of oceanic and coastal grid cells than any other constituent in Table 4.3. In (b), only constituents with a percentage of 1% or greater are displayed.

latitudes, including the Weddell and Ross Seas in the Antarctic region; and in the northern hemisphere in the area between Hudson and Baffin Bays, in the marginal seas of the Arctic Ocean, in the Sea of Okhotsk, and at a few isolated regions of the northeast Pacific coast. Additionally, at lower latitudes, significant cumulative amplitudes can be observed in several marginal seas located between Japan and Australia.

Figure 4.21b illustrates the number of waves in a grid cell with an amplitude larger than 6.5 $\mathrm{nm/s^2/\sqrt{Hz}}$ (approximately the maximum amplitude of the smallest constituent in Table 4.3). There appears to be a correlation with the total amplitude. The grid cell with the highest number of waves exceeding the defined threshold is located in the Weddell Sea region.

4.5.2 The S_2 Outlier due to Aliasing

For reference, Table 4.3 provides the approximate TGP of the HW95 catalogue (Hartmann and Wenzel, 1995) at the frequencies of the listed constituents, expressed as a percentage relative to the M_2 amplitude (1.24×10^6 $\mathrm{mm^2/s^2}$). Although the oceans' response to the theoretical TGP is quite complex, and therefore these values can only serve as a very broad criterion for assessing the reasonability of the residual amplitude values, the very general order of entries in Table 4.3 follows anticipated patterns: constituents with a substantial TGP, such as O_1, M_2, K_1 and P_1, exhibit larger amplitudes, while smaller tides like M_4, M_6 and ε_2 are listed at the end of the table. In Figure 4.22a, the amplitudes of the entries in Table 4.3 are plotted against the corresponding TGP values. Larger discrepancies between amplitudes and TGP are evident for constituents O_1 and S_2. The overall amplitudes of O_1 are comparable to those of the largest constituent M_2, even slightly larger, although its TGP is only 41% of M_2. However, when examining the data in Figure 4.22b, which shows the percentage of grid cells over the ocean and along the coasts where the amplitude of a specific constituent is larger than that of any other constituent, the significance of O_1 relative to M_2, and also relative to the larger K_1, diminishes and aligns with the TGP values. Another partial tide with a noticeable deviation in Figure 4.22a is S_2, the second-largest constituent in the semidiurnal band and the third-largest overall, with 46% of the M_2 potential. While the presence of a significantly larger amplitude, e.g., located similarly to O_1 above the upper blue line, could indicate ocean tide modeling challenges in certain regions, its unusually small amplitude compared to its large TGP seems quite suspect.

Furthermore, when examining the amplitude map of S_2 in Figure 4.19, a noticeable discrepancy emerges compared to the other maps, since S_2 is solely characterized by an increase in amplitudes in the northernmost and southernmost grid cells, while globally, except for a few grid cells along the Antarctic coast in the Weddell Sea and in the Amazon basin, the amplitudes remain relatively small, showing absolutely no indications of potential geophysical processes. It is uncertain whether the increased amplitudes in the polar regions are due to a geophysical contribution or are merely artifacts. The overall small amplitudes at this period suggest, in

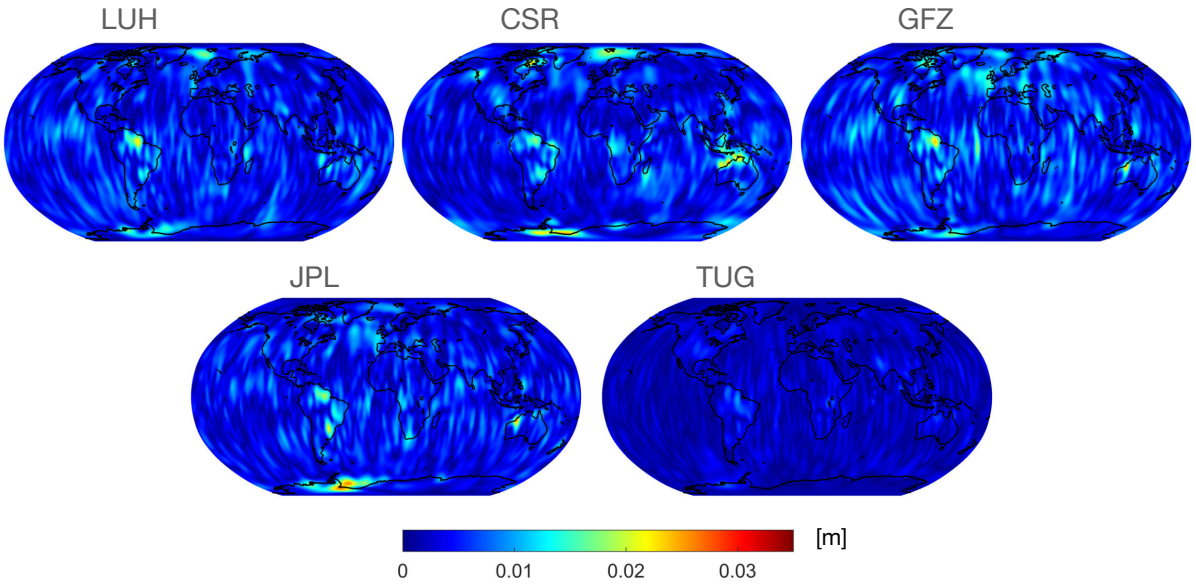

FIGURE 4.23: EWH amplitudes at the aliasing period of S_2 (160.5 days).

contrast to the other periods listed in Table 4.3, a significant absorption especially of the residual S_2 signal by the parameters estimated during gravity field recovery.

Residual ocean tide signal present at the aliasing period of S_2 (≈161 days) in monthly gravity field solutions is well-known (see e.g., Han et al., 2005c; Chen et al., 2009; Schrama et al., 2007; Kvas et al., 2019a), which here is additionally confirmed by the relatively small amplitudes of the post-fit residuals at the S_2 period. Figure 4.23 shows the amplitudes at the S_2 aliasing period of 160.5 days fitted along with a bias, trend, annual and semiannual variation (see Section 3.6) to the EWH maps of the GRACE time series. The C_{20} coefficient in these EWH maps was replaced with SLR estimates, so the maps do not show the S_2 error absorbed by this coefficient. The map of the TUG series does not show any significant variations, likely due to the inclusion of an additional S_2 tidal correction (see Kvas et al., 2019a). In contrast, the maps from LUH and other analysis centers exhibit clear patterns of increased amplitudes, particularly prominent in shallow water regions such as the Weddell Sea, near Svalbard, and along the northwest coast of Australia (especially in the CSR solutions). The increased amplitudes observed in South America might be attributed to atmospheric tides, particularly since the S_2 atmospheric tide is most pronounced along the equator; however, it seems more likely that they represent residual hydrological signal.

4.5.3 Linear Admittance Partial Tides

Overall, through linear admittance (see Section 2.3.4), in addition to the 34 constituents of the ocean tide model, 327 long-period, diurnal, and semidiural degree-2 tides were taken into account for orbit modeling. If one considers only the tides that differ from the 34 constituents by at least the last two Doodson numbers, the number is considerably smaller. Noticeable in the GRACE(-FO) post-fit residuals are increased amplitudes at the periods of β_2, OO_1, τ_1, α_2, SO_1. Upon examining Figure 2.7, it is evident that these tides exhibit large TGP amplitudes, although they are not necessarily the largest among the gravitationally excited tides not included in the ocean tide model. Therefore, a strict correlation with the amplitude of the TGP is not given.

By examining OO_1 and SO_1, which do not have overlapping frequencies with non-linear tides, it appears plausible that the increased amplitudes observed in Figures 4.18 and 4.19 might largely reflect errors in the ocean tide solutions used for their inference. Figure 2.7 shows that OO_1 and SO_1 are located at the boundary of the diurnal band, with no diurnal model solutions available for periods shorter than those of OO_1 and SO_1. The closest constituent included in the ocean tide model is J_1, with which OO_1 and SO_1 share similar

locations of increased amplitudes. When deriving the ocean tide amplitudes from two waves as defined in Equation 2.79, K_1, for which a solution is available in the employed ocean tide model, may serve as the second reference point to extrapolate OO_1 and SO_1. In the utilized admittance matrix, diurnal waves are inferred from all diurnal constituents of the ocean tide model, excluding the radiationally dominated S_1 tide. The lack of solutions for periods shorter than those of OO_1 and SO_1 introduces an uncertainty factor that grows with the extent of extrapolation. An additional uncertainty factor is that the J_1 solution of FES2014b is not data-constrained (see Table 2.8). By substituting the hydrodynamic J_1 solution from FES2014b with the altimetry-constrained J_1 from EOT20 (incorporates residual tidal signal relative to FES2014b), the data-constrained solution from the recently published FES2022 catalogue, or those from several other recent ocean tide models (see Table 2.8) and recomputing the time series of GRACE(-FO) post-fit residuals, the potential influence of data assimilation on J_1 and the inference of OO_1 and SO_1 could be examined. As demonstrated later in Section 4.5.6, OO_1 exhibits a favorable signal-to-noise ratio in TOPEX/Poseidon altimetry data. Data-constrained OO_1 solutions are available in the recently published TPXO10 and GOT5.6 catalogues (see Table 2.8). For OO_1, this enables the study of the effects of data-assimilation versus linear admittance, while for SO_1, then bounded by solutions on both sides, it allows for assessing the impact of extrapolation versus interpolation.

The first two larger tides to be extrapolated on the other side of the diurnal band are σ_2 and $2Q_1$, both with an astronomical TGP larger than that of SO_1 and a similar distance of extrapolation as SO_1 and OO_1 (see Figure 2.7). Increased amplitudes in GRACE(-FO) post-fit residuals are indeed also visible at the periods of σ_2 and $2Q_1$, but only at a few grid cells; the same applies to the data-constrained Q_1, which would be the pendant of J_1 on the other side of the band (see Figure 4.15f). All of these three tides slightly underpass the threshold of $n_p = 25$ and are therefore not listed in Table 4.3. Considering that the astronomical potential of Q_1 is about twice as large as that of J_1, it seems quite plausible that the increased residuals of OO_1 and SO_1 might be caused by the lack of data assimilation.

The locations of the increased amplitudes of τ_1 in Figure 4.18 strongly correlate with the locations where the total amplitude of this constituent is the largest, see e.g., the maps of the hydrodynamic TiME22 solutions (Sulzbach, 2023) and also the altimetry amplitudes in Section 4.5.6. This might be suggestive of a significant over- or underestimation of the amplitudes at the period of τ_1. A potentially relevant non-linear contribution from MP_1 might also explain the relatively large observed amplitudes at the period of τ_1; possibly also the non-linearity included in the diurnal ocean tide model solutions used for linear interpolation. Utilizing the hydrodynamic TiME22 solution (contains the gravitationally excited part) for orbit modeling instead of the inclusion of τ_1 through linear admittance could possibly provide a bit more insight.

Among the semidiurnal tides considered via linear admittance and listed in Table 4.3 are α_2 and β_2, both with a TGP smaller than that of the previously discussed diurnal tides. Both of these gravitationally excited constituents share the same frequencies with the non-linear tides $M(SK)_2$ and $M(KS)_2$. Directly adjacent to α_2 and β_2, and inseparable from these tides, are the non-linear tides MPS_2 and MSP_2. The periods of the latter coincide with MA_2 and MB_2, which are the seasonal lines of the principal semidiurnal tide M_2 (e.g., Müller et al., 2014; Ray, 2022). Consequently, it is possible that a rather complex combination of contributions from various non-linear sources may be responsible for the relatively large amplitudes of $\alpha_2/M(SK)_2$ and $\beta_2/M(KS)_2$ presented in Table 4.3. A simulation of the M_2 seasonal modulation using a high-resolution ocean circulation and tide model was carried out by Müller et al. (2014). According to these simulations, seasonal modulations of M_2 are particularly pronounced in the Arctic region and several non-Arctic coastal regions. Therefore, especially the increased amplitudes present in the GRACE(-FO) post-fit residuals in the Artic region (and the absence of variations around Antarctica) may be indicative of a seasonal modulation of M_2 (compare with Figure 3 of Müller et al., 2014). Indeed, when considering only data from the periods May to October or November to April for spectral analysis, the seasonality of M_2 in the GRACE(-FO) post-fit residuals across the Arctic region becomes clearly evident. The difference of the amplitudes of these two

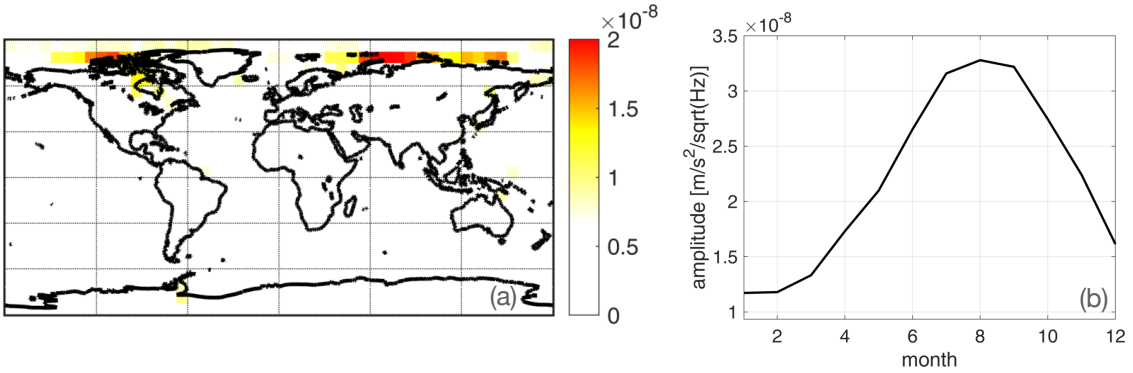

FIGURE 4.24: Seasonality of the residual M_2 signal in GRACE(-FO) post-fit residuals. (a): Difference of spectral amplitudes computed from post-fit residuals of the months May to October and November to April on a 7.5°×7.5° grid. Units: $m/s^2/\sqrt{Hz}$. (b): Seasonal variation between Novaya Zemlya and Franz Josef Land from a 6-month sliding window spectral analysis (1: November to March, 2: December to April,...).

periods can be seen in Figure 4.24a. A certain seasonality is present in most grid cells; however, the most substantial differences are to be found in the Arctic region, which correlates with the location of increased amplitudes in the maps of α_2 and β_2. As can be recognized in Figure 4.24b, which depicts the monthly spectral amplitudes for a grid cell located between Novaya Zemlya and Franz Josef Land, derived from a 6-month sliding window spectral analysis (where the January amplitude is based on data from November to March, February from December to April, etc.), the largest residual signal is to be found in summer and the beginning of autumn, while in winter the M_2 amplitude is dampened, presumably due to the friction with ice (e.g., St-Laurent et al., 2008). To further investigate the elevated residuals at the frequencies of α_2 and β_2, ocean tide solutions for MA_2, MB_2, as well as the non-linear components, would be required. However, currently, there are no solutions that have been made accessible in the form of amplitudes and phases or as spherical harmonic coefficients. To explore the potential influence of the M_2 error in the Arctic region on α_2 and β_2 through linear admittance, recently published solutions including CryoSat-2 data are of interest (Andersen et al., 2023).

4.5.4 Unmodeled Partial Tides

The major part of the unmodeled constituents found in the GRACE(-FO) ll-SST residuals and mentioned in Table 4.3, are not part of present-day data-constrained ocean tide models (compare Table 2.8), and have never been mapped globally (Koch et al., 2024b).[2] Only a few years ago, the four largest degree-3 tides $^3L_2$, $^3N_2$, $^3M_1$ and $^3M_3$ were mapped on a near-global scale (latitudes: −66° to +66°) using TOPEX/Poseidon and Jason altimetry observations (Ray, 2020b). The empirical nearly-global solutions of these four degree-3 tides are part of the GOT5.6 ocean tide model. For the degree-3 tides, altimetry data has been assimilated solely into the $^3M_3$ solution of TPXO9 and TPXO10. So far, no data-constrained ocean tide solutions have been published for the other identified unmodeled partial tides.

For the tidal constituents discussed in this section, several data-unconstrained simulations are available. In Platzman (1984), $^3M_1$ and $^3N_2$ are simulated on a coarse grid by means of the synthesis of normal modes. A numerical model of $^3M_1$ is presented in Woodworth (2019). The response of the oceans to the atmospheric tides R_3, T_3, S_3 is simulated in Ray et al. (2023). A hydrodynamic map for the non-linear tide $2SM_2$ is shown in Weis et al. (2008). The TiME22 model provides an extensive catalog of over 50 hydrodynamically modeled partial tides Sulzbach et al. (2021, 2022), including $^3L_2$, $^3N_2$, $^3M_1$, $^3M_3$, and R_3, T_3, and S_3. No hydrodynamic simulations are available for the compound tides $2MK_3/MO_3$.

[2] This of course also applies to some of the frequencies discussed previously in Section 4.5.3. However, in contrast to the partial tides discussed here, the linear admittance can be used to model the gravitational part, although with its limitations.

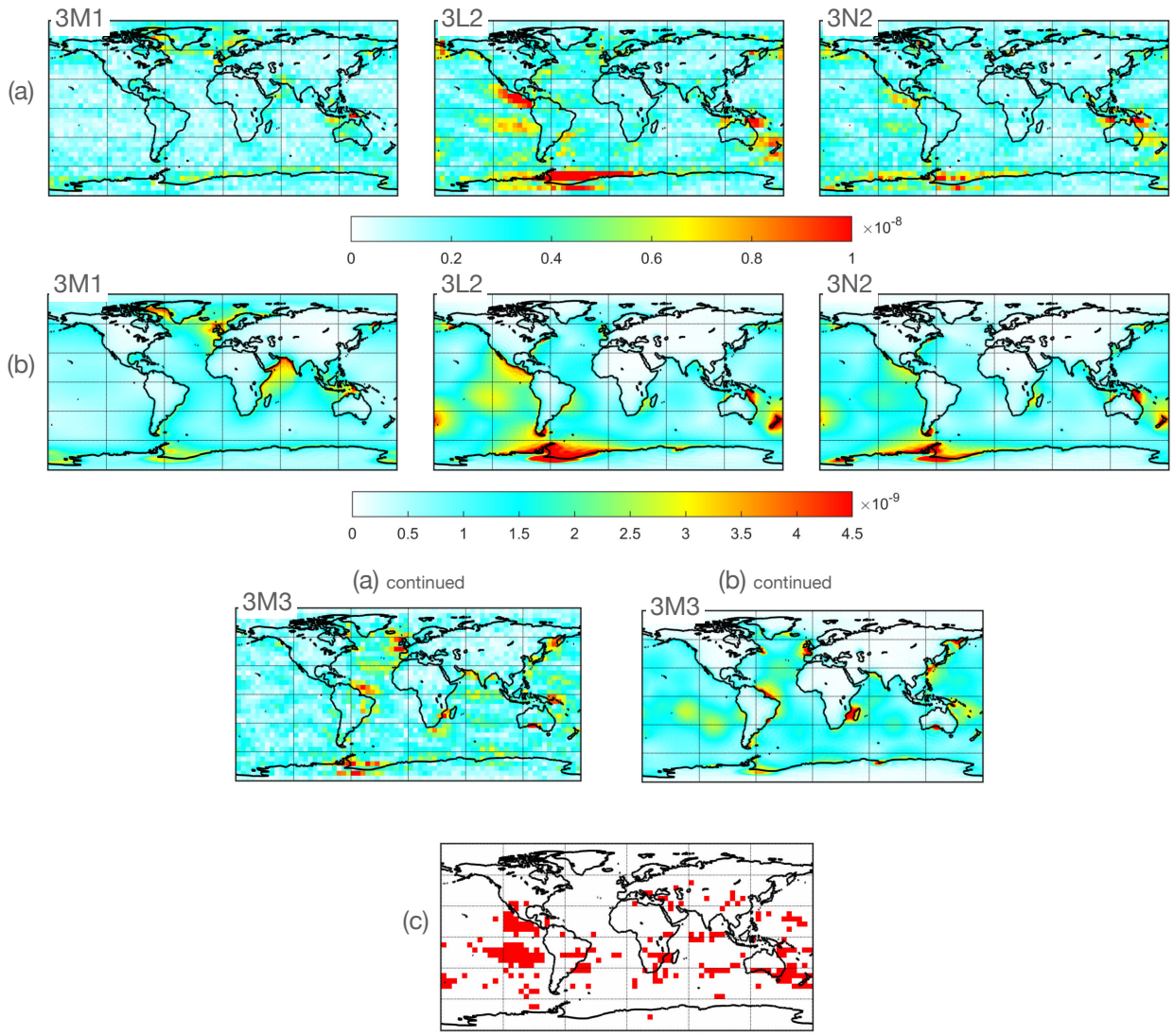

FIGURE 4.25: Comparison of amplitude patterns in RMS spectral amplitude maps with hydrodynamic TiME22 solutions. (a): Amplitude maps of astronomical degree-3 constituents ${}^3M_1$, ${}^3L_2$, ${}^3N_2$, ${}^3M_3$ on a $5°\times5°$ grid. (b): Daily maximum acceleration norm amplitudes computed from hydrodynamic TiME22 solutions on a $1°\times1°$ grid for the 1 January 2000. Units of the color axes are $m/s^2/\sqrt{Hz}$ for RMS amplitude maps, and m/s^2 for hydrodynamic solutions. (c): Grid cells where ${}^3M_1$, ${}^3L_2$, ${}^3N_2$, ${}^3M_3$ amplitudes are larger than the amplitudes of any other constituent.

In Figures 4.25 and 4.26, amplitude maps derived from GRACE(-FO) ll-SST residuals are compared to the hydrodynamic TiME22 solutions. The maps from TiME22 illustrate the maximum daily amplitude in terms of acceleration vector magnitude computed on a $1°\times1°$ grid. These values refer to the surface of the Earth. Amplitudes evaluated at satellite altitude appear smoothed and spatially blurred, making them in terms of details of smaller spatial features less comparable to the ll-SST maps (see supporting information of Koch et al., 2024b).

For the diurnal degree-3 tide ${}^3M_1$, identified in Table 4.3 by its TGP as the smallest of the four astronomical degree-3 tides, clear distinctive similarities with the hydrodynamic model TiME22 are apparent (see Figure 4.25a,b). These include increased amplitudes in the northern Atlantic, along the coast of Antarctica, and the total maximum located at the southern coast of Papua. The location of the maximum amplitude of ${}^3M_1$ also perfectly aligns with altimetry observations (Ray, 2020b). Relative to the hydrodynamic solutions, and also to altimeter measurements, where the amplitudes in the Indian Ocean are even stronger than in the Atlantic, the ll-SST data amplitudes in the Indian Ocean are significantly dampened. The ll-SST maps for the semidiurnal partial tides ${}^3N_2$ and ${}^3L_2$, exhibit very similar amplitude patterns, featuring notable

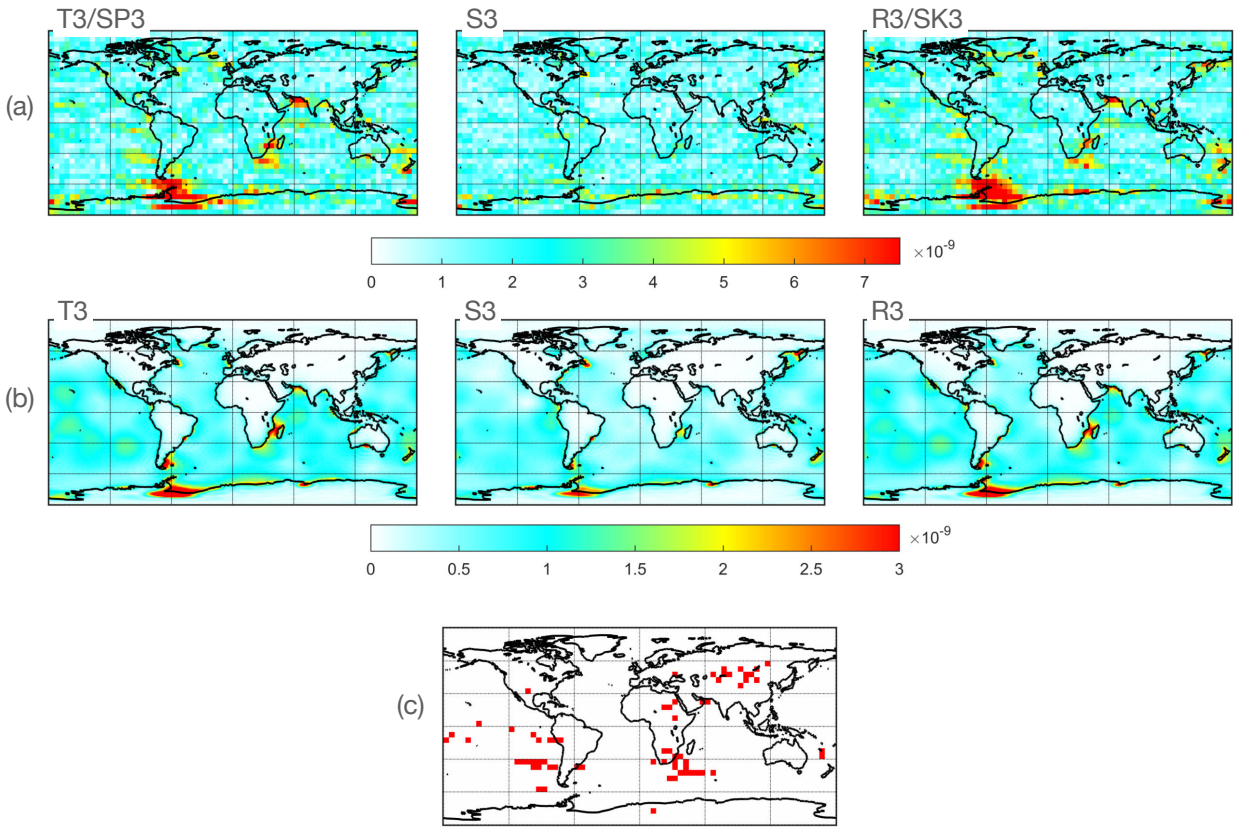

FIGURE 4.26: Comparison of amplitude patterns in RMS spectral amplitude maps with hydrodynamic TiME22 solutions. (a): Amplitude maps of T_3/SP_3, S_3, R_3/SK_3 on a $5^\circ \times 5^\circ$ grid. (b): Daily maximum acceleration norm amplitudes computed from hydrodynamic TiME22 solutions on a $1^\circ \times 1^\circ$ grid for the 1 January 2000. Units of the color axes are $m/s^2/\sqrt{Hz}$ for RMS amplitude maps, and m/s^2 for hydrodynamic solutions. (c): Grid cells where T_3/SP_3, S_3, R_3/SK_3 amplitudes are larger than the amplitudes of any other constituent.

oscillations in the Pacific Ocean (including eastern Coral Sea), the Weddell Sea, coasts of New Zealand, and somewhat less pronounced oscillations in the Atlantic and Indian Oceans. These general patterns, along with the relatively larger amplitudes of $^3L_2$ compared to $^3N_2$—even though $^3L_2$ has a slightly weaker TGP—and the generally larger amplitudes relative to $^3M_1$, align with the TiME22 solutions and altimetry observations. The data-unconstrained "M_3" solution included in FES2014b has rather small amplitudes and models only the non-linear contribution at this frequency. The larger gravitational excitation is not considered. In terms of acceleration at an altitude of 425 km, the maximum values differ by one magnitude (few 10^{-10} m/s^2 for FES2014b and 10^{-9} m/s^2 for the degree-3 tide from TiME22). Consequently, the $^3M_3$ ll-SST signal shown in Figure 4.25a shares amplitude pattern similarities with the hydrodynamic TiME22 solution (see Figure 4.25b) with notable oscillations, for example, northeast of Brazil, in the northern Atlantic between the British Isles and Spain, the Mozambique Channel, the Sea of Okhotsk, and the Great Australian Bight. These patterns can also be observed in altimetry data (see Ray, 2020b, Figure 1), and altimetry-constrained solutions of TPXO9 model (Egbert and Erofeeva, 2002, updated). A map of the amplitude of the latter can be found in Devlin et al. (2023, Figure 1). As can be seen in Figure 4.25c, the ll-SST amplitudes of one of the four degree-3 tides are always greater than those of any other constituent listed in Table 4.3 across extensive ocean regions, particularly in the Eastern Pacific.

Unlike the previously discussed tides, which are of astronomical origin, S_3 has a negligible gravitational contribution (e.g., Hartmann and Wenzel, 1995), and the constituent is assumed to have a mainly radiational origin (e.g., Balidakis et al., 2022; Ray et al., 2023). Although S_3 has the smallest amplitudes among

the constituents in Table 4.3 and therefore a relatively low signal-to-noise ratio, several distinct features are still noticeable in the corresponding ll-SST map in Figure 4.26a. Some prominent features of S_3 are the increased amplitudes along the Antarctic coast, accompanied by localized resonances in the Sea of Okhotsk, Celebes Sea, northeast of Papua New Guinea, and near New Zealand and Newfoundland. Most of these locations also stand out in the TiME22 solutions (see Figure 4.26b) and, to some extent, in the modeled ocean's response to the S_3 air pressure tides presented in Ray et al. (2023, Figure 6). R_3 and T_3 are annual side lines of S_3, differing from it by one cycle per year, and at the same time respectively share their frequencies with the compound tides SK_3 and SP_3 (Ray et al., 2023). The ll-SST amplitude maps of R_3/SK_3 and T_3/SP_3, as illustrated in Figure 4.26a, exhibit pattern similarity, with the most prominent amplitude clusters located in Antarctica, the northern Arabian Sea, at Africa's southeastern coast, and around New Zealand. This similarity is characteristic for a radiational origin (compare Figure 4.26b and Ray et al. (2023)). As can be seen in Figure 4.26c, also these three tides are significant in a few oceanic regions, where they exhibit larger amplitudes than any other constituent.

There are no publicly available solutions for the compound tides $2SM_2$ (the combination S2+S2−M2) and $2MK_3/MO_3$ (M_2+M_2−K_1 and M_2+O_1, respectively), so a comparison like the one shown in Figures 4.25 and 4.26 for the previously discussed tides cannot be made. However, an amplitude map of $2SM_2$ from hydrodynamic modeling is depicted in Weis et al. (2008, Figure 7a), with which the ll-SST amplitudes share several similarities, including increased amplitudes northwest of Australia and in the Weddell Sea. Noticeable larger oscillations in the ll-SST map, occurring in the Bay of Bengal and the Arctic region, as well as several other localized resonances, are not apparent in the hydrodynamic solution. Contrary, the significant amplitudes in the Mozambique Channel present in the hydrodynamic solution do not appear in the ll-SST maps. The combined ll-SST map of $2MK_3/MO_3$ highlights increased amplitudes in the western Weddell Sea, around the Antarctic Peninsula, and in the Patagonian shelf. From in situ GPS measurements it is known that MO_3, M_4 and SP_3 are among the largest non-linear tides in the Weddell Sea (King et al., 2011).

Section 4.5.6 will attempt to qualitatively validate the global structures of the just recently discussed frequencies, which lack available data-based references, by using independent altimetry data. However, the logical next step for the other partial tides is to incorporate the respective hydrodynamic solutions from TiME22 into the gravity field processing. To evaluate the impact of the degree-3 tides on the post-fit residuals, reprocessing only the GRACE time series is completely sufficient, as the data length allows for the separation of $^3L_2$ and $^3N_2$ from the degree-2 components (see Koch et al., 2024b, Figure 7), and is also long enough to study terdiurnal effects. Figure 4.27 illustrates the impact of including the four degree-3 tides and the radiational tides on the GRACE post-fit residuals. The shown maps of the diurnal and semidiurnal constituents were evaluated in the period boundaries as defined in Table 4.3. For the terdiurnal tides observed at the spectral replica periods in the diurnal band, the offset of the left and right boundaries was chosen 2.5 times larger, to take into account the influence of the missing GRACE-FO data on the spectral location and variance of the replicas. For all of the four degree-3 tides, a significant reduction of the residuals can be observed. In the map of $^3L_2$ still increased amplitudes are to be found in the Argentine Basin near the Zapiola rise. Large-scale variations at intraseasonal periods from 20 to 30 days are well known here (e.g., Fu et al., 2001; Weijer et al., 2007; Yu et al., 2018). Therefore, due to the 27-day aliasing period of $^3L_2$, the remaining elevated amplitudes may represent non-tidal variability. In fact, in the maps of the GRACE(-FO) post-fit residuals, relatively large variations in the Argentine Basin are evident across broader period bands (around 15–75 days), whereas the patterns of increased amplitudes typical for $^3L_2$, e.g., in the Pacific Ocean, are very sharply localized, and disappear even after a small deviation from the $^3L_2$ period. A similar observation can be made for the elevated amplitudes in the Arctic region, which could indeed also depict intraseasonal non-tidal variability. In the case of $^3M_3$, relatively large amplitudes remain present in

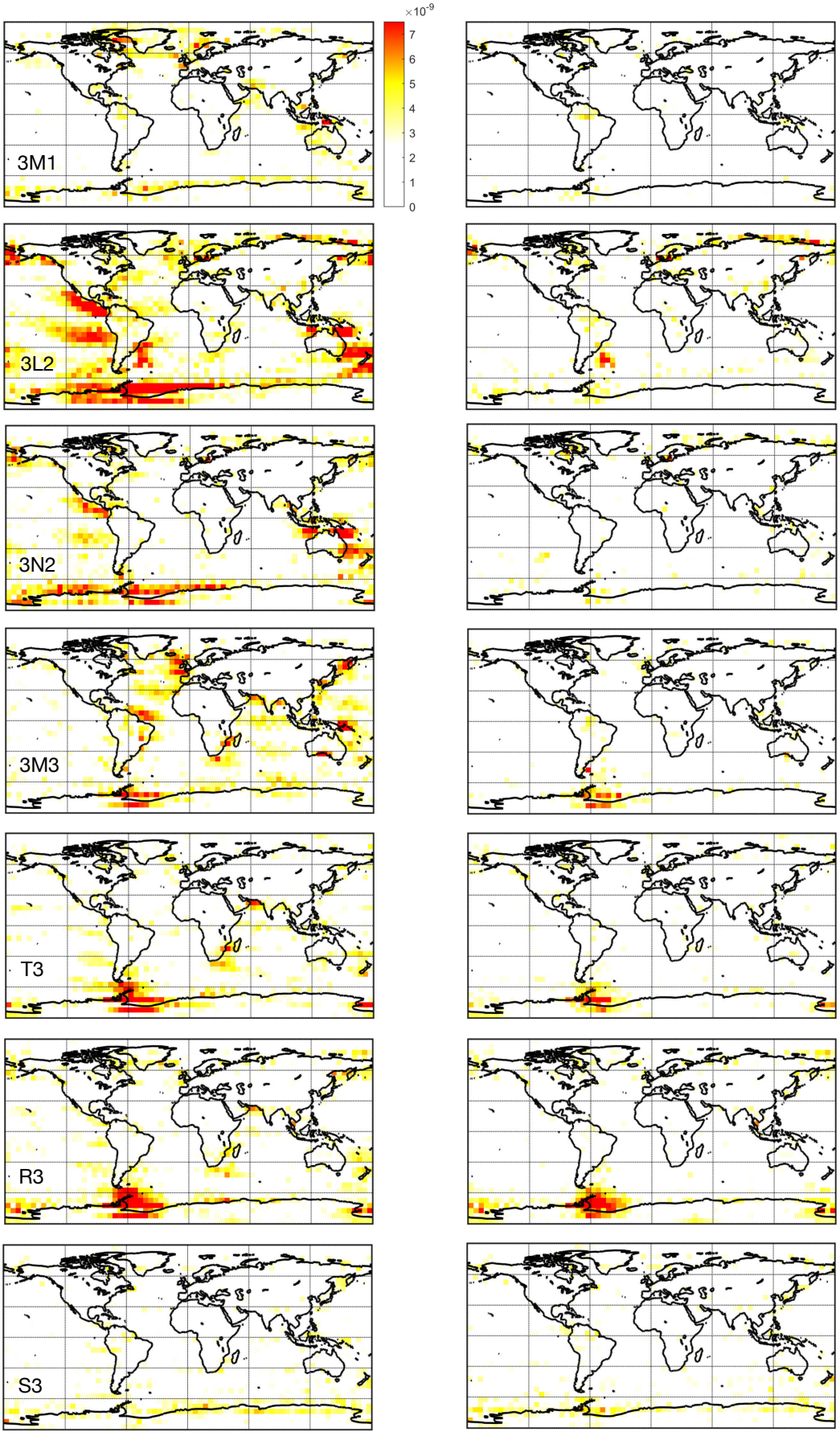

FIGURE 4.27: Amplitude maps from GRACE range-rate post-fit residuals without (left) and with the degree-3 and radiational tides from TiME22 (right). Units: $\mathrm{m/s^2/\sqrt{Hz}}$.

the Weddell Sea, possibly highlighting regional challenges in modeling of the hydrodynamic solution. A significant reduction of the amplitudes can also be observed for R_3 and T_3, with the exception of the two larger marginal seas of the Southern Ocean. In this context, aside from the potential under- or overestimation of the R_3 and T_3 amplitudes, it cannot be dismissed that the remaining signal is related to the compound tides SK_3 and SP_3. Generally, the map of S_3 also tends to have slightly smaller amplitudes after the inclusion of the hydrodynamic solution, although the improvements on a global level are not as clear as for the other tidal components. In a few separate grid cells, however, slightly higher amplitudes can be observed. It should be noted again that, according to Table 4.3, S_3 exhibits relatively small amplitudes in the GRACE(-FO) post-fit residuals, making it more uncertain to validate the influence of the S_3 hydrodynamic model.

4.5.5 Examples of Aliasing in Submonthly Gravity Field Solutions

The aliasing periods for each of the constituents, given by $1/\min(f_A)$ (with f_A as defined in Equation 4.1), are listen in Table 4.3. Consistent with the spectral replication scheme outlined in Table 4.2, for even band waves, such as those from the semidiurnal band, amplitude maps evaluated at the aliasing period or any other identified spectral replica period will exhibit nearly identical amplitude patterns, with differences that mainly occur at highest latitude grid cells. In contrast, no agreement can be expected for periods from an uneven band. Potential aliasing can therefore only be expected for constituents from one of the even bands if the high-polar regions are disregarded. Since most of these even band constituents have submonthly aliasing periods, the associated model errors cannot be directly observed in the time series of the monthly gravity field solutions. As the temporal resolution of the gravity field time series improves, the likelihood of detecting submonthly aliasing signals also increases, when assuming the amplitude of the residual or unmodeled signal is significant enough. In this section, examples of aliasing are illustrated for the following time series:

- TUG: daily ITSG-Grace2018 gravity fields (Mayer-Gürr et al., 2018; Kvas et al., 2019a)
- CSR: RL05 daily swath mascon solutions over the oceans (Save, 2019b)
- CNES/GRGS: RL05 10-day gravity fields (Lemoine and Bourgogne, 2020).

Considering the insufficient global coverage by the GRACE(-FO) satellites over periods significantly shorter than one month, these higher temporal resolution solutions rely on stabilization strategies compared to the typical unconstrained monthly gravity fields. The daily TUG solutions provided up to degree and order 40 combine GRACE observations with information from geophysical models in a Kalman smoother (Kurtenbach et al., 2009, 2012). The signal definition of the daily solutions aligns with the monthly solutions of the ITSG-Grace2018 series, with ocean tides reduced using the FES2014b model. Solutions of CNES/GRGS traditionally combine GRACE observations with data of SLR missions, particularly to obtain more accurate C_{20} coefficients and to solve for the degree-1 coefficients. The RL05 CNES/GRGS 10-day solutions are expanded up to degree and order 90, and are derived by combining three 10-day normal matrices, with the central matrix given double weighting (Lemoine et al., 2007). As ocean background model FES2014b is used.[3] The CSR daily swath mascon solutions are given in terms of EWH for the oceans and are limited to latitudes between $-66°$ and $66°$. A specific mascon of the daily solution is updated each time the GRACE satellites overfly it within a threshold of 250 km to the center of the mascon element (Bonin and Save, 2020). Expected signal from constrained GRACE solutions of the respective month are used as a constraint to regularize the daily solutions. Moreover, a land-ocean boundary mask is employed for regularization. CSR RL05 solutions utilize GOT4.8 for modeling the contribution of diurnal and semidiurnal ocean tides, as well as selected long-periodic components from other models (see Bettadpur, 2012). The contribution of these

[3]Details on background models, processing, and the inversion method of the CNES/GRGS RL05 solutions can be found here: `https://grace.obs-mip.fr/variable-models-grace-lageos/grace-solutions-release-05/rl05-products-description/` (last accessed on 2025-01-30).

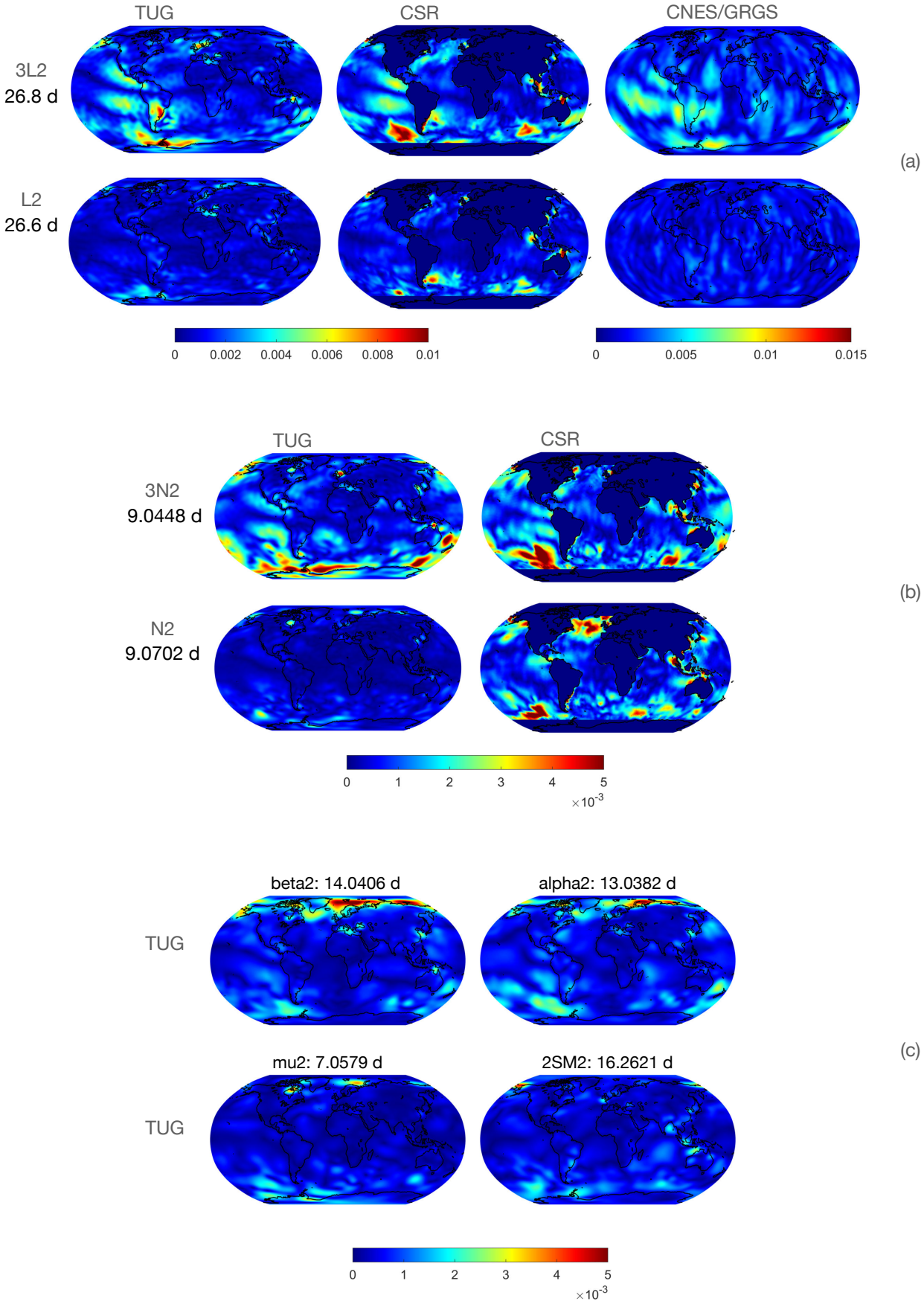

FIGURE 4.28: EWH amplitudes in meters at the aliasing periods of $^3L_2$, L_2 in daily TUG solutions, daily swath solutions over the oceans of CSR, and 10-day solutions of CNES/GRGS (a); $^3N_2$, N_2 in daily TUG and CSR solutions (b); α_2, β_2, μ_2 and $2SM_2$ in daily TUG solutions (c).

tidal components is reduced from the daily solutions. While the other two submonthly series do not include non-tidal mass variation over the oceans and in the atmosphere (AOD1B RL06 was applied as a background model during gravity field recovery), the non-tidal contribution from AOD1B RL05 products (Dobslaw et al., 2013) is restored in the CSR daily swath solutions.

The 10-day resolution of the CNES/GRGS solutions allows for the study of only a few additional constituents with aliasing periods of 20 days or longer. In contrast, from a temporal resolution perspective, the daily solutions enable the examination of the spatial amplitude structures at every aliasing period listed in Table 4.3. Figure 4.28 illustrates the EWH amplitude maps at the aliasing periods of the semidiurnal degree-3 tides $^3L_2$, $^3N_2$ and their degree-2 counterparts L_2 and N_2. These amplitudes were obtained by adding the respective harmonic tidal term to the model in Equation 2.51, with the model being extended by just one tidal period for each constituent studied. Simultaneously estimating reasonable amplitudes for a degree-2 and its degree-3 counterpart is also impossible because of the very close proximity of these periods, especially for N_2 and $^3N_2$. The C_{20} coefficients were not substituted in any of the time series. In the case of the CSR daily swath solutions, no reduction of AOD was carried out. The EWH time series of CNES/GRGS was filtered with a Gaussian filter with a smooothing radius of 400 km. The $^3L_2$ EWH amplitude maps of all three submonthly time series clearly highlight increased amplitude structures in the Pacific Ocean, around New Zealand, and in the Weddell Sea that are also present in the GRACE(-FO) post-fit residuals and in the hydrodynamic solutions (see e.g., Figure 4.25). The increased amplitudes in South America present in the TUG and CNES maps cannot be observed in the post-fit residuals maps. In the post-fit residuals, however, increased residuals can be found on the coast, which would lead to the hypothesis that the patterns over the continent might be an artifact of the stabilization strategy. In contrast, no notable mass variations are observed in the L_2 maps of TUG and CNES, which to a certain degree is in alignment with the overall smaller amplitudes observed in the post-fit residuals, although the L_2 map also highlights several distinct regions of increased amplitudes (see Figure 4.20). Also in the L_2 map of CSR the larger degree-3 related structures disappear. The remaining signal that can be seen, particularly the larger structures such as north of Antarctica in the Pacific and Indian Oceans, can likely be attributed to the restored non-tidal mass variations. As discussed in Section 4.5.4, increased values for $^3N_2$ are expected at similar locations as for $^3L_2$, but with an overall slightly smaller amplitude. Indeed, the typical structures in the Pacific Ocean, around New Zealand, and in the Weddell Sea (only TUG) can also be observed for $^3N_2$. EWH maps from the daily solutions of TUG for four additional constituents are shown in Figure 4.28c. As expected, qualitative agreements with the ll-SST maps can also be observed here.

4.5.6 Amplitude Patterns of Selected Constituents in Altimetry Data

The methods for analyzing GRACE(-FO) post-fit residuals, introduced at the beginning of this chapter, which involve geographical binning of data followed by spectral analysis using Lomb–Scargle periodograms, can certainly also be applied to other data time series. In this section, SLA data (see Equation 2.63) obtained from the measurements of satellite altimetry missions TOPEX/Poseidon, and Jason-1, Jason-2 and Jason-3 are analyzed. As discussed in Section 2.3.3, data-constrained ocean tide models primarily rely on measurements from these altimetry missions. This is because their orbit design, with a 9.9156-day repeat cycle, is specifically optimized for observing the largest ocean tide constituents (Parke et al., 1987; Fu et al., 1994), although limited to the low- to mid-latitudes ($\pm 66°$) and a rather coarse ground track. The SLAs are obtained from DGFI's OpenADB[4]. The data utilized contains the following time series:

- TOPEX/Poseidon from 1992-09-25 to 2002-08-15
- TOPEX/Poseidon Extended Mission (EM) from 2002-09-17 to 2005-10-08

[4] `https://openadb.dgfi.tum.de` (last accessed on 2025-08-04)

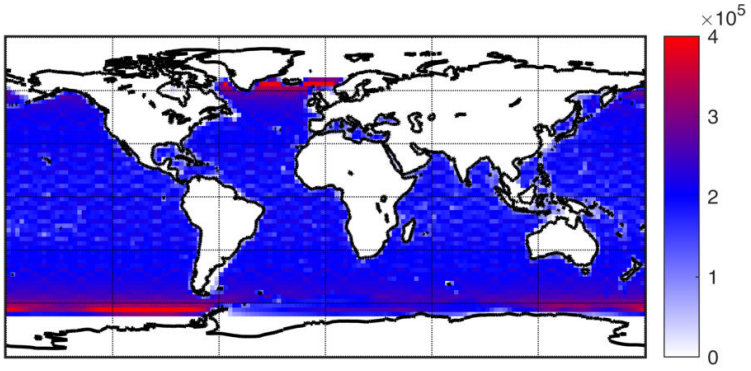

FIGURE 4.29: Number of SLA observations for the TOPEX/Poseidon, Jason-1, -2, and -3 time series binned on a 2.5°×2.5° grid.

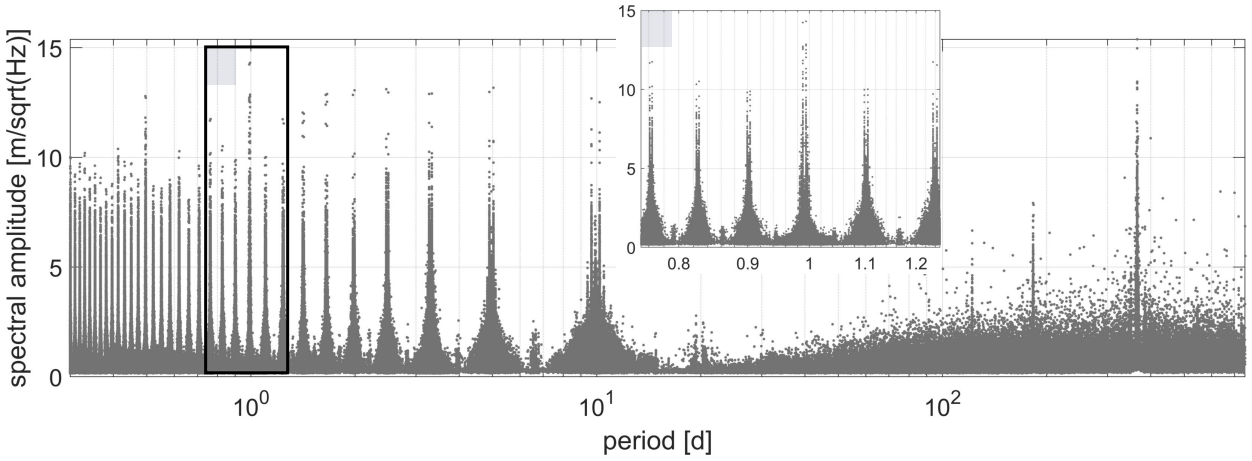

FIGURE 4.30: Above 3-sigma periodogram (compare Section 4.3.1 and Figure 4.12) of TOPEX/Poseidon and Jason-1, -2, -3 SLA on a 2.5°×2.5° grid. X-axis limited to periods from 0.3 to 750 days.

- Jason-1 from 2002-01-15 to 2009-01-26
- Jason-1 EM from 2009-02-10 to 2012-03-03
- Jason-2 from 2008-07-12 to 2016-10-02
- Jason-2 EM from 2016-10-13 to 2017-05-17
- Jason-3 from 2016-02-17 to 2022-04-07.

Data collected during the geodetic mission phases are not considered due to their different signal sampling characteristics. The number of SLA observations per 2.5°×2.5° grid cell is shown in Figure 4.29. Due to the orbit design of TOPEX/Poseidon, Jason-1, -2, and -3, no SLA observations are available for latitudes beyond −66° and +66°. Moreover, for several shallow water regions no SLA observations are provided.

Figure 4.30 shows the "above 3-sigma" periodogram derived from the SLA time series of TOPEX/Poseidon and Jason. The SLA values were binned into a 2.5°×2.5° grid. The algorithm shown in Figure 4.11 to minimize spectral leakage and replication from the GRACE(-FO) periodograms was not applied here due to the different characteristics of the altimetry periodograms. Accumulation of energy can be observed at integer multiples of the 1 per 9.9156 days sampling frequency. Even though the annual and semiannual constituents of the ocean tide model subtracted from the SLA account for the full signal at these frequencies, the accumulations at integer multiples of the sampling frequency are primarily dominated by seasonal signal, with the largest contributions from the annual and semiannual peaks, alongside significant mesoscale

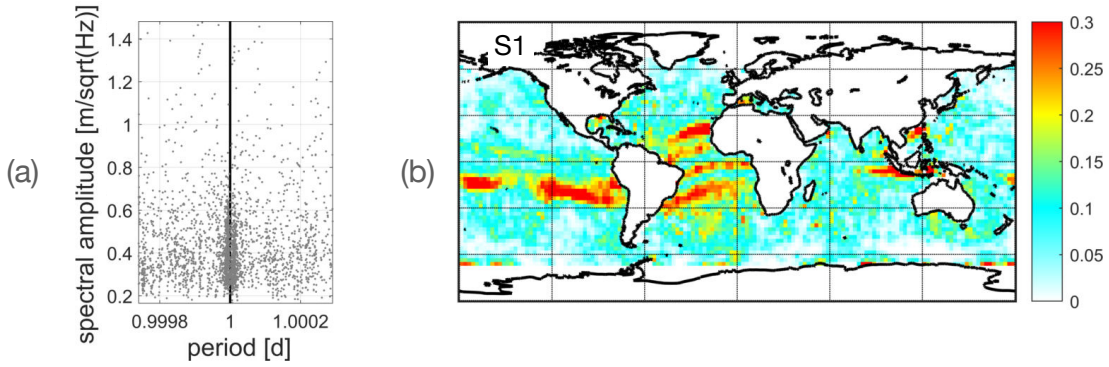

FIGURE 4.31: Residual SLA signal at the period of the S_1 constituent in TOPEX/Poseidon and Jason altimetry data. (a): Zoom on S_1 in Figure 4.30, (b): amplitude map in m/$\sqrt{\text{Hz}}$.

and interannual contributions. The informational content therefore differs significantly from that of the GRACE(-FO) range-rate post-fit residuals.

For visualizing the amplitude maps, the algorithm used earlier in this chapter for the GRACE(-FO) post-fit residuals is slightly extended. Similarly, the RMS value is calculated within a predefined range around a tidal line of period p (see Figure 4.17). For simplicity, an empirical and constant half-width of $\delta = 1{\times}10^{-5}$ or $\delta = 4{\times}10^{-5}$ days is chosen, depending on the variance of the constituent. In addition, the RMS maps to the left $(p - 3\delta \pm \delta)$ and right side $(p + 3\delta \pm \delta)$ of the tidal lines are evaluated. The mean value of the map to the right and left is subtracted from the map of the tidal line at $p \pm \delta$. The half-width δ is is selected to be sufficiently small to prevent overlap between degree-2 and degree-3 tides. The most significant signal in the mean amplitude maps is often found along the various ocean currents. Consequently, after subtracting the mean, a positive amplitude value indicates that the signal at the tidal period is greater than at the surrounding periods, where no tidal signal is anticipated. Finally, the negative amplitude values are set to zero and a slight Gaussian smoothing is applied to the obtained map.

Since the SLA products have already been corrected for ocean tides using the EOT20 model—an empirical model derived from a residual harmonic analysis of satellite altimetry data relative to FES2014—significant variations at the periods of the 17 tidal constituents included in the model (see Table 2.8) are not expected, except for Sa and Ssa. Indeed, the periodograms at the frequencies of these constituents reveal no evidence of significant residual tidal signal. However, an exception is S_1, where clustering typical of residual tidal signal can be observed (see Figure 4.31a). In the corresponding amplitude map presented in Figure 4.31b, increased amplitudes are observed near the geomagnetic equator, likely indicating errors in the ionospheric delay correction (Ray, 2020a; Hart-Davis et al., 2021). In the amplitude maps of the annual side lines of S_1 which capture its seasonal variability, i.e., P_1 and K_1 (Ray, 2020a), similar patterns can be seen, albeit in a much attenuated form. In contrast, no anomalies are observed at S_2 and its annual side lines. In the amplitude maps of the other constituents included in EOT20 (not shown), there is little, if any, significant residual tidal signal to be seen, except closer to the Antarctic region for several constituents, and for J_1 along the Pacific coast of North and South America.

There are altimetry-constrained solutions of 5 constituents in the a pirori model (FES2014), but for which no empirical solution in EOT20 is available: L_2, λ_2, ν_2, μ_2 and ε_2. For μ_2, and to a certain degree L_2, relatively large residual signal is evident over extensive ocean areas in the analyzed SLA time series (see Figure 4.32). The constituent μ_2, with an excellent signal-to-noise ratio, emerges as a promising candidate for an updated version of the EOT model, followed by L_2 and then λ_2. Among the five constituents, ν_2 and ε_2 have the smallest signal-to-noise ratio. Nevertheless, also in the maps of these constituents (not shown), signal likely of tidal origin is evident in several marginal seas.

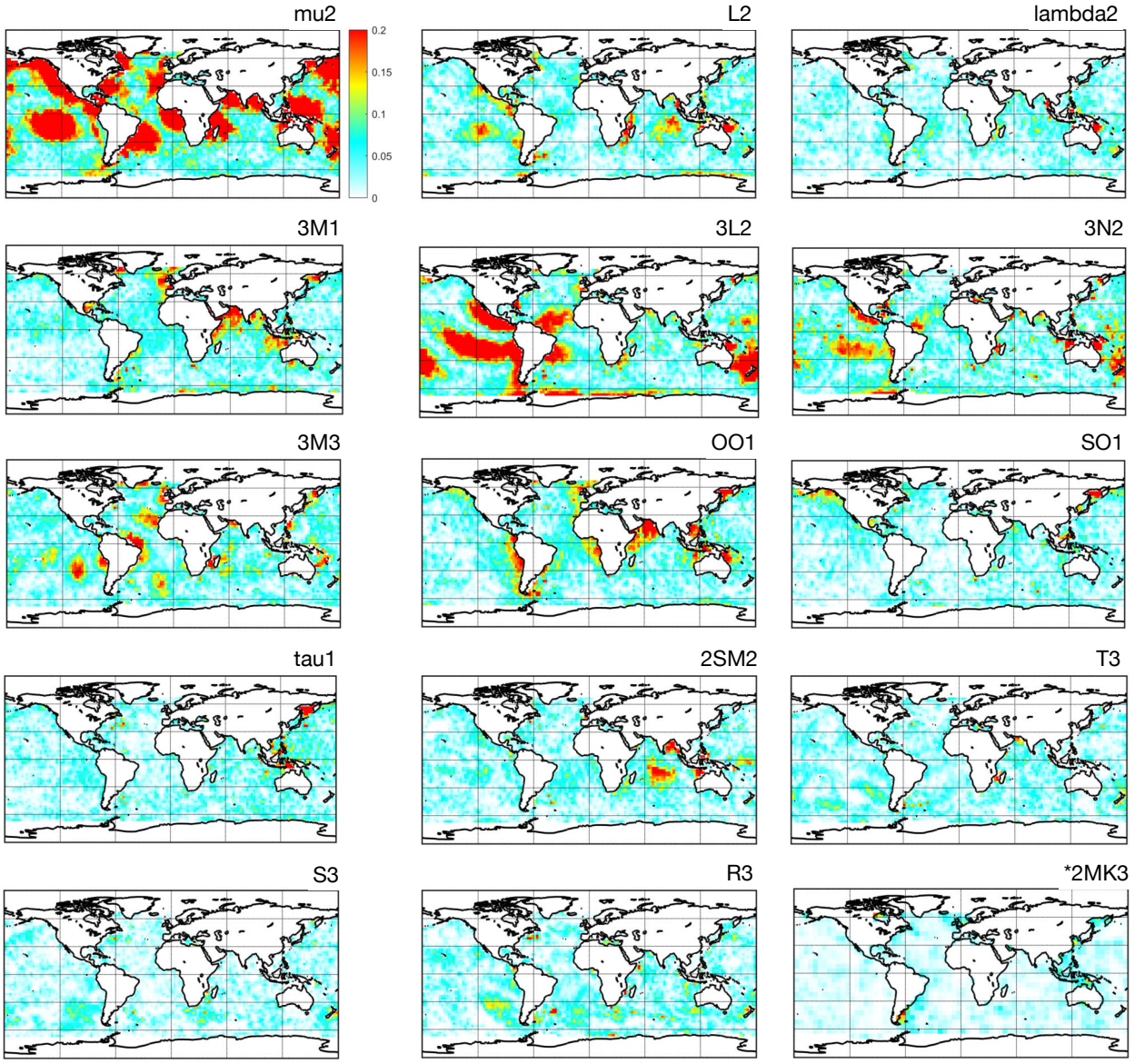

FIGURE 4.32: TOPEX/Poseidon and Jason altimetry SLA amplitudes in m/$\sqrt{\text{Hz}}$ at the periods of selected constituents. For $2MK_3$ the amplitudes refer to the ERS-1, -2, and Envisat time series.

The amplitude patterns of the four largest degree-3 tides, illustrated in Figure 4.32, display similarities to patterns found in GRACE(-FO) post-fit residuals, hydrodynamic solutions, and altimetry solutions of Ray (2020b). Interestingly, and somewhat counterintuitively, the amplitudes of $^3L_2$ are more pronounced than of L_2, despite the latter having a larger TGP.

The three radiational frequencies T_3, S_3, R_3 exhibit in the TOPEX/Poseidon and Jason SLA time series a rather small signal-to-noise ratio. Nonetheless, it is evident that in several regions—such as the Pacific Ocean east of South America, the Mozambique Channel, around New Zealand, and the northern Arabian Sea—the ocean tide signal emerges distinctly from the noise. However, in the map of R_3, several grid cells exhibit increased amplitudes that are likely of non-tidal origin. These areas are located in the southern Atlantic and Indian Oceans, as well as east of North America. These amplitudes are present in the R_3 map because the TOPEX/Poseidon and Jason aliasing period for R_3 is closer to seasonal periods.

For the compound tide $2SM_2$, the amplitude distribution shows a qualitative agreement with the GRACE(-FO) ll-SST amplitude maps with pronounced sea level variations in the Bay of Bengal, northwest of Australia, around Great Britain and France, and in the marginal seas of the Pacific between Indonesia and the Philippines. The TOPEX/Poseidon, Jason-1, -2, and -3 altimetry data highlights notable variations in the middle

of the Indian Ocean, not noticeable in the GRACE(-FO) ll-SST maps. However, slightly elevated EWH values were previously recognizable at the aliasing frequency of $2SM_2$ in the daily Kalman-filtered gravity field solutions of TUG. Also in the hydrodynamic simulation of Weis et al. (2008) slight variations in this region are recognizable with an amplitude of 0.5 to 1 cm.

According to the GRACE(-FO) ll-SST maps, the amplitudes of $2MK_3/MO_3$ are most pronounced in the regions of the Antarctic Peninsula and the Patagonian Shelf (see Figure 4.19). Due to the inclination of TOPEX/Poseidon and Jason-1, -2, and -3 orbits, the signal in the region of the Antarctic Peninsula cannot be verified. For the grid cells in the Patagonian Shelf, either no data is available or there is only a very limited number of SLA observations (see Figure 4.29). Therefore, also in this region the signal at the period of the compound tide cannot be verified with TOPEX/Poseidon, Jason-1, -2, and -3 data. Specifically for $2MK_3/MO_3$, data from the time series of the ERS-1, ERS-2, and Envisat missions was utilized. The analyzed data includes the 35-day repeat cycle phases from August 1992 to October 2010. Despite the area being significantly better covered by measurements from these satellites, the amount of data remains insufficient to adequately capture the frequency of interest on a $2.5°\times2.5°$ grid. Therefore, a $5°\times5°$ grid was utilized instead. The corresponding map in Figure 4.32, similar to the GRACE(-FO) case, shows pronounced variations localized on the Patagonian Shelf. For the assessment of the variations around the Antarctic Peninsula, unfortunately, no data is available in the analyzed dataset.

Chapter 5

Summary and Conclusions

The quality of gravity field recovery results from GRACE(-FO) data is primarily limited by the inherent noise of the electrostatic accelerometers, as well as the model inaccuracies for ocean tides and non-tidal mass variations within the Earth system—despite significant advancements in the development of background models for satellite orbit modeling and de-aliasing over the past two decades. Post-fit residuals as a byproduct of gravity field recovery are particularly valuable for assessing model inaccuracies because of their high temporal resolution and the extensive data availability spanning over two decades. In the context of this work, a time series of over two decades of post-fit residuals was examined more closely to understand the errors and identify which ocean tide constituents are the most significant.

This work showed that the ll-SST post-fit residuals contain a considerable amount of information on residual and unmodeled geophysical effects that can be effectively extracted from the K-band range-rate residuals using filtering, and to a certain degree disentangled to individual periodic components using spectral analysis tools. The Lomb–Scargle approach revealed that the periodograms in the diurnal band are almost exclusively dominated by ocean tide effects, whereas the semidiurnal band also contains significant information of a non-tidal nature. Due to the satellite sampling characteristics, these do not necessarily have to be of semidiurnal origin, since long-period mass variations also create redundant periodogram peaks in the semidiurnal band. Nevertheless, the highest peaks in the semidiurnal band can be attributed to ocean tides. Moreover, the diurnal and semidiurnal periodogram bands contain information on higher-frequency ocean tide signal by way of spectral replicas, e.g., from terdiurnal and fourth-diurnal ocean tide constituents. In total, increased amplitudes were detected at over 30 tidal frequencies, which correspond not only to the major astronomical tides but also to minor degree-2 astronomical tides, major degree-3 tides, overtides, compound tides, radiational tides, and potentially seasonal tidal modulations. Since tides of different origin can often share the same frequency, it is not always clear which specific tidal component is responsible for the increased amplitudes.

With the exception of a few tidal constituents, the amplitude maps at the respective frequencies almost exclusively show increased amplitudes in polar regions, along coastlines and confined to some regions of the open ocean, with no additional widespread variations over continents indicative of atmospheric tides. The most complex region where a large number of tidal frequencies show increased amplitudes is the Weddell Sea. The largest residual signal can be found at the periods of the major constituents O_1, M_2, K_1 and P_1. In contrast, a disproportionate discrepancy between the rather small observed error at the period of the major solar semidiurnal constituent S_2 and its large astronomical TGP is evident, suggesting that the error is being absorbed by the estimated gravity field parameters, i.e., is aliased at a period of around 161 days into the gravity field products.

Among the gravitationally excited tides not included in the ocean tide model but accounted for in the orbit modeling through linear admittance, OO_1, SO_1, τ_1, α_2 and β_2 are prominent in the GRACE(-FO) post-fit residuals. While these tides show relatively large astronomical forcing as indicated by the TGP, they are not necessarily the largest tides that are not part of the ocean tide model, suggesting that there is no strict correlation between the TGP and the observations in the GRACE(-FO) post-fit residuals. The relatively large residual signal observed at the periods of OO_1 and SO_1 might be related to their location at the edge of the diurnal band necessitating an extrapolation of the admittance, coupled with the purely hydrodynamic character of J_1, which is the nearest constituent included in the ocean tide model. By replacing the hydrodynamic J_1 solution from FES2014b with an altimetry-constrained solution from one of the recently

published ocean tide models, one could investigate the influence of data assimilation on the inference of OO_1 and SO_1. Also data-constrained OO_1 solutions have been recently published (TPXO10 and GOT5.6), which opens the opportunity to assess the OO_1 linear admittance solution, while for SO_1, then bounded by data-constrained solutions on both sides, this enables an assessment of the impact of extrapolation versus interpolation. The increased residuals at the frequencies of α_2 and β_2, which are particularly significant in the Arctic region, possibly represent seasonal modulations of M_2 due to ice friction. A pronounced seasonality of M_2 can be observed in the GRACE(-FO) post-fit residuals in the Arctic region, with the M_2 amplitudes being dampened during the winter months and reaching maximum values in the late summer. The seasonality cannot be accounted for using linear admittance, so dedicated solutions for the seasonal side lines MA_2, MB_2 are required for further investigations. The areas with heightened amplitudes of τ_1 closely align with the regions where the overall amplitude of this constituent is greatest, indicating a general underestimation or overestimation of the amplitudes. For further investigation, the hydrodynamic solution of τ_1 available in TiME22 is of interest. Data-constrained solutions for τ_1, as well as hydrodynamic solutions for the non-linear contribution at its frequency, are not yet available.

It was demonstrated that the ll-SST amplitude maps of the unmodeled partial tides $^3M_1$, $^3L_2$, $^3N_2$, $^3M_3$, T_3/SP_3, S_3, R_3/SK_3 and hydrodynamic TiME22 solutions of the corresponding degree-3 and radiational components show similarities in the location of the increased amplitudes. Analyzing a recomputed full GRACE time series, with these hydrodynamic solutions accounted for, revealed a significant reduction in the residual signal for the degree-3 tides, as well as T_3 and R_3. However, for $^3M_3$, T_3, and R_3, particularly in the Weddell Sea, prominent residual signal remains evident, which potentially highlights regional modeling challenges, or, in the case of the radiational tides, the contribution of the unmodeled compound tides SP_3 and SK_3.

In general, owing to the sampling characteristics of GRACE(-FO), the absorption of ocean tide signal by the monthly gravity field solutions can be anticipated for even period bands, for example, the semidiurnal band. Most of the relevant constituents in these bands have GRACE(-FO) aliasing periods ranging from a few days to up to a month. Therefore, a disturbing signal at these aliasing periods cannot be evaluated using the standard monthly solutions, but it can be examined in alternative gravity field products with submonthly resolution. Examples of ocean tide signal absorption have been demonstrated for daily and 10-day spherical harmonic solutions, as well as for daily mascon solutions.

The Lomb–Scargle spectral analysis method was applied to the SLA time series of satellite altimetry missions TOPEX/Poseidon, Jason-1, -2, and -3. The analyzed time series had already been corrected for 17 larger tidal constituents from the EOT20 model, but not for the smaller tides identified in the GRACE(-FO) post-fit residuals. It was shown that the locations of increased amplitudes of several constituents observable in the altimetry data exhibit similarities with those in the GRACE(-FO) data, for example, the four degree-3 tides and τ_1. The altimetry maps at the frequencies of the radiational terdiurnal triple exhibit a rather low signal-to-noise ratio. However, in several expected regions, a clear radiational ocean tide signal, previously observed in the amplitude maps from GRACE(-FO) and TiME22, can be recognized. For the compound tide $2SM_2$, for which there are currently no publicly available hydrodynamic solutions, a qualitative agreement in the amplitude distributions is also observed. Interestingly, although $2SM_2$ is a compound tide, i.e., is generated in shallow water regions, according to the TOPEX/Poseidon, Jason-1, -2, and -3 SLA time series it also exhibits pronounced variations in the middle of the Indian Ocean. In contrast, in the GRACE(-FO) ll-SST maps, no pronounced amplitudes are evident there. However, slightly elevated EWH values at the aliasing frequency of $2SM_2$ are present in alternative daily gravity field products. The signal detected in the ll-SST maps at the frequencies of $2MK_3/MO_3$ could not be verified with SLA data from TOPEX/Poseidon, Jason-1, -2, and -3, due to the coarse ground track, the inclination of the satellites, and the highly localized nature of the signal close to the coastlines. However, similar to GRACE(-FO), the SLA data from the ERS-1, ERS-2, and Envisat missions, show pronounced variations in one of the two critical regions.

Based on the findings presented, it can be concluded that analyzing GRACE(-FO) ll-SST post-fit residuals derived from monthly gravity field modeling holds tremendous potential to assess the quality of ocean tide models globally, which has not yet been fully exploited. This relates not only to the usual larger ocean tide constituents but also to smaller tides that have received little to no study thus far. The analysis of GRACE(-FO) post-fit residuals can contribute to various aspects within the domain of ocean tide modeling, gravity field recovery, and beyond that. Some thoughts on the applicability of GRACE(-FO) residual analysis, as well as ideas for future research directions, are given below:

- For smaller tides that are now increasingly being integrated into newer models and are generally more challenging to observe using satellite altimetry due to an unfavorable signal-to-noise ratio and the more complex spatial patterns, the question arises whether an assimilated solution is better than a purely hydrodynamic solution, or, in the case of gravitationally induced tides, a solution derived through admittance. The analysis of ll-SST post-fit residuals could contribute to answering these questions.

- For the hydrodynamic modeling of smaller tides, the analysis of post-fit residuals can provide valuable background information on the choice of optimal hydrodynamic variables and parametrization, while also contributing to disentangling tidal frequencies with complex contributions from different origins.

- Disregarding long-period tides, generally, up until now, the common approach in gravity field recovery is to utilize only a single specific ocean tide model, rather than a combination of individual constituents from different models. Just recently, the Institute of Geodesy of TUG published a mixed ocean tide model (MIXED2025), which consists of the GOT5.6 model extended with constituents from FES2022 and TiME22. An analysis of a broader set of ocean tide models using the methodology applied in this thesis for FES2014b could possibly aid in fine-tuning the selection of solutions for such models.

- Since differences in quality between the various ocean tide models can be expected not only for individual constituents but additionally also for different regions of a single constituent, the assessment based on the post-fit residuals could contribute to a patched ocean tide model. Depending on the position of the satellite, the better performing ocean tide model is chosen for the evaluation of the acceleration due to ocean tides.

- In combination with other common gravity field solution quality indicators, the analysis of post-fit residual could help to assess and fine-tune the choice of parameters to be estimated along the gravitational potential coefficients to effectively address the influence of the imperfect ocean tide models. For instance, this could be particularly interesting for the (co-)estimation of low-resolution tidal corrections or high-frequency empirical parameters. In particular, the analysis of residuals time series from different GRACE(-FO) analysis centers could potentially provide additional context.

- The examined Lomb–Scargle periodograms encompass a broader spectrum of geophysical effects. Future studies could also focus on assessing information related to rapid non-tidal effects in the oceans and the atmosphere, aiming to improve AOD products.

- In addition to its role as a validation tool, an important question for future studies is the degree to which ll-SST measurements are suitable for assimilation into or combination with hydrodynamic models.

List of Figures

List of Tables

Bibliography

[A et al. 2012] A, G.; Wahr, J.; Zhong, S.: Computations of the viscoelastic response of a 3-D compressible Earth to surface loading: an application to glacial isostatic adjustment in Antarctica and Canada. *Geophysical Journal International* 192 (2012), No. 2, pp. 557–572 – doi:10.1093/gji/ggs030

[Abich et al. 2019] Abich, K.; Abramovici, A.; Amparan, B.; Baatzsch, A.; Bachman Okihiro, B.; Barr, D. C.; Bize, M. P.; Bogan, C.; Braxmaier, C.; Burke, M. J.; Clark, K. C.; Dahl, C.; Dahl, K.; Danzmann, K.; Davis, M. A.; de Vine, G.; Dickson, J. A.; Dubovitsky, S.; Eckardt, A.; et al.: In-orbit performance of the GRACE Follow-on laser ranging interferometer. *Physical Review Letters* 123 (2019) – doi:10.1103/PhysRevLett.123.031101

[Agnew 2009] Agnew, D. C.: Earth tides. Herring, T. (Eds.): *Treatise on Geophysics, Volume 3: Geodesy*. Amsterdam: Elsevier, 2009. – ISBN: 978-0-444-53460-6

[Agnew and Farrell 1978] Agnew, D. C.; Farrell, W. E.: Self-consistent equilibrium ocean tides. *Geophysical Journal International* 55 (1978), No. 1, pp. 171–181 – doi:10.1111/j.1365-246X.1978.tb04755.x

[Altamimi et al. 2011] Altamimi, Z.; Collilieux, X.; Métivier, L.: ITRF2008: an improved solution of the International Terrestrial Reference Frame. *Journal of Geodesy* 85 (2011), No. 8, pp. 457–473 – doi:10.1007/s00190-011-0444-4

[Andersen 1999] Andersen, O. B.: Shallow water tides in the northwest European shelf region from TOPEX/POSEIDON altimetry. *Journal of Geophysical Research: Oceans* 104 (1999), No. C4, pp. 7729–7741 – doi:10.1029/1998JC900112

[Andersen 2023] Andersen, O. B.: DTU23 global ocean tide model (DTU23_OceanTide). (2023) – doi:10.11583/DTU.23828874.v1

[Andersen et al. 2006] Andersen, O. B.; Egbert, G. D.; Erofeeva, S. Y.; Ray, R. D.: Mapping nonlinear shallow-water tides: a look at the past and future. *Ocean Dynamics* 56 (2006), No. 5, pp. 416–429 – doi:10.1007/s10236-006-0060-7

[Andersen et al. 2023] Andersen, O. B.; Rose, S. K.; Hart-Davis, M. G.: Polar ocean tides—revisited using Cryosat-2. *Remote Sensing* 15 (2023), No. 18 – doi:10.3390/rs15184479

[Andersen and Scharroo 2011] Andersen, O. B.; Scharroo, R.: Range and geophysical corrections in coastal regions: and implications for mean sea surface determination. Vignudelli, S. (Eds.); Kostianoy, A. G. (Eds.); Cipollini, P. (Eds.); Benveniste, J. (Eds.): *Coastal Altimetry*. Berlin, Heidelberg: Springer, 2011, pp. 103–145. – ISBN: 978-3-642-12796-0 – doi:10.1007/978-3-642-12796-0_5

[Andersen et al. 2016] Andersen, O. B.; Stenseng, L.; Piccioni, G.; Knudsen, P.: The DTU15 MSS (Mean Sea Surface) and DTU15LAT (Lowest Astronomical Tide) reference surface. *ESA Living Planet Symposium 2016, Prague, Czech Republic, 09-13 May 2016* (2016). – `https://ftp.space.dtu.dk/pub/DTU15/DOCUMENTS/MSS/DTU15MSS%2BLAT.pdf`. – Accessed on: 2025-08-08

[Andersen et al. 1995] Andersen, O. B.; Woodworth, P. L.; Flather, R. A.: Intercomparison of recent ocean tide models. *Journal of Geophysical Research: Oceans* 100 (1995), No. C12, pp. 25261–25282 – doi:10.1029/95JC02642

[Archer 2013] Archer, A. W.: World's highest tides: Hypertidal coastal systems in North America, South America and Europe. *Sedimentary Geology* 284-285 (2013), pp. 1–25 – doi:10.1016/j.sedgeo.2012.12.007

[Arnold and Jäggi 2020a] Arnold, D.; Jäggi, A.: AIUB GRACE-FO kinematic orbits, Release 2, Astronomical Institute, University of Bern. (2020). – `http://www.aiub.unibe.ch/download/LEO_ORBITS/GRACE-FO`. – Accessed on: 2025-08-08 – doi:10.48350/169040

[Arnold and Jäggi 2020b] Arnold, D.; Jäggi, A.: AIUB GRACE kinematic orbits, Release 01, Astronomical Institute, University of Bern. (2020). – `http://www.aiub.unibe.ch/download/LEO_ORBITS/GRACE`. – Accessed on: 2025-08-08 – doi:10.48350/158372

[Arnold et al. 2019] Arnold, D.; Montenbruck, O.; Hackel, S.; Sośnica, K.: Satellite laser ranging to low Earth orbiters: orbit and network validation. *Journal of Geodesy* 93 (2019), No. 11, pp. 2315–2334 – doi:10.1007/s00190-018-1140-4

[Aviso+ Altimetry 2024] Aviso+ Altimetry: FES2022 (Finite Element Solution) ocean tide product handbook. *SALP-MU-P-EA-23561-CLS* (2024) – doi:10.24400/527896/a01-2024.004

[Balidakis et al. 2022] Balidakis, K.; Sulzbach, R.; Shihora, L.; Dahle, C.; Dill, R.; Dobslaw, H.: Atmospheric contributions to global ocean tides for satellite gravimetry. *Journal of Advances in Modeling Earth Systems* 14 (2022), No. 11 – doi:10.1029/2022MS003193

[Bandikova and Flury 2014] Bandikova, T.; Flury, J.: Improvement of the GRACE star camera data based on the revision of the combination method. *Advances in Space Research* 54 (2014), No. 9, pp. 1818–1827 – doi:10.1016/j.asr.2014.07.004

[Bandikova et al. 2019] Bandikova, T.; McCullough, C.; Kruizinga, G. L.; Save, H.; Christophe, B.: GRACE accelerometer data transplant. *Advances in Space Research* 64(3) (2019), pp. 623–644 – doi:10.1016/j.asr.2019.05.021

[Barning 1963] Barning, F. J. M.: The numerical analysis of the light-curve of 12 Lacertae. *Bulletin of the Astronomical Institutes of the Netherlands* 17 (1963), pp. 22–28

[Baur et al. 2009] Baur, O.; Kuhn, M.; Featherstone, W. E.: GRACE-derived ice-mass variations over Greenland by accounting for leakage effects. *Journal of Geophysical Research: Solid Earth* 114 (2009), No. B6 – doi:10.1029/2008JB006239

[Behzadpour et al. 2019] Behzadpour, S.; Mayer-Gürr, T.; Flury, J.; Klinger, B.; Goswami, S.: Multiresolution wavelet analysis applied to GRACE range-rate residuals. *Geoscientific Instrumentation, Methods and Data Systems* 8 (2019), No. 2, pp. 197–207 – doi:10.5194/gi-8-197-2019

[Behzadpour et al. 2021] Behzadpour, S.; Mayer-Gürr, T.; Krauss, S.: GRACE Follow-On accelerometer data recovery. *Journal of Geophysical Research: Solid Earth* 126(5) (2021) – doi:10.1029/2020JB021297

[Berry and Healy 2004] Berry, M. M.; Healy, L. M.: Implementation of Gauss-Jackson integration for orbit propagation. *The Journal of the Astronautical Sciences* 52 (2004), No. 3, pp. 331–357 – doi:10.1007/BF03546367

[Bertiger et al. 2002] Bertiger, W.; Bar-Sever, Y.; Bettadpur, S.; Desai, S.; Dunn, C.; Haines, B.; Kruizinga, G.; Kuang, D.; Nandi, S.; Romans, L.; Watkins, M.; Wu, S.: GRACE: millimeters and microns in orbit. *Proceedings of the 15th International Technical Meeting of the Satellite Division of The Institute of Navigation (ION GPS 2002)* (2002), pp. 2022–2029. – `https://hdl.handle.net/2014/10373`. – Accessed on: 2025-08-08

[Bertiger et al. 2000] Bertiger, W.; Bar-Sever, Y.; Desai, S.; Duncan, C.; Haines, B.; Kuang, D.; Lough, M.; Reichert, A.; Romans, L.; Srinivasan, J.; Webb, F.; Young, L.; Zumberge, J.: Precise orbit determination for the Shuttle Radar Topography Mission using a new generation of GPS receiver. *Proceedings of the 13th International Technical Meeting of the Satellite Division of The Institute of Navigation (ION GPS 2000)* (2000), pp. 1646–1654. – `https://hdl.handle.net/2014/16088`. – Accessed on: 2025-08-08

[Bettadpur 2012] Bettadpur, S.: UTCSR Level-2 processing standards document (For Level-2 product release 0005), (Rev 4.0 May 29, 2012). *GRACE 327–742, (CSR-GR-12-xx)* (2012). – `ftp://isdcftp.gfz-potsdam.de/grace/DOCUMENTS/Level-2/GRACE_CSR_L2_Processing_Standards_Document_for_RL05.pdf`. – Accessed on: 2025-08-08

[Bettadpur 2019] Bettadpur, S.: UTCSR Level-2 processing standards document (For Level-2 product release 0006). *CSR GRFO-19-01 (GRACE-FO D-103920)* (2019). – `ftp://isdcftp.gfz-potsdam.de/grace/DOCUMENTS/Level-2/GRACE_CSR_L2_Processing_Standards_Document_for_RL06.pdf`. – Accessed on: 2025-08-08

[Beutler 2004] Beutler, G.: *Methods of Celestial Mechanics: Volume I: Physical, Mathematical, and Numerical Principles*. Berlin, Heidelberg: Springer, 2004 (Astronomy and Astrophysics Library). – ISBN: 3-540-40749-9

[Bij de Vaate et al. 2021] Bij de Vaate, I.; Vasulkar, A. N.; Slobbe, D. C.; Verlaan, M.: The influence of Arctic landfast ice on seasonal modulation of the M2 tide. *Journal of Geophysical Research: Oceans* 126 (2021), No. 5 – doi:10.1029/2020JC016630

[Bluestein 1970] Bluestein, L.: A linear filtering approach to the computation of discrete Fourier transform. *IEEE Transactions on Audio and Electroacoustics* 18 (1970), pp. 451–455 – doi:10.1109/TAU.1970.1162132

[Bonin and Save 2020] Bonin, J. A.; Save, H.: Evaluation of sub-monthly oceanographic signal in GRACE "daily" swath series using altimetry. *Ocean Science* 16 (2020), No. 2, pp. 423–434 – doi:10.5194/os-16-423-2020

[Bosch et al. 2009] Bosch, W.; Savcenko, R.; Flechtner, F.; Dahle, C.; Mayer-Gürr, T.; Stammer, D.; Taguchi, E.; Ilk, K.-H.: Residual ocean tide signals from satellite altimetry, GRACE gravity fields, and hydrodynamic modelling. *Geophysical Journal International* 178 (2009), No. 3, pp. 1185–1192 – doi:10.1111/j.1365-246X.2009.04281.x

[Bretagnon and Francou 1988] Bretagnon, P.; Francou, G.: Planetary theories in rectangular and spherical variables: VSOP87 solution. *Astronomy and Astrophysics* 202 (1988), pp. 309–315

[Brumberg and Kopejkin 1989] Brumberg, V. A.; Kopejkin, S. M.: Relativistic reference systems and motion of test bodies in the vicinity of the Earth. *Il Nuovo Cimento B (1971-1996)* 103 (1989), No. 1, pp. 63–98 – doi:10.1007/BF02888894

[Brzeziński and Capitaine 2003] Brzeziński, A.; Capitaine, N.: Lunisolar perturbations in Earth rotation due to the triaxial figure of the Earth: geophysical aspects. Capitaine, N. (Eds.): *Journées 2001 - Systèmes de Référence Spatio-Temporels. Influence of Geophysics, Time and Space Reference Frames on Earth Rotation Studies, Brussels, 24-26 September 2001*. 2003, pp. 51–58. – ISBN: 2-901057-46-2

[Capitaine et al. 2000] Capitaine, N.; Guinot, B.; McCarthy, D. D.: Definition of the celestial ephemeris origin and of UT1 in the International Celestial Reference Frame. *Astronomy Astrophysics* 355 (2000), pp. 398–405

[Capitaine and Wallace 2006] Capitaine, N.; Wallace, P. T.: High precision methods for locating the celestial intermediate pole and origin. *Astronomy Astrophysics* 450 (2006), No. 2, pp. 855–872 – doi:10.1051/0004-6361:20054550

[Capitaine et al. 2003] Capitaine, N.; Wallace, P. T.; Chapront, J.: Expressions for IAU 2000 precession quantities. *Astronomy Astrophysics* 412 (2003), No. 2, pp. 567–586 – doi:10.1051/0004-6361:20031539

[Carton 1983] Carton, J. A.: The variation with frequency of the long-period tides. *Journal of Geophysical Research: Oceans* 88 (1983), No. C12, pp. 7563–7571 – doi:10.1029/JC088iC12p07563

[Cartwright and Ray 1990] Cartwright, D. E.; Ray, R. D.: Oceanic tides from Geosat altimetry. *Journal of Geophysical Research: Oceans* 95 (1990), No. C3, pp. 3069–3090 – doi:10.1029/JC095iC03p03069

[Cartwright and Tayler 1971] Cartwright, D. E.; Tayler, R. J.: New computations of the tide-generating potential. *Geophysical Journal International* 23 (1971), No. 1, pp. 45–73 – doi:10.1111/j.1365-246X.1971.tb01803.x

[Case et al. 2010] Case, K.; Kruizinga, G.; Wu, S.-C.: GRACE Level 1B data product user handbook. *JPL D-22027* (2010). – `ftp://isdcftp.gfz-potsdam.de/grace/DOCUMENTS/Level-1/GRACE_L1B_Data_Product_User_Handbook.pdf`. – Accessed on: 2025-08-08

[Cazenave et al. 1977] Cazenave, A.; Daillet, S.; Lambeck, K.: Tidal studies from the perturbations in satellite orbits. *Philosophical Transactions of the Royal Society of London. Series A, Mathematical and Physical Sciences* 284 (1977), No. 1326, pp. 595–606 – doi:10.1098/rsta.1977.0036

[Chao 2016] Chao, B. F.: Caveats on the equivalent water thickness and surface mascon solutions derived from the GRACE satellite-observed time-variable gravity. *Journal of Geodesy* 90 (2016), No. 9, pp. 807–813 – doi:10.1007/s00190-016-0912-y

[Chelton et al. 2001] Chelton, D. B.; Ries, J. C.; Haines, B. J.; Fu, L.-L.; Callahan, P. S.: Satellite altimetry. Fu, L.-L. (Eds.); Cazenave, A. (Eds.): *Satellite Altimetry and Earth Sciences: A Handbook of Techniques and Applications* Vol. 69. San Diego, London: Academic Press, 2001. – ISSN: 0074-6142 – doi:10.1016/S0074-6142(01)80146-7

[Chen and Lin 2000] Chen, G.; Lin, H.: The effect of temporal aliasing in satellite altimetry. *Photogrammetric Engineering & Remote Sensing* 66 (2000), No. 5, pp. 639–644. – `https://www.asprs.org/wp-content/uploads/pers/2000journal/may/2000_may_639-644.pdf`. – Accessed on: 2025-04-25

[Chen et al. 2022] Chen, J.; Cazenave, A.; Dahle, C.; Llovel, W.; Panet, I.; Pfeffer, J.; Moreira, L.: Applications and challenges of GRACE and GRACE Follow-On satellite gravimetry. *Surveys in Geophysics* 43 (2022), No. 1, pp. 305–345 – doi:10.1007/s10712-021-09685-x

[Chen et al. 2017a] Chen, J. L.; Pekker, T.; Wilson, C. R.; Tapley, B. D.; Kostianoy, A. G.; Cretaux, J.-F.; Safarov, E. S.: Long-term Caspian sea level change. *Geophysical Research Letters* 44 (2017), No. 13, pp. 6993–7001 – doi:10.1002/2017GL073958

[Chen et al. 2015] Chen, J. L.; Wilson, C. R.; Li, J.; Zhang, Z.: Reducing leakage error in GRACE-observed long-term ice mass change: a case study in West Antarctica. *Journal of Geodesy* 89 (2015), No. 9, pp. 925–940 – doi:10.1007/s00190-015-0824-2

[Chen et al. 2009] Chen, J. L.; Wilson, C. R.; Seo, K.-W.: S2 tide aliasing in GRACE time-variable gravity solutions. *Journal of Geodesy* 83 (2009), No. 7, pp. 679–687 – doi:10.1007/s00190-008-0282-1

[Chen et al. 2017b] Chen, J. L.; Wilson, C. R.; Tapley, B. D.; Save, H.; Cretaux, J.-F.: Long-term and seasonal Caspian sea level change from satellite gravity and altimeter measurements. *Journal of Geophysical Research: Solid Earth* 122 (2017), No. 3, pp. 2274–2290 – doi:10.1002/2016JB013595

[Chen et al. 2019] Chen, Q.; Shen, Y.; Chen, W.; Francis, O.; Zhang, X.; Chen, Q.; Li, W.; Chen, T.: An optimized short-arc approach: methodology and application to develop refined time series of Tongji-Grace2018 GRACE monthly solutions. *Journal of Geophysical Research: Solid Earth* 124 (2019), No. 6, pp. 6010–6038 – doi:10.1029/2018JB016596

[Cheng and Ries 2017] Cheng, M.; Ries, J.: The unexpected signal in GRACE estimates of C_{20}. *Journal of Geodesy* 91 (2017), No. 8, pp. 897–914 – doi:10.1007/s00190-016-0995-5

[Ciracì et al. 2020] Ciracì, E.; Velicogna, I.; Swenson, S.: Continuity of the mass loss of the world's glaciers and ice caps from the GRACE and GRACE Follow-On missions. *Geophysical Research Letters* 47 (2020), No. 9 – doi:10.1029/2019GL086926

[Colombo 1986] Colombo, O. L.: Ephemeris errors of GPS satellites. *Bulletin Géodésique* 60 (1986), No. 1, pp. 64–84. ISBN: 1432-1394 – doi:10.1007/BF02519355

[Combrinck 2010] Combrinck, L.: Satellite laser ranging. Xu, G. (Eds.): *Sciences of Geodesy - I: Advances and Future Directions*. Berlin, Heidelberg: Springer, 2010, pp. 301–338. – ISBN: 978-3-642-11741-1 – doi:10.1007/978-3-642-11741-1_9

[Cooley and Tukey 1965] Cooley, J. W.; Tukey, J. W.: An algorithm for the machine calculation of complex Fourier series. *Mathematics of Computation* 19 (1965), No. 90, pp. 297–301 – doi:10.1090/S0025-5718-1965-0178586-1

[Courtier 1938] Courtier, A.: Clasification of tides in four types. *Conférences sur les Marées* (1938). – `https://journals.lib.unb.ca/index.php/ihr/article/view/27428`. – Accessed on: 2025-08-08

[Dahle et al. 2019a] Dahle, C.; Flechtner, F.; Murböck, M.; Michalak, G.; Neumayer, H.; Abrykosov, O.; Reinhold, A.; König, R.: GFZ Level-2 processing standards document for Level-2 product release 06 (Rev. 1.0, June 3, 2019). *GRACE-FO D-103919, Scientific Technical Report STR - Data; 19/09* (2019). – `ftp://isdcftp.gfz-potsdam.de/grace-fo/DOCUMENTS/Level-2/GRACE-FO_GFZ_L2_`

Processing_Standards_Document_for_RL06.pdf. – Accessed on: 2025-08-08 – doi:10.2312/GFZ.b103-19098

[Dahle et al. 2019b] Dahle, C.; Murböck, M.; Flechtner, F.; Dobslaw, H.; Michalak, G.; Neumayer, K. H.; Abrykosov, O.; Reinhold, A.; König, R.; Sulzbach, R.; Förste, C.: The GFZ GRACE RL06 monthly gravity field time series: processing details and quality assessment. *Remote Sensing* 11 (2019), No. 18 – doi:10.3390/rs11182116

[Darwin 1907] Darwin, G. H.: *The Scientific Papers of Sir George Darwin: Oceanic Tides and Lunar Disturbance of Gravity.* Cambridge University Press, 1907 (Cambridge Library Collection - Physical Sciences) – doi:10.1017/CBO9780511703461

[Dee et al. 2011] Dee, D. P.; Uppala, S. M.; Simmons, A. J.; Berrisford, P.; Poli, P.; Kobayashi, S.; Andrae, U.; Balmaseda, M. A.; Balsamo, G.; Bauer, P.; Bechtold, P.; Beljaars, A. C. M.; Berg, L. van de; Bidlot, J.; Bormann, N.; Delsol, C.; Dragani, R.; Fuentes, M.; Geer, A. J.; Haimberger, L.; et al.: The ERA-Interim reanalysis: Configuration and performance of the data assimilation system. *Quarterly Journal of the Royal Meteorological Society* 137 (2011), No. 656, pp. 553–597 – doi:10.1002/qj.828

[Desai 2002] Desai, S. D.: Observing the pole tide with satellite altimetry. *Journal of Geophysical Research* 1078(C11) (2002), pp. 7–1–7–13 – doi:10.1029/2001JC001224

[Desai and Yuan 2006] Desai, S. D.; Yuan, D.-N.: Application of the convolution formalism to the ocean tide potential: results from the Gravity Recovery and Climate Experiment (GRACE). *Journal of Geophysical Research: Oceans* 111 (2006), No. C6 – doi:10.1029/2005JC003361

[Devaraju 2015] Devaraju, B.: *Understanding Filtering on the Sphere: Experiences from Filtering GRACE Data*, University of Stuttgart, Doctoral dissertation, 2015. – Retrieved from OPUS - Publication Server of the University of Stuttgart: http://dx.doi.org/10.18419/opus-3985

[Devlin et al. 2023] Devlin, A. T.; Pan, J.; Idier, D.: Multi-regional observations and validation of the M3 ocean tide. *Science China Earth Sciences* 66 (2023), No. 10, pp. 2265–2277 – doi:10.1007/s11430-022-1151-0

[Dobslaw et al. 2017a] Dobslaw, H.; Bergmann-Wolf, I.; Dill, R.; Poropat, L.; Flechtner, F.: Product description document for AOD1B release 06, (Rev. 6.1, October 19, 2017). *GRACE 327–750* (2017). – ftp://isdcftp.gfz-potsdam.de/grace/DOCUMENTS/Level-1/GRACE_AOD1B_Product_Description_Document_for_RL06.pdf. – Accessed on: 2025-08-08

[Dobslaw et al. 2017b] Dobslaw, H.; Bergmann-Wolf, I.; Dill, R.; Poropat, L.; Thomas, M.; Dahle, C.; Esselborn, S.; König, R.; Flechtner, F.: A new high-resolution model of non-tidal atmosphere and ocean mass variability for de-aliasing of satellite gravity observations: AOD1B RL06. *Geophysical Journal International* 211(1) (2017), pp. 263–269 – doi:10.1093/gji/ggx302

[Dobslaw et al. 2013] Dobslaw, H.; Flechtner, F.; Bergmann-Wolf, I.; Dahle, C.; Dill, R.; Esselborn, S.; Sasgen, I.; Thomas, M.: Simulating high-frequency atmosphere-ocean mass variability for dealiasing of satellite gravity observations: AOD1B RL05. *Journal of Geophysical Research: Oceans* 118 (2013), No. 7, pp. 3704–3711 – doi:10.1002/jgrc.20271

[Dobslaw and Thomas 2005] Dobslaw, H.; Thomas, M.: Atmospheric induced oceanic tides from ECMWF forecasts. *Geophysical Research Letters* 32 (2005), No. 10 – doi:10.1029/2005GL022990

[Doodson 1921] Doodson, A. T.: The harmonic development of the tide-generating potential. *Proceedings of the Royal Society of London. Series A, Containing Papers of a Mathematical and Physical Character* 100 (1921), No. 704, pp. 305–329 – doi:10.1098/rspa.1921.0088

[Dunn et al. 2003] Dunn, C.; Bertiger, W.; Bar-Sever, Y.; Desai, S.; Haines, B.; Kuang, D.; Franklin, G.; Harris, I.; Kruizinga, G.; Meehan, T.; Nandi, S.; Nguyen, D.; Rogstad, T.; Thomas, J. B.; Tien, J.; Romans, L.; Watkins, M.; Wu, S.-C.; Bettadpur, S.; Kim, J.: Instrument of GRACE: GPS augments gravity measurements. *GPS World* (2003), pp. 16–28

[Duwe et al. 2024] Duwe, M.; Koch, I.; Flury, J.: Residual patterns in GRACE Follow-On laser ranging interferometry post-fit range rate residuals. *Advances in Space Research* 73 (2024) – doi:10.1016/j.asr.2024.03.035

[Eanes and Bettadpur 1995] Eanes, R. J.; Bettadpur, S.: The CSR3.0 global ocean tide model: diurnal and semi-diurnal ocean tides from TOPEX/POSEIDON altimetry. *Technical Memorandum, CSR-TM-95-06* (1995). – `https://iers-conventions.obspm.fr/content/supporting_material/chapter6/TM-95-06.pdf`. – Accessed on: 2025-08-08

[Egbert and Erofeeva 2002] Egbert, G. D.; Erofeeva, S. Y.: Efficient inverse modeling of barotropic ocean tides. *Journal of Atmospheric and Oceanic Technology* 19 (2002), No. 2, pp. 183–204 – doi:10.1175/1520-0426(2002)019<0183:EIMOBO>2.0.CO;2

[Egbert et al. 2009] Egbert, G. D.; Erofeeva, S. Y.; Han, S.-C.; Luthcke, S. B.; Ray, R. D.: Assimilation of GRACE tide solutions into a numerical hydrodynamic inverse model. *Geophysical Research Letters* 36 (2009), No. 20 – doi:10.1029/2009GL040376

[Egbert and Ray 2003] Egbert, G. D.; Ray, R. D.: Deviation of long-period tides from equilibrium: Kinematics and geostrophy. *Journal of Physical Oceanography* 33 (2003), No. 4, pp. 822 – 839 – doi:10.1175/1520-0485(2003)33<822:DOLTFE>2.0.CO;2

[Eisenman et al. 1997] Eisenman, A. R.; Liebe, C. C.; Jørgensen, J. L.: New generation of autonomous star trackers. *Proceedings of the Society of Photo-Optical Instrumentation Engineers (SPIE); Sensors, Systems, and Next-Generation Satellites* Vol. 3221. 1997, pp. 524–535 – doi:10.1117/12.298121

[Fey et al. 2015] Fey, A. L.; Gordon, D.; Jacobs, C. S.; Ma, C.; Gaume, R. A.; Arias, E. F.; Bianco, G.; Boboltz, D. A.; Böckmann, S.; Bolotin, S.; Charlot, P.; Collioud, A.; Engelhardt, G.; Gipson, J.; Gontier, A.-M.; Heinkelmann, R.; Kurdubov, S.; Lambert, S.; Lytvyn, S.; et al.: The second realization of the International Celestial Reference Frame by very long baseline interferometry. *The Astronomical Journal* 150 (2015), No. 2, pp. 58 – doi:10.1088/0004-6256/150/2/58

[Fienga et al. 2021] Fienga, A.; Deram, P.; Di Ruscio, A.; Viswanathan, V.; Camargo, J. I. B.; Bernus, L.; Gastineau, M.; Laskar, J.: INPOP21a planetary ephemerides. *Notes Scientifiques et Techniques de l'Institut de Mecanique Celeste* (2021). – `https://www.imcce.fr/content/medias/recherche/equipes/asd/inpop/inpop21a.pdf`. – Accessed on: 2025-08-08. ISBN: 978-2-910015-84-8

[Flechtner et al. 2016] Flechtner, F.; Neumayer, K.-H.; Dahle, C.; Dobslaw, H.; Fagiolini, J.-C.; Güntner, A.: What can be expected from the GRACE-FO laser ranging interferometer for Earth science applications? *Surveys in Geophysics* 37 (2016), No. 2, pp. 453–470 – doi:10.1007/s10712-015-9338-y

[Flechtner et al. 2021] Flechtner, F.; Reigber, C.; Rummel, R.; Balmino, G.: Satellite gravimetry: A review of its realization. *Surveys in Geophysics* 42 (2021), No. 5, pp. 1029–1074 – doi:10.1007/s10712-021-09658-0

[Flury et al. 2008] Flury, J.; Bettadpur, S.; Tapley, B. D.: Precise accelerometry onboard the GRACE gravity field satellite mission. *Advances in Space Research* 42 (2008), No. 8, pp. 1414–1423 – doi:10.1016/j.asr.2008.05.004

[Folkner et al. 2014] Folkner, W. M.; Williams, J. G.; Boggs, D. H.; Park, R. S.; Kuchynka, P.: The planetary and lunar ephemerides DE430 and DE431. *IPN Progress Report* (2014). – `https://naif.jpl.nasa.gov/pub/naif/generic_kernels/spk/planets/de430_and_de431.pdf`. – Accessed on: 2025-08-08

[Foreman et al. 2009] Foreman, M. G. G.; Cherniawsky, J. Y.; Ballantyne, V. A.: Versatile harmonic tidal analysis: improvements and applications. *Journal of Atmospheric and Oceanic Technology* 26 (2009), No. 4, pp. 806–817 – doi:10.1175/2008JTECHO615.1

[Fox 1984] Fox, K.: Numerical integration of the equations of motion of celestial mechanics. *Celestial Mechanics* 33 (1984), No. 2, pp. 127–142 – doi:10.1007/BF01234151

[Fu et al. 2001] Fu, L.-L.; Cheng, B.; Qiu, B.: 25-day period large-scale oscillations in the Argentine Basin revealed by the TOPEX/Poseidon altimeter. *Journal of Physical Oceanography* 31 (2001), No. 2, pp. 506–517 – doi:10.1175/1520-0485(2001)031<0506:DPLSOI>2.0.CO;2

[Fu et al. 1994] Fu, L.-L.; Christensen, E. J.; Yamarone Jr., C. A.; Lefebvre, M.; Ménard, Y.; Dorrer, M.; Escudier, P.: TOPEX/POSEIDON mission overview. *Journal of Geophysical Research: Oceans* 99 (1994), No. C12, pp. 24369–24381 – doi:10.1029/94JC01761

[Gerlach et al. 2003] Gerlach, C.; Földvary, L.; Švehla, D.; Gruber, T.; Wermuth, M.; Sneeuw, N.; Frommknecht, B.; Oberndorfer, H.; Peters, T.; Rothacher, M.; Rummel, R.; Steigenberger, P.: A CHAMP-only gravity field model from kinematic orbits using the energy integral. *Geophysical Research Letters* 30 (2003), No. 20 – doi:10.1029/2003GL018025

[GFZ 2024] GFZ German Research Centre for Geosciences: Gravity Recovery and Climate Experiment (GRACE) mission. (2024). – `https://www.gfz-potsdam.de/en/grace`. – Accessed on: 2025-08-08

[Godin 1972] Godin, G.: *The Analysis of Tides*. University of Toronto Press, 1972. – ISBN: 9780853234418

[Goswami et al. 2018] Goswami, S.; Devaraju, B.; Weigelt, M.; Mayer-Gürr, T.: Analysis of GRACE range-rate residuals with focus on KBR instrument system noise. *Advances in Space Research* 62 (2018), No. 2, pp. 304–316 – doi:10.1016/j.asr.2018.04.036

[Haines et al. 2004] Haines, B.; Bar-Sever, Y.; Bertiger, W.; Desai, S.; Willis, P.: One-centimeter orbit determination for Jason-1: new GPS-based strategies. *Marine Geodesy* 27 (2004), No. 1-2, pp. 299–318 – doi:10.1080/01490410490465300

[Hairer et al. 2008] Hairer, E.; Nørsett, S. P.; Wanner, G.: *Solving Ordinary Differential Equations I: Nonstiff Problems*. Second revised edition. Berlin, Heidelberg: Springer, 2008 (Springer Series in Computational Mathematics). – ISBN: 978-3-540-56670-0 – doi:10.1007/978-3-540-78862-1

[Han et al. 2020] Han, S.-C.; Ghobadi-Far, K.; Ray, R. D.; Papanikolaou, T.: Tidal geopotential dependence on Earth ellipticity and seawater density and its detection with the GRACE Follow-On laser ranging interferometer. *Journal of Geophysical Research: Oceans* 125 (2020), No. 12 – doi:10.1029/2020JC016774

[Han et al. 2004] Han, S.-C.; Jekeli, C.; Shum, C. K.: Time-variable aliasing effects of ocean tides, atmosphere, and continental water mass on monthly mean GRACE gravity field. *Journal of Geophysical Research: Solid Earth* 109 (2004), No. B4 – doi:10.1029/2003JB002501

[Han et al. 2007] Han, S.-C.; Ray, R. D.; Luthcke, S. B.: Ocean tidal solutions in Antarctica from GRACE inter-satellite tracking data. *Geophysical Research Letters* 34 (2007), No. 21 – doi:10.1029/2007GL031540

[Han et al. 2010] Han, S.-C.; Ray, R. D.; Luthcke, S. B.: One centimeter-level observations of diurnal ocean tides from global monthly mean time-variable gravity fields. *Journal of Geodesy* 84 (2010), No. 12, pp. 715–729 – doi:10.1007/s00190-010-0405-3

[Han et al. 2008] Han, S.-C.; Rowlands, D. D.; Luthcke, S. B.; Lemoine, F. G.: Localized analysis of satellite tracking data for studying time-variable Earth's gravity fields. *Journal of Geophysical Research: Solid Earth* 113 (2008), No. B6 – doi:10.1029/2007JB005218

[Han et al. 2006] Han, S.-C.; Shum, C. K.; Bevis, M.; Ji, C.; Kuo, C.-Y.: Crustal dilatation observed by GRACE after the 2004 Sumatra-Andaman earthquake. *Science* 313 (2006), No. 5787, pp. 658–662 – doi:10.1126/science.1128661

[Han et al. 2005a] Han, S.-C.; Shum, C. K.; Braun, A.: High-resolution continental water storage recovery from low–low satellite-to-satellite tracking. *Journal of Geodynamics* 39 (2005), No. 1, pp. 11–28 – doi:10.1016/j.jog.2004.08.002

[Han et al. 2005b] Han, S.-C.; Shum, C. K.; Jekeli, C.; Alsdorf, D.: Improved estimation of terrestrial water storage changes from GRACE. *Geophysical Research Letters* 32 (2005), No. 7 – doi:10.1029/2005GL022382

[Han et al. 2005c] Han, S.-C.; Shum, C. K.; Matsumoto, K.: GRACE observations of M2 and S2 ocean tides underneath the Filchner-Ronne and Larsen Ice Shelves, Antarctica. *Geophysical Research Letters* 32 (2005), No. 20 – doi:10.1029/2005GL024296

[Hart-Davis et al. 2021] Hart-Davis, M. G.; Piccioni, G.; Dettmering, D.; Schwatke, C.; Passaro, M.; Seitz, F.: EOT20: a global ocean tide model from multi-mission satellite altimetry. *Earth System Science Data* 13 (2021), No. 8, pp. 3869–3884 – doi:10.5194/essd-13-3869-2021

[Hartmann and Wenzel 1995] Hartmann, T.; Wenzel, H.-G.: The HW95 tidal potential catalogue. *Geophysical Research Letters* 22 (1995), No. 24, pp. 3553–3556 – doi:10.1029/95GL03324

[Harvey et al. 2024] Harvey, N.; Bertiger, W.; McCullough, C. M.; Miller, M.; Save, H.; Yuan, D.-N.: Recovering differential forces from the GRACE-D accelerometer. *Earth and Space Science* 11 (2024), No. 4 – doi:10.1029/2023EA003200

[Harvey et al. 2017] Harvey, N.; Dunn, C. E.; Kruizinga, G. L.; Young, L. E.: Triggering conditions for GRACE ranging measurement signal-to-noise ratio dips. *Journal of Spacecraft and Rockets* 54 (2017), No. 1, pp. 327–330 – doi:10.2514/1.A33578

[Heiskanen and Moritz 1967] Heiskanen, W. A.; Moritz, H.: *Physical Geodesy.* W. H. Freeman and Company: San Francisco, London, 1967

[Hoffman 2001] Hoffman, J. D.: *Numerical Methods for Engineers and Scientists.* 2nd, revised and expanded. New York, Basel: Marcel Dekker, 2001. – ISBN: 9780824704438

[Hofmann-Wellenhof et al. 2007] Hofmann-Wellenhof, B.; Lichtenegger, H.; Wasle, E.: *GNSS – Global Navigation Satellite Systems: GPS, GLONASS, Galileo, and more.* 1. Springer, 2007. – ISBN: 978-3-211-73012-6 – doi:10.1007/978-3-211-73017-1

[Huess and Andersen 2001] Huess, V.; Andersen, O. B.: Seasonal variation in the main tidal constituent from altimetry. *Geophysical Research Letters* 28 (2001), No. 4, pp. 567–570 – doi:10.1029/2000GL011921

[IERS 2019a] IERS Conventions Centre: Chapter 5 (Updated): Transformation between the International Terrestrial Reference System and Geocentric Celestial Reference System. (2019). – `https://iers-conventions.obspm.fr/chapter5.php`. – Accessed on: 2025-08-08

[IERS 2019b] IERS Conventions Centre: Chapter 6 (Updated): Geopotential. (2019). – `https://iers-conventions.obspm.fr/chapter6.php`. – Accessed on: 2025-08-08

[IERS 2024] International Earth Rotation and Reference Systems Service: Leap_Second.dat. (2024). – `https://hpiers.obspm.fr/eoppc/bul/bulc/Leap_Second.dat`. – Accessed on: 2025-08-08

[IERS Conventions 2010] Petit, G. (Eds.); Luzum, B. (Eds.): *IERS Conventions (2010), IERS Technical Note No. 36.* Frankfurt am Main: Verlag des Bundesamts für Kartographie, 2010. – ISBN: 3-89888-989-6

[IERS Conventions 2010, 01 Feb. 2018 update] Petit, G. (Eds.); Luzum, B. (Eds.): *IERS Conventions (2010), IERS Technical Note No. 36 (01 Feb. 2018 Update).* Frankfurt am Main: Verlag des Bundesamts für Kartographie. – `https://iers-conventions.obspm.fr/conventions_material.php`. – Accessed on: 2025-08-08

[IHO 2017] International Hydrographic Organization (IHO): Tidal Constituents. (2017). – `https://iho.int/mtg_docs/com_wg/IHOTC/IHOTC_Misc/TWCWG_Constituent_list.pdf`. – Accessed on: 2025-08-08

[Ilk 2021] Ilk, K. H.: *Potentialtheorie.* 1. Berlin: Springer Spektrum, 2021. – ISBN: 978-3-662-62360-2 – doi:10.1007/978-3-662-62361-9

[ISDC 2023] Information System and Data Center: Global Earth science data. (2023). – `https://isdc.gfz-potsdam.de/homepage/`. – Accessed on: 2024-04-16

[Jäggi et al. 2008] Jäggi, A.; Bock, H.; Pail, R.; Goiginger, H.: Highly-reduced dynamic orbits and their use for global gravity field recovery: a simulation study for GOCE. *Studia Geophysica et Geodaetica* 52 (2008), No. 3, pp. 341–359 – doi:10.1007/s11200-008-0025-z

[Jäggi et al. 2006] Jäggi, A.; Hugentobler, U.; Beutler, G.: Pseudo-stochastic orbit modeling techniques for low-Earth orbiters. *Journal of Geodesy* 80 (2006), No. 1, pp. 47–60 – doi:10.1007/s00190-006-0029-9

[Jäggi et al. 2007] Jäggi, A.; Hugentobler, U.; Bock, H.; Beutler, G.: Precise orbit determination for GRACE using undifferenced or doubly differenced GPS data. *Advances in Space Research* 39 (2007), No. 10, pp. 1612–1619 – doi:10.1016/j.asr.2007.03.012

[Jäggi et al. 2020] Jäggi, A.; Meyer, U.; Lasser, M.; Jenny, B.; Lopez, T.; Flechtner, F.; Dahle, C.; Förste, C.; Mayer-Gürr, T.; Kvas, A.; Lemoine, J.-M.; Bourgogne, S.; Weigelt, M.; Groh, A.: International Combination Service for Time-variable Gravity Fields (COST-G). Freymueller, J. T. (Eds.); Sánchez, L. (Eds.): *Beyond 100: The Next Century in Geodesy*. Cham: Springer International Publishing, 2020, pp. 57–65. – ISBN: 978-3-031-09857-4 – doi:10.1007/1345_2020_109

[Jekeli 1981] Jekeli, C.: Alternative methods to smooth the Earth's gravity field. *Reports of the Department of Geodetic Science and Surveying Report No. 327* (1981). – `https://ntrs.nasa.gov/citations/19820014947`. – Accessed on: 2025-08-08

[Jekeli 1999] Jekeli, C.: The determination of gravitational potential differences from satellite-to-satellite tracking. *Celestial Mechanics and Dynamical Astronomy* 75 (1999), No. 2, pp. 85–101 – doi:10.1023/A:1008313405488

[Jørgensen 2000] Jørgensen, J. L.: In-orbit performance of a fully autonomous star tracker. *ESA 4th Symposion on Spacecraft Guidance Navigation and Control*. ESTEC, European Space Agency, 2000, pp. 103–110

[Jørgensen and Liebe 1996] Jørgensen, J. L.; Liebe, C. C.: The advanced stellar compass, development and operations. *Acta Astronautica* 39 (1996), No. 9, pp. 775–783 – doi:10.1016/S0094-5765(97)00061-1

[Jungclaus et al. 2013] Jungclaus, J. H.; Fischer, N.; Haak, H.; Lohmann, K.; Marotzke, J.; Matei, D.; Mikolajewicz, U.; Notz, D.; Storch, J. S. von: Characteristics of the ocean simulations in the Max Planck Institute Ocean Model (MPIOM) the ocean component of the MPI-Earth system model. *Journal of Advances in Modeling Earth Systems* 5 (2013), No. 2, pp. 422–446 – doi:10.1002/jame.20023

[Kang et al. 2002] Kang, S. K.; Foreman, M. G. G.; Lie, H.-J.; Lee, J.-H.; Cherniawsky, J.; Yum, K.-D.: Two-layer tidal modeling of the Yellow and East China Seas with application to seasonal variability of the M2 tide. *Journal of Geophysical Research: Oceans* 107 (2002), No. C3, pp. 6–1–6–18 – doi:10.1029/2001JC000838

[Kang et al. 2020] Kang, Z.; Bettadpur, S.; Nagel, P.; Save, H.; Poole, S.; Pie, N.: GRACE-FO precise orbit determination and gravity recovery. *Journal of Geodesy* 94 (2020), No. 9, pp. 85 – doi:10.1007/s00190-020-01414-3

[Kang et al. 2003] Kang, Z.; Nagel, P.; Pastor, R.: Precise orbit determination for GRACE. *Advances in Space Research* 31 (2003), No. 8, pp. 1875–1881 – doi:10.1016/S0273-1177(03)00159-5

[Kaula 1966] Kaula, W. M.: *Theory of Satellite Geodesy*. Waltham, Toronto, London: Blaisdell Publishing Company, 1966

[Killett et al. 2011] Killett, E.; Wahr, J.; Desai, S.; Yuan, D.; Watkins, M.: Arctic ocean tides from GRACE satellite accelerations. *Journal of Geophysical Research: Oceans* 116 (2011), No. C11 – doi:10.1029/2011JC007111

[Kim 2000] Kim, J.: *Simulation Study of a Low-Low Satellite-to-Satellite Tracking Mission*, The University of Texas at Austin, Doctoral dissertation, 2000. – Retrieved from University of Texas Libraries: `http://dx.doi.org/10.26153/tsw/12695`

[King and Padman 2005] King, M. A.; Padman, L.: Accuracy assessment of ocean tide models around Antarctica. *Geophysical Research Letters* 32 (2005), No. 23 – doi:10.1029/2005GL023901

[King et al. 2011] King, M. A.; Padman, L.; Nicholls, K.; Clarke, P. J.; Gudmundsson, G. H.; Kulessa, B.; Shepherd, A.; Gourmelen, N.: Ocean tides in the Weddell Sea: New observations on the

Filchner-Ronne and Larsen C Ice Shelves and model validation. *Journal of Geophysical Research: Oceans* 116 (2011), No. C6 – doi:10.1029/2011JC006949

[Kinoshita and Souchay 1990] Kinoshita, H.; Souchay, J.: The theory of the nutation for the rigid Earth model at the second order. *Celestial Mechanics and Dynamical Astronomy* 48 (1990), No. 3, pp. 187–265 – doi:10.1007/BF02524332

[Klinger and Mayer-Gürr 2016] Klinger, B.; Mayer-Gürr, T.: The role of accelerometer data calibration within GRACE gravity field recovery: results from ITSG-Grace2016. *Advances in Space Research* 58 (2016), No. 9, pp. 1597–1609 – doi:10.1016/j.asr.2016.08.007

[Klokočník et al. 2015] Klokočník, J.; Wagner, C. A.; Kostelecký, J.; Bezděk, A.: Ground track density considerations on the resolvability of gravity field harmonics in a repeat orbit. *Advances in Space Research* 56 (2015), No. 6, pp. 1146–1160 – doi:10.1016/j.asr.2015.06.020

[Knudsen 2003] Knudsen, P.: Ocean tides in GRACE monthly averaged gravity fields. Beutler, G. (Eds.); Drinkwater, M. R. (Eds.); Rummel, R. (Eds.); Von Steiger, R. (Eds.): *Earth Gravity Field from Space — From Sensors to Earth Sciences: Proceedings of an ISSI Workshop 11–15 March 2002, Bern, Switzerland.* Dordrecht: Springer Netherlands, 2003, pp. 261–270. – ISBN: 978-94-017-1333-7 – doi:10.1007/978-94-017-1333-7_22

[Koch et al. 2024a] Koch, I.; Duwe, M.; Flury, J.: LUH GRACE(-FO) K-band range-rate post-fit residuals [Data set]. *Zenodo* (2024) – doi:10.5281/zenodo.13607650

[Koch et al. 2024b] Koch, I.; Duwe, M.; Flury, J.: Residual and unmodeled ocean tide signal from 20+ years of GRACE and GRACE-FO global gravity field models. *Journal of Geophysical Research: Solid Earth* 129 (2024), No. 9 – doi:10.1029/2024JB029345

[Koch et al. 2021] Koch, I.; Duwe, M.; Flury, J.; Shabanloui, A.: Earth's time-variable gravity from GRACE Follow-On K-band range-rates and pseudo-observed orbits. *Remote Sensing* 13 (2021), No. 9 – doi:10.3390/rs13091766

[Koch et al. 2020] Koch, I.; Flury, J.; Naeimi, M.; Shabanloui, A.: LUH-GRACE2018: A new time series of monthly gravity field solutions from GRACE. *International Association of Geodesy Symposia.* Berlin: Springer, 2020, pp. 1–9 – doi:10.1007/1345_2020_92

[Koch 1999] Koch, K.-R.: *Parameter Estimation and Hypothesis Testing in Linear Models.* Second, updated and enlarged edition. Berlin, Heidelberg: Springer, 1999. – ISBN: 978-3-642-08461-4 – doi:10.1007/978-3-662-03976-2

[Koch and Kusche 2002] Koch, K.-R.; Kusche, J.: Regularization of geopotential determination from satellite data by variance components. *Journal of Geodesy* 76 (2002), No. 5, pp. 259–268 – doi:10.1007/s00190-002-0245-x

[König et al. 2019] König, R.; Schreiner, P.; Dahle, C.: Monthly estimates of C(2,0) generated by GFZ from SLR satellites based on GFZ GRACE/GRACE-FO RL06 background models. *GFZ Data Services* (2019) – doi:10.5880/GFZ.GRAVIS_06_C20_SLR

[Koop 1993] Koop, R.: *Global Gravity Field Modelling Using Satellite Gravity Gradiometry.* Delft: Nederlandse Commissie voor Geodesie, 1993. – `https://repository.tudelft.nl/record/uuid:23cc2941-6de3-4faa-85fb-e2faa06b0e88`. – Accessed on: 2025-08-08. – ISBN: 90-6132-246-4

[Kudryavtsev 2004] Kudryavtsev, S. M.: Improved harmonic development of the Earth tide-generating potential. *Journal of Geodesy* 77 (2004), No. 12, pp. 829–838 – doi:10.1007/s00190-003-0361-2

[Kulikov et al. 2018] Kulikov, M. E.; Medvedev, I. P.; Kondrin, A. T.: Seasonal variability of tides in the Arctic seas. *Russian Journal of Earth Sciences* 18 (2018), No. 5, pp. 1–14 – doi:10.2205/2018ES000633

[Kurtenbach et al. 2012] Kurtenbach, E.; Eicker, A.; Mayer-Gürr, T.; Holschneider, M.; Hayn, M.; Fuhrmann, M.; Kusche, J.: Improved daily GRACE gravity field solutions using a Kalman smoother. *Journal of Geodynamics* 59-60 (2012), pp. 39–48 – doi:10.1016/j.jog.2012.02.006

[Kurtenbach et al. 2009] Kurtenbach, E.; Mayer-Gürr, T.; Eicker, A.: Deriving daily snapshots of the Earth's gravity field from GRACE L1B data using Kalman filtering. *Geophysical Research Letters* 36 (2009), No. 17 – doi:10.1029/2009GL039564

[Kusche and Springer 2017] Kusche, J.; Springer, A.: Parameter estimation for satellite gravity field modeling. Naeimi, M. (Eds.); Flury, J. (Eds.): *Global Gravity Field Modeling from Satellite-to-Satellite Tracking Data*. Cham: Springer International Publishing, 2017. – ISBN: 978-3-319-49940-6 – doi:10.1007/978-3-319-49941-3_1

[Kvas et al. 2019a] Kvas, A.; Behzadpour, S.; Ellmer, M.; Klinger, B.; Strasser, S.; Zehentner, N.; Mayer-Gürr, T.: ITSG-Grace2018: overview and evaluation of a new GRACE-only gravity field time series. *Journal of Geophysical Research: Solid Earth* 124 (2019), No. 8, pp. 9332–9344 – doi:10.1029/2019JB017415

[Kvas et al. 2021] Kvas, A.; Brockmann, J. M.; Krauss, S.; Schubert, T.; Gruber, T.; Meyer, U.; Mayer-Gürr, T.; Schuh, W.-D.; Jäggi, A.; Pail, R.: GOCO06s – a satellite-only global gravity field model. *Earth System Science Data* 13(1) (2021), pp. 99–118 – doi:10.5194/essd-13-99-2021

[Kvas et al. 2019b] Kvas, A.; Mayer-Gürr, T.; Krauss, S.; Brockmann, J. M.; Schubert, T.; Schuh, W.-D.; Pail, R.; Gruber, T.; Jäggi, A.; Meyer, U.: The satellite-only gravity field model GOCO06s. *GFZ Data Services* (2019) – doi:10.5880/ICGEM.2019.002

[Lahijani et al. 2023] Lahijani, H.; Leroy, S. A. G.; Arpe, K.; Crétaux, J.-F.: Caspian sea level changes during instrumental period, its impact and forecast: a review. *Earth-Science Reviews* 241 (2023), pp. 104428 – doi:10.1016/j.earscirev.2023.104428

[Lambeck 1977] Lambeck, K.: Tidal dissipation in the oceans: astronomical, geophysical and oceanographic consequences. *Philosophical Transactions of the Royal Society of London. Series A, Mathematical and Physical Sciences* 287 (1977), No. 1347, pp. 545–594 – doi:10.1098/rsta.1977.0159

[Landerer et al. 2020] Landerer, F. W.; Flechtner, F. M.; Save, H.; Webb, F. H.; Bandikova, T.; Bertiger, W. I.; Bettadpur, S. V.; Byun, S. H.; Dahle, C.; Dobslaw, H.; Fahnestock, E.; Harvey, N.; Kang, Z.; Kruizinga, G. L. H.; Loomis, B. D.; McCullough, C.; Murböck, M.; Nagel, P.; Paik, M.; et. al.: Extending the global mass change data record: GRACE Follow-On instrument and science data performance. *Geophysical Research Letters* 47(12) (2020) – doi:10.1029/2020GL088306

[Lasser et al. 2023] Lasser, M.; Meyer, U.; Arnold, D.; Jäggi, A.: AIUB-GRACE-FO-operational - operational GRACE Follow-On monthly gravity field solutions - Release 02. *GFZ Data Services* (2023) – doi:10.5880/icgem.2023.004

[Lasser et al. 2020] Lasser, M.; Meyer, U.; Jäggi, A.; Mayer-Gürr, T.; Kvas, A.; Neumayer, K. H.; Dahle, C.; Flechtner, F.; Lemoine, J.-M.; Koch, I.; Weigelt, M.; Flury, J.: Benchmark data for verifying background model implementations in orbit and gravity field determination software. *Advances in Geosciences* 55 (2020), pp. 1–11 – doi:10.5194/adgeo-55-1-2020

[Le Provost 1991] Le Provost, C.: Generation of overtides and compound tides (Review). Parker, B. B. (Eds.): *Tidal Hydrodynamics*. New York: John Wiley & Sons, 1991. – ISBN: 0-471-51498-5

[Lemoine and Bourgogne 2020] Lemoine, J.-M.; Bourgogne, S.: RL05 monthly and 10-day gravity field solutions from CNES/GRGS. *GRACE/GRACE-FO Science Team Meeting 2020, Online, 27–29 October 2020* (2020) – doi:10.5194/gstm2020-51

[Lemoine et al. 2007] Lemoine, J.-M.; Bruinsma, S.; Loyer, S.; Biancale, R.; Marty, J.-C.; Perosanz, F.; Balmino, G.: Temporal gravity field models inferred from GRACE data. *Advances in Space Research* 39 (2007), No. 10, pp. 1620–1629 – doi:10.1016/j.asr.2007.03.062

[Liebe 1993] Liebe, C. C.: Pattern recognition of star constellations for spacecraft applications. *IEEE Aerospace and Electronic Systems Magazine* 8 (1993), No. 1, pp. 31–39 – doi:10.1109/62.180383

[Lindzen and Chapman 1969] Lindzen, R. S.; Chapman, S.: Atmospheric tides. *Space Science Reviews* 10 (1969), No. 1, pp. 3–188 – doi:10.1007/BF00171584

[Liu 2019] Liu, W.: *Understanding Ocean Tide Aliasing in Satellite Gravimetry*, University of Stuttgart, Doctoral dissertation, 2019. – Retrieved from OPUS - Publication Server of the University of Stuttgart: http://dx.doi.org/10.18419/opus-10485

[Liu and Sneeuw 2021] Liu, W.; Sneeuw, N.: Aliasing of ocean tides in satellite gravimetry: a two-step mechanism. *Journal of Geodesy* 95 (2021), No. 12 – doi:10.1007/s00190-021-01586-6

[Lomb 1976] Lomb, N. R.: Least-squares frequency analysis of unequally spaced data. *Astrophysics and Space Science* 39 (1976), No. 2, pp. 447–462 – doi:10.1007/BF00648343

[Long et al. 2016] Long, D.; Chen, X.; Scanlon, B. R.; Wada, Y.; Hong, Y.; Singh, V. P.; Chen, Y.; Wang, C.; Han, Z.; Yang, W.: Have GRACE satellites overestimated groundwater depletion in the Northwest India Aquifer? *Scientific Reports* 6 (2016), No. 1 – doi:10.1038/srep24398

[Loomis et al. 2012] Loomis, B. D.; Nerem, R. S.; Luthcke, S. B.: Simulation study of a follow-on gravity mission to GRACE. *Journal of Geodesy* 86 (2012), No. 5, pp. 319–335 – doi:10.1007/s00190-011-0521-8

[Loomis et al. 2020] Loomis, B. D.; Rachlin, K. E.; Wiese, D. N.; Landerer, F. W.; Luthcke, S. B.: Replacing GRACE/GRACE-FO with satellite laser ranging: impacts on Antarctic ice sheet mass change. *Geophysical Research Letters* 47 (2020), No. 3 – doi:10.1029/2019GL085488

[Luthcke et al. 2013] Luthcke, S. B.; Sabaka, T. J.; Loomis, B. D.; Arendt, A. A.; McCarthy, J. J.; Camp, J.: Antarctica, Greenland and Gulf of Alaska land-ice evolution from an iterated GRACE global mascon solution. *Journal of Glaciology* 59 (2013), No. 216, pp. 613–631 – doi:10.3189/2013JoG12J147

[Lyard et al. 2006] Lyard, F.; Lefevre, F.; Letellier, T.; Francis, O.: Modelling the global ocean tides: modern insights from FES2004. *Ocean Dynamics* 56 (2006), No. 5, pp. 394–415 – doi:10.1007/s10236-006-0086-x

[Lyard et al. 2021] Lyard, F. H.; Allain, D. J.; Cancet, M.; Carrère, L.; Picot, N.: FES2014 global ocean tide atlas: design and performance. *Ocean Science* 17 (2021), No. 3, pp. 615–649 – doi:10.5194/os-17-615-2021

[Lyons 2004] Lyons, R. G.: *Understanding Digital Signal Processing*. 2. London: Pearson Education, 2004. – ISBN: 0-13-108989-7

[MacArthur and Posner 1985] MacArthur, J. L.; Posner, A. S.: Satellite-to-satellite range-rate measurement. *IEEE Transactions on Geoscience and Remote Sensing* GE-23 (1985), No. 4, pp. 517–523 – doi:10.1109/TGRS.1985.289443

[Marchuk and Kagan 1989] Marchuk, G. I.; Kagan, B. A.: *Dynamics of Ocean Tides*. Dordrecht, Boston, London: Kluwer Academic Publishers, 1989 (Oceanographic Sciences Library). – ISBN: 978-94-010-7661-6 – doi:10.1007/978-94-009-2571-7

[Mayer-Gürr et al. 2010] Mayer-Gürr, T.; Eicker, A.; Kurtenbach, E.; Ilk, K.-H.: ITG-GRACE: global static and temporal gravity field models from GRACE data. Flechtner, F. M. (Eds.); Gruber, T. (Eds.); Güntner, A. (Eds.); Mandea, M. (Eds.); Rothacher, M. (Eds.); Schöne, T. (Eds.); Wickert, J. (Eds.): *System Earth via Geodetic-Geophysical Space Techniques*. Berlin, Heidelberg: Springer, 2010, pp. 159–168. – ISBN: 978-3-642-10228-8 – doi:10.1007/978-3-642-10228-8_13

[Mayer-Gürr et al. 2018] Mayer-Gürr, T.; Behzadpour, S.; Ellmer, M.; Kvas, A.; Klinger, B.; Strasser, S.; Zehentner, N.: ITSG-Grace2018 - monthly, daily and static gravity field solutions from GRACE. *GFZ Data Services* (2018) – doi:10.5880/ICGEM.2018.003

[Mayer-Gürr et al. 2012] Mayer-Gürr, T.; Savcenko, R.; Bosch, W.; Daras, I.; Flechtner, F.; Dahle, C.: Ocean tides from satellite altimetry and GRACE. *Journal of Geodynamics* 59-60 (2012), pp. 28–38 – doi:10.1016/j.jog.2011.10.009

[Mayer-Gürr et al. 2023] Mayer-Gürr, T.; Öhlinger, F.; Sulzbach, R.; Dobslaw, H.: Exploiting the full potential of ocean tide models for space geodetic techniques. *EGU General Assembly 2023, Vienna, Austria, 23–28 April 2023* (2023) – doi:10.5194/egusphere-egu23-13235

[Melchior 1966] Melchior, P. J.: *The Earth Tides*. 1. Oxford, London, Edinburgh: Pergamon Press, 1966

[Meyer et al. 2019] Meyer, U.; Jean, Y.; Kvas, A.; Dahle, C.; Lemoine, J. M.; Jäggi, A.: Combination of GRACE monthly gravity fields on the normal equation level. *Journal of Geodesy* 93 (2019), No. 9, pp. 1645–1658 – doi:10.1007/s00190-019-01274-6

[Meyer et al. 2016] Meyer, U.; Jäggi, A.; Jean, Y.; Beutler, G.: AIUB-RL02: an improved time-series of monthly gravity fields from GRACE data. *Geophysical Journal International* 205 (2016), No. 2, pp. 1196–1207 – doi:10.1093/gji/ggw081

[Meyer et al. 2023] Meyer, U.; Lasser, M.; Dahle, C.; Förste, C.; Behzadpour, S.; Koch, I.; Jäggi, A.: Combined monthly GRACE-FO gravity fields for a global gravity-based groundwater product. *Geophysical Journal International* 236 (2023), No. 1, pp. 456–469 – doi:10.1093/gji/ggad437

[Mohr et al. 2008] Mohr, P. J.; Taylor, B. N.; Newell, D. B.: CODATA recommended values of the fundamental physical constants: 2006. *Reviews of Modern Physics* 80 (2008), pp. 633–730 – doi:10.1103/RevModPhys.80.633

[Montenbruck and Gill 2005] Montenbruck, O.; Gill, E.: *Satellite Orbits – Models, Methods and Applications*. 3. Berlin: Springer Science & Business Media, 2005. – ISBN: 978-3-642-63547-2 – doi:10.1007/978-3-642-58351-3

[Montenbruck and Kroes 2003] Montenbruck, O.; Kroes, R.: In-flight performance analysis of the CHAMP BlackJack GPS receiver. *GPS Solutions* 7 (2003), No. 2, pp. 74–86 – doi:10.1007/s10291-003-0055-5

[Müller et al. 2014] Müller, M.; Cherniawsky, J. Y.; Foreman, M. G. G.; Storch, J.-S. von: Seasonal variation of the M2 tide. *Ocean Dynamics* 64 (2014), No. 2, pp. 159–177 – doi:10.1007/s10236-013-0679-0

[Munk and Cartwright 1966] Munk, W. H.; Cartwright, D. E.: Tidal spectroscopy and prediction. *Philosophical Transactions of the Royal Society of London. Series A, Mathematical and Physical Sciences* 259 (1966), No. 1105, pp. 533–581 – doi:10.1098/rsta.1966.0024

[Munk and MacDonald 1975] Munk, W. H.; MacDonald, G. J. F.: *The rotation of the Earth: A geophysical discussion*. reprinted with corrections. Cambridge, London, New York, Melbourne: Cambridge University Press, 1975. – ISBN: 0 521 20778 9

[Naeije et al. 2000] Naeije, M.; Schrama, E.; Scharroo, R.: The Radar Altimeter Database System project RADS. *IGARSS 2000. IEEE 2000 International Geoscience and Remote Sensing Symposium. Taking the Pulse of the Planet: The Role of Remote Sensing in Managing the Environment. Proceedings (Cat. No.00CH37120)* Vol. 2. 2000, pp. 487–490 – doi:10.1109/IGARSS.2000.861605

[Naeimi 2018] Naeimi, M.: A modified Gauss-Jackson method for the numerical integration of the variational equations. *EGU General Assembly 2018, Vienna, Austria, 8–13 April 2018* (2018)

[Naeimi and Flury 2017] Naeimi, M. (Eds.); Flury, J. (Eds.): *Global Gravity Field Modeling from Satellite-to-Satellite Tracking Data*. Cham: Springer International Publishing, 2017 (Lecture Notes in Earth System Sciences). – ISBN: 978-3-319-49941-3 – doi:10.1007/978-3-319-49941-3

[Naeimi et al. 2018] Naeimi, M.; Koch, I.; Khami, A.; Flury, J.: IfE monthly gravity field solutions using the variational equations. *EGU General Assembly 2018, Vienna, Austria, 8–13 April 2018* (2018) – doi:10.15488/4452

[NASA 2002] National Aeronautics and Space Administration (NASA): GRACE launch press kit. (2002). – `https://www.jpl.nasa.gov/news/press_kits/gracelaunch.pdf`. – Accessed on: 2025-08-08

[NASA 2018] National Aeronautics and Space Administration (NASA): GRACE-FO launch press kit. (2018). – `https://www.jpl.nasa.gov/news/press_kits/grace-fo/download/grace-fo_launch_press_kit.pdf`. – Accessed on: 2025-08-08

[Nerem et al. 1995] Nerem, R. S.; Jekeli, C.; Kaula, W. M.: Gravity field determination and characteristics: Retrospective and prospective. *Journal of Geophysical Research: Solid Earth* 100 (1995), No. B8, pp. 15053–15074 – doi:10.1029/94JB03257

[Niemeier 2008] Niemeier, W.: *Ausgleichungsrechnung: Statistische Auswertemethoden*. 2. Berlin, Germany: Walter de Gruyter, 2008. – ISBN: 978-3-11-019055-7 – doi:10.1515/9783110206784

[Oki and Sud 1998] Oki, T.; Sud, Y. C.: Design of Total Runoff Integrating Pathways (TRIP)—a global river channel network. *Earth Interactions* 2 (1998), No. 1, pp. 1–37 – doi:10.1175/1087-3562(1998)002<0001:DOTRIP>2.3.CO;2

[Panet et al. 2018] Panet, I.; Bonvalot, S.; Narteau, C.; Remy, D.; Lemoine, J.-M.: Migrating pattern of deformation prior to the Tohoku-Oki earthquake revealed by GRACE data. *Nature Geoscience* 11 (2018), No. 5, pp. 367–373 – doi:10.1038/s41561-018-0099-3

[Panet et al. 2007] Panet, I.; Mikhailov, V.; Diament, M.; Pollitz, F.; King, G.; De Viron, O.; Holschneider, M.; Biancale, R.; Lemoine, J.-M.: Coseismic and post-seismic signatures of the Sumatra 2004 December and 2005 March earthquakes in GRACE satellite gravity. *Geophysical Journal International* 171 (2007), No. 1, pp. 177–190 – doi:10.1111/j.1365-246X.2007.03525.x

[Parke et al. 1987] Parke, M. E.; Stewart, R. H.; Farless, D. L.; Cartwright, D. E.: On the choice of orbits for an altimetric satellite to study ocean circulation and tides. *Journal of Geophysical Research: Oceans* 92 (1987), No. C11, pp. 11693–11707 – doi:10.1029/JC092iC11p11693

[Parker 2007] Parker, B. B.: *Tidal Analysis and Prediction*. Silver Spring, MD: NOAA, NOS Center for Operational Oceanographic Products and Services, 2007 (NOAA Special Publication NOS CO-OPS;3) – doi:10.25607/OBP-191

[Pearlman et al. 2019] Pearlman, M.; Arnold, D.; Davis, M.; Barlier, F.; Biancale, R.; Vasiliev, V.; Ciufolini, I.; Paolozzi, A.; Pavlis, E. C.; Sośnica, K.; Blossfeld, M.: Laser geodetic satellites: a high-accuracy scientific tool. *Journal of Geodesy* 93 (2019), No. 11, pp. 2181–2194 – doi:10.1007/s00190-019-01228-y

[Peltier 2004] Peltier, W. R.: Global glacial isostasy and the surfacce of the ice-age Earth: the ICE-5G (VM2) model and GRACE. *Annual Review of Earth and Planetary Sciences* 32 (2004), pp. 111–149 – doi:10.1146/annurev.earth.32.082503.144359

[Peltier et al. 2018] Peltier, W. R.; Argus, D. F.; Drummond, R.: Comment on "An assessment of the ICE-6G_C (VM5a) glacial isostatic adjustment model" by Purcell et al. *Journal of Geophysical Research: Solid Earth* 123 (2018), No. 2, pp. 2019–2028 – doi:10.1002/2016JB013844

[Pitjeva 2005] Pitjeva, E. V.: High-precision ephemerides of planets—EPM and determination of some astronomical constants. *Solar System Research* 39 (2005), No. 3, pp. 176–186 – doi:10.1007/s11208-005-0033-2

[Platzman 1984] Platzman, G. W.: Normal modes of the world Ocean. Part IV: synthesis of diurnal and semidiurnal tides. *Journal of Physical Oceanography* 14 (1984), No. 10, pp. 1532 – 1550 – doi:10.1175/1520-0485(1984)014<1532:NMOTWO>2.0.CO;2

[PO.DAAC 2018] Physical Oceanography Distributed Active Archive Center (PO.DAAC): GRACE_L1B_GRAV_JPL_RL03. (2018). – `https://podaac.jpl.nasa.gov/dataset/GRACE_L1B_GRAV_JPL_RL03`. – Accessed on: 2025-08-08 – doi:10.5067/GRJPL-L1B03

[PO.DAAC 2019] Physical Oceanography Distributed Active Archive Center (PO.DAAC): GRACE-FO Level-1B release version 4.0 from JPL in ASCII. (2019). – `https://podaac.jpl.nasa.gov/dataset/GRACEFO_L1B_ASCII_GRAV_JPL_RL04`. – Accessed on: 2025-08-08 – doi:10.5067/GFL1B-ASJ04

[Press and Rybicki 1989] Press, W. H.; Rybicki, G. B.: Fast algorithm for spectral analysis of unevenly sampled data. *Astrophysical Journal* 338 (1989), pp. 277 – doi:10.1086/167197

[Proudman 1960] Proudman, J.: The condition that a long-period tide shall follow the equilibrium-law. *Geophysical Journal of the Royal Astronomical Society* 3 (1960), No. 2, pp. 244–249 – doi:10.1111/j.1365-246X.1960.tb00392.x

[Pugh and Woodworth 2014] Pugh, D.; Woodworth, P.: *Sea-Level Science: Understanding Tides, Surges, Tsunamis and Mean Sea-Level Changes*. 2. Cambridge University Press, 2014. – ISBN: 978-1-107-02819-7 – doi:10.1017/CBO9781139235778

[Ray 1999] Ray, R. D.: A global ocean tide model from TOPEX/POSEIDON altimetry: GOT99.2. *Technical Memorandum, NASA/TM-1999-209478* (1999). – https://ntrs.nasa.gov/citations/19990089548. – Accessed on: 2025-08-08

[Ray 2017] Ray, R. D.: On tidal inference in the diurnal band. *Journal of Atmospheric and Oceanic Technology* 34 (2017), No. 2, pp. 437–446 – doi:10.1175/JTECH-D-16-0142.1

[Ray 2020a] Ray, R. D.: Daily harmonics of ionospheric total electron content from satellite altimetry. *Journal of Atmospheric and Solar-Terrestrial Physics* 209 (2020) – doi:10.1016/j.jastp.2020.105423

[Ray 2020b] Ray, R. D.: First global observations of third-degree ocean tides. *Science Advances* 6 (2020), No. 48 – doi:10.1126/sciadv.abd4744

[Ray 2022] Ray, R. D.: Technical note: On seasonal variability of the M_2 tide. *Ocean Science* 18 (2022), No. 4, pp. 1073–1079 – doi:10.5194/os-18-1073-2022

[Ray 2025] Ray, R. D.: Documentation for Goddard ocean tide solution GOT5: global tides from multimission satellite altimetry. *Technical Memorandum, NASA TM-20250002085* (2025). – https://ntrs.nasa.gov/citations/20250002085. – Accessed on: 2025-09-01

[Ray et al. 2023] Ray, R. D.; Boy, J.-P.; Erofeeva, S. Y.; Egbert, G. D.: Terdiurnal radiational tides. *Journal of Physical Oceanography* 53 (2023), No. 4, pp. 1139–1150 – doi:10.1175/JPO-D-22-0175.1

[Ray et al. 2011] Ray, R. D.; Egbert, G. D.; Erofeeva, S. Y.: Tide predictions in shelf and coastal waters: status and prospects. Vignudelli, S. (Eds.); Kostianoy, A. G. (Eds.); Cipollini, P. (Eds.); Benveniste, J. (Eds.): *Coastal Altimetry*. Berlin, Heidelberg: Springer, 2011, pp. 191–216 – doi:10.1007/978-3-642-12796-0_8

[Ray and Erofeeva 2014] Ray, R. D.; Erofeeva, S. Y.: Long-period tidal variations in the length of day. *Journal of Geophysical Research: Solid Earth* 119 (2014), No. 2, pp. 1498–1509 – doi:10.1002/2013JB010830

[Ray et al. 2019] Ray, R. D.; Loomis, B. D.; Luthcke, S. B.; Rachlin, K. E.: Tests of ocean-tide models by analysis of satellite-to-satellite range measurements: an update. *Geophysical Journal International* 217 (2019), No. 2, pp. 1174–1178 – doi:10.1093/gji/ggz062

[Ray and Luthcke 2006] Ray, R. D.; Luthcke, S. B.: Tide model errors and GRACE gravimetry: towards a more realistic assessment. *Geophysical Journal International* 167 (2006), No. 3, pp. 1055–1059 – doi:10.1111/j.1365-246X.2006.03229.x

[Ray et al. 2009] Ray, R. D.; Luthcke, S. B.; Boy, J.-P.: Qualitative comparisons of global ocean tide models by analysis of intersatellite ranging data. *Journal of Geophysical Research: Oceans* 114 (2009), No. C9 – doi:10.1029/2009JC005362

[Ray et al. 2003] Ray, R. D.; Rowlands, D. D.; Egbert, G. D.: Tidal models in a new era of satellite gravimetry. *Space Science Reviews* 108 (2003), No. 1, pp. 271–282 – doi:10.1023/A:1026223308107

[Ray et al. 1994] Ray, R. D.; Steinberg, D. J.; Chao, B. F.; Cartwright, D. E.: Diurnal and semidiurnal variations in the Earth's rotation rate induced by oceanic tides. *Science* 264 (1994), No. 5160, pp. 830–832 – doi:10.1126/science.264.5160.830

[Reichert et al. 2002] Reichert, A.; Meehan, T.; Munson, T.: Toward decimeter-level real-time orbit determination: a demonstration using the SAC-C and CHAMP spacecraft. *Proceedings of the 15th International Technical Meeting of the Satellite Division of The Institute of Navigation (ION GPS 2002)* (2002), pp. 1996–2003. – https://www.gdgps.net/system-desc/papers/Reichert_IONGPS2002.pdf. – Accessed on: 2025-08-08

[Rieser et al. 2012] Rieser, D.; Mayer-Gürr, T.; Savcenko, R.; Bosch, W.; Wünsch, J.; Dahle, C.; Flechtner, F.: The ocean tide model EOT11a in spherical harmonics representation, Technical note. (2012). – http://ftp.tugraz.at/outgoing/ITSG/COTAGA/TN_EOT11a.pdf. – Accessed on: 2025-08-08

[Riva et al. 2009] Riva, R. E. M.; Gunter, B. C.; Urban, T. J.; Vermeersen, B. L. A.; Lindenbergh, R. C.; Helsen, M. M.; Bamber, J. L.; van de Wal, R. S. W.; van den Broeke, M. R.; Schutz, B. E.:

Glacial isostatic adjustment over Antarctica from combined ICESat and GRACE satellite data. *Earth and Planetary Science Letters* 288 (2009), No. 3, pp. 516–523 – doi:10.1016/j.epsl.2009.10.013

[Rodell et al. 2018] Rodell, M.; Famiglietti, J. S.; Wiese, D. N.; Reager, J. T.; Beaudoing, H. K.; Landerer, F. W.; Lo, M.-H.: Emerging trends in global freshwater availability. *Nature* 557 (2018), No. 7707, pp. 651–659 – doi:10.1038/s41586-018-0123-1

[Rodell et al. 2004] Rodell, M.; Houser, P. R.; Jambor, U.; Gottschalck, J.; Mitchell, K.; Meng, C.-J.; Arsenault, K.; Cosgrove, B.; Radakovich, J.; Bosilovich, M.; Entin, J. K.; Walker, J. P.; Lohmann, D.; Toll, D.: The global land data assimilation system. *Bulletin of the American Meteorological Society* 85 (2004), No. 3, pp. 381–394 – doi:10.1175/BAMS-85-3-381

[Rodell and Reager 2023] Rodell, M.; Reager, J. T.: Water cycle science enabled by the GRACE and GRACE-FO satellite missions. *Nature Water* 1 (2023), No. 1, pp. 47–59 – doi:10.1038/s44221-022-00005-0

[Rodell et al. 2009] Rodell, M.; Velicogna, I.; Famiglietti, J. S.: Satellite-based estimates of groundwater depletion in India. *Nature* 460 (2009), No. 7258, pp. 999–1002 – doi:10.1038/nature08238

[Roosbeek 1996] Roosbeek, F.: RATGP95: a harmonic development of the tide-generating potential using an analytical method. *Geophysical Journal International* 126 (1996), No. 1, pp. 197–204 – doi:10.1111/j.1365-246X.1996.tb05278.x

[Rummel et al. 1978] Rummel, R.; Reigber, C.; Ilk, K.-H.: The use of satellite to satellite tracking for gravity parameter recovery. *Proceedings of the European Workshop on Space Oceanography, Navigation and Geodynamics (SONG), ESA SP-137.* 1978, pp. 153–161

[Sasgen et al. 2020] Sasgen, I.; Wouters, B.; Gardner, A. S.; King, M. D.; Tedesco, M.; Landerer, F. W.; Dahle, C.; Save, H.; Fettweis, X.: Return to rapid ice loss in Greenland and record loss in 2019 detected by the GRACE-FO satellites. *Communications Earth & Environment* 1 (2020), No. 1 – doi:10.1038/s43247-020-0010-1

[Savcenko and Bosch 2008] Savcenko, R.; Bosch, W.: EOT08a - empirical ocean tide model from multi-mission satellite altimetry. *DGFI Report No. 81* (2008). – `https://mediatum.ub.tum.de/doc/1300708/1300708.pdf`. – Accessed on: 2025-08-08

[Savcenko and Bosch 2012] Savcenko, R.; Bosch, W.: EOT11A - empirical ocean tide model from multi-mission satellite altimetry. *DGFI Report No. 89* (2012). – `https://mediatum.ub.tum.de/doc/1300842/1300842.pdf`. – Accessed on: 2025-08-08

[Save 2019a] Save, H.: CSR Level-2 processing standards document (For Level-2 product release 06). *CSR GRFO-19-01 (GRACE-FO D-103920)* (2019). – `ftp://isdcftp.gfz-potsdam.de/grace-fo/DOCUMENTS/Level-2/GRACE-FO_CSR_L2_Processing_Standards_Document_for_RL06.pdf`. – Accessed on: 2025-08-08

[Save 2019b] Save, H.: CSR RL05 GRACE daily swath mass anomaly estimates over the ocean. *Texas Data Repository* (2019) – doi:10.18738/T8/95ITIK

[Save et al. 2016] Save, H.; Bettadpur, S.; Tapley, B. D.: High-resolution CSR GRACE RL05 mascons. *Journal of Geophysical Research: Solid Earth* 121 (2016), No. 10, pp. 7547–7569 – doi:10.1002/2016JB013007

[Scargle 1982] Scargle, J. D.: Studies in astronomical time series analysis. II. Statistical aspects of spectral analysis of unevenly spaced data. *The Astrophysical Journal* 263 (1982), pp. 835–853 – doi:10.1086/160554

[Schaffer et al. 2016] Schaffer, J.; Timmermann, R.; Arndt, J. E.; Kristensen, S. S.; Mayer, C.; Morlighem, M.; Steinhage, D.: A global, high-resolution data set of ice sheet topography, cavity geometry, and ocean bathymetry. *Earth System Science Data* 8 (2016), No. 2, pp. 543–557 – doi:10.5194/essd-8-543-2016

[Schlax and Chelton 1994] Schlax, M. G.; Chelton, D. B.: Aliased tidal errors in TOPEX/POSEIDON sea surface height data. *Journal of Geophysical Research: Oceans* 99 (1994), No. C12, pp. 24761–24775 – doi:10.1029/94JC01925

[Schmidt et al. 2007] Schmidt, R.; Meyer, U.; Dahle, C.; Kusche, J.; Flechtner, F.: Monthly and weekly EIGEN-GRACE05S gravity field solutions for monitoring mass variations in the Earth system. *Second Space for Hydrology Workshop - Surface Water Storage and Runoff: Modeling, In-Situ Data and Remote Sensing, 12-14 November 2007, Geneva/Switzerland* (2007)

[Schrama and Ray 1994] Schrama, E. J. O.; Ray, R. D.: A preliminary tidal analysis of TOPEX/POSEIDON altimetry. *Journal of Geophysical Research: Oceans* 99 (1994), No. C12, pp. 24799–24808 – doi:10.1029/94JC01432

[Schrama et al. 2007] Schrama, E. J. O.; Wouters, B.; Lavallée, D. A.: Signal and noise in Gravity Recovery and Climate Experiment (GRACE) observed surface mass variations. *Journal of Geophysical Research: Solid Earth* 112 (2007), No. B8 – doi:10.1029/2006JB004882

[Schwatke et al. 2024] Schwatke, C.; Dettmering, D.; Passaro, M.; Hart-Davis, M.; Scherer, D.; Müller, F. L.; Bosch, W.; Seitz, F.: OpenADB: DGFI-TUM's Open Altimeter Database. *Geoscience Data Journal* 11 (2024), No. 4, pp. 573–588 – doi:10.1002/gdj3.233

[Seeber 2003] Seeber, G.: *Satellite geodesy.* 2. Berlin: Walter de Gruyter, 2003. – ISBN: 978-3-110-17549-3

[Seo et al. 2008] Seo, K. W.; Wilson, C. R.; Han, S. C.; Waliser, D. E.: Gravity Recovery and Climate Experiment (GRACE) alias error from ocean tides. *Journal of Geophysical Research: Solid Earth* 113 (2008), No. B3 – doi:10.1029/2006JB004747

[Sharifi 2004] Sharifi, M. A.: *Satellite Gradiometry Using a Satellite Pair*, University of Stuttgart, Doctoral dissertation, 2004. – Retrieved from OPUS Universität Stuttgart: `http://dx.doi.org/10.18419/opus-3685`

[Sheard et al. 2012] Sheard, B. S.; Heinzel, G.; Danzmann, K.; Shaddock, D. A.; Klipstein, W. M.; Folkner, W. M.: Intersatellite laser ranging instrument for the GRACE follow-on mission. *Journal of Geodesy* 86 (2012), pp. 1083–1095 – doi:10.1007/s00190-012-0566-3

[Shum et al. 1997] Shum, C. K.; Woodworth, P. L.; Andersen, O. B.; Egbert, G. D.; Francis, O.; King, C.; Klosko, S. M.; Le Provost, C.; Li, X.; Molines, J-M; Parke, M. E.; Ray, R. D.; Schlax, M. G.; Stammer, D.; Tierney, C. C.; Vincent, P.; Wunsch, C. I.: Accuracy assessment of recent ocean tide models. *Journal of Geophysical Research: Oceans* 102 (1997), No. C11, pp. 25173–25194 – doi:10.1029/97JC00445

[Simon et al. 1994] Simon, J. L.; Bretagnon, P.; Chapront, J.; Chapront-Touze, M.; Francou, G.; Laskar, J.: Numerical expressions for precession formulae and mean elements for the Moon and the planets. *Astronomy and Astrophysics* 282 (1994), No. 2, pp. 663–683

[Smith 1999] Smith, A. J. E.: *Application of Satellite Altimetry for Global Ocean Tide Modeling*, Delf University of Technology, Doctoral dissertation, 1999. – Retrieved from TU Delft Repository: `http://resolver.tudelft.nl/uuid:5e9c5527-220f-4658-b516-459528e62733` – Accessed on: 2025-08-08

[Smith et al. 2000] Smith, A. J. E.; Ambrosius, B. A. C.; Wakker, K. F.: Ocean tides from T/P, ERS-1, and GEOSAT altimetry. *Journal of Geodesy* 74 (2000), No. 5, pp. 399–413 – doi:10.1007/s001900000101

[Souchay et al. 1999] Souchay, J.; Loysel, B.; Kinoshita, H.; Folgueira, M.: Corrections and new developments in rigid Earth nutation theory - III. Final tables "REN-2000" including crossed nutation and spin-orbit coupling effects. *Astronomy and Astrophysics Supplement Series* 135 (1999), No. 1, pp. 111–131 – doi:10.1051/aas:1999446

[St-Laurent et al. 2008] St-Laurent, P.; Saucier, F. J.; Dumais, J.-F.: On the modification of tides in a seasonally ice-covered sea. *Journal of Geophysical Research: Oceans* 113 (2008), No. C11 – doi:10.1029/2007JC004614

[Stammer et al. 2014] Stammer, D.; Ray, R. D.; Andersen, O. B.; Arbic, B. K.; Bosch, W.; Carrère, L.; Cheng, Y.; Chinn, D. S.; Dushaw, B. D.; Egbert, G. D.; Erofeeva, S. Y.; Fok, H. S.; Green, J. A. M.; Griffiths, S.; King, M. A.; Lapin, V.; Lemoine, F. G.; Luthcke, S. B.; Lyard, F.; et al.: Accuracy assessment of global barotropic ocean tide models. *Reviews of Geophysics* 52 (2014), No. 3, pp. 243–282 – doi:10.1002/2014RG000450

[Steffen and Wu 2011] Steffen, H.; Wu, P.: Glacial isostatic adjustment in Fennoscandia—A review of data and modeling. *Journal of Geodynamics* 52 (2011), No. 3, pp. 169–204 – doi:10.1016/j.jog.2011.03.002

[Su et al. 2022] Su, Y.; Li, J.; Zou, X.; Xu, X.; Wang, C.; Yu, B.; Li, Q.: SWPU-GRACE2021: a new temporal gravity model from GRACE. *GFZ Data Services* (2022) – doi:10.5880/icgem.2022.001

[Sulzbach et al. 2022] Sulzbach, R.; Balidakis, K.; Dobslaw, H.; Thomas, M.: TiME22: periodic disturbances of the terrestrial gravity potential induced by oceanic and atmospheric tides. *GFZ Data Services* (2022) – doi:10.5880/GFZ.1.3.2022.006

[Sulzbach et al. 2021] Sulzbach, R.; Dobslaw, H.; Thomas, M.: High-resolution numerical modeling of barotropic global ocean tides for satellite gravimetry. *Journal of Geophysical Research: Oceans* 126 (2021), No. 5 – doi:10.1029/2020JC017097

[Sulzbach 2023] Sulzbach, R. L.: *Versatile Hydrodynamic Modelling of Global Ocean Tides and their Derived Variables for Geodesy and Paleo Sea Level Reconstruction*, Freie Universität Berlin, Doctoral dissertation, 2023. – Retrieved from Refubium - Freie Universität Berlin Repository: `http://dx.doi.org/10.17169/refubium-41358`

[Sun et al. 2016] Sun, Y.; Riva, R.; Ditmar, P.: Optimizing estimates of annual variations and trends in geocenter motion and J2 from a combination of GRACE data and geophysical models. *Journal of Geophysical Research: Solid Earth* 121 (2016), No. 11, pp. 8352–8370 – doi:10.1002/2016JB013073

[Svehla 2017] Svehla, D.: *Geometrical Theory of Satellite Orbits and Gravity Field*, Technical University of Munich, Doctoral dissertation, 2017. – Retrieved from mediaTUM – the media and publications repository of the Technical University of Munich: `https://nbn-resolving.org/urn:nbn:de:bvb:91-diss-20170529-1355925-1-6` – Accessed on: 2025-08-08

[Svehla and Rothacher 2003] Svehla, D.; Rothacher, M.: Kinematic and reduced-dynamic precise orbit determination of low earth orbiters. *Advances in Geosciences* 1 (2003), pp. 47–56 – doi:10.5194/adgeo-1-47-2003

[Swenson et al. 2008] Swenson, S.; Chambers, D.; Wahr, J.: Estimating geocenter variations from a combination of GRACE and ocean model output. *Journal of Geophysical Research: Solid Earth* 113 (2008), No. B8 – doi:10.1029/2007JB005338

[Tapley et al. 2004] Tapley, B. D.; Bettadpur, S.; Watkins, M.; Reigber, C.: The Gravity Recovery And Climate Experiment: mission overview and early results. *Geophysical Research Letters* 31 (2004), No. 9 – doi:10.1029/2004GL019920

[Tapley et al. 2019] Tapley, B. D.; Watkins, M. M.; Flechtner, F.; Reigber, C.; Bettadpur, S.; Rodell, M.; Sasgen, I.; Famiglietti, J. S.; Landerer, F. W.; Chambers, D. P.; Reager, J. T.; Gardner, A. S.; Save, H.; Ivins, E. R.; Swenson, S. C.; Boening, C.; Dahle, C.; Wiese, D. N.; Dobslaw, H.; et al.: Contributions of GRACE to understanding climate change. *Nature Climate Change* 9 (2019), pp. 358–369 – doi:10.1038/s41558-019-0456-2

[Teunissen and Montenbruck 2017] Teunissen, P.; Montenbruck, O.: *Springer Handbook of Global Navigation Satellite Systems*. 1. Springer, 2017 (Springer Handbooks). – ISBN: 978-3-319-42928-1 – doi:10.1007/978-3-319-42928-1

[Thomas 1999] Thomas, J. B.: An analysis of gravity-field estimation based on intersatellite dual-1-way biased ranging. *JPL Publication 98-15* (1999). – `https://apps.dtic.mil/sti/pdfs/ADA410563.pdf`. – Accessed on: 2025-08-08

[Tien et al. 2012] Tien, J. Y.; Bachman Okihiro, B.; Esterhuizen, S. X.; Franklin, G. W.; Meehan, T. K.; Munson, T. N.; Robison, D. E.; Turbiner, D.; Young, L. E.: Next generation scalable spaceborne GNSS science receiver. *Proceedings of the 2012 International Technical Meeting of the Institute of Navigation* (2012), pp. 882–914. – `https://hdl.handle.net/2014/42520`. – Accessed on: 2025-08-08

[Torge and Müller 2012] Torge, W.; Müller, J.: *Geodesy*. 4. Berlin: De Gruyter, 2012. – ISBN: 978-3-11-020718-7 – doi:10.1515/9783110250008

[Touboul et al. 2012] Touboul, P.; Foulon, B.; Christophe, B.; Marque, J. P.: CHAMP, GRACE, GOCE instruments and beyond. Kenyon, S. (Eds.); Pacino, M. C. (Eds.); Marti, U. (Eds.): *Geodesy for Planet Earth, International Association of Geodesy Symposia, Vol 136*. Berlin, Heidelberg: Springer, 2012, pp. 215–221. – ISBN: 978-3-642-20338-1 – doi:10.1007/978-3-642-20338-1_26

[Touboul et al. 1999] Touboul, P.; Willemenot, E.; Foulon, B.; Josselin, V.: Accelerometers for CHAMP, GRACE and GOCE space missions: synergy and evolution. *Bollettino di Geofisica Teorica ed Applicata* 40 (1999), pp. 321–327

[Tregoning et al. 2022] Tregoning, P.; McGirr, R.; Pfeffer, J.; Purcell, A.; McQueen, H.; Allgeyer, S.; McClusky, S. C.: ANU GRACE data analysis: characteristics and benefits of using irregularly shaped mascons. *Journal of Geophysical Research: Solid Earth* 127 (2022), No. 2 – doi:10.1029/2021JB022412

[Tscherning 1976] Tscherning, C. C.: Computation of the second-order derivatives of the normal potential based on the representation by a Legendre series. *Manuscripta Geodetica* 1 (1976), pp. 71–92

[Vallado 2004] Vallado, D. A.: *Fundamentals of Astrodynamics and Applications*. 2. El Segundo, Dordrecht: Microcosm Press; Kluwer Academic Publishers, 2004. – ISBN: 0-7923-6903-3

[VanderPlas 2018] VanderPlas, J. T.: Understanding the Lomb–Scargle periodogram. *The Astrophysical Journal Supplement Series* 236 (2018), No. 1 – doi:10.3847/1538-4365/aab766

[Vaníček 1969] Vaníček, P.: Approximate spectral analysis by least-squares fit. *Astrophysics and Space Science* 4 (1969), No. 4, pp. 387–391 – doi:10.1007/BF00651344

[Velicogna et al. 2020] Velicogna, I.; Mohajerani, Y.; A, G.; Landerer, F.; Mouginot, J.; Noel, B.; Rignot, E.; Sutterley, T.; Broeke, M. van den; Wessem, M. van; Wiese, D.: Continuity of ice sheet mass loss in Greenland and Antarctica from the GRACE and GRACE Follow-On missions. *Geophysical Research Letters* 47 (2020), No. 8 – doi:10.1029/2020GL087291

[Vetterli et al. 2014] Vetterli, M.; Kovačević, J.; Goyal, V. K.: *Foundations of Signal Processing*. Cambridge University Press, 2014

[Visser et al. 2010] Visser, P. N. A. M.; Sneeuw, N.; Reubelt, T.; Losch, M.; Van Dam, T.: Space-borne gravimetric satellite constellations and ocean tides: aliasing effects. *Geophysical Journal International* 181 (2010), No. 2, pp. 789–805 – doi:10.1111/j.1365-246X.2010.04557.x

[Vondrák et al. 2005] Vondrák, J.; Weber, R.; Ron, C.: Free core nutation: direct observations and resonance effects. *Astronomy and Astrophysics* 444 (2005), No. 1, pp. 297–303 – doi:10.1051/0004-6361:20053429

[Wagner et al. 2006] Wagner, C.; McAdoo, D.; Klokočník, J.; Kostelecký, J.: Degradation of geopotential rrecovery from short repeat-cycle orbits: application to GRACE monthly fields. *Journal of Geodesy* 80 (2006), No. 2, pp. 94–103 – doi:10.1007/s00190-006-0036-x

[Wahr et al. 1998] Wahr, J.; Molenaar, M.; Bryan, F.: Time variability of the Earth's gravity field: hydrological and oceanic effects and their possible detection using GRACE. *Journal of Geophysical Research: Solid Earth* 103 (1998), No. B12, pp. 30205–30229 – doi:10.1029/98JB02844

[Wahr 1981] Wahr, J. M.: Body tides on an elliptical, rotating, elastic and oceanless Earth. *Geophysical Journal International* 64 (1981), No. 3, pp. 677–703 – doi:10.1111/j.1365-246X.1981.tb02690.x

[Wang et al. 2015] Wang, C.; Xu, H.; Zhong, M.; Feng, W.: Monthly gravity field recovery from GRACE orbits and K-band measurements using variational equations approach. *Geodesy and Geodynamics* 6 (2015), No. 4, pp. 253–260 – doi:10.1016/j.geog.2015.05.010

[Wang et al. 2012] Wang, L.; Shum, C. K.; Simons, F. J.; Tapley, B.; Dai, C.: Coseismic and postseismic deformation of the 2011 Tohoku-Oki earthquake constrained by GRACE gravimetry. *Geophysical Research Letters* 39 (2012), No. 7 – doi:10.1029/2012GL051104

[Watkins et al. 2015] Watkins, M. M.; Wiese, D. N.; Yuan, D.-N.; Boening, C.; Landerer, F. W.: Improved methods for observing Earth's time variable mass distribution with GRACE using spherical cap mascons. *Journal of Geophysical Research: Solid Earth* 120 (2015), No. 4, pp. 2648–2671 –

doi:10.1002/2014JB011547

[Weatherall et al. 2015] Weatherall, P.; Marks, K. M.; Jakobsson, M.; Schmitt, T.; Tani, S.; Arndt, J. E.; Rovere, M.; Chayes, D.; Ferrini, V.; Wigley, R.: A new digital bathymetric model of the world's oceans. *Earth and Space Science* 2 (2015), No. 8, pp. 331–345 – doi:10.1002/2015EA000107

[Weijer et al. 2007] Weijer, W.; Vivier, F.; Gille, S. T.; Dijkstra, H. A.: Multiple oscillatory modes of the Argentine Basin. Part I: statistical analysis. *Journal of Physical Oceanography* 37 (2007), No. 12, pp. 2855–2868 – doi:10.1175/2007JPO3527.1

[Weis et al. 2008] Weis, P.; Thomas, M.; Sündermann, J.: Broad frequency tidal dynamics simulated by a high-resolution global ocean tide model forced by ephemerides. *Journal of Geophysical Research: Oceans* 113 (2008), No. C10 – doi:10.1029/2007JC004556

[Wen et al. 2019] Wen, Y. H.; Kruizinga, G.; Paik, M.; Landerer, F.; Bertiger, W.; Sakamura, C.; Bandikova, T.; McCullough, C.: Gravity Recovery and Climate Experiment Follow-On (GRACE-FO), Level-1 data product user handbook. *JPL D-56935 (URS270772)* (2019). – `ftp://isdcftp.gfz-potsdam.de/grace-fo/DOCUMENTS/Level-1/GRACE-FO_L1_Data_Product_User_Handbook_20190911.pdf`. – Accessed on: 2025-08-08

[Wenzel 1997] Wenzel, H.-G.: Tide-generating potential for the Earth. Wilhelm, H. (Eds.); Zürn, W. (Eds.); Wenzel, H.-G. (Eds.): *Tidal Phenomena*. Berlin, Heidelberg: Springer, 1997, pp. 9–26. – ISBN: 978-3-540-68700-9 – doi:10.1007/BFb0011455

[Wenzel 2022] Wenzel, H.-G.: Eterna - Programs for tidal analysis and prediction. Karlsruhe Institute of Technology. (2022) – doi:10.35097/746

[Whitehouse et al. 2012] Whitehouse, P. L.; Bentley, M. J.; Milne, G. A.; King, M. A.; Thomas, I. D.: A new glacial isostatic adjustment model for Antarctica: calibrated and tested using observations of relative sea-level change and present-day uplift rates. *Geophysical Journal International* 190 (2012), No. 3, pp. 1464–1482 – doi:10.1111/j.1365-246X.2012.05557.x

[Wickert et al. 2005] Wickert, J.; Beyerle, G.; König, R.; Heise, S.; Grunwaldt, L.; Michalak, G.; Reigber, C.; Schmidt, T.: GPS radio occultation with CHAMP and GRACE: a first look at a new and promising satellite configuration for global atmospheric sounding. *Annales Geophysicae* 23 (2005), No. 3, pp. 653–658 – doi:10.5194/angeo-23-653-2005

[Wickert et al. 2009] Wickert, J.; Michalak, G.; Schmidt, T.; Beyerle, G.; Cheng, C.-Z.; Healy, S. B.; Heise, S.; Huang, C.-Y.; Jakowski, N.; Köhler, W.; Mayer, C.; Offiler, D.; Ozawa, E.; Pavelyev, A. G.; Rothacher, M.; Tapley, B.; Arras, C.: GPS radio occultation: results from CHAMP, GRACE and FORMOSAT-3/COSMIC. *Terrestrial Atmospheric and Oceanic Sciences* 20 (2009), No. 1, pp. 35–50 – doi:10.3319/TAO.2007.12.26.01(F3C)

[Wiese et al. 2016] Wiese, D. N.; Killett, E.; Watkins, M. M.; Yuan, D.-N.: Antarctic tides from GRACE satellite accelerations. *Journal of Geophysical Research: Oceans* 121 (2016), No. 5, pp. 2874–2886 – doi:10.1002/2015JC011488

[Winograd 1978] Winograd, S.: On computing the discrete Fourier transform. *Mathematics of Computation* 32 (1978), No. 141, pp. 175–199 – doi:10.1090/S0025-5718-1978-0468306-4

[Wolff 1969] Wolff, M.: Direct measurements of the Earth's gravitational potential using a satellite pair. *Journal of Geophysical Research (1896-1977)* 74 (1969), No. 22, pp. 5295–5300 – doi:10.1029/JB074i022p05295

[Woodworth 2019] Woodworth, P. L.: The global distribution of the M1 ocean tide. *Ocean Science* 15 (2019), No. 2, pp. 431–442 – doi:10.5194/os-15-431-2019

[Wouters et al. 2014] Wouters, B.; Bonin, J. A.; Chambers, D. P.; Riva, R. E. M.; Sasgen, I.; Wahr, J.: GRACE, time-varying gravity, Earth system dynamics and climate change. *Reports on Progress in Physics* 77 (2014), No. 11 – doi:10.1088/0034-4885/77/11/116801

[Wu 2016] Wu, H.: *Gravity Field Recovery from GOCE Observations*, Leibniz University Hannover, Doctoral dissertation, 2016. – https://dgk.badw.de/fileadmin/user_upload/Files/DGK/docs/c-777.pdf. – Accessed on: 2025-08-08

[Wu et al. 2006] Wu, S-C.; Kruizinga, G.; Bertiger, W.: Algorithm theoretical basis document for GRACE Level-1B data processing V1.2. *JPL D-27672, GRACE 327-741* (2006). – ftp://isdcftp.gfz-potsdam.de/grace/DOCUMENTS/Level-1/GRACE_Algorithm_Theoretical_Basis_Document_for_GRACE_L1B_Data_Processing.pdf. – Accessed on: 2025-08-08

[Yu et al. 2021] Yu, B.; You, W.; Fan, D.-M.; Su, Y.; Nigatu, Z. M.: A comparison of GRACE temporal gravity field models recovered with different processing details. *Geophysical Journal International* 227 (2021), No. 2, pp. 1392–1417 – doi:10.1093/gji/ggab279

[Yu et al. 2018] Yu, Y.; Chao, B. F.; García-García, D.; Luo, Z.: Variations of the Argentine Gyre observed in the GRACE time-variable gravity and ocean altimetry measurements. *Journal of Geophysical Research: Oceans* 123 (2018), No. 8, pp. 5375–5387 – doi:10.1029/2018JC014189

[Yuan 2018] Yuan, D.-N.: JPL Level-2 processing standards document, For Level-2 product release 06. (2018). – ftp://isdcftp.gfz-potsdam.de/grace/DOCUMENTS/Level-2/GRACE_JPL_L2_Processing_Standards_Document_for_RL06.pdf. – Accessed on: 2025-08-08

[Yuan 2019] Yuan, D.-N.: JPL Level-2 processing standards document, For Level-2 Product release 06 (v 1.0). *GRACE-FO D-103921* (2019). – ftp://isdcftp.gfz-potsdam.de/grace-fo/DOCUMENTS/Level-2/GRACE-FO_JPL_L2_Processing_Standards_Document_for_RL06.pdf. – Accessed on: 2025-08-08

[Zaglauer and Pitz 2003] Zaglauer, A.; Pitz, W.: CHAMP – The first Flexbus in orbit. *Acta Astronautica* 52 (2003), No. 9, pp. 747–751 – doi:10.1016/S0094-5765(03)00047-X

[Zahel 1997] Zahel, W.: Ocean tides. Wilhelm, H. (Eds.); Zürn, W. (Eds.); Wenzel, H.-G. (Eds.): *Tidal Phenomena*. Berlin, Heidelberg: Springer, 1997, pp. 113–143. – ISBN: 978-3-540-68700-9 – doi:10.1007/BFb0011460

[Zehentner and Mayer-Gürr 2016] Zehentner, N.; Mayer-Gürr, T.: Precise orbit determination based on raw GPS measurements. *Journal of Geodesy* 90 (2016), No. 3, pp. 275–286 – doi:10.1007/s00190-015-0872-7

[Zhong et al. 2022] Zhong, B.; Li, X.; Chen, J.; Li, Q.; Lu, B.: WHU-GRACE-GPD01s: Monthly gravity field models derived from GRACE intersatellite geopotential differences. *GFZ Data Services* (2022) – doi:10.5880/icgem.2022.002

[Zhou et al. 2024] Zhou, H.; Zheng, L.; Li, Y.; Guo, X.; Zhou, Z.; Luo, Z.: HUST-Grace2024: a new GRACE-only gravity field time series based on more than 20 years of satellite geodesy data and a hybrid processing chain. *Earth System Science Data* 16 (2024), No. 7, pp. 3261–3281 – doi:10.5194/essd-16-3261-2024

[Zingerle et al. 2020] Zingerle, P.; Pail, R.; Gruber, T.; Oikonomidou, X.: The combined global gravity field model XGM2019e. *Journal of Geodesy* 94 (2020), No. 7 – doi:10.1007/s00190-020-01398-0

[Zuber et al. 2013] Zuber, M. T.; Smith, D. E.; Watkins, M. M.; Asmar, S. W.; Konopliv, A. S.; Lemoine, F. G.; Melosh, H. J.; Neumann, G. A.; Phillips, R. J.; Solomon, S. C.; Wieczorek, M. A.; Williams, J. G.; Goossens, S. J.; Kruizinga, G.; Mazarico, E.; Park, R. S.; Yuan, D.-N.: Gravity field of the moon from the Gravity Recovery and Interior Laboratory (GRAIL) mission. *Science* 339 (2013), No. 6120, pp. 668–671 – doi:10.1126/science.1231507

[Zubov 1963] Zubov, N. N.: *Arctic Ice*. U.S. Navy Electronics Laboratory, 1963

Acknowledgements

I would like to express my deepest gratitude to Prof. Dr.-Ing. Jakob Flury for offering me the opportunity to join the institute, as well as for his professional guidance, support, and encouragement throughout my research and the writing of this thesis. I would like to extend my thanks to Prof. Dr.-Ing. habil. Florian Seitz and PD Dr.-Ing. Hamza Alkhatib for dedicating their time to review this thesis.

I also wish to thank all the colleagues at IfE for their support throughout my time at the institute. I am especially grateful to Dr.-Ing. Akbar Shabanloui for inspiring my interest in satellite geodesy during my master studies, for his mentorship, and for the engaging conversations we shared. A special thank you also to my dear colleague Mathias Frye, who consistently motivated me to make progress during the writing phase of this thesis and who also took the time to proofread large portions of it. This work would also not have been possible without the years of preliminary work on gravity field recovery conducted at IfE by Dr.-Ing. Majid Naeimi, as well as the continuous feedback on my research from colleagues in the GRACE community during the numerous meetings and conferences I had the opportunity to attend.

Finally, I would like to thank my friends and family for their support throughout this journey.